ADDIS ABABA UNIVERSITY

DEPARTMENT OF CHEMISTRY

Study of Charge Transport in Conjugated Polymers and Tuning Photovoltaic Performance in Bulk heterojunction Solar Cells

By

Fedlu Kedir

A Thesis Submitted to

The Department of Chemistry

Presented in Fulfilment of the Requirements for the Degree of

Doctor of Philosophy (Physical Chemistry)

ADDIS ABABA UNIVERSITY

ADDIS ABABA, ETHIOPIA

June 2015

Chemistry Department College of Natural Sciences Addis Ababa University

Study of Charge Transport in Conjugated Polymers and Tuning Photovoltaic Performance in Bulk heterojunction Solar Cell.

By Fedlu Kedir

Approved by:

1. Professor Teketel Yohannes
   Advisor
2. Professor Dr Vladimir Dyakonov
   External Examiner
3. Professor Tewodros Solomon
   Examiner
4. Dr. Mesfin Redi
   Examiner
5. Dr. Ahmed Mustefa
   Chairman

04.06.15

18.06.2015

June 4, 2015

ABSTRACT

Study of Charge Transport in Conjugated Polymers and Tuning Photovoltaic Performance in Bulk heterojunction Solar Cells

Fedlu Kedir Sabir

Addis Ababa University, Chemistry Department
Ethiopia, 2015

In this study, the effects of a moderate variation of macromolecular properties of poly(*p*-phenylene-ethynylene)-alt-poly(*p*-phenylene-vinylene)(PPE-PPV) statistical copolymers (AnE-PV*stat*) on charge transport properties were studied using differential time of flight (TOF) method. The influence of the macromolecular properies on bulk-heterojunction photovoltaic parameters was also investigated. Appreciable effects were obtained in both charge transport and photovoltaic properties.

Structural effects on drift mobility of holes and electrons also were investigated in series of the six anthracene-containing AnE-PV-*ab*, AnE-PV-*ae*, AnE-PV-*bb*, AnE-PV*stat*, AnE-PV*stat-4* and AnE-PV*stat-5* copolymers with different nature of side chains using TOF techniques. AnE-PV polymer with longer and linear octyloxy and dodecyloxy chains has shown negative effect on carriers mobility (μ) because of decreased interaction between adjacent hoping sites. AnE-PV polymers with the short and branched substituents of ethyl-hexyloxy exhibited higher mobility both for holes and electrons.

Impact of changing position of anthracene unit in poly{1,4-(5-[(2-ethylhexyl) oxy]-2-methoxy)phenylene-ethynylene-1,4-(5-[(2-ethylhexyl)oxy]-2-methoxy)phenyl -lene-vinylene-9,10-anthracenylene-vinylene}(MEH-PPE1-PAnV2) and poly{(1,4-(5-(2-ethylhexyl)-oxy)-2-methoxy)-phenylene-ethynylene-9,10-anthracenylene-vinyl-

ene-1,4-[(5-(2-ethylhexyl)-oxy)-2-methyloxy]-phenylene-vinylene}(MEH-PAnE1-PPV2) copolymers backbone on the hole and electron mobility was investigated using TOF method. The polymer having anthracene unit at the center between double bond and triple bond (MEH-PAnE1-PPV_2) has shown higher hole and electron mobility than the one having anthracene unit between two double bonds at edge of backbone (MEH-PPE1-$PAnV_2$). Effect of shifting position of anthracene unit is more significant in electrons mobility between the two polymers.

Moreover we studied hole mobility of phenylene-ethynylene (PE)/phenylene-vinylene (PV) hybrid conjugated polymer of general constitutional structure (-Ar-C≡C-Ar-CH=CH-)n using integration mode time-of-flight (I-TOF). The hole mobilities showed positive field dependent as expected for dispersive transport.

We have also studied the transport of holes in thin films of AnE-PVs copolymers by means of admittance spectroscopy as a function of field and temperature. The hole mobility exhibited strong field and temperature dependence. The study in this thesis was also extended to investigate the effect of barrier height between cathode work function and LUMO of AnE-PVstat copolymer on the bulk hole mobility using admittance spectroscopy. Devices of AnE-PVstat with the same anode material indium-tin-oxide (ITO)/poly(3,4-ethylene dioxythiophene):poly styrene sulfonic acid (PEDOT:PSS) and different cathode materials of Al, Ag, Au and Ag/PEDOT:PSS were prepared. Different hole transport properties were obtained from devices having different cathode materials. This might be due to the differences in electron injection efficiency among these cathode materials.

The influence of the low boiling point solvent additives such as iodomethane (IMe), iodoethane (IEt), iodobutane (IBu) and di-iodomethane (DiMe), and the

addition of poly(3-hexylthiophene-2,5-diyl) (P3HT) on the performance of poly[2,6-(4,4‟-bis(2-ethylhexyl)dithieno[3,2-b:2‟,3‟-d]silole)-alt-5,5‟-(3,6-bis[4-(2-ethylhexyl) thienyl-2-yl]-s-tetrazine] (PDTSTTz) and [6,6]-phenyl-C_{61}-butyric acid methyl ester (PCBM) BHJ solar cells were studied. The results have shown that the power conversion efficiency (PCE) of PDTSTTz:PCBM blend cell increased with the increase in length of carbon chains of the additives. Addition of P3HT on the PDTSTTz/PCBM system also brought enhancement in J_{sc} as well as PCE in PDTSTTz/PCBM solar cells.

Keywords: Charge transport, Time of flight, Admittance spectroscopy, Conjugated polymer, Macromolecular properties, side chain, interface barrier height, solvent additive, bulk heterojunction solar cells

This Dissertation is dedicated to My Mother Zahra Ahmed for Being Light of My Life.

ACKNOWLEDGEMENTS

These works come to realized to this level because of positive contributions of many individuals and institutions. I would like, in general, to acknowledge all of them for their support.

First of all, I would like to express my deep and especial gratitude to my supervisor, Prof. Teketel Yohannes, for his excellent guidance and motivation he made througout the whole period of my PhD study. Thanks him for sharing me his perspectives on the area of organic electronics and photovoltaic research. Thanks him also for facilitating my research fellowship in ICTP-TRIL program. His unreserved and consistent follow up on the progress of my research work was extremely valuable.

My sincere thanks also should go to Dr. Nadia Camaioni who has hosted me in her laboratory at CNR-ISOF in Bologna, Italy. I appreciate her follow up to check every data I generated and give valuable comments and suggestions. Beyond her supervision in the lab, her kindness and approachability make me feel free to discuss my research related issues.

I am deeply grateful to Dr. Daniel A. M. Egbe (Johannes Kepler University, Linz, Austria) and his groups for providing most of the polymers used in research work.

I also express my thanks to Dr. Francesca Tinti, and Mss. Sara Righi for introducing how to use admittance spectroscopy and Time of flight technique for measuring mobility of charges.

I would like to acknowledge the contribution of the following institutions: Department of Chemistry, Addis Ababa University, for giving the opportunity to conduct my PhD study; The Abdus Salam International Center for Theoretical Physics (ICTP) for granting a research fellowship through ICTP-TRIL program to

conduct part of my research work in CNR-Bologna, Italy; Debre Markos University for giving research leave and sponsorship to pursue my PhD study.

My thank goes to Dr. Siraye Esubalew, Dr. Getachew Adam and Dr. Sisay Taddese for sharing their research experience in area of organic photovoltaics. I also thank my friends Mr. Bedasa Abdisa, Endale Tsegaye, Hagos Tesfay, Asegid Ergete, Girma Erjabo, Zekarias Teklu, Hagos Tikue, Dawit Tibebu and Yishak Tsegazeb for joyful time we had together at Addis Ababa University.

I would like to express my thanks to the staff members of Chemistry department of Addis Ababa University who have contributed for the success of my PhD study; Dr. Ahmed Mustefa, Dr. Shimelis Admassie, Dr. Mesfin Redi, Prof. Theodros Solomon, Prof. Wondimagegn Mammo, Dr. Edwardo Pérez, Ato Sahlemichael Demie and Saba Mesfin.

I would also like to extend my gratitude to Dr. Gabriella Ghermandi, Dr. Alberto Maurizi, Dr. Valeria Fattori, and Dr. Alberto Zaneli for sharing friendship and ideas during my stay in Bologna.

I am greatly indepted to my wife w/r Mahbuba Kedir and my sisters w/r Fedila Kedir and w/r Aziza Kedir for their unreserved support and encouragement they offered to me throughout the entire period of my PhD study.

Fedlu Kedir Sabir

Addis Ababa

Ethiopia

Table of Contents

List of Figures

List of Tables

List of Symbols and Abbrevations

AM1.5	Air mass 1.5
μ	Mobility
D	Diffusion coefficient
E	Electric field
E_t	Energy of trap state
μ_o	Mobility at zero electric field
β_h	Hole mobility dependent factor
β_e	Electron mobility dependent factor
γ	Poole-Frenkel constant
σ	Energetic disorder
Σ	Positional disorder
A	Area
J	Current density
d	Thickness of film
I-TOF	Integral-Time- Of-Flight
τ (τ_{tr})	Transit time
TOF	Time-Of Flight
τ_Q	Transit time in Integral TOF
Q_m	Maximum accumulated charge
Q_o	Total photogenerated charge in the devices
AS	Admittance Spectroscopy
T	Time
ω	Angular frequency

F	Frequency
G	Conductance
ITO	Tin-oxide doped with indium
TCO	Transparent and conducting oxide
PEDOT:PSS	Poly(3,4-ethylene dioxythiophene) : polystyrenesulfonic acid
LUMATION Green	The polymer known for green light emission
B	Susceptance
Y	Admittance
C	Capacitance
α	Dispersion parameter
PCE	Power conversion efficiency
P3HT	Poly-3-hexylthiophene
PCBM	[6,6]-phenyl-C_{61}-butyric acid methyl ester
HOMO	Highest occupied molecular orbital
LUMO	Lowest unoccupied molecular orbital
OPV	Organic photovoltaics
I_{sc}	Short circuit current
J_{sc}	Short circuit current density
I_{mp}	Maximum current point
V_{mp}	Maximum voltage point
P_{mp}	Maximum power point
V_{oc}	Open circuit voltage
FF	Fill factor
P_i	Power of incident light

P_{out}	Power output
R_s	Series resistance
R_{sh}	Shunt resistance
V_{bi}	Build-in- voltage
IMe	Iodomethane
IEt	Iodoethane
IBu	Iodobutane
DIMe	Di-iodomethane
AnE-PV	anthracene-containing poly(*p*-phenylene-ethynylene)-alt-poly (*p*-phenylene-vinylene) (PPE-PPV)
AnE-PV*stat*	Statistical anthracene-containing poly(*p*-phenylene-ethyny lene)-alt-poly(*p*-phenylene-vinylene) (PPE-PPV)
PDTSTTz	poly[2,6-(4,4‟-bis(2-ethylhexyl)dithieno[3,2-b:2‟,3‟-d]silole)-alt-5,5‟-(3,6-bis[4-(2-ethylhexyl)thienyl-2-yl]-s-tetrazine]
MEH-PPE_1-$PAnV_2$	poly{1,4-(5-[(2-ethylhexyl)oxy]-2-methoxy)phenylene-ethy nylene-1,4-(5-[(2-ethylhexyl)oxy]-2-methoxy) phenylene-vin ylene-9,10-anthracenylene-vinylene}
MEH-$PAnE_1$-PPV_2	poly{(1,4-(5-(2-ethylhexyl)oxy)-2-methoxy)-phenylene-ethynylene-9,10-anthracenylene-vinylene-1,4-[(5-(2-ethyl-hexyl) oxy)-2-methyloxy]-phenylene-vinylene}
PL	Photoluminescence

1. Basics of charge transport properties in conjugated polymers and bulk heterojunction photovoltaics

1.1. Introduction

Before 37 years, all carbon-based polymers were rigidly regarded as insulators. The idea that plastics could be made to conduct electricity would have been considered to be absurd. Indeed, plastics have been extensively used by the electronics industry because of this very property. They were utilized as inactive packaging and insulating material. This very narrow perspective is rapidly changing as a new class of polymer known as intrinsically conductive polymer or electroactive polymers are being discovered [1].

The electrical conductivity of conjugated polymers was first discovered by Alan J. Heeger, Alan G. MacDiarmid, and Hideki Shirakawa on doped polyacetylene in 1977 [1]. This magnificent finding earned them the 2000 Nobel Prize in Chemistry. Thanks to their pioneering discoveries, this versatile plastic conductor, which is a type of polymer with extended conjugated backbone, is now researched in a large international field with significant academic and industrial activities [2]. The type of conjugated polymer called „polyacetylene" could become highly electrically conductive after undergoing a structural modification process called doping. The polymer is called a „conjugated polymer" because of the alternating single and double bonds in the polymer chain.

Due to the special conjugation in their chains, it enables the electrons to delocalize throughout the whole system and thus many atoms may share them. The delocalized electrons may move around the whole system and become the charge carriers to make them conductive [3]. Then the polymer can be transformed into a conducting form

when electrons are removed from the backbone resulting in cations or added to the backbone resulting in anions. Anions and cations act as charge carriers, hopping from one site to another under the influence of an electrical field, thus increasing conductivity [3 - 5].

After thirty-seven years of maturation, the studies on conjugated polymers and oligomers have been a flourishing branch of materials science with many opportunities for applications in electronic and photonics. In conjugated polymers, the π-conjugated system extends over the whole polymer chain, thus allowing for delocalized states in one direction. Therefore, conjugated polymers were initially regarded as one-dimensional semiconductors. In their pioneering work Su, Schrieffer, and Heeger [6], studied the interaction of an excitation with an ideal one-dimensional lattice, neglecting Coulomb interactions and disorder effects.

In the 1980s, the future for conjugated polymers in commercial development further attracted tremendous scientific and industrial interest due to their potential in achieving the goal of light emitting device technology. That is economically viable for solid-state lighting and displays, which offer significant gains in power efficiency, colour quality, and lifetime at lower cost and less environmental impact than traditional incandescent and fluorescent lighting [7 - 12].

Extensive studies have been made on the synthesis, properties and applications of a wide variety of conjugated polymers, including polyacetylene (PA), polypyrrole (PPy), polythiophene (PT), polyphenylene (PP), poly(phenylenevinylene) (PPV), poly(thienylene vinylene) (PTV), poly(para-phenylene) (PPP), polythiophene (PT). The structures, names, and bandgap of these polymers are indicated in Table 1.1. At the same time, various chemical structure modifications have been made to improve

solubility, processibility, and morphology to achieve better performance in a variety of applications [13].

Semiconducting polymers are key materials to transform the scenario of the modern electronics and display technology. Beginning from few decades back, a lot of research works has been conducted to produce devices with low cost, reasonable stability and good performance [13].

Table 1. 1. Structure, name, bandgap and conductivity of the common conjugated polymers.

structure	polymer	π–π* bandgap (eV)	condcutivity (s/cm)
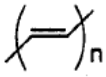	polyacetylene	1.5	10^3 - 1.7x10^5
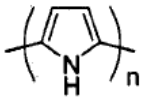	polypyrrole	3.1	10^2 - 7.5x10^3
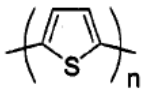	polythiophene	2.0	10-10^3
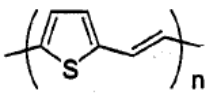	poly(thienylene vinylene)	1.6	40
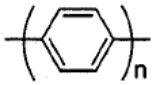	poly(*para*-phenylene)	3.0	10^2 -10^3
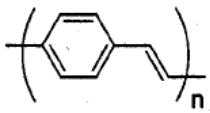	poly(*p*-phenylene vinylene)	2.5	3-5x10^3
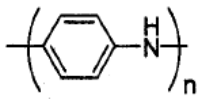	polyaniline	3.2	0-200

1.1.1. Electronic properties of conjugated polymers

Mode of charge carrier conduction in semiconducting (conjugated) polymers is carried out with help of delocalization of π-electrons over alternating single and

double bonds. In addition to in-plane sigma orbitals of carbon in conjugated polymers, there is also one π-orbital perpendicular to the plane of the polymer in that carbon. π-electron system is formed by the p_z - orbitals of the sp^2 - hybridized carbon atoms. From the four valence electrons of carbon, three of them occupy the strong sigma bonds with two carbons and one hydrogen atom; and the fourth valence electron occupies the non-hybridized p_z - orbital. The overlapping π-elecectron wave functions together form a π-band. The delocalization of the π-electrons in over several sequential carbon atoms in chain forms the π-bands. The presence of an energy gap between the filled and empty bands gives a semiconducting nature to the polymer. Optical and electrical properties of conjugated systems are directly related with the degree of delocalization of the π-electrons.

One of prominent advantages of using conducting polymers as optoelectronic and photovoltaic devices is their ability to be modified with physical, chemical, electrochemical properties. Hence, the properties of semiconductor devices can be easily tailored for selected application, for example, the bandgap in these systems can be easily tuned by gentle modification of the chemical structure.

The role of side chain groups, inter-chain interactions, and π-π stacking are very immense factors in controlling the degree or effectiveness of charge carriers delocalization. Even though charge carriers delocalization along the polymers back bone are contributing the greatest share, a weak inter-chain coupling also helps charge carriers transfer across carbon chains between scattering events from defects and disorder [14].

Conjugated polymers are characterized by an extended π-conjugated system along which charge carriers can be delocalized. Conjugated polymers have degenerate

molecular orbital of double bonds as highest occupied molecular orbital (HOMO) band and a lowest unoccupied molecular orbital (LUMO) band, which are analogue of the valence band and the conduction band of the inorganic semiconductors. The energy difference between these two bands is called the bandgap, E_g. The neutral or undoped conjugated polymers are usually semiconductors. Chemical or electrochemical oxidation (p-doping) introduces holes onto the conjugated backbone [15]; and reduction (n-doping) adds electrons on it. After doping, the electrical conductivity increases by either mobility of holes or electrons dramatically, and the doped conjugated polymers behave as conductors.

1.1.2. Advantages and applications of conjugated polymers

Compared with the traditional inorganic semiconductors, conjugated polymers have a number of advantages. Most of conjugated polymers are processed from solution or they can be melted in to a large area polymer film; they are also flexible and with lightweight which are prominent advantages in comparison with the brittle and heavy inorganic materials [16 - 18]. Furthermore, there are many possibilities/options to tailor the electronic structures of conjugated polymers to tune the physical properties. In their undoped (the neutral state) conjugated polymers are used as active semiconducting materials in electronic and optical devices such as photovoltaic cells (PV), light emitting diodes (LED) [19], and field effect transistors (FET) [20]. The recent studies have shown that conjugated polymers are promising and cost effective electrode materials in energy storage devices [21]. In the doped state, conjugated polymers are used for electrostatic dissipation purpose, electromagnetic shielding materials, and electronic conductors. Furthermore, the reversible switching between

neutral and doped states leads to the electrochromic devices, battery electrodes, and biosensors [22, 23].

The main limitations to a larger exploitation of OPV, OFET and OLED come from their poor mobility of charge carriers. By tuning some properties of conjugated polymers during synthesis, solution processing, and through film treatments after deposition carriers‟ mobility in these optoelectronic devices can be improved. During synthesis, side chains and polymer backbone repeating units (molecular weights) can be controlled. Solution preparation process starting from type of solvent used through concentration of the solution to film casting techniques (such as drop-casting, spin-coating, doctor Blade, and evaporation techniques) differently affect the morphology and crystallinity of the active organic/polymer/small molecule sandwiched by the two electrodes of the devices [24]. The quality of the morphology and crystallinity of the film limits the mobility of charge carriers in the devices. Molecular weight, side chain nature, polydispersity index and etc. (which are discussed later) are major properties that control mobility of carriers by monitoring morphology of the active layer in the device [25].

1.1.3. Anthracene –based conjugated polymers/copolymers

Anthracene-based conjugated polymers are conjugated polymer semiconductors that have an anthracene unit in the backbone of the polymer and copolymer repeating unit. Anthracene based conjugated polymers, poly(p-phenylene-ethylene)-alt-poly(p-phenylene-vinylene)s (PPE–PPVs), are a new class of conjugated compounds combining the intrinsic properties of both poly(p-phenylene-ethylene) (PPE) and poly(p-phenylene-vinylene) (PPV) into a single polymeric backbone structure with specific properties [26].

High-molecular-weight and thermostable series of anthracene-based polymers have been synthesized *via* the Wittig polycondensation and Horner-Wadsworth-Emmons olefination reaction with good yields. These organic materials are soluble in common organic solvents and show good film-forming abilities. Their macromolecular structures were characterized by NMR, FT-IR spectroscopies and steric exclusion chromatography, their thermal behaviors were analyzed by differential scanning calorimetry and their HOMO-LUMO energy levels were estimated by cyclic voltammetry. They exhibit high molar masses with polydispersity indices below 2.5 [27 - 29]. The optical properties of these π-conjugated systems were investigated by UV-visible absorption and photoluminescence spectroscopies. The PPV backbone involving acetylene units opened way to new types of conjugated systems denoted as PPE–PPVs, showing outstanding optical and electrical properties, for LED, FET and PV applications [28 - 31].

These class of conjugated polymers has successfully been used either as donor or acceptor components in solar cell devices. Open-circuit voltages, V_{oc}, as high as 0.95 V and 1.50 V have been obtained from polymer-PCBM heterojunction cells [32 - 34] and from polymer-polymer bilayer cells [35, 36], respectively. The short circuit currents, I_{sc}, and the filling factors, FF, were found to be greatly dependent on the triple bond/double bond ratio as well as the nature and size of the soluble alkoxy side groups [37].

The effect of the spacer group structure on the photo-physical behavior, π-π stacking ability and charge carrier transport properties of the polymer has been studied [38] and the effect of conjugation pattern on the photo physical properties of poly(arylene-ethynylene)-alt-poly(arylene-vinylene)s (PAE-PAVs) combine the intrinsic features

of both poly(arylene-ethynylene) (PAE) and poly(arylene-vinylene) (PAV) in a single polymeric backbone. They exhibit enhanced electron affinity, as compared to parent poly(p-phenylene-vinylene) (PPV), making electron injection easier, placing them as potential candidates for low turn-on voltage organic light emitting diodes (OLEDs). Depending on the chemical structures, PAE-PAVs have been efficiently used either as donor materials in polymer-PCBM (phenyl-C61-butyric acid methylester) or polymer-vinazene (2-vinyl-4,5-dicyanoimidazole) bulk heterojunction solar cells or as acceptor materials in polymer-polymer bilayer and blend of solar cells [39].

The charge carrier mobility and photovoltaic response of the two anthracene-containing families of polymers such as MEH-PPE_1-$PAnV_2$ and MEH-$PAnE_1$-PPV_2 were investigated; where by the position of anthracene has been shifted from between two double bonds to the bridge between triple bond and double bond. The better photovoltaic performance was obtained for the polymer having anthracene unit between triple bond and double bond at the center of the backbone [40].

The side chains and their statistical distributions in anthracene based polymers can also significantly affect the photovoltaic device performance [41, 42]. Organic field-effect transistors also were fabricated to investigate hole mobilities in these new materials. Large variance was observed, falling in the range of almost two orders of magnitude, indicating rather different π–π stacking behavior of the polymer backbones owing to side-chain modifications. Moreover, ambipolar nature of these polymers makes them good materials for light-emitting diode (LED) applications. Polymer LEDs using the polymers AnE-PV*stat*, AnE-PV*stat3*, AnE-PV*stat4*, and AnE-PV*stat5*, as the active layer showed turn-on voltage of ~ 2 V and exhibited red light emission [41].

Other series of anthracene based conjugated polymers, the alkoxy-substituted arylene-ethynylene and arylene-vinylene conjugated polymers, were compared for their difference in photophysical properties. The presence of anthracene units in arylene-vinylene conjugated polymer leads to a red shift of its absorption and emission spectra relative to arylene-ethylene. Strong self-reabsorption after excitation in solution was observed for arylene-vinylene conjugated polymer. The solid-state photophysical properties of arylene-vinylene conjugated polymer greatly depend on the nature (linear or branched), length, and location of the grafted alkoxy side groups [32].

The effect of the amount of PCBM on anthracene-containing poly(p-phenylene-ethynylene)-alt-poly(p-phenylene-vinylene)(PPE–PPV)polymer (AnE-PVstat) for solar cells performance was investigated [43]. The anthracene-containing poly(p-phenylene-ethynylene)-alt-poly(p-phenylene-vinylene)(PPE–PPV) polymer (AnE-PV stat) with 75% PCBM content gave improved efficiencies (η = 2.13%) and fill factors (57%) in the resulting solar cells under standard solar irradiation of 100 mW/ cm^2 (AM 1.5 G) with ambient conditions [43].

Impact of solely linear and solely branched as well as mixed linear and branched alkoxy side chains in the anthracene containing copolymers on π-π stacking ability of the material and, absorptive behavior, hole mobility and solar cell active nano-scale morphology were studied [44]. The best performance was achieved from mixed linear and branched side chain (AnE-PVab) showing better stacking ability with stacking distance of 0.386 nm compared to the others. Poor photovoltaic performance was obtained from anthracene based polymers that have low stacking ability, but they exhibit higher charge carrier mobility [44].

1.1.4. Charge transporting materials and their characteristics

Charge carrier‟s mobility, solid- state anodic potential (ionization potential), cathodic reduction potential (solid-state electron affinity), and optical bandgap are some fundamental characteristics of charge carriers‟ transporting materials. In the case of thin films, electron affinity and ionization potential of the charge transporting materials (conducting polymers) determined by ultraviolet photoelectron spectroscopy and inverse photon spectroscopy. In the case of solution samples, oxidation and reduction potential of conducting polymers can be determined using cyclic voltammetry [45]. Energy levels of highest occupied molecular orbital (HOMO) is corresponding to ionization or oxidation potential of transporting materials, and that of lowest unoccupied molecular orbital (LUMO) is corresponding to electron affinity or reduction potential of the charge transporting materials. The information about how much of the energy barriers exist for the injecting of hole from ITO anode into hole transporting material is obtained from the measure of ionization or oxidation potential of the materials. In the same analogy, the energy barriers exist upon injecting electrons from cathodic electrode in to electron transporting medium is determined from reduction potential of the material [45, 46].

1.2. The most widely accepted models for explaining charge transport

The special case of dispersive systems is described below. Broadly speaking, most common transport models that attempt to describe the observed behavior of mobility in dispersive systems fall into three categories: such as (1) Hopping in a Gaussian disorder model (GDM), (2) Poole Frenkel (PF) model, and Multiple trap and release (MTR) model

1.2.1. Hopping in Gaussian disorder model (GDM)

In the 1990s, the field-dependent mobility model was initially proposed by B*ä*ssler, as the result of assuming hopping transport in a Gaussian density of states (DOS) and he is pioneer for the Gaussian disorder-based hopping model for transport in disordered semiconducting polymers [47, 48]. The mechanisms of charge transport in organic conducting materials are different from those for inorganic semiconductors. The DOS is easily determined for inorganic semiconductors from optical transitions, from the valence band (VB) to the conducting energy band (CB). The same approach is difficult to apply for disordered organic systems, as the optical spectra involve excitonic transitions. B*ä*ssler suggested a Gaussian profile for the DOS based on the observed shapes of absorption and fluorescence bands [48]. The organic materials do not have energy bands, rather the molecules or chains of the system interact by weak Van der Waals forces. Charge carriers, that is, hole and electron, for organic materials corresponds to the cation and anion radicals of a molecule. It has generally been accepted that charge transport in organic disordered systems, for example, polymers and molecularly dispersed polymers, takes place by a hopping process. That means, charge transport in organic disordered systems is considered as a sequential oxidation and reduction process over molecules/conjugated polymers [45].

Since the extent of the π-electron delocalization length in the polymer main chain is random, there is a fluctuation in the lattice polarization energy that leads to energetic disorder [48]. This random variation manifests itself in the Gaussian profile of the DOS, and the transport is assumed to involve charge carrier hopping among localized sites.

The disorder formalism assumes that charge transport in disordered systems like in conjugated polymers takes place by hopping through a manifold of localized states subject to the fluctuations of both hopping site energy and intermolecular wave function overlap and that both the hopping site energy and the intermolecular distance follow the Gaussian distributions.

Gaussial distribution model (GDM) assumes Gausian distribution of hopping site energies and distances. The Miller and Abraham‟s expression [49] can describe the jumping rates of charge carriers. The empirical equation for the dependence of mobility on field and temperature, as suggested by GDM, is

$$\mu = \mu_0 \exp[-\left(\frac{2\sigma}{3kT}\right)^2] \exp[C \{ \left(\frac{\sigma}{kT}\right)^2 - \Sigma^2 \} E^{1/2}] \quad (1.1)$$

where μ_0 is the pre-factor mobility, σ is the energetic disorder (the width of Gaussian distribution of site energies), Σ is the measure of positional disorder, k is the Boltzmann constant, T is temperature in Kelvin, and C is an empirical constant. Hopping probability of charge carriers strongly related to the site energies and on the inter-site distances. Positional disorder (Σ) arises due to spacial and structural randomness of the dopant. Energetic disorder is usually due to the dipolar interactions between dopants, dopant and polymer, and dopant and impurities [50].

1.2.2. Poole Frenkel (PF) model

Original PF mechanism was for a long time considered unacceptable for explanation of the field dependent mobility in disordered organic materials due to absence of charged traps [51]. Yet in a recent paper the PF model was revitalized by Rackovsky and Scher [52] who argued that a very low density of Coulomb traps is enough to produce an essentially non-dispersive PF charge transport.

Calculation of the PF effect was carried out for the usual case of an isolated Coulomb trap only [52]. Yet charged traps produce strongly correlated energy landscape, and the hopping charge motion in such landscape usually has many features that cannot be captured by the approximation taking into account interaction of charge carrier with the isolated force center.

Poole-Frenkel effect has been observed in many disordered molecules [53 - 55]. In disordered systems, electric conductivity or drift mobility, is inversely proportional to the square root of the electric field E. The applied electric field assists in lowering the Coulomb potential barrier that a charge carrier needs to overcome before leaving the charge center traps (Figure 1.1) [56]. The conductivity then shows the following field dependence:

$$\sigma = \sigma_0 \exp(\beta_p E^{1/2}/2kT) pEkT \quad (1.2)$$

$$\beta_p = 2(e^3/4\pi\varepsilon_o\varepsilon_r)^{\frac{1}{2}} \quad (1.3)$$

where σ_0 is the low field conductivity; β_p is the Poole-Frenkel field lowering coefficient; E is the applied electric field; ε_o is the vacuum permittivity; ε_r is the high frequency dielectric constant; e is the unit of electronic charge.

The application of an electric field E lowers the potential barrier in the direction of the field by an amount proportional to $E^{1/2}$ [57]. In Figure 1.1, solid curves show the lowering of effect of electric field on the barrier and dashed lines represent Coulomb potential barrier without applying electric field.

Sometime negative electric field dependence is found in disordered polymers, which has been a subject of debate during the last several decades [53].

1.2.2.1. Temperature and field dependent mobility

Mobility has a strong dependence on both temperature and applied electric field. It is a phenomenon that helps to understand the underlying transport mechanism. Usually, a Poole–Frenkel (PF)-type dependence of the mobility on the electric field over an extended range is observed ($\ln \mu \sim SE^{1/2}$, where S is the slope parameter) [58]. This holds true for a large number of systems along with other features such as sign-reversal of the coefficient S at a particular temperature, deviation from PF law at low electric fields, etc.

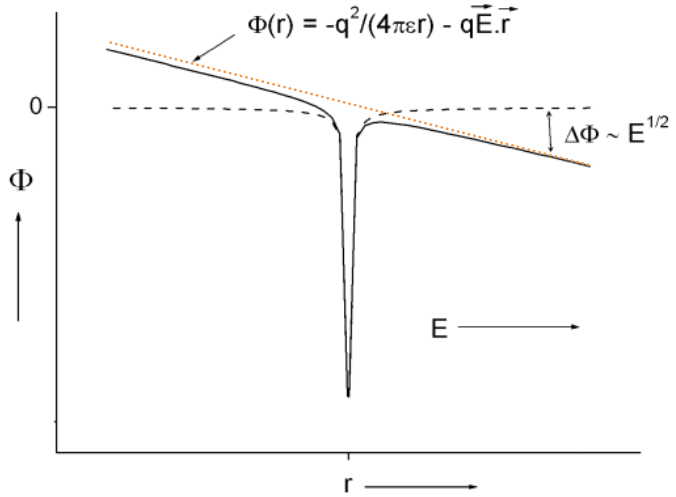

Figure 1. 1. Potential barriers in the Poole–Frenkel model. Solid curves represent the lowering effect of electric field on the barrier and dashed lines represent Coulomb potential barrier without applying electric field. Dotted line represents lowering effect of uniform electric field.

The PF law arises naturally from the theory of trapping/detrapping in disordered materials [58]. The application of electric field results in a lowering of the potential barrier in the direction of the electric field, shown schematically in Figure 1.1. This favors charge carrier motion from a trapping center. With applications of an electric

field *E,* the potential around an immobile positive trapping center (which traps/detraps electrons) is given by Equation 1.4a.

$$\Phi_{(\vec{r})} = -\frac{q^2}{4\pi\varepsilon r} - q\vec{E}.\vec{r} \qquad (1.4a)$$

The lowering of the energy barrier [58] in the direction of the field is then obtained by

$$d\Phi/dr = 0 \text{ or } \Delta\Phi \sim E^{1/2} \qquad (1.4b)$$

However, PF-type dependence is also seen in the absence of traps and this creates the scope for interpretation of the phenomenon from alternative models. Furthermore, negative field dependence has been observed in some systems in a range of fields, which is contrary to intuition. The temperature dependence of ln μ has been usually described as $\frac{1}{T^2}$ but in many cases, Arrhenius-type $\frac{1}{T}$ dependence is suggested [58 - 63].

1.2.3. The multiple trapping and release model

Another model used to account for the low mobility in amorphous organic materials is the multiple trapping and release model. In this model, a narrow band is associated with a high concentration of trap levels. Traps are levels localized at lattice defects or impurities in which the charge carriers are immobilized. These traps can be deep traps, which are located near the center of the band gap, or shallow traps, which are located close to the conduction or valence band. Developed for hydrogenated amorphous silicon (a-Si:H) by Tong *et al* [64], the multiple trapping and release model has been used more recently by Horowitz et al [65] to explain the transport in sexithiophene FETs. This model assumes an exponential distribution of gap states. The charges injected or the charges that are already present in the organic

semiconductor are trapped into localized states with a probability close to one and then released through a thermally activated process. The drift mobility μ_D is given by:

$$\mu_D = \mu_0 \alpha \exp\left(\frac{E_T}{k_B T}\right) \quad (1.5)$$

where μ_0 is the mobility at the band edge, α is the ratio between the effective density of states at the transport band edge and the density of traps, and E_T is the energy of the trap state. It has been demonstrated that the transport of carriers depends on the energy level of the trap states, the temperature and the voltage applied [65].

1.3. Structural effects on charge transport properties in Conjugated polymers

The charge transport mechanisms in organic systems depend upon the morphology of films, order, and molecular structure. Molecular weight, nature of side chains, molecular chain packing are some of structural properties of polymer that can influence morphology and chain organizations of the organic film in the mobility devices. The morphology and chain organization in turn affect charge carriers‟ mobility.

1.3.1. Effect of Molecular weight (MW) on charge carriers transport property

The basis for assuming the effect of molecular weight of conjugated polymers on the charge transport and photovoltaic properties lies on the experimental facts that polymers with different molecular weights have different degree of solubility in the same solvent they have been prepared. The films deposited from these polymers with different molecular weight and solubility leads to the different morphology of the resulting polymer films [66, 67]. Therefore, the change in morphology of the polymer films lead to variation in charge carriers mobility in OFET, OLED and OPV devices.

Several structural features of most polymers such as chain planarity, extent of π-stacking, type of supramolecular aggregation, etc. can be tuned controllably by changing the type of macromolecular properties such as molecular weight (MW) and polydispersity [60]. These properties have an impact on the electrical and optical properties of conjugated polymer based devices.

The effects of MW and the processing conditions on the polymer supramolecular organization, its morphology and charge carriers mobility have been investigated for regioregular poly(3-hexylthiophene) (RR-P3HT) thin layers used for the fabrication of field-effect transistors (FETs). It has been demonstrated that the chain length of the deposited polymer is the determining factor in the fabrication of layers with high carriers mobility (hole mobility) which changes from 10^{-5} $cm^2/(Vs)$ for the shortest chains (Mn = 1 kDa) to 0.04 $cm^2/(Vs)$ for the longest ones (Mn = 27 kDa) [61].

Some other groups in this area have reported independently that the mobility of field-effect transistors made from regioregular poly(3-hexylthiophene) (P3HT) increases strongly with molecular weight. Two different models were presented: one proposing carrier trapping at grain boundaries and the second putting emphasis on the conformation and packing of the polymer chains in the thin layers for different MWs [62]. According to some reports, the transport properties of charges in films of P3HT with different MW were largely determined by the crystallinity of the samples; and not by the perfection of the packing of the chains in the individual crystallites [62].

For the same polymer, P3HT, the dependence of electrical properties on the molecular weight was investigated by Zen *et al* [63]. In P3HT charge carriers mobility was observed strongly depending on MW, with low mobility ($\mu_{sat} \sim 10^{-7} cm^2/Vs$) was

obtained from high MW polymer and high mobility ($\mu_{sat} \sim 10^{-3}$ cm^2/Vs) was obtained from the low MW polymer [63].

Kline *et al* [68], has reported correlation between the field effect mobility of charge carriers in RR-P3HT and its MW, with mobility values increased from 1.7 x 10^{-6} cm^2/Vs to 9.4 x 10^{-3} cm^2/Vs for the MW increased from 3.2 to 36.5 kD. The variations in MWs were also accompanied by significant change in the active layer film morphology.

According to other reports [64], increasing the MW of the low-bandgap semiconducting copolymer, poly[(4,4-didecyldithieno[3,2-b:2‟,3′ -d]silole)-2,6-diyl-alt-(2,1,3- benzothiadiazole)-4,7-diyl], Si-PDTBT, from 9 kDa to 38 kDa improves both photoresponsivity and charge transport properties dramatically. The photocurrent measured under steady state conditions is 20 times larger in the higher MW polymer (Si-PDTBT). These polymers showed that the field effect mobility of high MW Si-PDTBT, $\mu = 3.6 \times 10^{-2}$ cm^2/Vs, is a factor of 700 larger than the mobility obtained for the low MW Si- PDTBT (9 kDa) polymer [64].

Cooper *et al* [69] also studied the effects of MW on the dissolution rates of thin poly(methyl methacrylate) (PMMA) films, and found that dissolution results in a non-linear behavior when the logarithm of dissolution rate was plotted against the logarithm of number average molecular weight (Mn). In addition, Manjkow *et al* [70] discovered that dissolution not only can be affected by the polymer MW, but also by its polydispersity. They found that polydisperse samples dissolved about twice as fast as monodisperse ones of the same Mn [71].

1.3.2. Impact of side chain nature on charge carries' mobility in conjugated polymers

The nature or behavior of side chains substituted to backbone of the conjugated polymers affects both optical and electronic properties of the material device. Side-chain variation on the polymer backbone has been studied in terms of steric hindrance and electronic effects and related to morphology and charge-carrier mobility [72]. For instance, bulky alkyl substituents directly linked to the conjugated rod hampers a planar conformation [73]. Systems employing linear or branched side-chain substituents have been compared based on their photophysics and charge transport. The linear substituents showing emission at higher wavelength due to formation of π-stacked aggregates, while the branched substituents show blue-shifted emission lacking higher order [74].

In the investigation made on effect of side chain length on transport and film crystalline properties of linear derivatives of thiophene, side chain length-property relation was clearly indicated. An X-ray, atomic force microscopy (AFM), and FT-IR data indicated that the film prepared from P3BT was more ordered than that of P_3OT. The field effect mobility of P3BT is $0.01 cm^2V^{-1}s^{-1}$ and that of P3OT is 5.2×10^{-4} $cm^2V^{-1}s^{-1}$. The mobility of the film with shorter side chain is 20 times greatert than that of the mobility for longer side chains. This difference suggested being due to the difference in number of perpendicularly oriented layers with respect to substrate in P3BT and P3OT. Molecules with short butyl side chains had a higher density of π-stacked ordered structures in the charge transport region [75].

In contrast, there are some reports that show that crystallinity or orderings increases with increasing the length of substituent group. The structures of ASE-

Ns(poly[oxy(N-alkylsulfonylmethyl)ethylene]s were strongly dependent on the alkyl side-chain length. X-ray, IR and DSC data have shown that structural order of the polymer increase with increasing alkyl substituent from C-2 to C-16 (from amorphous to well ordered crystalline structure) [76].

Electronic nature of the substituent group also affects the properties and the performance of optoelectronic devices. The effects of alkyl substituent and alkoxy substituents on charge transport properties were compared. The electronic and charge transport properties of poly(3-hexyl thiophene) and poly(3-oxylhexyl thiophene) were studied. The hole mobility calculated for alkyl derivative is $0.15 cm^2\ V^{-1}S^{-1}$ (experimental value is 0.10 $cm^2V^{-1}s^{-1}$) while for alkoxy derivative is 0.49 $cm^2V^{-1}s^{-1}$. This is because the oxygen atom in the alkoxy chain improves electrical properties, such as lower ionization potential and reorganization energies; alkoxy chains produce a larger electronic delocalization along the polymer backbone, alkoxy chain that is coplanar with backbone, allowing polymer chains to approach each other [77].

Linearity and branchedness of side chains to conjugated polymers is another phenomenon to affect optoelectronic properties of polymer-based organic electronic devices. The polymers with branched side chains have less π-π stacking tendency than with linear once. In the case of branched side chain conjugated polymers photoconductivity is dominated only in intra-molecular system. Molecular dynamic (MD) simulation of charge mobility and transport mechanism suggested for P3HT that the resultant mobility along the π-π inter-chain direction is significantly less than that of along the intra-chain direction. There is no better stacking ability in the case of branched substituent conjugated AnE-PVba and AnE-PVbb polymers, but the amorphous nature in case of linear ones favors high miscibility between donor and

acceptor. That in turn enhances the charge carrier recombination and that have negative impact on FF and J_{sc} [78]. As the result, the main charge transfer route in P3HT ordered domains is an intra-molecular rather than an inter-molecular [79].

According to Rathgeber *et al* and others [80, 81], the inter-chain interactions and degree of π-π interaction between main polymer chain systems were systematically tuned by decorating conjugated polymer backbone with linear or branched or combination of linear and branched alkoxy/alkyl side chains.

The conjugated polymers with all-linear side chains attached close to the anthracenylene-ethynylene unit (AnE) show a layered structure. In contrast, attachment of branched side chains at AnE unit leads to amorphous polymers. Due to structural difference, the first group of polymers exhibit red shift emission and better degree of order and shorter π-π stacking distance than the second ones [44].

The all-linear substituted regular copolymer (AnE-PV) well ordered and organize in a stacked structure with edge-on orientation relative to the substrate. This order is preserved (or even enhanced) in the presence of PCBM, but the photovoltaic performance in the BHJ solar cells is only moderate. Well-aligned edge-on orientation is not fosters charge transport from active layer to the electrodes due to the isolating character of the side chain layers.

However, the branched side chains prefer face-on alignment. Most likely, the branched side chains can minimize their unfavorable contact with the interfaces just by bringing the methyl group of the branches into direct contact with the surface. This reduction in unfavorable interactions seems to be sufficient so that favorable phenyl-substrate interactions can promote face-on configuration. Together with the absence (reduction) of grain boundaries, the better contact with the electrodes, and the less

efficient blockade of the hole transport through the active layer by the isolating side chains, seem to result in an improved performance in the devices compared to the all-linear substituted polymer [80].

Not only nature of side chains but also the numbers of substituent groups to the backbone of the conducting polymer affect transport property of carriers in the polymer system. The high number of substituents can prevent π- stacking between polymeric chains, resulting in a worm-like cylindrical conformation. When the concentration of the side chains is reduced, an increase of the planarity of the polymeric chain will result in stronger π- stacking, leading to lamellar arrangements which intern enhances charge carriers transport property in the polymer device [82].

Branched alkyl chains are more effective than their straight-chain counterparts for inducing solubility. It should be stressed that increasing the content of insulating alkyl chains relative to the hole-conductor portion in the polymer may result in deterioration in the charge mobility function. As a result, depending on the nature of the conjugated backbone, judicious choice of a suitable solubilizing group at an appropriate location is of crucial importance for fine-tuning the structure-property relationship [83 - 85].

1.4. Bulk heterojunction Solar cell

Organic solar cells specially bulk heterojunction (BHJ) ones are more preferable than their inorganic counter parts for their advantages of solution processibility, flexibility, cheap in the market, light weightiness, and environmentally friendliness [86]. Even though BHJ solar cells have these attractive advantages, they could not penetrate to power market and used in light energy conversion into electricity in wider scale up to

now [87]. The main reasons why BHJ solar cells could not be used in light energy conversion in the wider scale are poor performance and stability [87].

As far as performance is concerned, the performance of BHJ solar cells can be enhanced through multiple experimental approaches [88]. These approaches can be carried out within the three different processing steps of solar cells manufacturing. The first step is synthesis of the donor polymer or copolymer materials. In this level solar cell performing ability of the polymer material can be optimized by increasing molecular weight (or backbone repeating unit) of the polymer or copolymer only up to optimum amount, as polymer chain entanglement (polymer backbone twisting) is a problem at higher molecular weight [89].

Another approach to improve solar cells performance in the synthesis level is through polymer side chain engineering to attain the polymer with suitable photovoltaic properties. As nature, size and position of side chains in the polymer backbone could play a big role in affecting solubility of the polymer, film organization of the active layer (polymer), the polymer chain packing and crystallininty of the resulting film [90], studying impact of side chains on the photovoltaic parameters is important. Since these effects in turn directly or indirectly affect the performance of resulting BHJ solar cells, optimizing side chain conditions is very important [91].

The other means to improve performance or efficiency of BHJ solar cells are during solar cell devices fabrication [92]. In this level of solar cell processing, type and nature of host solvents used in preparing donor:acceptor BHJ blend, concentration of the blend solution, donor to acceptor ratio in the blend, application of multiple donor depending on the compatibility of the polymers used, processing additives (solvent additives), the blend film deposition techniques (spin-coating, drop-casting, doctor-

blade, etc.) and deposition conditions (spin-coating speed) have an impact on the performance of BHJ solar cells [92].

The third approach is to improve BHJ solar cells efficiency is through post device preparation treatments. The common post treatment made to solar cells is thermal annealing and solvent annealing. The solvent and thermal annealing steps also must be optimized in order to improve efficiency of the solar cells. In order to attain solar cells with better efficiency, thermal annealing temperature, and annealing duration should be optimized for the type of active layer used in BHJ system [93].

Here our study on solar cell part mainly focused in investigating effects of processes and conditions or factors related with synthesis process (effect of macromolecular properties) and device fabrication steps (effect of processing solvent additives and multiple donor effect) on the performances of BHJ solar cells. Towards this purpose effects of macromolecular properties of AnE-PV*stat* copolymers on the efficiency of AnE-PV*stat*:PCBM BHJ solar cell was investigated using AnE-PV*stat*-a, AnE-PV*stat*-b, and AnE-PV*stat*-c as donor polymers having the same nature, size and types of side chains, but different macromolecular properties (molecular weight and polydispersity index).

Effects of low boiling point solvent additives on the photovoltaic performances of polymer-based BHJ solar cells were also investigated in this work. The low band-gap polymer PDTSTTz as an electron donor material and PCBM as acceptor material were used in blend of PDTSTTz:PCBM (1:1) solar cells. Multiple donor effect on the power conversion efficiency of PDTSTTz:PCBM (1:1) blended solar cells was also studied by incorporating P3HT as secondary donor. In this study multiple donor approach (ternary system) was used to improve power conversion efficiency of

PDTSTTz:PCBM (1:1) blend solar cells by extending light harvesting capabilty of the cells up on addition of P3HT .

1.4.1. Effect of Macromolecular properties on Photovoltaic performance of BHJ solar cells

Effect of molecular weight on polymer bulk heterojunction (BHJ) solar cells was studied on P3HT: PCBM solar cells [94]. The increased molecular weight (MW) of P3HT will affect not only the hole mobility, but also can cause significant changes in the morphology of the BHJ solar cell active material. Since the device efficiency is critically dependent upon the morphology of the BHJ material, an investigation of the morphology and the associated PV performance is better with longer chains (higher MW) than shorter counter parts [94].

Effects of (MW) on the photovoltaic properties were also investigated in double-crystalline block copolymers system (BCS). The two BCPs P3HT-*b*-poly(perylene bisimide acrylate)(P3HT-*b*-PPerAcr 1 and 2, with molecular weight 16.12 and 29.5kg/mol, respectively) possesses the same composition but differ in molecular weight by a factor of 2, are compared in single component single layer solar cells. P3HT-*b*-PPerAcr 1 with lower MW (16.1 kg/mol) gave very low short circuit currents J_{sc}, around 0.08 mA/cm^2 and open circuit voltages, V_{oc}, of 0.51 V, resulting in poor power conversion efficiencies, η, of 0.007%. BCP 2 with a WM (29.5 kg/mol) again shows a drastic improvement; a J_{sc} of 1.5 mA/cm^2 and power conversion efficiency, η, of 0.2% are observed. The fill factor also increases from 0.17 to 0.25, and the open circuit voltage, V_{oc}, was 0.44 V [95].

Furthermore, the effect of the MW of poly[9,9-didecanefluorene-alt-(bis-thienylene) benzothiadiazole] (PF10TBT) on the photovoltaic performance of fullerene-based

bulk heterojunction solar cells was investigated by Huang *et al* [96]. The polymer with higher MW can stack much better due to the stronger π-π interaction and was found to exhibit better charge transfer property and lower internal resistance [95]. An increase in MW of two orders of magnitude results in a 30% increase of the short-circuit current and a rise of the fill factor from 0.45 to 0.63. Electron and hole transport are found to be virtually unaffected by changing MW, which means that space-charge effects do not play a role in low molecular weight devices [97].

1.4.2. Effect of processing solvent additives

This method is based on the usage of non-reacting chemical additive or processing solvent additive, to the donor and acceptor solution. It was demonstrated that the addition of a copolymer containing thieno-thiophene units (DHPT3) in P3HT/PCBM thin films induces a structural ordering of the polythiophene phase, leading to improved charge carrier transport properties and stronger active layer absorption [98]. The incorporation of other solvents into the host solvent is capable of controlling the film morphology.

In some cases, changes in the solvent composition lead to interchain order that cannot be obtained by any other method. The use of nitrobenzene as an additive has been shown to improve the phase-separation between the donor and acceptor (P3HT/PCBM blend), where P3HT was shown to be present in both amorphous and crystalline phase [99]. The mechanism how solvent additives affect nano-scale morphology of film is not clearly known; but many of researchers in this area arguing that the solvent additives control morphology through two different mechanisms [100].

Processing additives control nano-scale morphology of BHJ solar cells through two mechanisms. First methods is using selective solubility of the additive, which means it makes more solublizing effect either on polymer or on PCBM. This type of additive does not effectively work on the high aggregative polymer systems. In the second case, the boiling point of the additive must be significantly greater than that of the host solvent to maximize the interaction time between the additive and the active layer components during thin film formation.

The recent promising additives fulfilling these guidelines include di(X) octanes, where X is a small, polarisable group such as a halogen [101]. For BHJ systems containing donor polymers di-iodooctane (DIO) affords the largest PCE enhancements observed to date. Several studies reveal that processing additives promote more favourable BHJ morphologies [102], little is understood about the microstructural evolution occurring in the transformation from solution-phase BHJ precursors to thin photoactive films.

1.4.3. Effect of additional donor (ternary blend system)

The most common BHJ solar cells have a binary system composed of a donor and an acceptor blended together. The role of light absorption in these types of cells can be carried out by the two components. Light absorbing processes takes place mainly by one of the two components (donor) [103 - 106].

As far as the absorption range is concerned, the organic donors (polymers) have intrinsically narrow absorption width, commonly with full width at half - maximum (FWHM) of ~ 200 nm [107]. Due to these, binary blend BHJ solar cells exhibit poor light absorption and then weak power conversion efficiency compared to the highly efficient inorganic solar cells [108].

Therefore, to address the limitation of narrow absorption width within the solar spectra (typically in visible light region) by single BHJ devices, using multiple donor material is interesting options. Currently a lot of research works have focused on extending the capability of light harvesting through ternary system up to near-infrared region by blending two donor polymers of different bandgap with one acceptor molecule (having suitable energy offset among the components)[109] in order to enhance the degree of light harvesting through single BHJ device [110].

Ternary blend bulk heterojunction solar cells are prepared by mixing two donor polymers and one acceptor material [111]; or one donor material and two acceptor molecules together in some defined proportion between donor and acceptor [112]. Recently, in addition to the conjugated polymers, the low-bandgap small molecules such as silicon phthalocyanine and its derivatives were incorporated into P3HT:PCBM blend film so as to stretch the spectral responses of solar cells into near-infrared region [113 - 115].

1.5. Techniques of charge carrier transport measurement

1.5.1. Time of Flight (TOF) technique

The TOF technique was first developed by Kepler [116] and Le Blanc [117] in the late 50‟s, and this technique was pioneered by Spear [118] and widely applied. In a TOF experiment, an organic layer of a few microns thick is sandwiched between two electrodes. A laser pulse is first used to generate charges in the organic material near an electrode. Then, the photogenerated charges migrate across the material toward the other electrode by applying an electric field (in the 10^4 - 10^6 V/cm range). TOF is a well known technique and it is widely used to measure the charge carrier transport in various low mobility (and low conductivity) semiconductors [119].

In this case, the mobility of charge carriers is measured using the transit time (t_{tr}), the time taken by sheet of photogenerated charge carriers from active layer near one electrode to transit to another electrode [120]. In this technique mobility is calculated with Equation 1.6,

$$\mu = \frac{d^2}{(V\, t_{tr})} \tag{1.6}$$

Where d is the sample thickness, V is the applied voltage, and t_{tr} is transit time. The TOF method in disordered material is limited to moderate electric fields, according to Mozer *et al* [120], ranging between 4 x 10^4 Vcm^{-1} up to 10^6 Vcm^{-1} when signals are less dispersive.

The sample with thickness d is sandwiched between the two electrodes. One of the two electrodes is transparent and both of them must be blocking/non-injecting electrode for charge carriers‟ transport. Both of the electrodes are connected to an external circuit *via* a resistor with resistance R and potential V [121].

Eventhough it is possible to apply TOF technique in the volume photogeneration case (in integral mode), the most commonly used mode of TOF is differential (low light intensity TOF with surface absorption), ensuring that a small amount of charges is generated near the transparent electrode compared to the charge stored on the contacts (CV) [122]. Charge carrier generation takes place using a short pulse of N_2 laser absorbed up to ≈ 10% of the film thickness *d*. By monitoring the intensity of laser light using filters, it is possible to control depth of absorption by the thin film. Low light intensity TOF mode ensures that the externally applied electric field inside the film is distributed only fractionally throughout the film which simplifies the interpretation of the current transients.

Initially, the short laser pulse creates electron-hole pairs near the transparent electrode, and then with application of electric field, the pairs separate to electrons and holes. The generated charge carriers (electrons or holes) drift from the irradiated side to the counter-side. This carrier drift is observed by an oscilloscope as photo-generated transient current. Depending on the polarity of applied electric field, either holes or electrons drift across the sample as a sheet of charges, but not simultaneously. This is one of advantages of TOF technique to measure hole and electron mobility alternately. The transient photocurrent is recorded with digital oscilloscope [123, 124].

Measurements of TOF mobility of organic semiconductors become difficult when the mobility values are high, since the electronic signals overlap with the noise of the short part in drift time. Such noise in the short part of the drift time in the TOF method for measurements of carrier mobility could be reduced by three methods: (1) longer distance (3.5 m) between sample and the N_2 laser, (2) optical connection (photo coupler) between the N_2 laser and the pulse generator, and (3) using a digital filter to remove characteristic pulses caused by N_2 laser [123].

First condition of TOF technique is that the amount of charges generated should be small enough so that space–charge effects do not perturb the internal field strength. That is, q_0 (generated charge), $q_0 << CV$ (capacitive charge, the charge stored between two parallel electrodes, and C is sample capacitance). A disadvantage of time of flight technique is the requirement that the number of charges created must be a small fraction of the number of charges stored on the electrodes in order to avoid space charge effects [125, 126]. Second condition of TOF technique is that the circuit

reaction time, τ = RC, should be smaller compared with the average transit time of the charges.

In the case of measuring a hole drift mobility, the transparent electrode is held at a positive potential with respect to the ground, while the other one is grounded through a resistance, *R,* which has a much smaller resistance than the sample. Photo-generated charge carriers will start moving to the negative electrode. The drifting carriers build a current equal to Ne ν /*d*; where *N* is the number of charge carriers in the material, *e* is the elementary charge, *d* is the film thickness, and ν is the velocity. For current measurements, the condition *CR* << τ (*C* the total capacitance across resistance *R*) is necessary to prevent the rising time of the signal from being longer than the transit time τ [127]. Figure 1.5.1 shows the typical device setup used in the TOF experiment.

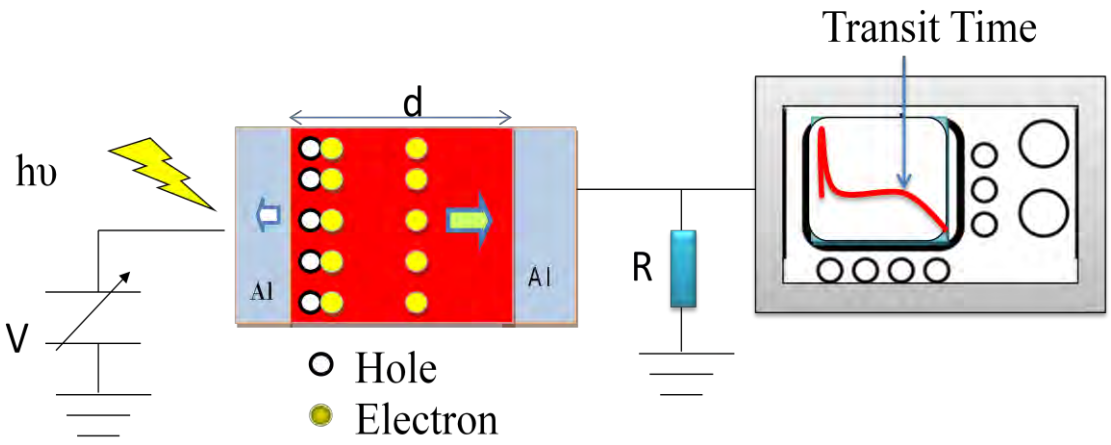

Figure 1. 5. 1. Typical device setup used in the TOF experiment, indicating device structure, source of excitation (pulsed laser light), external electric field, and data extracting unit (oscilloscope).

Experimentally, time of flight (TOF) may be the most used technique to extract the carrier mobility of organic materials. Since TOF technique is independent of the electrical contact at the metal/organic interface, the problems of charge injection can

be neglected. Thus, TOF can be viewed as a standard means to measure carrier mobilities. TOF, however, suffers from several limitations [128].

Because of the finite photon penetration length of laser, a thick film is required to provide a well defined flight distance, which results in large material consumption. Due to carrier dispersion or trapping, transit time technique such as TOF is not the best choice in evaluating carrier mobilities in dispersive materials. There is a clear need to look for alternative techniques, such as admittance spectroscopy [119].

1.5.2. Mobility determination from TOF technique

In order to extract transit time from the resulting transient, two primary procedures can be used based on the nature of the charge transport. That means, if the degree of spreading of sheet of charges is very small and the charges exit the sample almost completely and cleanly, transport is non-dispersive. This transient gives a flat plateau, as could be seen in Figure 1.5.2, up to the time charges begin exiting the device and the photocurrent decays down to zero as all of the charges finish their transit.

After the initial spike, the current settles to a plateau. When the first carriers arrive at the counter electrode, the current drops and a typical tail can be observed in the transient. The arrival of the first carriers usually determines the transit time, t_{tr}, which can be determined by the intersection of the tangent lines to the plateau and to the tail.

The response of transient photocurrent could be either non-dispersive or dispersive types based on the transport mechanism of the charge carriers. A sharp signal is obtained in the case of ordered materials (non-dispersive transport) while in disordered systems a broadening of the signal (dispersive transport) occurs due to a distribution of transient times across the material. Transit time is determined from the intersection

of the two tangent lines to the plateau and linear region decaying to zero photocurrent [129].

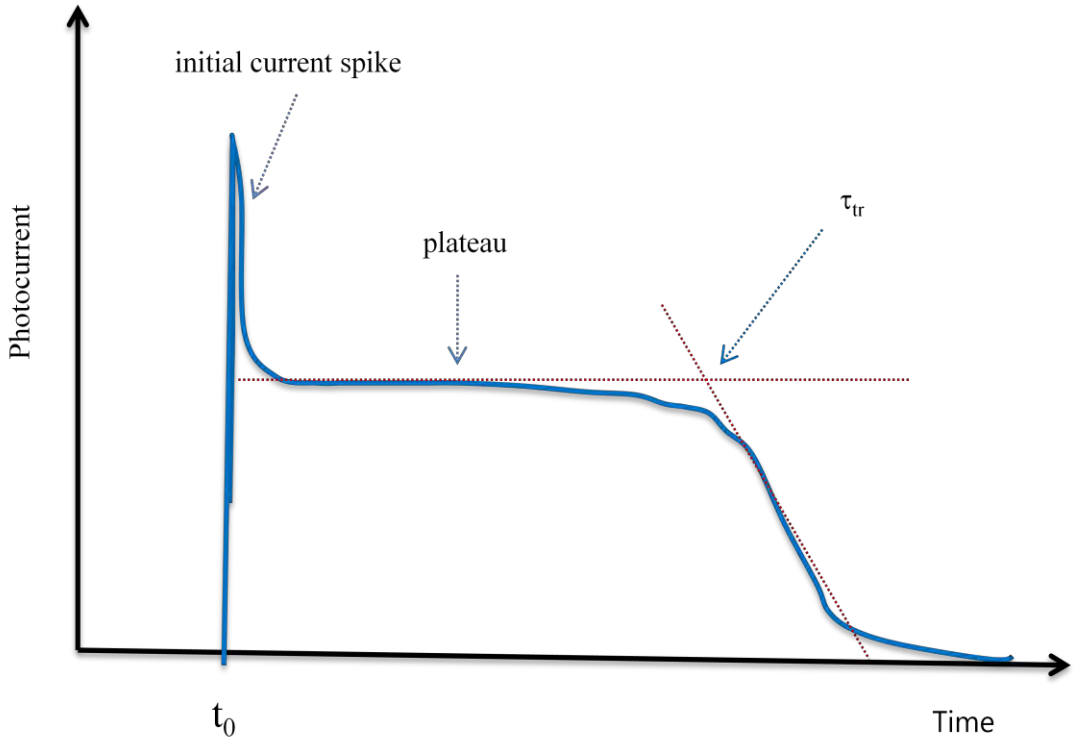

Figure 1. 5. 2. Typical photocurrent transients of well-ordered material in time-of-flight (TOF) method.

Figure 1.5.3a shows a typical transient of non-dispersive transport while Figure 1.5.3b shows the photocurrent response for dispersive transport, which is without any definite cusp (clear inflection point). In the dispersive transport the transit time, τ, is determined from the double logarithmic plots of transient photocurrents as shown in the inset of Figure 1.5.3b. This shape is due to a charge trap or dispersion effect in a material, which means that some charge carriers are hold in different energy levels from a transporting level for a certain time during traveling from one electrode to the other. Therefore, TOF measurements clearly show the impact on mobility of structural defects present in the material.

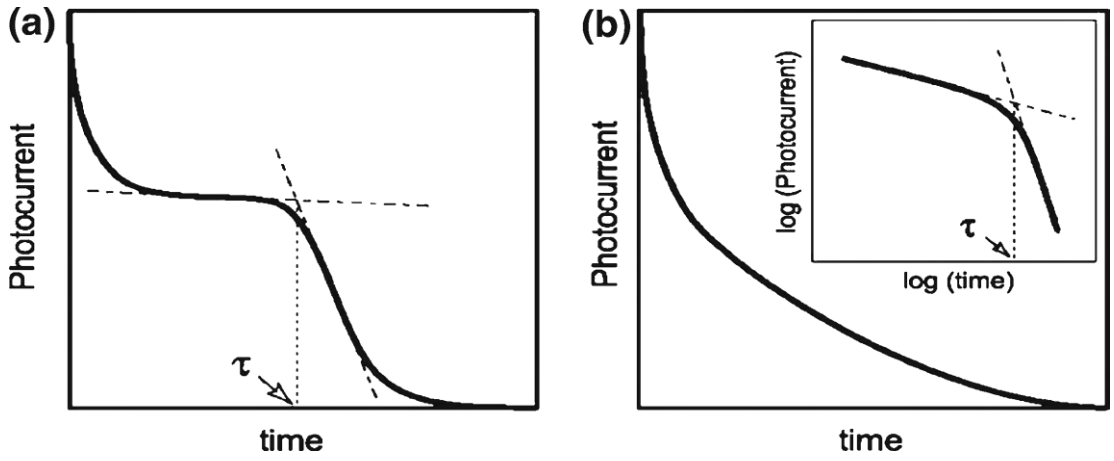

Figure 1. 5. 3. Typical transient photocurrents: (a) non-dispersive; (b) dispersive. *Inset* double logarithmic plot**.**

In dispersive type transport where there is a significant distribution of hopping sites; transit time can be determined from the log-log plot of the resulting transient. In addition to the transit time, the slopes of the pre- and post-transit currents have often been used to characterize the TOF transients. The fact that the slopes of the two transit currents are negative in both regions is due to carrier trapping into localised states (located deep enough) to prevent re-emission of the charge within the elapsed time. This behavior is one indication for the material to be dispersive type. According to theory of Scher-Montroll, the sum of the two slopes adds up to -2 [130].

The dispersive nature of the transient is due to the high degree of disorder in the samples and its effect on carrier transport (disorder parameters would be calculated if we could use mobility at different temperatures).

1.5.3. Integral Time of Flight method

Differential (traditional) TOF is inherently a small-signal technique [131]. There are two primary reasons that differential TOF must deal with small signals, in this case a small amount of charge are photogenerated from the device. First, too much charge

results in space-charge perturbation of the resulting transient, as the charges repel each other enough to accelerate their transit through the bulk sample [132]. Second, at even greater amounts of moving (or photo-generated) charge the assumptions involved in extracting the mobility are broken.

In the differential or photocurrent mode of TOF measurements, the RC time constant of the sample (which acts as a capacitor) and measuring circuit must be much smaller than the transit time to resolve it, RC << τ. In order to solve these limitations differential TOF, integrating-mode TOF is introduced by Spear *et al* [133].

Integrating-mode TOF provides some unique advantages [118]. Here the opposite condition to differential TOF is required, namely for integrating-mode TOF the RC time constant must be much larger than the transit time, $RC >> \tau$. Thus, the RC time constant is no longer a limiting factor enabling integrating mode TOF to be more sensitive and also excellent for very fast transit times [134], and can be used for high mobility materials in relatively thin samples. Integrating-mode TOF can also be considered voltage-mode TOF, as the voltage build up on a capacitor ultimately results in the signal. It also sometimes called charge integration time-of-flight, due to the buildup of charge causing the voltage build up on a capacitor. Typical current mode and integral-mode TOF signals are displayed in Figure 1.5.4 (Figure 1.5.4a current-mode signal for non-dispersive transport and Figure 1.5.4b for dispersive transport materials, Figure 1.5.4c is an Integral-mode signal for non-dispersive and Figure 1.5.4d is the integral-mode signal for dispersive transport).

Transit time extraction in integral-TOF mode is different from that of current –mode. The relative comparisons on how to determine charge carries transit time in current-

mode and integral-mode are indicated in Figure 1.5.4. The resulting charge carriers‟ mobility is determined from Equations;

$$\mu = \frac{d}{V\tau} \quad \text{(In current mode TOF)} \tag{1.7}$$

$$\mu = \frac{d}{Vt_Q} \quad \text{(In Integral mode TOF)} \tag{1.8}$$

Where d, τ, t_Q, V are thickness of the film, transit time in current mode, transit time in integral mode and applied voltage, respectively.

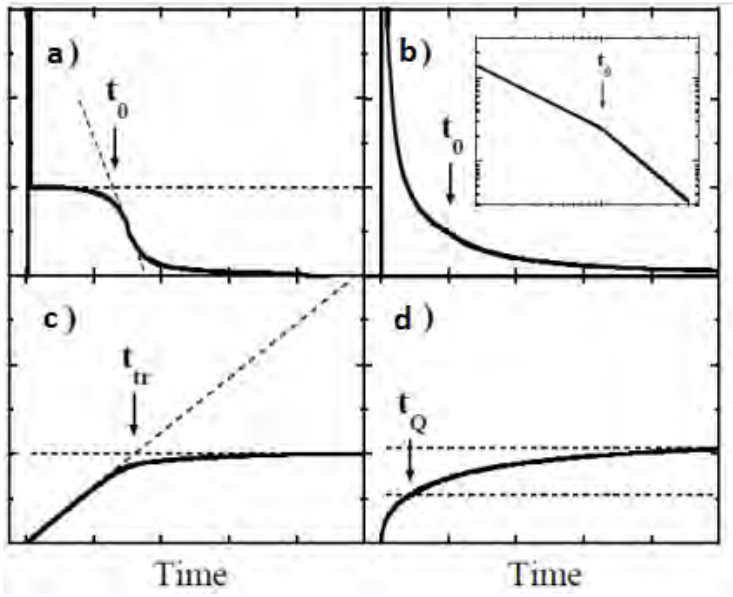

Figure 1. 5. 4. Typical transients for current-mode TOF, a) for non-dispersive and b) for dispersive materials) on top and integrating-mode c) for non-dispersive and d) for dispersive material) on bottom [118, 135].

1.5.4. Admittance spectroscopy

Admittance spectroscopy (AS) is a very useful technique for characterizing the electrical properties of materials. It is Shao *et al* [136], who developed analytical model in 1961 for first time to analyze the space charge effect by admittance

technique [136]. During the experiment, along with the application of AC voltage, a DC voltage will be superimposed in order to inject a charge carrier, Figure 1.5.5a.

In this method, a two-terminal device consisting of an organic semiconductor with a dielectric constant, ε, and a thickness, d, sandwiched between two electrodes is considered. One of the electrodes is expected to form an injecting contact with the organic material. The other contact is blocking. The instruments used and the configuration is shown in Figure 1.5.5b. The injected charge carriers will be drifted to the opposite electrode.

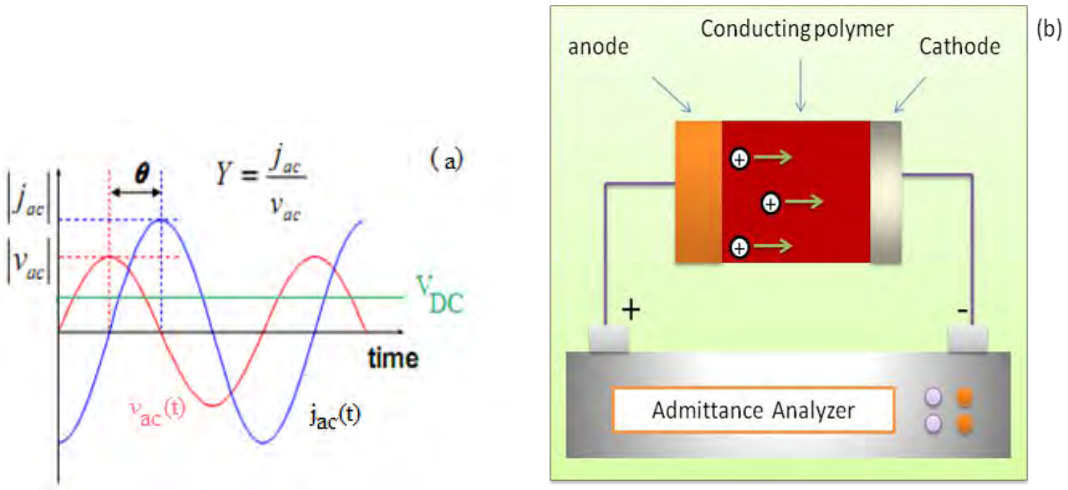

Figure 1. 5. 5. a) The AC and DC electrical waves; (b) Admittance spetroscopy (AS) configuration for measuring charge carriers mobility.

In Figure 1.5.6, the frequency dependent capacitance spectra are shown as function of applied bias. At V = 0 V the capacitance is frequency independent, is geometrical capacitance and is given by Equation,

$$C_{geo} = \varepsilon A/L \qquad (1.9)$$

At finite bias a negative contribution to C appears, shifting to higher frequencies when increasing V (as dc voltage increases from 2 V to 8 V in Figure 1.5.6a). This inductive contribution is more clearly resolved by plotting differential succeptance, $\Delta B(\omega) = -\omega(C-C_{geo})$. Figure 1.5.6a shows -ΔB with different applied bias. The inductive contribution arises from redistribution of space charge when the electric field is varied. Changing the applied voltage leads to injection of additional space charge. Under the influence of the applied field, the injected charge moves into the device to relax to the new equilibrium space charge distribution.

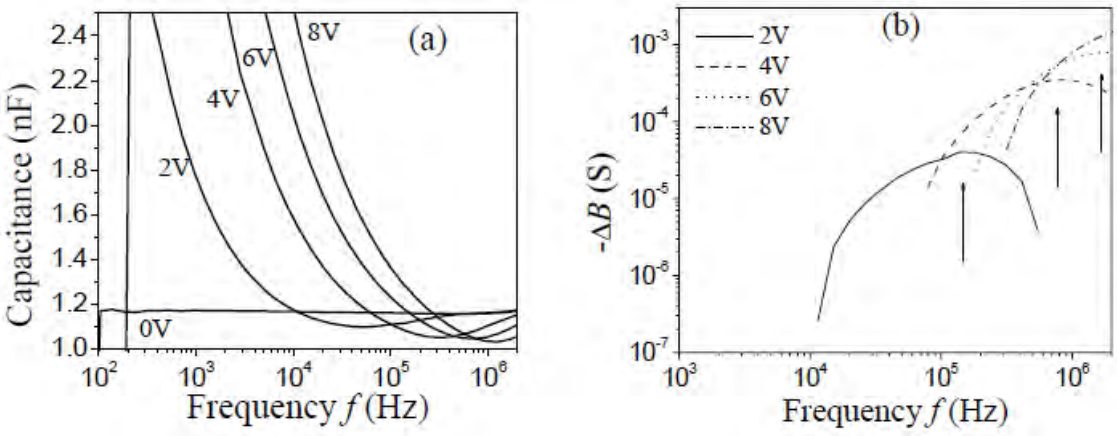

Figure 1. 5. 6. (a) Capacitance *versus* frequency for a 75 nm thick LUMATION Green electron-only device at different bias voltages. (b) The corresponding frequency dependence of the susceptance change, -Δ*B*. Peak positions, related to the carrier transit time, are indicated by the arrows [138].

Due to the finite transit time, τ_{tr}, the corresponding current lags behind the V_{ac}, AC voltage, and this give an inductive contribution to the capacitance, shown in Figure 1.5.6a [137]. For the more dispersive samples, AS is more powerful than TOF technique in the measurement of carrier transit time. The preference of AS from TOF

is probably related to the nature of data acquisition. Data capturing from AS is easier than that of TOF technique.

The charge carriers‟ transit time is affected by the combined *RC* time constant of the sample and the sensing resistor. For the highly dispersive sample, the effective time constant is larger (due to the increase in sample resistance). The TOF signal of the more dispersive sample is then overwhelmed by the *RC* decay, rendering the determination of the transit time impossible.

In contrast, AS extracts carrier transit times in the frequency domain. AS simultaneously probes the real and the imaginary parts of the complex impedance (Equation 1.10). The extraction of the carrier transit time only needs to involve the imaginary part of the complex impedance (i.e., the frequency-dependent capacitance) and is independent of the conductivity of the sample. Thus, the extraction of the carrier transit time remains effective for AS [128, 137, 138].

In AS, the material under investigation (conjugated polymer material) is sandwiched between an anode and a cathode. In order to investigate hole transport properties, an anode should make an ohmic or quasi-ohmic contact with the material under investigation (conjugated polymer materials) while non-injecting contact with cathode, whereas to probe electron transport properties, the cathode should make an ohmic or quasi-ohmic contact with the conjugated polymer material while non-injecting contact with anode [139]. While measuring, AS signal is recorded under the superposition of an applied DC voltage, V_{dc}, and a small AC excitation, V_{ac}, (with amplitude of 50 mV) at various frequencies *f*.

In the experiment of complex admittance spectroscopy, the current response, i_{ac}, of a system to an applied small alternating voltage, V_{ac}, is analyzed. By measuring the

amplitude, $|i_{ac}|$, and the phase shift, θ, the frequency dependent admittance can be determined by,

$$Y(\omega) = \frac{i_{ac}}{V_{ac}} = G(\omega) + iB(\omega) = G(\omega) + i\omega C(\omega) \quad (1.10)$$

where $\omega = 2\pi f$ is the angular frequency, f is linear frequency, G is the conductance, B *is* the susceptance and C the capacitance [140, 141].

1.6. Basic Processes, Techniques and photovoltaic characterizations of solar cells

1.6.1. Basic processes in organic solar cells

In general, for a successful organic photovoltaic cell five important processes have to be optimized to obtain a high conversion efficiency of solar energy into electrical energy:

1. Absorption of light and generation of excitons
2. Diffusion of excitons to an active interface
3. Charge separation
4. Charge transport
5. Charge collection

To create a working photovoltaic cell, the two photoactive materials (donors and acceptors) are sandwiched between two (metallic) electrodes (of which one is transparent), to collect the photogenerated charges (see Figure 1.6.1).

After the charge separation process, the charge carriers have to be transported to these electrodes without recombination. Finally, it is important that the charges enter the external circuit at the electrodes without interface problems [142].

Illumination of a donor material (indicated by D) through a transparent electrode (TCO) side results in the formation of an exciton. Subsequently, the exciton is transported by diffusion (2) to the interface between the donor material and an acceptor material (indicated by A).

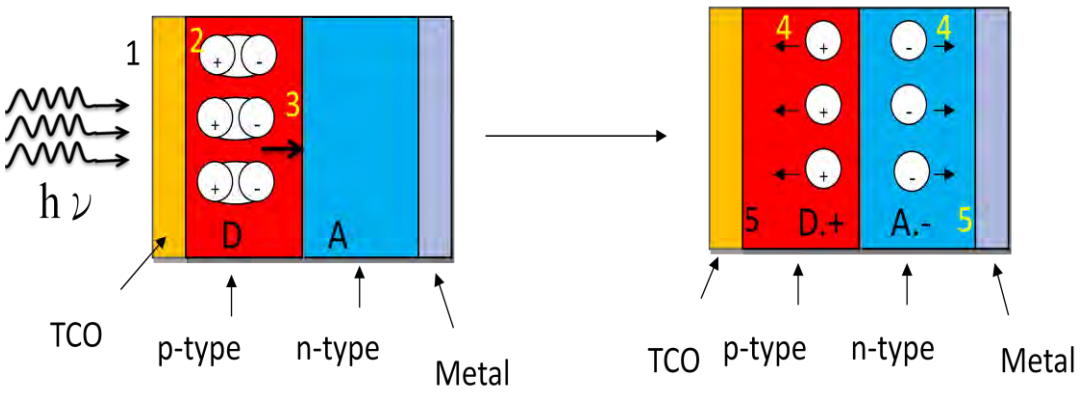

Figure 1. 6. 1. Schematic diagram of the working principles of an organic photovoltaic cell.

Electron is transferred to the acceptor material ($A^{\bullet-}$), leaving a hole at the donor material ($D^{\bullet+}$) (3). The photogenerated charged carriers are then transported (4) to and collected at opposite electrodes (5). A similar charge generation process can occur, when the acceptor is photoexcited instead of the donor.

1.6.1.1. Light absorption

For an efficient collection of photons (process 1), the absorption spectrum of the photoactive organic layer should match the solar emission spectrum and the layer should be sufficiently thick to absorb most of the incident light. Generally the optical absorption coefficient (α) of organic materials is much higher than that of crystalline or multicrystalline materials.

For a photovoltaic cell based on a single light absorbing medium a bandgap of approximately 1.1 eV is optimal [143]. By lowering the band gap of the organic material, it is possible to harvest more sunlight and therefore an increase in the photocurrent. For this reason much research effort is presently devoted to obtain organic polymers with an optical band in the NIR, so called small band-gap polymers [144]. Though increasing the layer thickness is often advantageous for light absorption, charge transport and fill factor are negatively affected.

1.6.1.2. Exciton transport

For realisation of an efficient organic solar cell all excitons formed due to light absorption should lead to the formation of free charge carriers [145]. However, exciton transport is in competition with other decay processes such as luminescence or non-radiative recombination to the ground state. The exponential lifetime of an exciton (τ_{EXC}) is determined by the reciprocal value of all radiative and non radiative decay rates together.

For an efficient solar cell all excitons have to reach the photo-active interface within τ_{EXC}. Transport of the excitons occurs by diffusion and the distance an exciton is able to cross, L_{EXC}, is given by:

$$L_{EXC} = \sqrt{D_{EXC}\ \tau_{EXC}} \qquad (1.11)$$

where D_{EXC} is the diffusion coefficient of the excitons. Since for molecular materials τ_{EXC} is often only several nanoseconds at most, L_{EXC} is generally limited to 10 nm. In practice this implies that only those excitons formed within a distance of L_{EXC} from the interface will contribute to charge separation. To avoid this problem, research has been devoted to increase the diffusion coefficient of excitons or to make the

interfacial area much larger, so that each generated exciton is always close to an interface.

1.6.1.3. Charge separation

Creation of charges is one of the key steps in the conversion of solar light into electrical energy. In most organic solar cells, charges are created by photoinduced electron transfer. In this process an electron is transferred from an electron donor (D) material to an electron acceptor (A) material with the aid of the additional input energy of an absorbed photon with energy $h\upsilon$. An electron donor is characterized by a molecular material with a small electron affinity. Whereas, an electron acceptor is a material with a high electron affinity. The difference between both electron affinity levels is the driving force required for the exciton dissociation. In the photoinduced electron transfer process an exciton at the D/A interface decays by creation of the charge-separated state consisting of the radical cation of the donor ($D^{\bullet+}$) and the radical anion of the acceptor ($A^{\bullet-}$) [146].

1.6.1.4. Charge transport

The charge transport mechanisms operating in inorganic photovoltaic (IPV) cells and organic solar cells to drive charge carriers towards the electrodes are again very different [147]. Light absorption in IPV cells leads directly to the production of electrons and holes in the same material. Since the two carrier types have the same spatial distribution, the concentration gradient, which is the driving force for the transport by diffusion. Therefore, both charge carriers are driven in the same direction. Since this is a small driving force in IPV cells, the electrical potential gradient present at the interface of a p-n junction (the band bending) is able to separate the photo-induced electrons from the holes effectively [147]. In contrast to

IPV cells in organic solar cells after the charge transfer the electrons and holes are in close proximity. Therefore, there is a large chemical potential gradient that drives the charge carriers away from the exciton dissociating interface.

1.6.1.5. Charge collection

The collection of charge carriers at the electrodes is regularly accomplished by a transparent conductive oxide (TCO) such as ITO or SnO_2:F on one side and a metal contact on the other side [148]. Care has to be taken that an ohmic contact between the electrodes and the molecular layers is formed. In practice special contact layers have been developed to obtain better performance of the solar cell. Examples of contact layers are a PEDOT:PSS layer, which is a charged conducting polymer layer at the TCO side and LiF layers at the metal contact.

For an organic solar cell based on two molecular materials as depicted in Figure 1.6.1, optical excitation leads to the formation of an exciton in one of the layers. For the charge separation process part of the original energy of the photon is lost, yielding an electron in the n-type material (acceptor) and a positive charge carrier in the p-type material (donor) [148].

1.6.2. Electrical characterization of photovoltaic devices

The basis for the characterization of solar cell is the I-V curve (current - voltage curve). The J-V curve of a solar cell can be measured by using a solar simulator. Typical J-V curves of solar cell is depicted schematically in Figure 1.6.2. The important photovoltaic parameters such as open-circuit voltage (V_{oc}), short circuit current (I_{sc}), and fill factor (FF) can be extracted from J-V curve.

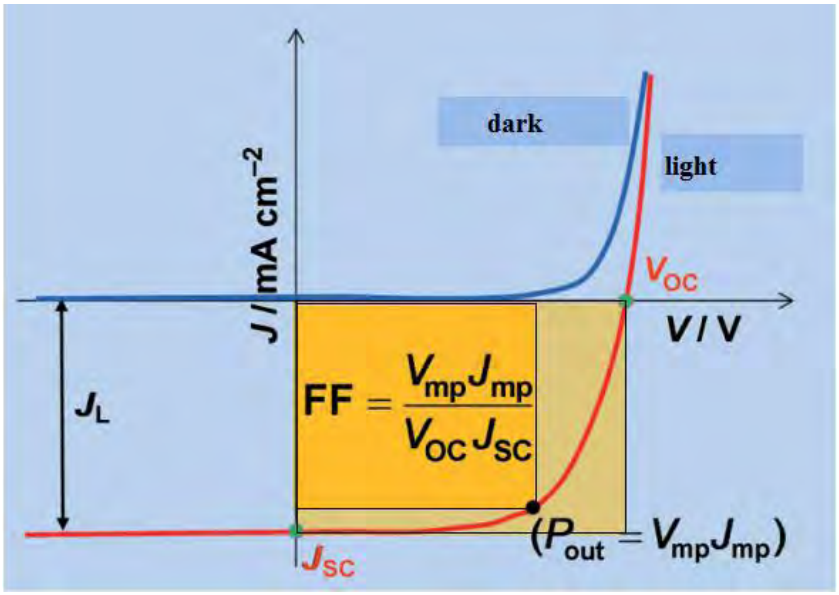

Figure 1. 6. 2. J-V curve of typical solar cells with important photovoltaic parameters [149].

1.6.2.1. Open-circuit voltage (V_{oc})

Under open-circuit conditions, the flow of charges through the illuminated device is interrupted. At these conditions, all charge carriers recombine within the photoactive layer. The open-circuit voltage is the intercept point of the illuminated J-V curve with the voltage-axis (x-axis in Figure 1.6.2) and represents the maximum voltage that the solar cell can provide under ideal conditions. The V_{oc} in organic solar cells is predominantly determined by the materials and their frontier orbitals used in the solar cell. However, also other factors connected to the processes in the cell can influence the open-circuit voltage. The V_{oc} can be for example lower due to charge recombination, which cannot be avoided [150].

1.6.2.2. Short-circuit current (J_{sc})

Under short-circuit conditions no resistance is present in the electric circuit. Consequentially there is no change in the voltage and thus no work is done

eventhough a current is flowing. The short-circuit current is the intercept point of the illuminated J–V curve with the current density-axis (y-axis in Figure 1.6.2) and represents the maximum current that could be withdrawn from the solar cell if the cell was ideal. Another important value strongly associated with the short-circuit current is the short circuit current density (Jsc). This value reports the short-circuit current per area (Equation 1.12).

$$J_{sc} = \frac{I_{sc}}{A} \tag{1.12}$$

The short-circuit current is directly proportional to the incident photons that can be used by the solar cell as long as no saturation effects occur. J_{sc} is therefore dependent on the surface area (A) of the solar cell, the light intensity, the device thickness, and the absorption range. J_{sc} is also dependent on the charge carrier mobility which in turn depends on the temperature through a thermally active hopping transport [151].

1.6.2.3. Fill Factor (FF)

The fill factor is a measure of the quality of the solar cell and describes the relation between the photogenerated charge carriers and the charge carriers that reach the electrodes [152]. In an ideal solar cell, all generated charge carriers reach the electrodes and the FF is 1. Due to charge recombination and resistances within the device not all generated charge carriers reach the electrodes. There are two types of resistance in the solar cell. The serial resistance, R_S, represents the sum of all layers, contacts, and current-resistances and is the reciprocal of slope of the tangent line to the J-V curve under open-circuit conditions (near J_{sc}) (Equation 1.13).

$$R_s = \left(\frac{dV}{dI}\right)_{I=0} \tag{1.13}$$

The shunt resistance, R_{SH}, represents the surface recombination losses, which occur at the different interfaces and leakage currents. R_{SH} is the reciprocal of slope of the tangent line to the J-V curve under short-circuit conditions (near V_{oc}) (Equation 1.14).

$$R_{SH} = \left(\frac{dV}{dI}\right)_{V=0} \quad (1.14)$$

In an ideal solar cell R_S should be minimized ($R_S \rightarrow 0$) and R_{SH} would be maximized ($R_{SH} \rightarrow \infty$). In this case the J-V curve would be rectangular and go along the outer area of rectangle in Figure 1.6.2. In a real solar cell losses cannot be avoided and the J-V curve is bended. The point on the J-V curve where the maximum power of the solar cell can be produced is called maximum power point (P_{mp}). The P_{mp} or P_{out} is located on the J-V curve exactly where the product of J and V reaches its maximal value. The inner rectangle area in Figure 1.6.2 indicates this maximal power value. The maximum power of an ideal solar cell is represented by area of outer rectangle [149]. The voltage at the maximum power point is V_{mp} and the current density is J_{mp}. The FF can be calculated using these values according to Equation 1.15

$$FF = \frac{V_{mp}\ J_{mp}}{V_{oc}\ J_{sc}} \quad (1.15)$$

1.6.2.4. Power conversion efficiency (η)

All the values mentioned above contribute to the overall power conversion efficiency that describes the relation between the electric power that the device produces (P_{out}) and the power of the incident light (P_i). The efficiency can be calculated according to Equation 1.16

$$\eta = \frac{P_{out}}{P_{in}} = \frac{V_{mp}\ J_{mp}}{P_{in}} = \frac{V_{oc}\ J_{sc}\ FF}{P_{in}} \quad (1.16)$$

1.6.2.5. Incident Photon to Current Efficiency (IPCE)

The incident photon to current efficiency (IPCE) or external quantum efficiency (EQE) describes the relation between the numbers of the dissipated charges nand the number of the incident photons at a certain wavelength (Equation 1.17). where J_{sc} is the short-circuit photocurrent density for monochromatic irradiation, and λ and P_i are the wavelength and the incident power, respectively, of the monochromatic light. If IPCE is 100, every absorbed photon injects an electron into the circuit.

$$\mathrm{IPCE\%} = \frac{1240\,[\mathrm{eV\ nm}]\,\mathrm{x}\,J_{sc}\,[\mathrm{mA\ cm^{-2}}]\mathrm{x}100}{\lambda[\mathrm{nm}]P_i} \qquad (1.17)$$

IPCE is a measure for the absorption quality of the solar cell at a certain wavelength combined with its charge transport quality [153]. If, e.g., the cell absorbs all incident photons at a certain wavelength but the charges cannot travel to the electrodes due to recombination, the IPCE will not be zero. Hence, the IPCE correlates often to the absorption spectrum of the active layer but a strong deviation cannot be excluded [154].

1.7. Objectives of the study

General objectives of this research work is to study transport properties of charge carriers in undoped conjugated polymers; to fabricate and characterize bulk heterojunction solar cells, and study their photovoltaic performances.

Specific objectives of the study are:

1. To show the effect of slight variation in macromolecular properties of AnE-PV*stat* copolymers in tuning charge transport properties and photovoltaic performances.
2. To draw relationship between charge carriers mobility and photovoltaic performances in AnE-PV*stat* copolymers.
3. To investigate the impact of changing location of anthracene moiety in the backbone of anthracene based copolymer on the hole and electron mobility.
4. To show effect of electric field, temperature and charge-injection barrier height on hole mobility of AnE-PV*stat* copolymers.
5. To study the influence of side chains on the charge transport properties of anthracene containing copolymers.
6. To explore influence of low boiling point solvent additives and P3HT on photovoltaic performance of PDTSTTz:PCBM blend solar cells.

2. Experimental Part

2.1. Materials

Anthracene-containing poly(*p*-phenylene-ethynylene)-alt-poly(*p*-phenylene-vinylene) (PPE-PPV) statistical copolymers with different macromolecular properties such as AnE-PV*stat-a*, AnE-PV*stat-b* and AnE-PV*stat-c* copolymers that were used in the study of the effect of macromolecular properties on charge transport and photovoltaic properties were synthesized by Egbe‟s group [44, 78].

The synthesis procedures of other six anthracene containing polymers, which were used for investigating impact of side chain on transport properties of charge carriers, were reported in references [41, 44]. The rest series of anthracene containing polymers such as MEH-PPE1-PAnV$_2$ and MEH-PAnE1-PPV$_2$ were also used in this work to study the effect of position of the anthracene unit in the backbone of the polymers on charge transport properties. Synthesis of these polymers MEH-PAnE1-PPV$_2$ (having anthracene unit in the center of the backbone) and MEH-PPE1-PAnV$_2$ (having anthracene unit at one edge of the backbone of the polymer) were reported in [27]. Schematic structures of anthracene containing copolymers used in this study are presented in Figure 2.1a-c.

Alkoxy-substituted phenylene-ethynylene (PE)/phenylene-vinylene (PV) hybrid polymer of general constitutional structure (-Ar-C≡C-Ar-CH=CH-)n of conjugated polymer synthesized by D. Egbe *et al* [155] was used in investigating hole mobility using integral time of flight method. The low bandgap polymer, poly[2,6-(4,4‟-bis(2-ethylhexyl)dithieno[3,2-b:2‟,3‟-d]silole)-alt-5,5‟-(3,6-bis[4-(2-ethylhexyl) thienyl-2-

yl]-s-tetrazine] abbreviated as PDTSTTz was synthesized in [156], and poly(3-hexylthiophene-2,5-diyl) (P3HT), purchased from Rekie, were used as electron donor materials, and PCBM (Aldrich) was used as electron acceptor in bulk heterojunction solar cell prepartions. Indium-Tin-oxide (ITO), aluminium (Al), silver (Ag) and gold (Au) were used as electrode materials.

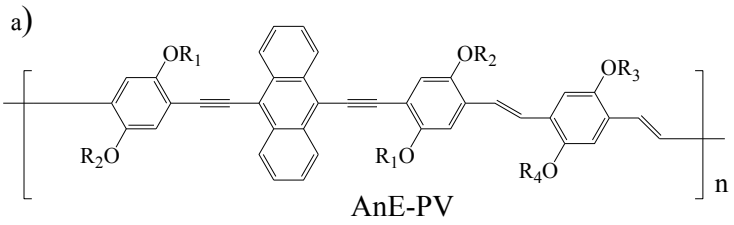

AnE-PV

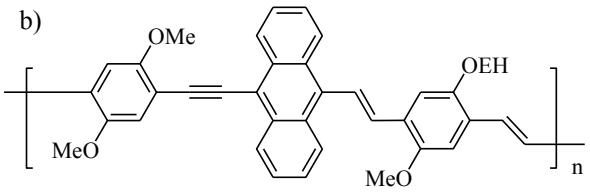

MEH-PAnE1-PPV2

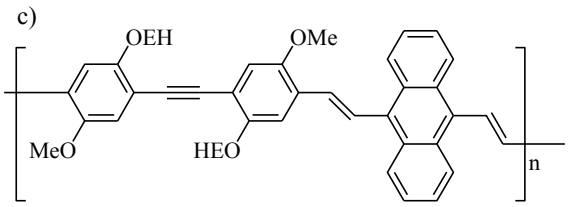

MEH-PPE1-PAnV2

Polymer	*Random*	*Side-chains*
AnE-PV-ab		R1, R2: octyl; R3, R4: 2-ethylhexyl
AnE-PV-ae		R1, R2: octyl; R3, R4: dodecyl
AnE-PV-bb		R1 – R4: 2-ethylhexyl
AnE-PV-*stat*	X	R1 – R4: octyl or 2-ethylhexyl
AnE-PV-*stat4*	X	R1, R3: octyl or 2-ethylhexyl; R2, R4: octyl or methyl
AnE-PV-*stat5*	X	R1, R3: octyl or 2-ethylhexyl; R2, R4: octyl or 2-ethylhexyl or methyl

Figure 2. 1. Molecular structures of anthracene containing polymers used in this investigation with definition of side groups in the polymers; a) AnE-PV, b) MEH-$PAnE_1$-PPV_2 and c) MEH-PPE_1-$PAnV_2$. For the random polymers, the ratio of each side chain type is indicated in the parenthesis.

Poly(3,4-ethylene dioxythiophene) : polystyrenesulfonic acid, PEDOT:PSS (Clevios P VP AI 4083), was used as hole transporting layer, and lithium flouride (LiF) was used as electron transporting layer in bulk heterojunction solar cells. Molecular structures of PEDOT:PSS, PCBM, P(PE-PV), PDTSTTz and P3HT are depicted in Figure 2.2a-e.

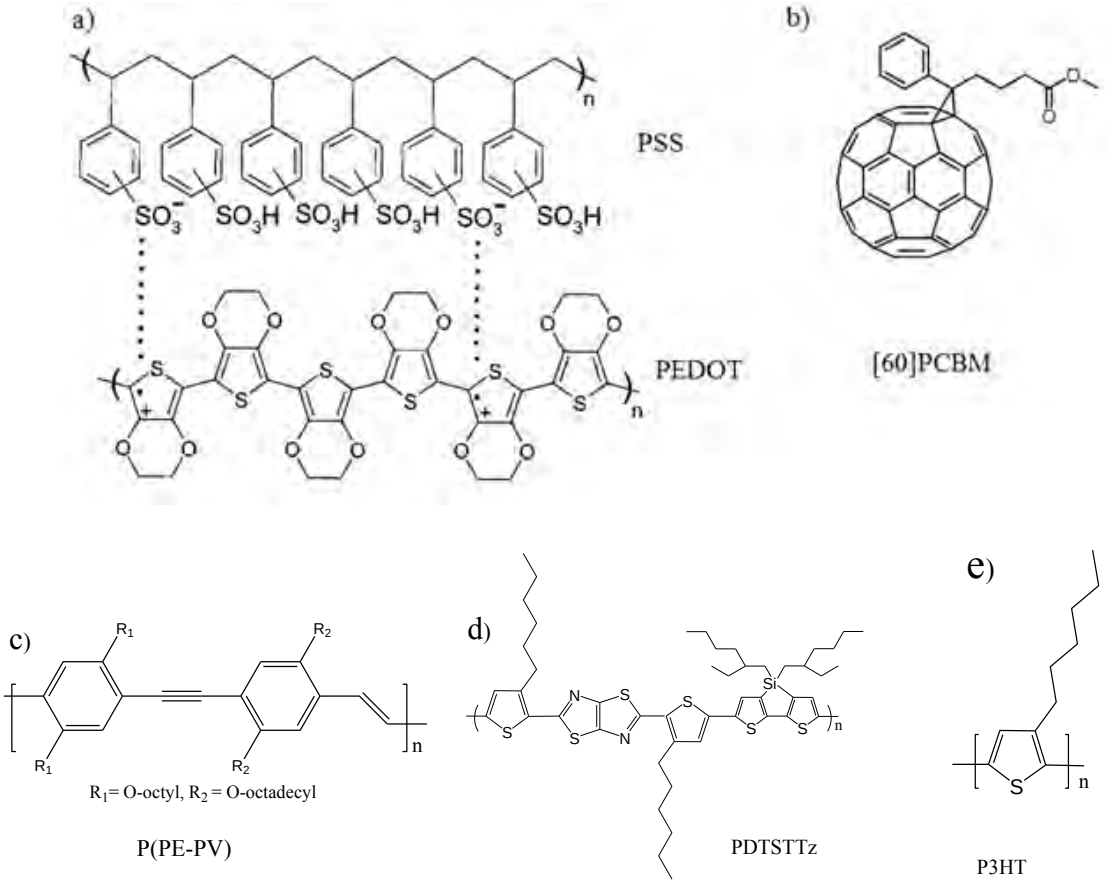

Figure 2. 2. Molecular structures of organic materials used in this investigations; a) PEDOT:PSS, b) PCBM, c) P(PE-PV), d) PDTSTTz and P3HT.

For the study of effect of solvent additives on photovoltaic performance, solvents such as iodomethane (BDH Chemicals), iodoethane (BDH Chemicals), iodobutane (BDH Chemicals) and diiodomethane (BDH Chemicals) were used as solvent additives to the blend of active material (PDTSTTz:PCBM). The molecular structures

of these solvent additives, their boiling (b.pt.) and dielectric constant (ε_r) are shown in Figure 2.3.

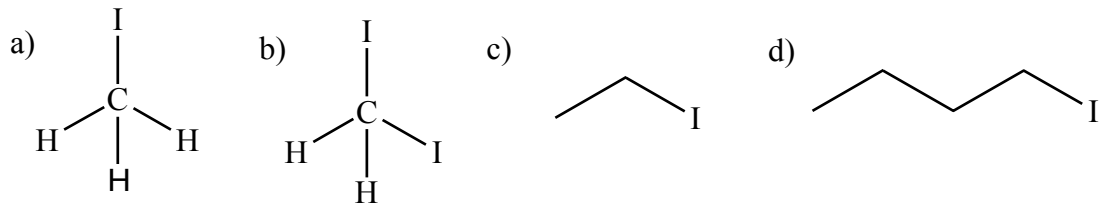

b.pt.	42^0C	181^0C	72^0C	130^0C
ε_r	7.0	5.3	7.8	4.5

Figure 2. 3. The molecular structures of solvent additives: a) Iodomethane (IMe), b) Diiodomethane (DiIMe), c) Iodoethane (IEt), and d) Iodobutane (IBu) with their boiling point (b.pt.) and dielectric constants ($\boldsymbol{\varepsilon_r}$).

2.2. Device Fabrication and charge carriers' mobility measurement

2.2.1. Substrate cleaning

2.5 x 2.5 cm ITO and quartz substrates were cleaned with water and detergent and then ethanol. Further cleaning of the substrates were done in ultrasonicating them with acetone and isopropanol sequentially for 15 minute each and dried with nitrogen gas. ITO substrates were further cleaned with Ultraviolet-ozone (UVO) cleaner, in order to remove organic dirt from the substrate.

2.2.2. Charge transport measurement using Time of flight (TOF)

2.2.2.1. Sample preparation for TOF Mobility measurement

Films of AnE-PV*stat*-a, AnE-PV*stat*-b, and AnE-PV*stat*-c (AnE-PVstat copolymers with different macromolecular properties) were drop-casted onto Al-coated quartz substrates from chlorobenzene solutions (30 g L^{-1}), stirred for 4 days at 45 - 50°C. After the deposition, the films were annealed overnight with cholorobenzene solvent-vapor. The device structure was completed with a vacuum evaporated semitransparent aluminum electrode (20 nm), acting as the illuminated electrode. The device area was 0.25 cm^2 and with the film thickness of 7.8 μm, 4.2 μm, and 3.6 μm for AnE-PV*stat*-a, AnE-PV*stat*-b, and AnE-PV*stat*-c, respectively.

For study of effect of side chain on charge transport properties, the polymer films of AnE- PVab, AnE-PVae, AnE-PVbb, AnE-PV*stat*, AnE-PV*stat4*, and AnE-PV*stat5* were drop-casted onto ITO-coated glass substrates from chlorobenzene solutions for mobility measurement through TOF method. The solutions of these polymers (ranging between 15 and 35 g L^{-1} of concentration) were stirred for 4 days at 45 - 50°C. After the deposition, the films were solvent-vapor annealed (with chlorobenzene atmosphere) overnight. The device structures of all samples of these six polymers were completed after a vacuum deposition of semitransparent aluminum electrode (18 nm thick) on top of the devices. The devices area were 0.25 cm^2; and the film thickness were 9.4, 1.4, 2.9, 3.6, 7.0 and 15.5 μm for AnE-PVab, AnE-PVae, AnE-PVbb, AnE-PV*stat*, AnE-PV*stat4*, and AnE-PV*stat5*, respectively.

In order to study impact of position of anthracene unit in the backbone of the polymer on hole and electron mobility, films of MEH-PPE1-PAnV_2 and MEH-PAnE1-PPV_2

were drop-casted onto Al-coated quartz substrates from chlorobenzene solutions with concentration of 25 g L^{-1} and 31 g L^{-1}, respectively and, the solutions were stirred for 4 days at 45 - 50°C. The deposited films were annealed with chlorobenzene atmosphere overnight. Devices with structures quartz/Al (18 nm)/ MEH-PPE1-$PAnV_2$ /Al (85 nm) and quartz/Al (18 nm)/ MEH-PAnE1-PPV_2 /Al (85 nm) and with areas of 0.25 cm^2 were completed after evaporating the top and transparent aluminum electrode in side glove box.

For integral TOF mobility measurment, the films of the alkoxy substituted P(PE-PV) polymer were prepared by drop-casting from chlorobenzene (CB) with concentration of 32.3 g/L. Active layer deposition was made by casting the solution on the quartz/Al(90nm) substrate. After CB solvent annealing, the films were immediately transferred into Argon filled glove box for metal evaporation. Top metal (Al) evaporation was made from base pressure of $\approx 2 \times 10^{-6}$ mbar with rate of evaporation of 0.1 - 0.2 nm/s. Aluminum of 18 nm thickness on the top of active layer and 90 nm thickness on the edge of samples (for contact) were evaporated in the clean room. Samples were transferred to TOF- measuring cryostat having vacuum of 5×10^{-5} mbar and filled with Argon gas and samples were left in the cryostat over night to remove residual solvents.

2.2.2.2. Mobility Measurement using Differential time of flight (TOF)

A nitrogen laser (λ = 337 nm) with a pulse duration of 6 - 7 ns was used to photogenerate charge carriers. The absorption coefficient at the excitation wavelength was found to be between 2.34×10^4 cm^{-1} and 2.97×10^4 cm^{-1} for the AnE-PVstat polymer samples, so most of light was absorbed within the first 300 - 400 nm of the

investigated films. A variable DC potential was applied to the samples and, in order to ensure a uniform electric field inside the device, the total photogenerated charge was kept less than 0.1 CV (where C is the sample capacitance and V is the applied potential) by attenuating the laser beam intensity with quartz neutral filters. The photocurrent was monitored across a variable load resistance by using a Tektronix TDS620A digital oscilloscope. TOF measurements were performed at room temperature and under dynamic vacuum (10^{-5} mbar).

To make sure that photogenerated charges in side devices are not more than 10% of capacitive charge (CV), at each and every laser pulse and voltage applied to the sample, charges were calculated (from integerated area in Figure 2.4**,** integrated area is equal to photogenerated charges) and compared with CV. TOF measurements were performed at room temperature and under dynamic vacuum (10^{-5} mbar).

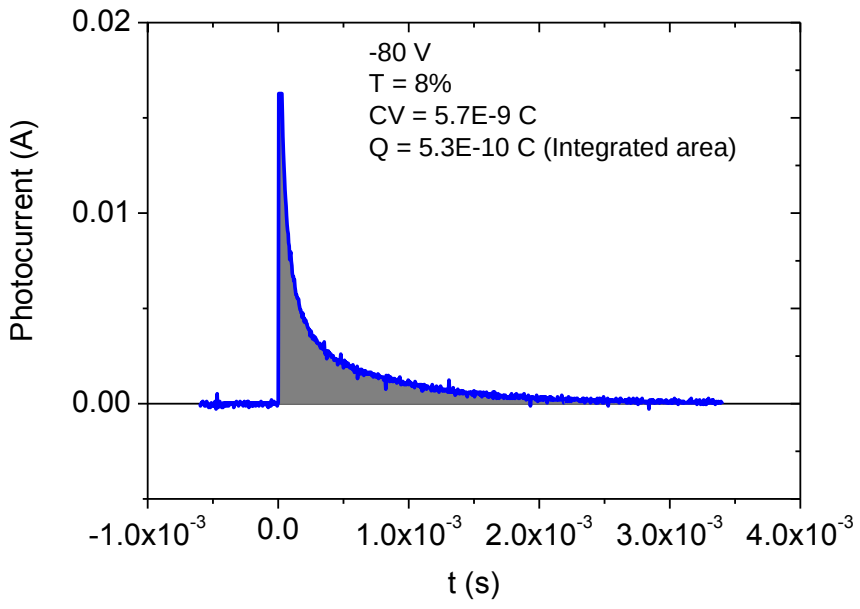

Figure 2. 4. TOF-transient signal as collected from osciloscope. The measurement was done at - 80 V applied bias with percent transmittance 8%.

2.2.2.3. Hole mobility measurement using Integral mode Time of flight (I-TOF) method

I-TOF characterization was made using the setup depicted in Figure 2.5 at constant capacitance of 100 nF and load resistance of 10 kΩ. As shown in the Figure 2.5, TOF devices consist of active materials of P(PE-PV) hybrid polymer sandwiched between two electrodes (Al coating). A short laser (N_2 laser with $\lambda = 337$ nm) with a pulse width of 10 ns was used to photo-generate Gaussian shape of charge carriers from one side of Al electrode (this electrode was semitransparent to allow the light to pass and excite charge). Dragged by the external applied electric field, the generated charge carriers drift through the material with certain thickness.

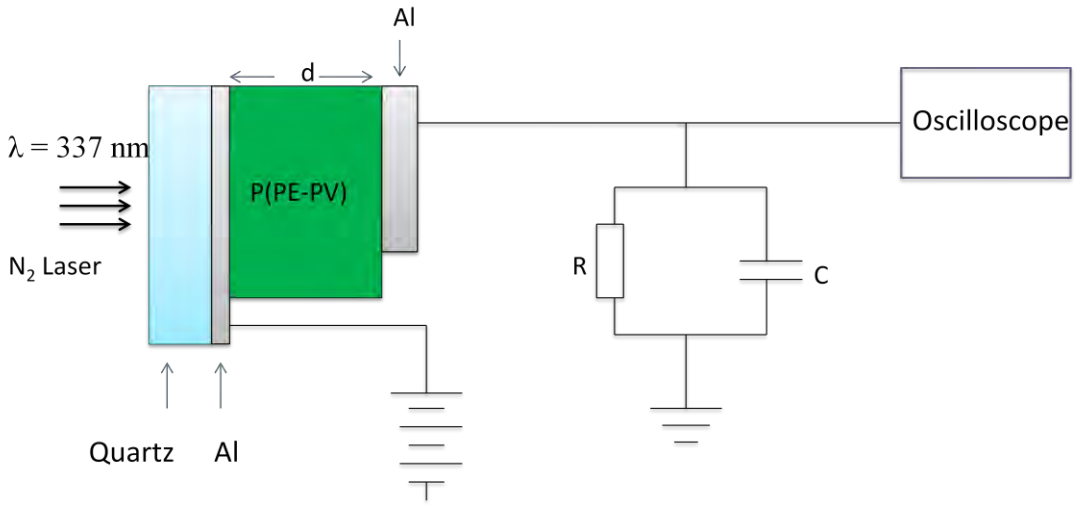

Figure 2. 5. Circuit diagram for integral mode time-of-flight (I-TOF) set up as of reference [158].

Both electron and hole mobilities were expected to be measured. Unfortunetly electron mobility measurment could not give expected signals. For the electrons there were trapping and signals were not clear [157]. Therefore only hole mobility of the devices were measured by applying positive potentials from 140 V to 250 V. Potentials were applied on transparent and illuminated electrode (Al with 18 nm

thickness). Before application of potential, TOF charges were collected for dark injection and photogenerated charges were obtained by subtracting dark injected charges from the total charges in side the devices. The integral TOF setup used in this study is presented in Figure 2.5.

2.2.3. Charge carrier mobility using Admittance Spectroscopy (AS)

2.2.3.1. Sample preparation for mobility measurement using AS

After cleaning of the patterned ITO glass substrates with ultrasonication in acetone and iso-propanol sequentially for 15 minutes in each, and dried with nitrogen gas, and then further cleaned with UV-ozone cleaner for 15 minute in order to remove organic residues. For all AS mobility measurements, hole injecting PEDOT:PSS was first filtered with a 0.45 μm filter and deposited with spin coating speed of 4000 rpm on cleaned ITO substrate and backed at temperature of 145^{o}C for 10 minutes to remove water and improve work function of it [159]. Active layers of AnE-PV*stat4* prepared in chloroform (19 g/L) were spin-coated with the spinning speed of 600 rpm. Then, the prepared samples were immediately transferred into Argon glove box; and then evaporation of Ag (70 nm) was done to complete device preparation with base pressure of 2-3 x 10^{-6} mBar and deposition rate of 0.1 - 0.2 nm/s. The resulting sample have the device structure of ITO/PEDOT:PSS/AnE-PV*stat4*(400 nm)/Ag (70 nm). Mobility measurements were done both at room temperature and at different temperatures. Samples for temperature dependent investigations were transferred into sample holding chamber and left under vacuum overnight in order to remove residual solvent and oxygen.

For study of effect of barrier height between polymer LUMO and cathode work function on charge carriers' mobility, the diode type mobility devices were prepared by sandwiching films of AnE-PVstat polymer between two electrodes. Al, Ag, PEDOT:PSS/Ag and Au were used as top electrodes of different work functions, keeping the same ITO/PEDOT:PSS as bottom electrode for all devices, that means devices with different cathode materials were prepared. The film deposition conditions for all devices were the same (deposited with spin-coating at spin speed of 500 rpm) except variations of the type of top electrodes. The device structures of the four diodes were ITO/PEDOT:PSS/AnE-PV*stat*/Al, ITO/PEDOT:PSS/AnE-PV*stat*/ Ag, ITO/PEDOT:PSS/AnE-PV*stat*/Au, and ITO/PEDOT:PSS/AnE-PV*stat*/PEDOT: PSS/Ag.

In case of the devices that use PEDOT:PSS/Ag as a top electrode, after the film of active layer was deposited and dried, 50 μL of ethanol was spin-coated on top of the polymer film; and then PEDOT:PSS containing 20% of isopropanol was spin-coated with 1000 rpm. Addition of isopropanol was to improve conductivity of the top PEDOT:PSS layer. The samples were completed after thermal evaporation of the top metal electrodes such as Au, Ag and Al without exposing them to air. The top electrode, Au, Ag and Al were evaporated at a base pressure of 1 - 3 x 10^{-6} mbar. The surface areas of the resulting devices were ~ 7 mm^2. After device completion, the samples were transferred to characterization glove box (which is in contact with evaporating glove box) without air contact to the samples.

2.2.3.2. Hole mobility measurement using AS

Before AS measurement, sample-holding chamber was filled with liquid nitrogen, in order to perform electrical characterization under controlled temperature. The

electrical characterization of the devices was carried out in a home-made chamber (at National Research Center of Bologna, Italy) under dynamic vacuum (5 x 10^{-4} mbar). Admittance spectroscopy measurements were conducted using an HP 4294A Agilent Technology impedance analyzer (10 Hz - 10 MHz). The device temperature was varied in the range 5 - 85^{o}C temperature with step of 20^{o}C. A Pt100 thermoresistor was used for the measurement of the temperature of the devices. At each fixed temperature, a series of DC bias voltages were applied to the device. Frequency dependent conductance (G) and capacitance (C) signals were recorded at different DC bias from 0 V - 10 V by superimposing AC signals with the amplitude of 50 mV. Positive bias was applied to the ITO/PEDOT:PSS electrode, in order to inject holes from ITO and the negatively biased top Ag electrode was used as electron blocking contact. Conductance and capacitance data were extracted with MS-Excel from the instrument. Origin software was used for data analysis purpose. The negative change in susceptance peak was deduced from capacitance spectra.

2.3. Solar Cells Preparation and Characterizations

2.3.1. Solar cells fabrications

Solar cells were fabricated on patterned ITO-coated glass substrates. Previously cleaned substrates with detergent and water were further cleaned by ultrasonication in acetone and isopropanol sequentially for 15 min in each. A PEDOT:PSS (Clevios P VP AI 4083) layer was spin-coated at 4000 rpm onto UV-Ozone-treated ITO-coated substrates to a thickness of around 40 nm, then baked in an oven at 140°C for 10 min. AnE-PV*stat* polymer samples were blended with PCBM (Aldrich) and dissolved in chlorobenzene (17 gL^{-1}) with AnE-PV*stat:*PCBM at ratio of 1:1. To investigate effects of macromolecular parameters on the performance of solar cells, solutions of

the blend with different donor to acceptor ratio that is AnE-PV*stat*: PCBM with 1:2 ratio were prepared with the same condition of that of AnE-PV*stat*: PCBM with 1:1. The solutions were stirred at 40°C overnight. The blend solutions were spin-coated at 500 rpm in air onto the ITO/PEDOT:PSS substrates.

The spin-coated blends were solvent-vapor annealed with chlorobenzene for one day before transferring to an Argon glove-box, where the device structure was completed with the thermal evaporation of the LiF (0.9 nm)/Al (80 nm) cathode at a base pressure of 3 x 10^{-6} mbar. The active device area, defined by the shadow mask used for the cathode deposition, was 8 mm^2. The thickness of the active layer was 135 nm, 130 nm and 93 nm for solar cells based on AnE-PV*stat*-a, AnE-PV*stat*-b, and AnE-PV*stat*-c, respectively.

To study effect of solvent additives on photovoltaic performance of PDTSTTz:PCBM bulk heterojunction solar cells, 10 mg/mL solutions of PDTSTTz:PCBM (1:1) blend were prepared in di-chlorobenzene in five different vials and left under stirring overnight. Keeping one of PDTSTTz: PCBM (1:1) solutions as a control, into each of rest of four solutions of PDTSTTz: PCBM (1:1) 2.5% (v/v) of low boiling point solvent additives such as iodomethane (IMe), iodoethane (IEt), iodobuthane (Ibu) and di-iodomethane (DiIMe) were added and left under stirring for half an hour at room temperature. Pre-cleaned and patterned ITO coated glass substrates were further cleaned by ultrasonication sequentially with acetone and isopropanol for 15 minutes and dried in air. Filtered PEDOT:PSS (Baytron PH) was spin coated on top of ITO with 4000 rpm and was baked at 140^{o}C on a hotplate for 15 minutes. The active layer (PDTSTTz:PCBM) solutions with and without 2.5% (v/v) of the different solvent additives were then spin-coated on top of PEDOT:PSS film with spin speed of 800

rpm. Then the samples were dried in air. The top electrode aluminum metal (~97 nm) deposition was done using thermal evaporator (EDWARDs 306) with vacuum of 5 x 10^{-6} mbar. Devices with a configuration of ITO/PEDOT:PSS/PDTSTTz:PCBM-/Al(97 nm), with active area of ~ 4 mm^2 were obtained.

To study impact of P3HT addition on the photovoltaic performance of PDTSTTz/PCBM solar cells, solutions with concentration of 10 mg/mL were prepared from the two donor polymers (P3HT and PDTSTTz) and PCBM. Keeping donor:acceptor (polymer:PCBM) ratio constant with 1:1, and with variation of proportion of P3HT/PDTSTTz in P3HT/PDTSTTz/PCBM blend, solar cell samples were prepared with spin-coating speed of 800 rpm. Solar cell samples of P3HT/PDTSTTz/PCBM blend with various compositions of P3HT, i.e, 25%, 50% and 75% (w/w) of P3HT with respect to PDTSTTz were prepared in di-chlorobenzene in the presence of 2.5% IBu. Evaporation of top aluminum electrode was done on to P3HT/PDTSTTz/PCBM (ternary) blends and resulted in the conventional device structure of ITO/PEDOT:PSS/P3HT:PDTSTTz:PCBM/Al (97 nm).

2.3.2. Current-voltage (J-V) and incident photon to current conversion efficiency (IPCE) measurement

For AnE-PV*stat-a*:PCBM, AnE-PV*stat-b*:PCBM and AnE-PV*stat-c*:PCBM bulk heterojunction solar cells, J-V electrical characterization was carried out using a computer-controlled Keithley 2400 source-measure unit in glove-box at room temperature. Solar cells were illuminated by using a solar simulator (SUN 2000 Abet Technologies, AM 1.5 G) and the light power intensity was calibrated using a certified silicon solar cell.

J-V charcteristics of solar cells of PDTSTTz:PCBM and P3HT:PDTSTTz:PCBM blend were measured in dark and with illumination of white light in the open air using an electrochemical analyzer (Model CHI600A) under white light illumination of 100 mW/cm^2 from a 150 W xenon lamp of Oriel type light source (Model 68830).

For incident photon to current conversion efficiency (IPCE) measurement, a grating monochromator (Model 77250) was used to select a monochromatic light while shining light to the samples. The photocurrent spectral responses of the lamp were corrected using a standard silicon photodiode (Hamamatsu, Model S1336-8BK). IPCE of PDTSTTZ:PCBM (1:1) solar cell samples without and with the additives of IMe, IEt, IBu and DiIMe were measured in wavelength range of 300 - 800 nm.

2.4. Optical property

Absorption and photoluminescence spectra were carried out on thin films spin-coated (1000 rpm) from chlorobenzene solutions (10 gL^{-1}) onto quartz substrates. Absorption spectra of AnE-PV*stat-a*, AnE-PV*stat-b*, AnE-PV*stat-c*, AnE-PVab, AnE-PVbb, AnE-PVae, AnE-PV*stat4*, AnE-PV*stat5* films were recorded with a Perkin Elmer 950 spectrophotometer. The absorption spectra of films of PDTSTTz:PCBM, P3HT:PCBM, and P3HT:PDTSTTz:PCBM (prepared from DCB, 10 mg/mL [160] were measured by UV-Vis Spectrometer (Spectronic Genesis, 2PC, USA). Photoluminescence (PL) spectra were recorded with a Spex Fluorolog II 1681 spectrofluorometer. PL spectra were measured for films of AnE-PV*stat-a*, AnE-PV*stat-b*, AnE-PV*stat-c* with excitation wavelength (λ_{ex}) of 450 nm. The solution and film preparation steps for absorption and photoluminescence spectra were the same to that of films of solar cells and mobility devices.

2.5. X-ray diffration investigation

AnE-PV*stat* films for XRD investigation were drop-casted onto quartz substrates from chlorobenzene solutions (30 gL^{-1}), stirred for 4 days at 45 - 50°C. After the deposition, the films were solvent-vapor chlorobenzene annealed overnight. X-ray diffraction analysis was carried out by means of a PANalytical X'Pert diffractometer equipped with a copper anode (λ_{mean} = 0.15418 nm) and a fast X'Celerator detector. Step 0.05° (2θ), counting time 120 sec/step. Mineral quartz „zero background" sample holders (The Gem Dugout, State College, PA-USA) were used in order to strongly minimize support contribution to the total scattering. The films were directly investigated in reflection geometry. Domain length L was calculated by the Scherrer equation [161] from parameters of the peak at 5.8° (2θ).

2.6. Atomic Force Microscopy (AFM)

AFM imaging was performed under ambient conditions using atomic force microscope (NanoScope Dimension IIIa, MultiMode Digital Instruments, Santa Barbara, CA, USA) in tapping mode. Tapping mode etched silicon probes OTESPA (Veeco Instrument) with aluminum reflective coating on the backside of the cantilever were used (cantilever resonance frequencies about 300 kHz, a typical spring constant 42 N/m, the tip radius of about 7 nm). The analysis of AFM images was performed with the NANOSCOPE software (Digital Instruments, Inc.). The AnE-PV*stat* films for AFM inspection were drop-casted onto glass substrates coved with Indium-Tin-Oxide from chlorobenzene solutions (30 gL^{-1}), which were stirred for 4 days at 45 - 50°C. After the deposition, the films were solvent-vapor cholorobenzene annealed overnight.

3. Result and Discussion

3.1. Tuning the charge transport properties and photovoltaic performance in anthracene-based PPE-PPV copolymer by fine variation of macromolecular parameters

The electronic properties of conjugated polymers are not simply dependent on their chemical structure but are highly affected by macromolecular parameters, such as molecular weight (MW) and polydispersity, so the advantages of monodisperse low molecular weight conjugated molecules over polymers are often underlined. Macromolecular parameters are known to have great effects on the optical and charge transport properties of conjugated polymer films, also through a different organization of polymer chains in the solid state induced by different MW [162, 163].

We report the effects of macromolecular parameters of an anthracene-containing poly(*p*-phenylene-ethynylene)-alt-poly(*p*-phenylene-vinylene) (PPE-PPV) copolymer, having randomly distributed linear octyl and branched 2-ethylhexyl side chains, denoted AnE-PV*stat.* Light-emitting diodes showing a turn-on voltages below 2 V [41] and solar cells exhibiting a state-of-art efficiency for PPV-based materials of around 5% have been already demonstrated by using AnE-PV*stat*, [164] and also series of this polymer have shown very good ambipolar charge transport properties [165].

Differently from other works, considering wide ranges of MW, with values of the number-average molecular weight (M_n) from a few to tens or hundreds of kg mol^{-1}, in this study the effects on the optical, structural, morphological and transport properties of AnE-PV*stat* films due to a moderate variation of the molecular weight are investigated. Only AnE-PV*stat* samples with high MW are here considered (M_n of the order of 10^4 g mol^{-1}), more promising for electronic applications, and it is shown

that relevant effects are observed even with a variation of M_w of about twice. More interestingly, it is demonstrated that the behaviour of charge carrier mobility with the applied field is affected by the macromolecular parameters in AnE-PV*stat* films, being the mobility trend with field rarely considered in this kind of studies. In addition, the comparison of polymer sample with comparable MW but different polydispersity index (PDI) clearly shows the crucial role of PDI in the organization of polymer chains. Finally, the effect of the properties of the investigated polymer samples on the photovoltaic parameters of bulk-heterojunction solar cells is also considered.

Different values of the macromolecular parameters such as number-average molecular weight, the weight-average molecular weight (M_w) and the polydispersity index of the three AnE-PV*stat* samples under this study [78] are collected in Table 3.1.1. M_w value for AnE-PV*stat*-b was nearly two times lower than that determined for AnE-PV*stat*-a and AnE-PV*stat*-c.

Table 3. 1. 1. Macromolecular parameters of the three polymer samples here investigated: number-average molecular weight M_n, weight-average molecular weight M_w, polydispersity index PDI [44, 78].

Sample	Macromolecular parameters		
	M_n (g mol^{-1})	M_w (g mol^{-1})	PDI
AnE-PV*stat*-a	30600	83900	2.74
AnE-PV*stat*-b	18000	43700	2.43
AnE-PV*stat*-c	41200	82700	2.01

3.1.1. Optical properties

The optical properties of the three polymer samples were investigated by UV-Vis absorption and photoluminescence (PL) spectroscopy, both in dilute solutions and in thin films spin-coated onto quartz substrate (Figure 3.1.1). As expected, no meaningful differences were observed in the optical spectra of dilute solutions, showing the same spectral features already reported for AnE-PV*stat*, [166] with the same emission peak position (579 nm) and very close absorption maxima at 548, 547 and 543 nm for AnE-PV*stat-a*, AnE-PV*stat-b* and AnE-PV*stat-c*, respectively.

Films of AnE-PV*stat* spin-cast from chlorobenzene solution are known to show a stacking behaviour [78], resulting in structured absorption and photoluminescence (PL) spectra exhibiting two peaks, as shown in Figure 3.1.1a for the AnE-PV*stat* samples here investigated. The spectra are also plotted in normalized scales in Figure 3.1.1b for a better comparison. Significant differences in the optical spectra were not expected, given the narrow molar mass range for the three polymer samples, nevertheless some considerations can be made.

The main difference in the absorption spectra is between AnE-PV*stat*-c and the other two samples, the former showing (i) the lower energy peak slightly blue-shifted (located at 579 nm, against 586 and 588 nm for samples AnE-PV*stat*-a, and AnE-PV*stat*-b, respectively), indicating a moderate reduction of the effective conjugation, and (ii) a different relative intensity of the two absorption peaks (Figure 3.1.1b). These features are not related to MW, given the comparable molecular weight of AnE-PV*stat*-c and AnE-PV*stat*-a, and could indicate a different molecular organization in the solid state due to the different polydispersity (Table 3.1.1). Indeed the lower and higher energy absorption peaks have been attributed to the formation of

H and J aggregate formation, respectively [75, 166 - 168], so the spectrum of AnE-PV*stat*-c seems to suggest a more balanced contribution of H- and J-type aggregations, the latter being in any case predominant for all the investigated samples.

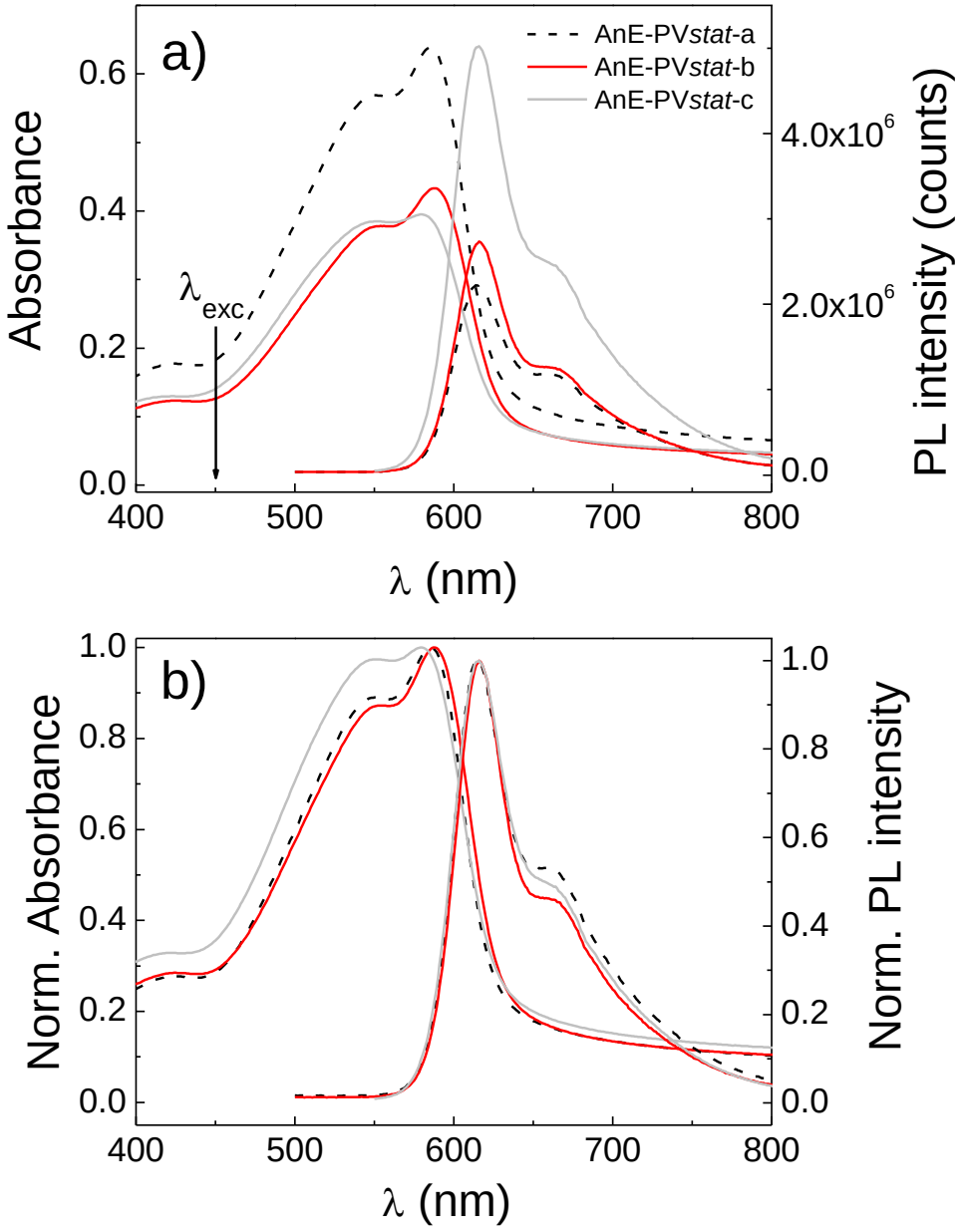

Figure 3. 1. 1. a) Absorption (left) and photoluminescence (right) spectra of thin films of comparable thickness of (about 55 nm) films of AnE-PV*stat-a*, AnE-PV*stat-b* and AnE-PV*stat-c* spin-cast from chlorobenzene solutions onto quartz substrate. b) The same spectra in normalized scales. The excitation wavelength, λ_{exc}, was 450 nm.

Concerning the PL spectra, somewhat different emission capability were observed by films showing a comparable absorbance at the excitation wavelength of 450 nm (Figure 3.1.1a), qualitatively indicating the highest luminescence quantum yield for AnE-PV*stat*-c and the lowest for AnE-PV*stat*-a. Again, this behaviour can be related to a different strength of π-π interchain interactions in the three samples, leading to a quenching of emission [168].

3.1.2. XRD study

The preliminary indications on the solid state organization of the three samples were confirmed by X-ray diffraction (XRD) experiments, conducted on films drop-cast from chlorobenzene solutions. The diffraction patterns shown in Figure 3.1.2 are characterized by a sharp intense reflection at low angle, due to interlayer staking, and by a wide band with no resolved peaks at high angle. The interlayer distance (d_i) and the mean domain length (L), determined from the peak parameters of the XRD patterns, are displayed in Table 3.1.2.

A low intensity second order peak is also detectable on the profile of AnE-PV*stat*-a sample at 11.8° (2θ). The distance between the planes shows only a slight variation in the three polymer samples, with a modest lengthening on lowering the molar mass. On the contrary, the domain length seems to be strongly dependent on M_n and M_w. Indeed, the AnE-PV*stat*-b sample, characterized by the lowest molecular mass parameters, displays an increase of L of about 30% with respect to the other samples and a corresponding increase of the number of lattice planes per domain (n_i).

A rough evaluation of the ratio of the area of the main peak to that of the overall area under the XRD profile suggests that the overall order degree of the investigated

polymer films follows the order: AnE-PV*stat*-a > AnE-PV*stat*-b > AnE-PV*stat*-c. However, if the number of lattice planes per domain is considered, AnE-PV*stat*-b results the sample with the largest ordered domains. The comparison of the XRD patterns of samples AnE-PV*stat*-a and AnE-PV*stat*-c, suggests that polydispersity plays an important role in polymer chains organization.

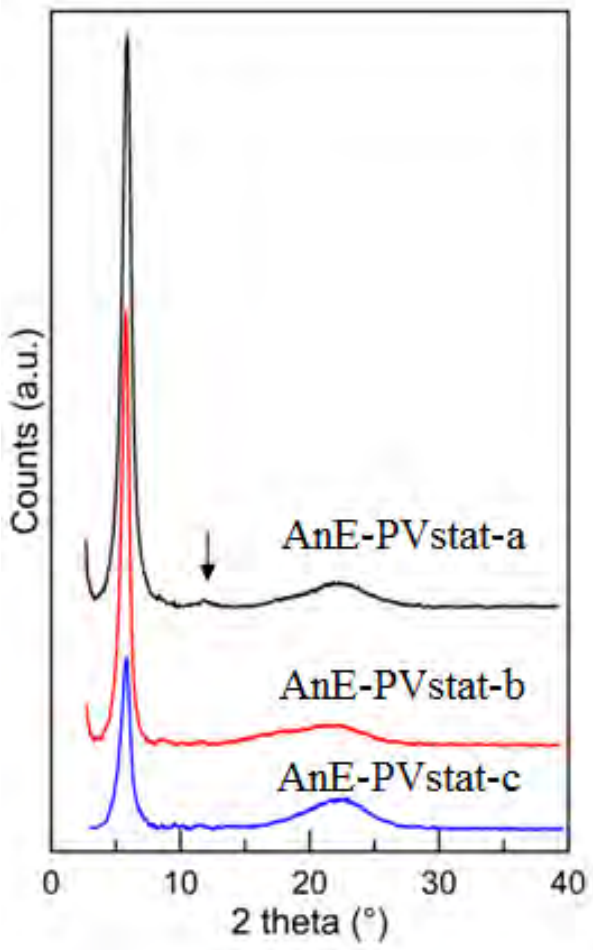

Figure 3. 1. 2. XRD patterns of films drop-cast from chlorobenzene solutions onto quartz holder. The arrow indicates the second order peak of the interlayer stacking for sample AnE-PV*stat*-a

3.1.3. AFM Inspection

The atomic force microscopy (AFM) inspection of films deposited in the same condition used for the XRD investigation revealed a close correlation between the macromolecular parameters and the film topology (Figure 3.1.3). Polymer chains in AnE-PV*stat*-b film, with the lowest MW, were able to pack in smaller domains, compared with the samples with higher molar mass, while a prevailing fibril-like formation was observed for samples AnE-PV*stat*-a and AnE-PV*stat*-c. The smaller-domain morphology of AnE-PV*stat*-b film was also accomplished by a higher root-mean-square roughness (R_q), compared to the films made of the polymers with higher molar weight. The values of R_q evaluated on a scan area of 0.5 μm x 0.5 μm were 1.34, 1.58 and 0.71 nm for AnE-PV*stat*-a, AnE-PV*stat*-b and AnE-PV*stat*-c, respectively, and maintained the same trend over a larger scan area of 1.0 μm x 1.0 μm. By comparing AnE-PV*stat*-a, AnE-PV*stat*-c, exhibiting a similar MW, the lower R_q was observed for the one showing the lower polydispersity, indicating that the distribution of molecular weight plays a role in the film morphology.

Table 3. 1. 2. XRD parameters of the three polymer samples investigated: interlayer distance, d_i, peak width, FWHM, mean domain length, L and mean number of interlayer lattice per domain, $n_i = L/d_i$.

Sample	XRD parameters			
	d_i (nm)	FWHM (°,2θ)	L (nm)	n_i
AnE-PV*stat*-a	1.50	0.84	10.5	7.0
AnE-PV*stat*-b	1.53	0.67	13.2	8.6
AnE-PV*stat*-c	1.52	0.86	10.3	6.8

The comparison of Figures 3.1.3a and 3.1.3c show the effect of the different polydispersity index on the film morphology. Indeed, the higher PDI of AnE-PV*stat*-a seems to be beneficial for a more regular arrangement of polymer chains, confirming the XRD data, and as previously suggested for poly(3-alkylthiophenes) [169].

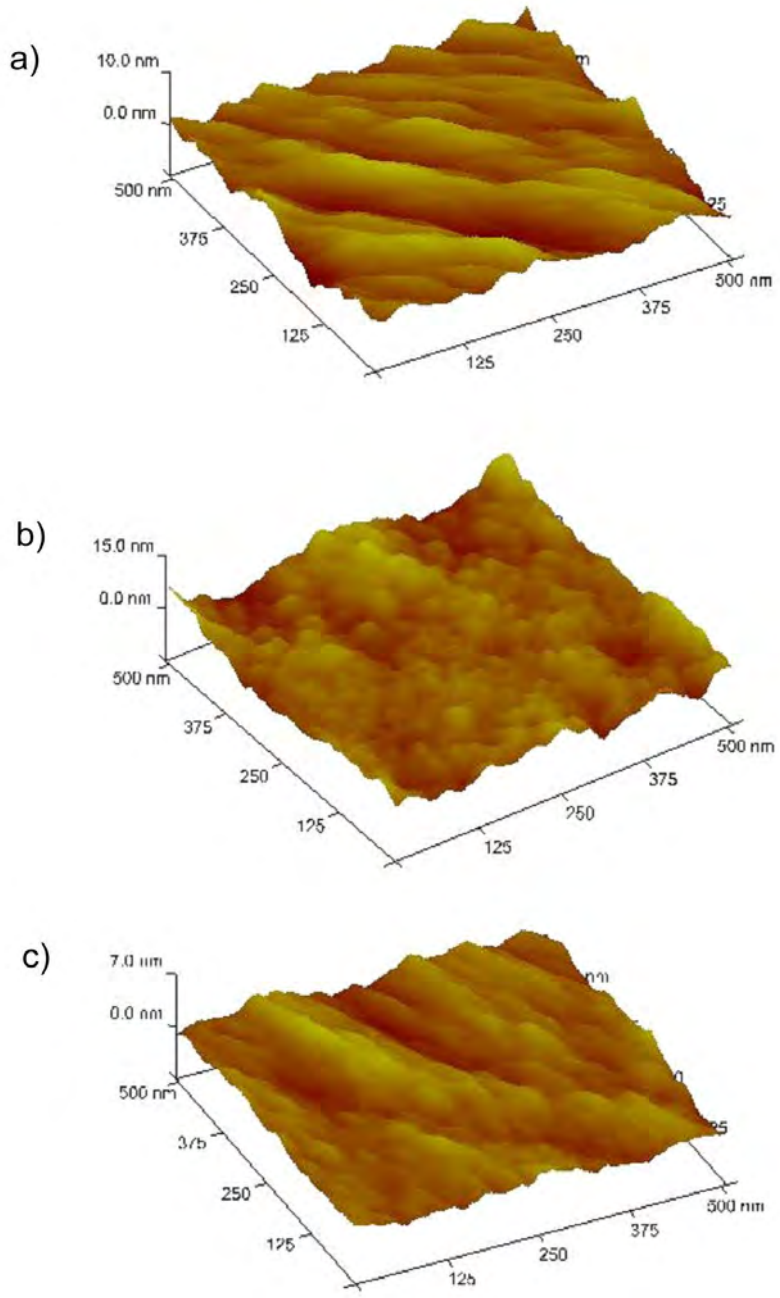

Figure 3. 1. 3. Three-dimensional AFM topography images of drop-casted films made of: a) AnE-PV*stat*-a; b) AnE-PV*stat*-b; c) AnE-PV*stat*-c.

The drift mobility (μ) of charge carriers in films of AnE-PV*stat* was investigated as a function of the electric field (E) by using differential small-signal Time Of Flight (TOF) [170], considered a "direct" method for the investigation of bulk transport properties in disordered materials. The TOF experiments were performed on sandwich-type devices with the structure Al/AnE-PV*stat*/Al, where the polymer layer was drop-casted from the same chlorobenzene solutions used for the preparation of the XRD and AFM samples. The sign of charges generating the photocurrent signals was selected by appropriately biasing the devices.

3.1.4. Hole and electron moblity investigation using TOF technique

The photocurrent transients for the three polymer samples are displayed in a double-logarithmic representation in Figure 3.1.4 for a comparable electric field of about 1 x 10^5 V cm^{-1}. The shape of TOF signals shown in the Figure 3.1.4 is representative for transients observed for different values of E and indicates a quite dispersive transport. Transit times of charge carriers were evaluated with the same method in all cases, that is from the inflection point visible in the double-logarithmic plots [171]. The values of charge carrier mobility, calculated through the well-known Equation,

$$\mu = \frac{d}{\tau E} \qquad (3.1)$$

where d is the thickness of the polymer layer, are shown as a function of the applied electric field in Figure 3.1.5 and Figure 3.1.6. As far as the trend of μ with E is concerned, being the same for both positive and negative carriers for each AnE-PV*stat* sample, again the main difference was observed between AnE-PV*stat*-c and the other two polymer samples, both showing a higher overall order of degree as observed with XRD. It has already been reported that charge carrier mobility in AnE-

PV*stat*-c films shows a Poole-Frenkel behavior both for holes and electrons [165], with an exponential increasing of μ with the square root of E. Differently, mobility in AnE-PV*stat*-a and AnE-PV*stat*-b films exhibits a decreasing trend for low fields and reaches a minimum before starting increasing with E.

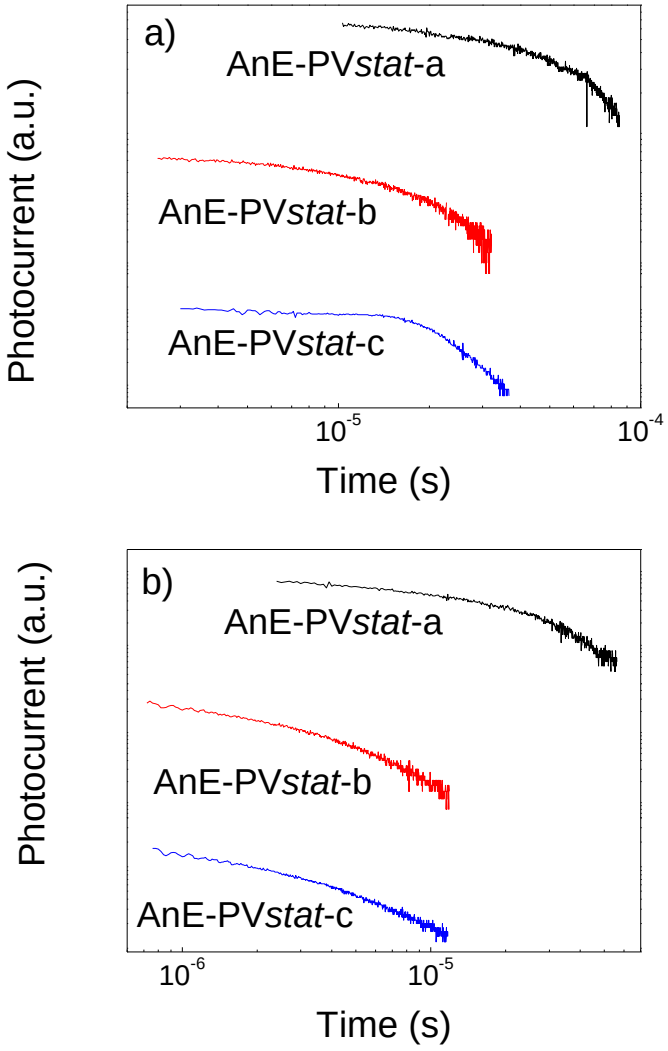

Figure 3. 1. 4. Log-log plots of photocurrent signals for holes (a) and electrons (b) for a comparable electric field of about 1 x 10^5 V cm^{-1}.

The Poole-Frenkel-like trend of mobility is often observed for disordered organic materials, while behaviour similar to that exhibited by AnE-PV*stat*-a and AnE-

PV*stat*-b samples is less common. As an example, a decreasing trend of μ at low field is usually observed for regioregular poly(3-hexylthiophene) [172, 173].

Both types of trend exhibited by the mobility in the three AnE-PV*stat* samples can be explained within the same model of hopping conduction in a Gaussian distribution of localized states, as demonstrated by Monte Carlo simulations [48, 174].

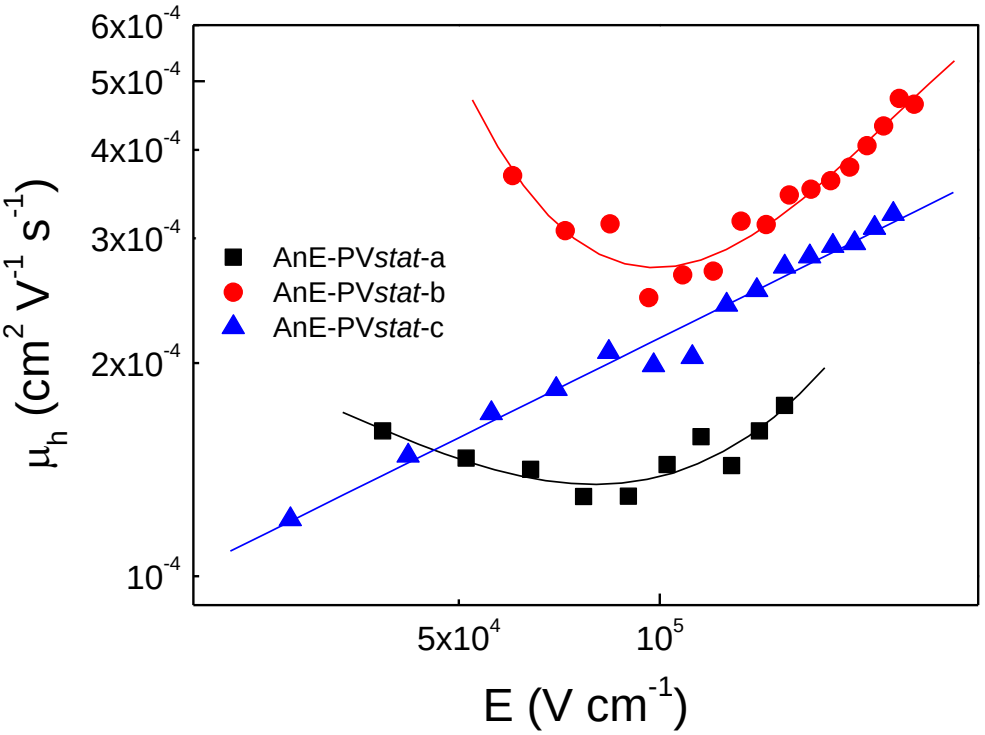

Figure 3. 1. 5. Hole drift mobility as a function of the applied electric field: AnE-PV*stat*-a (squares); AnE-PV*stat*-b (circles); AnE-PV*stat*-c (triangles). Lines are fits to the experimental data.

Indeed, depending on the relative contribution of energetic (diagonal) and positional (off-diagonal) disorder to the random walk of charge carriers, a Poole-Frenkel-like behaviour or a change of sign of the field dependence of mobility can be observed. Interestingly, the minimum of μ is reached both for AnE-PV*stat*-a and AnE-PV*stat*-b at the same field value of about 10^5 V cm^{-1}, suggesting that the role of energetic and

off-diagonal disorder is qualitatively similar for these two polymers samples showing higher polydispersity index.

As already reported for sample AnE-PV*stat*-c [165], AnE-PV*stat* shows a good ambipolar behaviour, with drift electron mobility even higher than that evaluated for holes (Figure 3.1.5 and Figure 3.1.6), at least in the investigated field range.

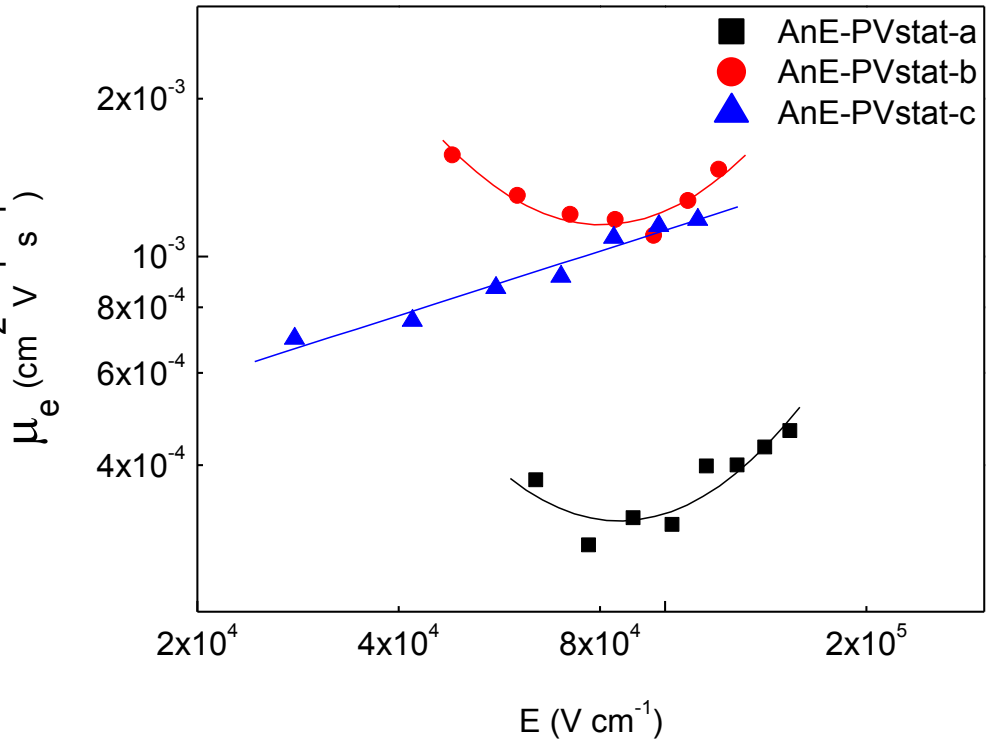

Figure 3. 1. 6. Eelectron drift mobility as a function of the applied electric field: AnE-PV*stat*-a (squares); AnE-PV*stat*-b (circles); AnE-PV*stat*-c (triangles). Lines are fits to the experimental data.

For both types of carriers, drift mobility shows a clear dependence on the macromolecular parameters. At low fields (below 5 x 10^4 V cm^{-1}), the hole mobility seems to be correlated to the mean domain length (Table 3.1.2), with more ordered polymer samples showing higher mobility. However hole mobility in sample AnE-

PV*stat*-c surpasses that in sample AnE-PV*stat*-a as E is increased, because of the strong field activation of the less ordered polymer also at moderate electric fields.

3.1.5. Effect of slight variation in macromolecular properties of AnE-PVstat polymer on the photovoltaic performance of AnE-PVstat :PCBM BHJ solar cells

In order to analyze the effect of the macromolecular parameters on the photovoltaic properties of AnE-PVstat polymer*s* (whose structure is shown in Figure 2.1 in the experimental part), bulk heterojunction solar cells were constructed with the three polymer samples (AnE-PVstat-a, AnE-PVstat-b and AnE-PVstat-c) as electron-donors and PCBM as acceptor. The device profiles of the three solar cell samples prepared for this investigation are presented by Figure 3.1.7.

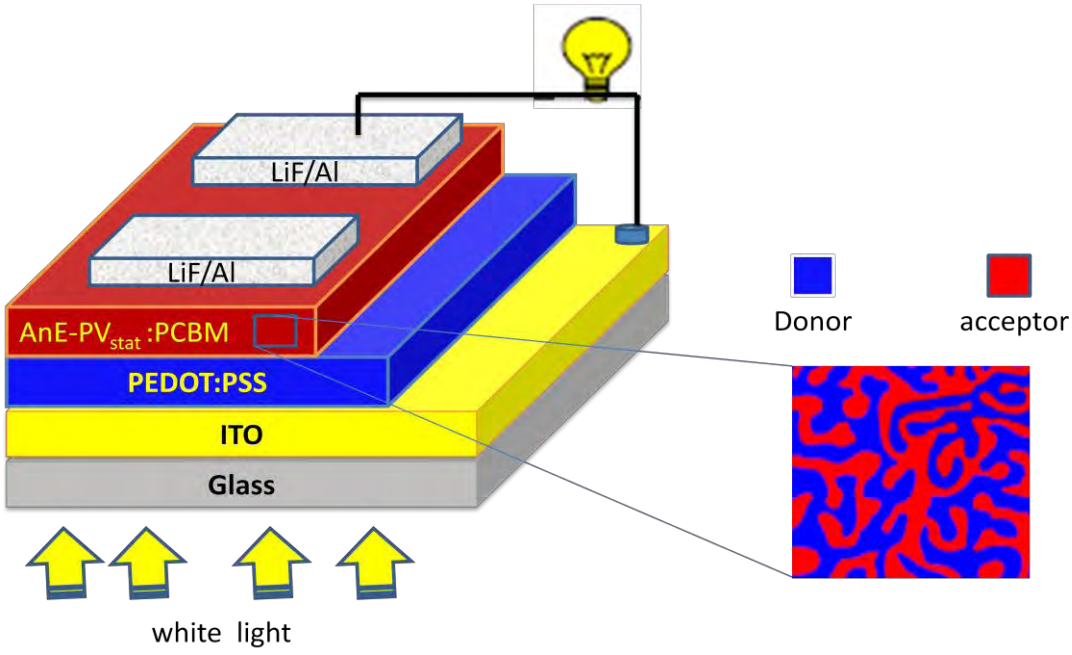

Figure 3. 1. 7. Stacking profile of AnE-PVstat :PCBM blend solar cells prepared from chlorobenzene.

Since for a given donor/acceptor (D/A) pair, the maximum photovoltaic performance of the related blends is determined by a critical interplay between different factors,

such as miscibility, deposition conditions, blend thickness, donor to acceptor ratio, pre- and/or post-treatments, [175] the comparison of different D/A pairs is not so straight forward. For this reason the aim of this work was not the optimization of solar cell devices, but to establish how the photovoltaic properties of AnE-PV*stat*:PCBM blends were affected when an organization of the donor phase close to that of drop-casted thick films already investigated was induced.

To this end, efforts were made to use deposition and treatment conditions able to induce such organization in spin-coated thin films, required for lab-scale solar cell preparation. The AnE-PV*stat*:PCBM active layers were deposited onto ITO-/PEDOT:PSS substrates by using a D/A ratio of weight (1:1) and (1:2), the same solvent chlorobenzene, the same solution concentration, the same low rotation speed of the spin-coater. After the deposition, the AnE-PV*stat*:PCBM films were solvent-vapor annealed for one hour, in order to foster the polymer chain organization through the slow-drying process. Solar cells preparation steps were completed with a LiF/Al vacuum evaporated cathode.

The photovoltaic parameters of AnE-PV*stat-a*:PCBM, AnE-PV*stat-b*:PCBM, and AnE-PV*stat-c*:PCBM solar cells are collected in Table 3.1.3, along with the thickness of the active layers, while the related current-voltage characteristics are displayed in Figure 3.1.8. A straight comparison can be done for the same active layer thickness. Solar cells made with AnE-PV*stat*-a show a slightly higher short-circuit current (J_{sc}) with respect to those with AnE-PV*stat*-b donor, which could arise from an increased A/D interface, leading to a slightly higher generation of charge carriers.

This could be due to a more intimate mixing with the PCBM moiety because of the longer polymer chains of AnE-PV*stat*-a. However, the striking difference in the

photovoltaic parameters of the two kinds of cells is given by fill factor (FF), raising from 0.46 for AnE-PV*stat*-a to 0.67 for AnE-PV*stat*-b, giving a strong indication of very different transport properties in the blends and confirming the mobility data.

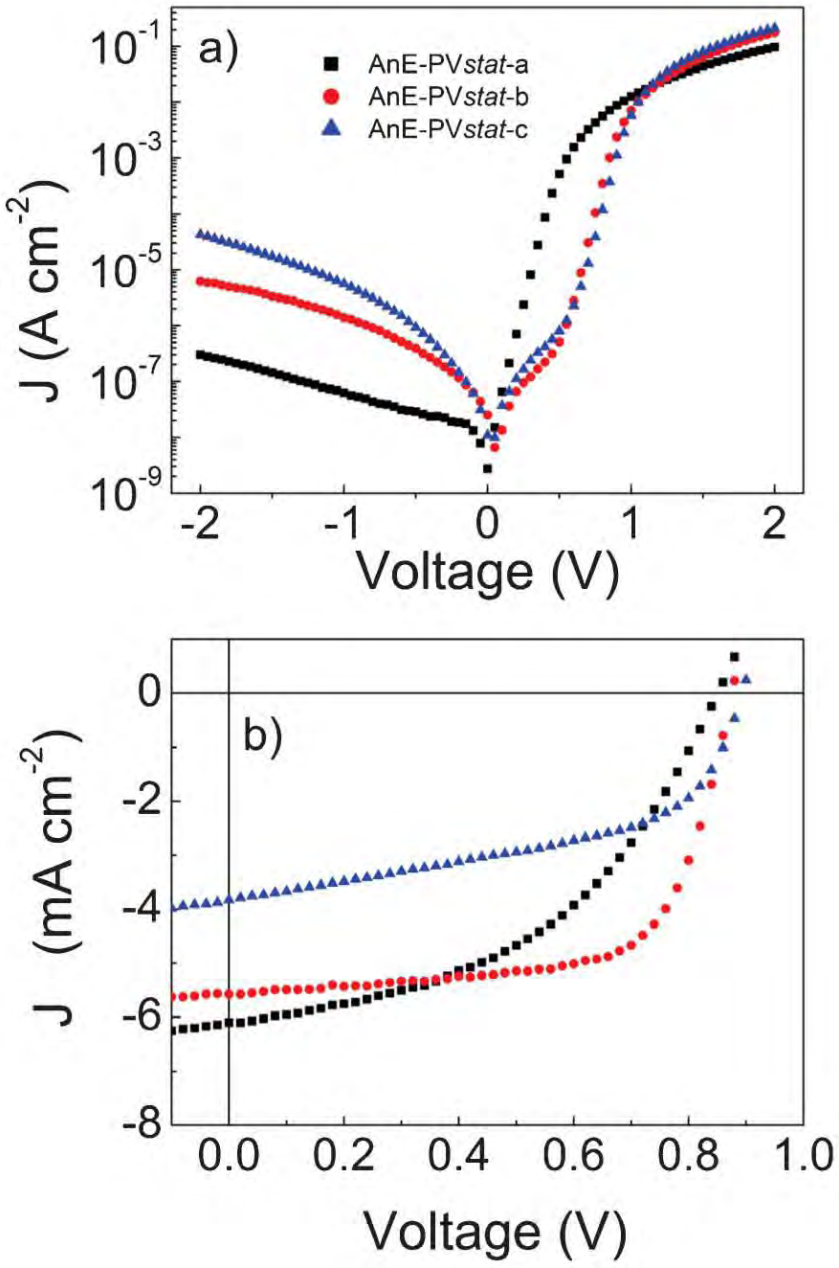

Figure 3. 1. 8. Current density – voltage (J-V) characteristics in the dark (a) and under (AM 1.5 G, 100 mW cm^{-2}) illumination (b) for solar cells made with the three electron-donors: AnE-PV*stat*-a (squares); AnE-PV*stat*-b (circles); AnE-PV*stat*-c (triangles).

As expected, [176] the open-circuit voltage (V_{oc}) was not meaningfully affected by the donor component (Table 3.1.3) and the enhanced FF of AnE-PV*stat*-b based cells led to a power conversion efficiency (PCE) of 3.26%, to be compared with 2.38% of AnE-PV*stat*-a based cells. As observed from Table 3.1.3, shunt resistance (R_{SH}) of AnE-PV*stat*-b is more than three times higher than AnE-PV*stat*-a and AnE-PV*stat*-c donors, and series resistance (R_s) of AnE-PVstat-b is lower than AnE-PV*stat*-a and AnE-PV*stat*-c donors almost by half.

The R_S and R_{SH} results of the solar cells of these donors further confirms charge carriers mobility and then fill factor differences observed in the three different cases. The differences in R_{SH} among these polymers corresponded to the differences in FF. Concerning AnE-PV*stat*-c donor, the short circuit current, thus PCE, can hardly be compared with the values observed for the other solar cells, because of the reduced active layer thickness.

Table 3. 1. 3. Active layer thickness and photovoltaic parameters (AM 1.5 G, 100 mW cm^{-2}) of solar cells made with AnE-PVstat donors and PCBM acceptor in 1:1 weight ratio.

Polymers	Thick.	R_S	R_{SH}	Photovoltaic parameters (AM 1.5 G, 100 mW cm^{-2})			
	(nm)	(Ω cm^{-2})	(Ω cm^{-2})	J_{sc} ($mAcm^{-2}$)	V_{oc} (V)	FF	PCE (%)
AnE-PV*stat*-a	135	55.50	549.4	6.10	0.85	0.46	2.38
AnE-PV*stat*-b	130	28.40	1612.9	5.57	0.87	0.67	3.26
AnE-PV*stat*-c	93	46.36	58.24	3.82	0.89	0.51	1.73

However, some consideration can be done on fill factor, which, differently from J_{sc}, is not affected by the lower solar light harvesting ability of cells made with AnE-PV*stat*-c donor.

Effect of macromolecular properties on AnE-PV*stat* polymers in AnE-PV*stat*:PCBM BHJ solar cell was also studied in different proportions of PCBM in the blend. The donor:acceptor composition of 1:2 weigh ratio was used. In this case the two polymers AnE-PV*stat-b* and AnE-PV*stat-c*, where molecular weight of AnE-PV*stat-c* is twice of that of AnE-PV*stat-b* were studied for the effect of their molecular weight on the resulting AnE-PV*stat*:PCBM (1:2) BHJ solar cells.

Unlike that of AnE-PV*stat*:PCBM (1:1) case, in this specific study, top metal electrode was made from Ca (20nm) and Al (80nm) sequentially evaporated. The J-V characteristics of AnE-PV*stat*:PCBM (1:2) BHJ solar cells were shown in Figure 3.1.9. From the Table 3.1.4 and Figure 3.1.9, the macromolecular effects were observed on J_{sc} and FF and thus PCE. Expected effect of macromolecular properties on FF and J_{sc} and then in PCE was observed also in AnE-PV*stat*:PCBM (1:2) BHJ solar cell. However, unexpectedly FF, J_{sc} and V_{oc} as well as PCE were decreased and series resistances were increased compared to AnE-PV*stat*:PCBM (1:1) case.

Upon increasing PCBM composition from 1:1 to 1:2 weight ration, FF and R_{sh} were expected to increase and R_s was expected to decrease, but may be because of the top electrode of Ca/Al interlayer, internal series resistances and contact resistances were increased (Table 3.1.4) as the result electrons collection efficiency of the top electrode was poor.

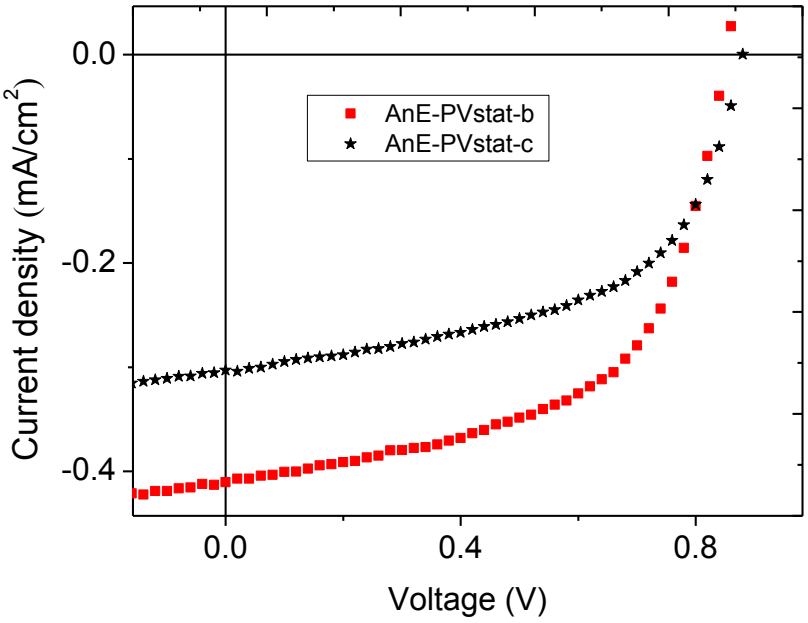

Figure 3. 1. 9. Current density (J-V) voltage characteristics (AM 1.5G, 100 mW cm^{-2}) for solar cells made with the two electron-donors: AnE-PV*stat*-b (square); AnE-PV*stat*-c (star) for AnE-PV*stat*:PCBM in 1:2 ratio.

Table 3. 1. 4. Series resistance (R_S), shunt resistance (R_{Sh}) and photovoltaic parameters (AM 1.5G, 100 mW cm^{-2}) of solar cells made with AnE-PV*stat* donors and PCBM acceptor in 1:2 weight ratio with ITO/PEDOT:PSS/AnE-PV*stat*/Ca (20 nm)/Al(80 nm).

Polymers	R_S	R_{SH}	photovoltaic parameters (AM 1.5G, 100 mW cm^{-2})			
	(Ωcm^{-2})	(Ωcm^{-2})	J_{sc} (mA cm^{-2})	V_{oc} (V)	FF	PCE (%)
AnE-PV*stat*-b	444.44	12048	0.443	0.85	0.60	2.3
AnE-PV*stat*-c	751.88	12820	0.303	0.88	0.56	1.84

Fill factor of AnE-PV*stat*-c :PCBM (1:1) cells was found to be 0.51, in between those of the other cells, again confirming the trend of hole mobility in pristine AnE-PV*stat* films. Figure 3.1.10 shows the straight correlation between fill factor of solar cells and

the mobility of positive carriers measured in pristine AnE-PV*stat* films at a field of about 1 x 10^5 V cm^{-1}.

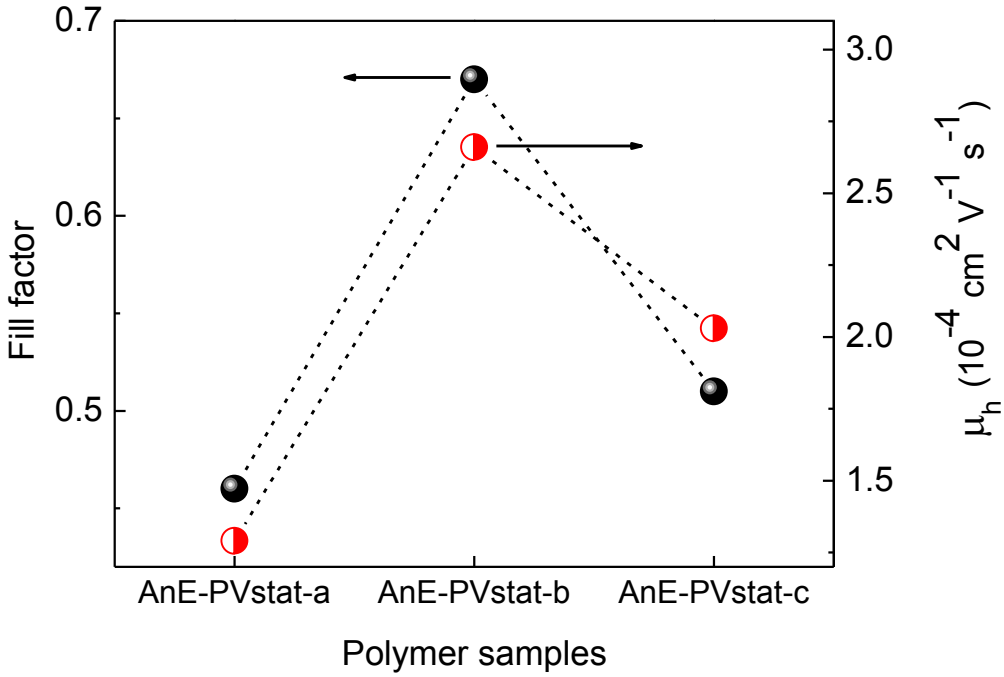

Figure 3. 1. 10. Fill factor of AnE-PV*stat*:PCBM solar cells (left, circles) and TOF hole mobility, at about 1 x 10^5 V^{-1} cm^{-1}, of pristine AnE-PV*stat* films (right, triangles).

Table 3. 1. 5. Sammary of hole mobility in AnE-PV*stat* donors, fill factors and power conversion efficiencies of a solar cells with AnE-PV*stat* as donors and PCBM as acceptor in 1:1 weight ratio solar cells

Polymers	Mobility (cm^{-2} V^{-1} S^{-1})	FF	PCE (%)
AnE-PV*stat*-a	1.29 x 10^{-4}	0.46	2.38
AnE-PV*stat*-b	2.66 x 10^{-4}	0.67	3.26
AnE-PV*stat*-c	2.03 x 10^{-4}	0.51	1.73

Table 3.1.5 shows direct relation of mobility of holes in AnE-PV*stat* polymers to the performance of the resulting photovoltaic devices. In bulk heterojunction solar cells of AnE-PV*stat-a* hole mobility is 1.29 x 10^{-4} cm^{-2} V^{-1} s^{-1}, and corresponding power conversion efficiency is 2.38. The increment in hole mobility in AnE-PV*stat-b* (2.66 x 10^{-4} cm^{-2} V^{-1} s^{-1}) is manifested by improvent in power conversion efficiency of 3.26%. Here the fill factors (FF) collected in the Table 3.1.5 (extracted from Figure 3.1.8b) for AnE-PV*stat-a*:PCBM, AnE-PV*stat-b*:PCBM and AnE-PV*stat-c*:PCBM demonistrating strong relationship with hole mobility in the polymers.

3.1.6. Conclusions

A slight variation in the macromolecular properties of an anthracene-containing PPE-PPV copolymer (AnE-PV*stat*) lead to appreciable modifications in the optical, morphological, and transport properties of its films, These mocromolecular effect were also reflected by photovoltaic performances of AnE-PV*stat*:PCBM solar cells. The polydispersity index plays a significant role in the organization of polymer chains, thus affecting all the polymer properties.

Not only were the mobility data affected by the macromolecular parameters, but also the trend of μ with the applied electric field. A Poole-Frenkel-like behaviour was obtained for less ordered AnE-PV*stat*-c films, while a minimum of μ at around 1 x 10^{5} Vcm^{-1} was observed for the other two polymer samples giving more ordered arrangements in casted films.

A strong correlation between the fill factor of AnE-PV*stat*:PCBM solar cells and the hole mobility in pristine AnE-PV*stat* films obtained, might be suggesting that tuning of the donor macromolecular parameters is critical for improving performance of polymer/fullerene BHJ solar cells. This study clearly demonstrates the importance of

the fine tuning of the macromolecular parameters for the electronic properties of conjugated polymers.

3.2. Effect of side-chains on charge transport of anthracene-based PPE-PPV copolymers

In this study, the drift mobility of positive and negative charge carriers in a series of six anthracene-containing poly(*p*-phenylene-ethynylene)-alt-poly(*p*-phenylene-vinylene)s (AnE-PVs) are investigated and compared. AnE-PVs, with the anthracene unit between two triple bonds, are a relevant class of conjugated polymers [44], exhibiting outstanding optoelectronic properties. Light-emitting diodes showing a turn-on voltages below 2 V [41] and solar cells exhibiting a state-of-art efficiency of around 5%, for poly(*p*-phenylene-vinylene)-based materials, have been already demonstrated for this class of conjugated polymers [177].

The AnE-PV polymers (whose molecular structures are given in Figure 2.1), with the same conjugated backbone, differ for the nature of the grafted solubilising alkoxy side-chains (linear or branched), and were prepared either with well-defined or with randomly distributed side-chains (random polymers) [41]. Substituents can affect the electronic properties of conjugated polymers [76, 178], other than modifying their processability in organic solvents. Depending on their nature, size and position, substituents can influence the molecular packing of polymer chains, thus greatly affecting charge transport properties of polymer films.

In order to clearly establish the relationship between chemical structure and charge carrier mobility for the investigated polymers, the polymer films were prepared in the same way and the same technique, Time-Of-Flight, was used for their investigation. Indeed, Time-Of-Flight (TOF) technique [170], considered the "direct" method for

the investigation of bulk transport properties in disordered materials, has the great advantage of a facile selection of the sign of charge carriers, thus enabling the measurement of both hole and electron mobility on the same sample.

3.2.1. Optical properties

The effects of nature and size of side chain substituents on optical properties of the solid films of AnE-PV polymer series were observed in Figure 3.2.1. The differences in absorption spectra of these polymers were clearly seen in the spectra. The more redshift in absorption spectra for AnE-PV-ae (containing only linear octyl and octadecyl side chains) was observed compared to absorption spectra of others.

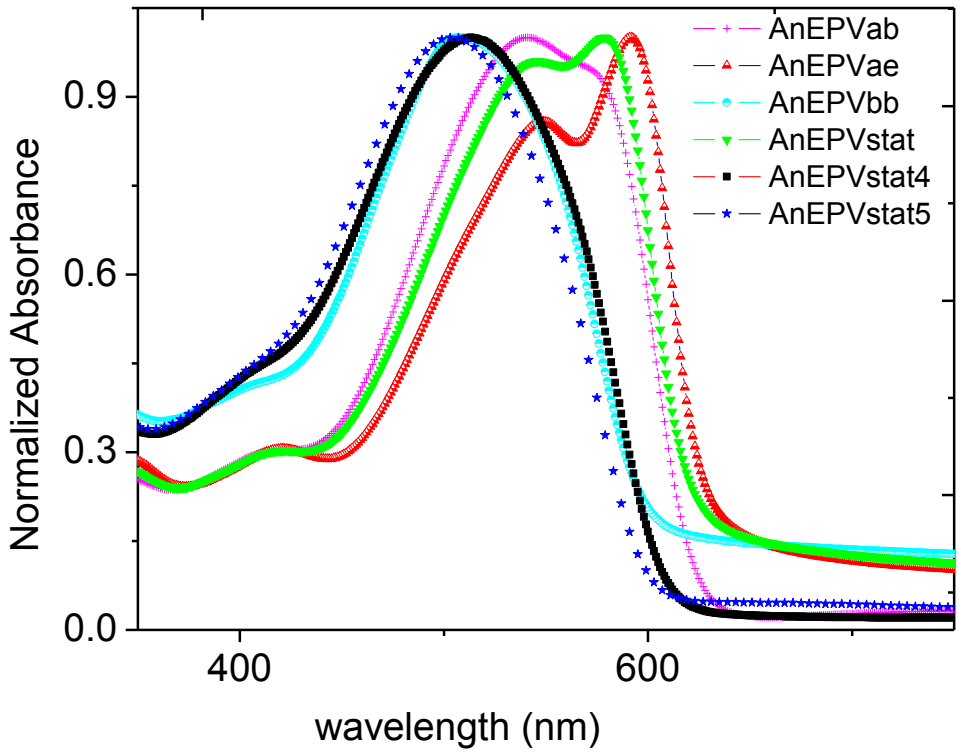

Figure 3. 2. 1. Absorption spectra of AnE-PV-ab (plus sign), AnE-PV-ae (half shade up triangle), AnE-PV-bb (half-shaded circle), AnE-PV*stat* (shaded down triangle), AnE-PV*stat4* (square), and AnE-PV*stat5* (star).

The degree of redshifting can be ordered as: AnE-PV-ae > AnE-PV*stat* > AnE-PVab > AnE-PV*stat4* >AnE-PV*stat5*. And vibronic peaks in high energy range decreasing from AnE-PV-ae spectrum, through AnE-PV*stat* spectrum, to spectra of AnE-PV*stat4* and AnE-PV*stat5* showing differences in crystallinity and order in their films [178].

3.2.2. Hole and electron mobility investigation using TOF technique

The drift mobility of charge carriers was studied as a function of the applied electric field (*E*) by using differential small-signal-mode TOF [170]. The TOF experiments were performed on sandwich-type devices with the structure glass/ITO/polymer/Al, with the top aluminum layer being semitransparent. For a better comparison of the charge transport properties of the investigated AnE-PVs, the same conditions were used for the deposition of all polymer films.

Transport of charge carriers is indeed highly affected by the organization of polymers chains in the solid state, depending on the used solvent, on the deposition technique and deposition parameters, as well as on post-deposition treatments [65, 179]. For this reason, the polymer layers were drop-casted from solutions prepared from the same solvent and treated in the same way onto the glass/ITO substrates and underwent solvent-vapor annealing overnight, in order to allow an optimum organization of polymer chains through a very slow drying process of the films. The sign of charge carriers generating the TOF photocurrent signals was selected by appropriately biasing the illuminated electrode (Al for holes, positively biased, and ITO for electrons, negatively biased).

Typical photocurrent transients, both for holes and electrons, are displayed in Figure 3.2.2 in a double-logarithmic representation and for a comparable applied electric field of about 1 x 10^5 V cm^{-1}. The comparison of the two signals of Figures 3.2.2a - 2f

confirms the usual finding that transport of electrons is more dispersed than that of positive carriers in conjugated polymers [135].

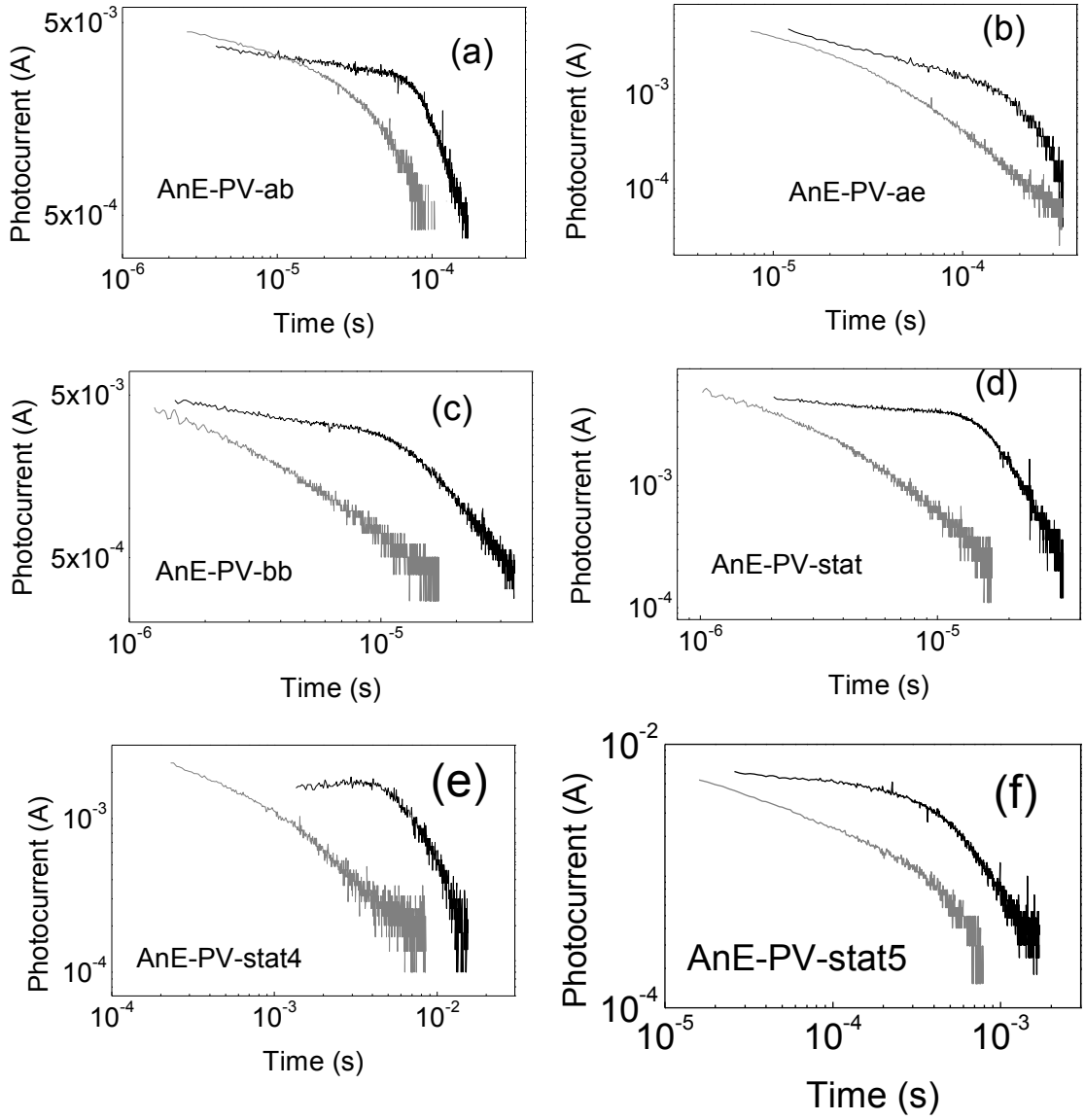

Figure 3. 2. 2. Typical TOF signals in log-log scales for an applied electric field of about 1 x 10^5 V cm^{-1}. Positive carriers (black lines) and negative carriers (light black lines).

This is commonly attributed to trapping effects by typical impurities, acting as trapping states for negative carriers, because of closeness of the trap state energy to the polymer LUMO (Lowest Unoccupied Molecular Orbital) level [180, 181].

Though the dispersion of photocurrent signals, an inflection point was visible also for electrons in the double-logarithmic plots, from which the transit time (τ) of charge carriers can be evaluated [171]. The inspection of Figures 3.2.3a - 3f also suggests that this class of conjugated polymers shows an ambipolar behaviour, as already reported for AnE-PV-*stat* [165], with the photocurrent due to negative carriers decreasing even more rapidly than that of holes and indicating that the time required for electrons to travel through the same sample is not longer than that for holes.

The values of charge carrier mobility were calculated as a function of the applied field through Equation 3.1, and with the transit times extracted from the TOF signals by using the same method in all cases, that is from the inflection point observed in the double-logarithmic representation.

By plotting the logarithm of mobility as a function of the square-root of *E*, a good linear trend was obtained in most cases, as shown in Figure 3.2.3, indicating a Poole-Frenkel behaviour [182, 183],

$$\mu(E) = \mu_{o\,\exp\,(\beta\sqrt{E})} \qquad (3.2)$$

where μ_0 denotes the mobility at zero-field and β is the parameter describing how strong is the dependence of μ(E) on the electric field.

The parameters obtained from the Poole-Frenkel fit to mobility data of Figure 3.2.3 are collected in Table 3.2.1. The only decreasing trend with E was observed for electron mobility, μ_e, in AnE-PV-bb films (Figure 3.2.3b).

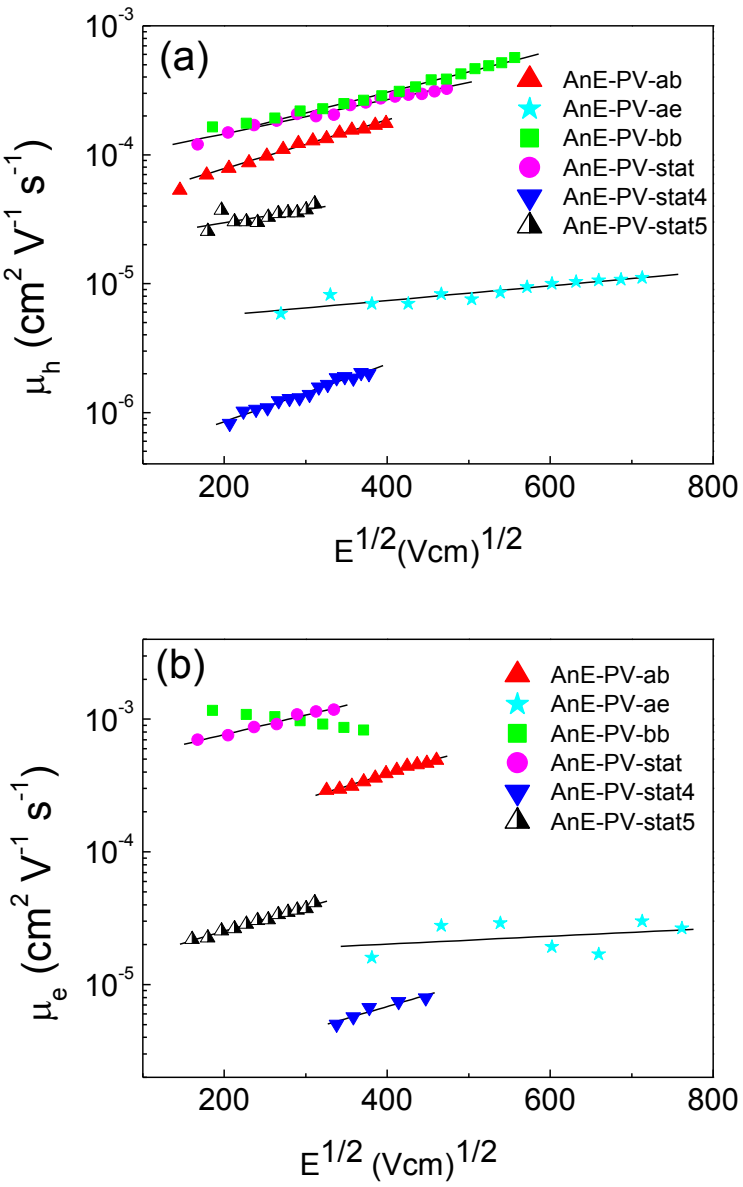

Figure 3. 2. 3. Hole mobility (a) and electron mobility (b) as a function of the square root of the electric field for: AnE-PV-ab (up triangles); AnE-PV-ae (stars); AnE-PV-bb (squares); AnE-PV-*stat* (circles); AnE-PV-*stat4* (down triangles); AnE-PV-*stat5* (half shaded triangle). The lines are the linear fits to the experimental data.

Table 3. 2. 1. Summary of mobility data: hole mobility (μ_h) and electron mobility (μ_e) for an applied electric field of about 1 x 10^5 V cm^{-1}, zero-field mobility (μ_{0h} and μ_{0e}, for holes and electrons respectively) and Poole-Frenkel factor (μ_h and μ_e, for holes and electrons, respectively) [42].

AnE-PV	ab	ae	bb	*stat*	*stat4*	*stat5*
Side-chains	octyl 2-ethylhexyl	octyl dodecyl	2-ethylhexyl	octyl 2-ethylhexyl	octyl 2-ethylhexyl methyl	octyl 2-ethylhexyl methyl
μ_h (@ ~ 10^5 V cm^{-1}) (cm^2 V^{-1} s^{-1})	$1.3x10^{-4}$	$8.2x10^{-6}$	$2.3x10^{-4}$	$2.0x10^{-4}$	$1.6x10^{-6}$	$4.0x10^{-5}$
μ_{0h} (cm^2 V^{-1} s^{-1})	$3.3x10^{-5}$	$3.8x10^{-6}$	$7.9x10^{-5}$	$7.9x10^{-5}$	$3.0x10^{-7}$	$1.3x10^{-5}$
β_h ($V\ cm^{-1}$)$^{-1/2}$	$4.3x10^{-3}$	$1.6x10^{-3}$	$3.4x10^{-3}$	$3.1x10^{-3}$	$5.1x10^{-3}$	$3.6x10^{-3}$
μ_e (@ ~ 10^5 V cm^{-1}) (cm^2 V^{-1} s^{-1})	$2.9x10^{-4}$	$1.6x10^{-5}$	$9.1x10^{-4}$	$1.2x10^{-3}$	$5.0x10^{-6}$	$4.1x10^{-5}$
μ_{0e} (cm^2 V^{-1} s^{-1})	$6.7x10^{-5}$	$1.5x10^{-5}$	n.a.	$3.9x10^{-4}$	$1.3x10^{-6}$	$1.1x10^{-5}$
β_e ($V\ cm^{-1}$)$^{-1/2}$	$4.4x10^{-3}$	$6.7x10^{-4}$	n.a.	$3.4x10^{-3}$	$4.1x10^{-3}$	$4.2x10^{-3}$

Both the Poole-Frenkel-like trend of mobility, often observed for disordered organic materials, and a decreasing μ with E can be explained within the same model of a hopping conduction in a Gaussian distribution of localized states, as demonstrated by Monte Carlo simulations [49, 174]. Indeed, depending on the relative contribution of energetic (diagonal) and positional (off-diagonal) disorder to the random walk of charge carriers, a Poole-Frenkel-like behaviour or a change of sign of the field-dependence of mobility can be observed.

The data of Figure 3.2.3 and Table 3.2.1 clearly show the great effect of lateral chains on charge carrier mobility of conjugated polymers, with μ varying by two orders of magnitude for the AnE-PVs here considered, both for holes (ranging between 1.6 x

10^{-6} and 2.3 x 10^{-4} cm^2 V^{-1} s^{-1} for E of about 10^5 V cm^{-1}) and electrons (between 5.0 x 10^{-6} and 1.2 x 10^{-3} cm^2 V^{-1} s^{-1} for the same field).

Apart from the case of AnE-PV-*stat5*, for which comparable hole and electron mobilities were obtained, the mobility of negative charge carriers was found to be higher than that of holes from two- to six-fold, as shown in Table 3.2.1, confirming the good ambipolar behaviour of this class of conjugated polymers. As expected, the polymer with the longest substituents (AnE-PV-ae, with octyl and dodecyl chains) shows low mobility compared with the other ones, consistent with the reduction of the electronic interaction between conjugated backbones [76, 178] as the extension of the later chains increases. This is also confirmed by the comparison between AnE-PV-ab and AnE-PV-bb, only differing for the octyl side-chains.

The latter, with only 2-ethylhexyl substituents, shows higher mobility values (2.3 x 10^{-4} against 1.3 x 10^{-4} cm^2 V^{-1} s^{-1} for holes, 9.1 x 10^{-4} against 2.9 x 10^{-4} cm^2 V^{-1} s^{-1} for electrons, for the field of about 10^5 V cm^{-1}). However, the most striking difference of AnE-PV-ae, compared with the other polymers, is represented by the low dependence of mobility on electric field, as demonstrated by the lowest values of β (Table 3.2.1). This could be due to a lower energetic disorder [184] in the fluctuation of the energy of the hopping sites for charge transport, which could be attributed to a more ordered arrangement of polymer chains in the film.

Indeed, a layered structure consisting of π-π stacked backbones has been already reported for films made of AnE-PVs with all-linear side chains attached close to the anthracenylene-ethynylene unit, in contrast to the more amorphous structure of polymers with branched lateral chains attached to the same backbone [80]. The other five polymers, all bearing branched 2-ethylhexyl chains, show a μ value ranging

between 3.1 x 10^{-3} and 5.1 x 10^{-3} cm^2V^{-1}, without a clear trend with the molecular structure. The comparison between statistical and non-statistical polymers can be done by considering AnE-PV-ab and AnE-PV-*stat*, bearing the same octyl and 2-ethylhexyl side-chains. Better values both for mobility and β were obtained for the polymer with lateral chains statistically distributed, confirming the superior features of the random polymer compared to the counterpart based on well-defined side-chain [78].

Finally, looking at the data of Table 3.2.1, it is surprising the difference of roughly one order of magnitude between the mobility values of AnE-PV-*stat4* and AnE-PV-*stat5*, two random polymers with the same side-chains and just differing for the different amount of short methyl chains. The former, with more methyl groups in the molecular structure, shows lower values compared with AnE-PV-*stat5*, as well as the lowest ones for the six considered polymers; indicating that the short methyl chains have a detrimental effect on the transport properties of charge carriers.

It is worth noting that the two polymers with methyl side-chains are among the ones exhibiting the lowest mobilities (Figure 3.2.3 and Table 3.2.1) of the six considered, confirming that the shortest lateral chains prevent a favourable organization of polymer films for the transport of charge carriers. To support this hypothesis, the XRD pattern of AnE-PV-*stat4* film is compared to that of AnE-PV-*stat*, without methyl chains and showing very good mobility values. The polymer films, prepared in the same conditions used for mobility investigation, showed very different XRD patterns (Figure 3.2.4).

Differently from AnE-PV-*stat*, showing a semicrystalline character, AnE-PV-*stat4* reveals its complete amorphous feature. Indeed, AnE-PV-*stat* sample shows a

crystalline peak at 5.53° (2θ), corresponding to a staking interlayer distance of 1.53 nm, while only a bell-shaped profile is visible in the wide angle region of the XRD pattern of AnE-PV-*stat4*, also present in the pattern of AnE-PV-*stat* and related to the amorphous component of the investigated films.

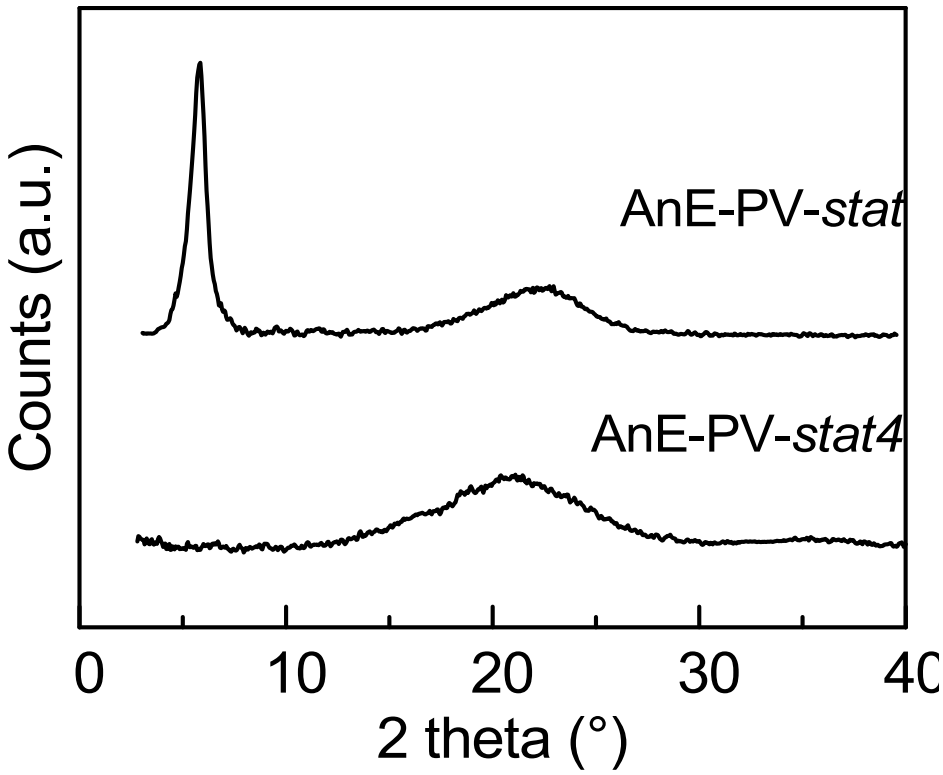

Figure 3. 2. 4. XRD patterns of AnE-PV-*stat* and AnE-PV-*stat4* films drop-cast onto quartz substrate.

Likely, the short methyl side-chains, reducing the overall rough symmetry of the repeating unit, could hinder the possibility of a regular stacking of the polymer main chains. This leads to a very different organization in the solid state and highly affects the charge transport properties of the films made with the two different polymers, with a variation of two orders of magnitude in the mobility values. It is worth noting that also the photophysical properties of the two statistical polymers are greatly

influenced, with AnE-PV-*stat* showing improved absorption and emission spectra compared to the amorphous AnE-PV-*stat 4* [41].

The very different transport properties of AnE-PV-*stat* and AnE-PV-*stat4* could be also attributed to a different extent of charge trapping processes. In this case, a different trend of charge carrier transit times with the applied electric field should be observed.

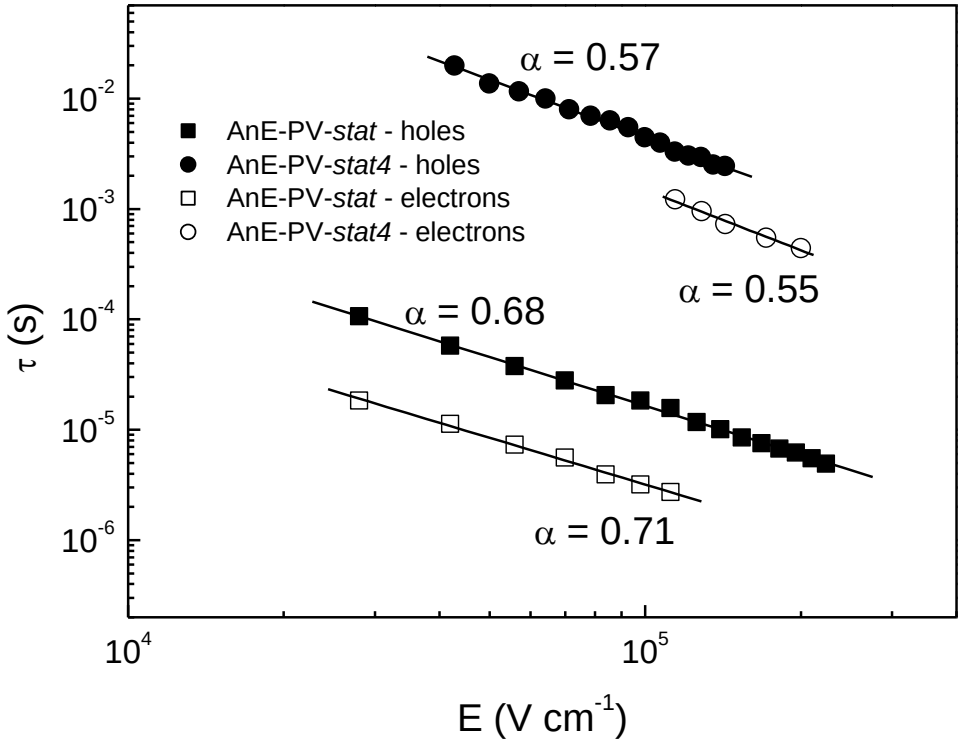

Figure 3. 2. 5. Transit time of holes of AnE-PV*stat* (filled square symbols), transit time of electrons of AnE-PV*stat* (open square symbols), transit of holes of AnE-PV*stat4* (filled circle symbols) and transit time of electrons of AnE-PV*stat4* (open circle symbols) as a function of the electric field

It has been shown [185] that, in a multiple trapping model, the transit time of charge carriers exhibits the electric field dependence of $\tau(E) \propto E^{-1/\alpha}$, where α is a dispersion parameter ($0 < \alpha < 1$; $\alpha = 1$ for non dispersive transport) introduced by

Scher and Montroll [171] in their model for the description of dispersive transport in amorphous solids. The electric field dependence of transit times derived from the TOF measurements are reported in Figure 3.2.5 for AnE-PV-*stat* and AnE-PV-*stat4*.

From the slope of the lines representing the linear fit to the experimental data the values of the dispersion parameter were extracted. 0.57 and 0.55 were obtained for AnE-PV-*stat4*, for holes and electrons, respectively, compared with the expected higher values for α of 0.68 (holes) and 0.71 (electrons) calculated for AnE-PV-*stat* and indicating that charge transport is less affected by charge trapping events in this latter polymer.

3.2.3. Conclusions

A systematic investigation of charge carrier mobility in a series of anthracene-containing poly(*p*-phenylene-ethynylene)-alt-poly(*p*-phenylene-vinylene)s, differing for the solubilising alkoxy lateral chains, has been performed, in order to establish a clear relationship between molecular structure and charge transport properties. The ambipolar behaviour of this class of conjugated polymers is confirmed, with transit times of electrons even higher than those of holes, but with a higher dispersion of the photocurrent signals generated by the drift of negative carriers. The nature of the substituents has a great impact on charge carrier mobility of the investigated polymers, with a variation observed of 2-3 orders of magnitude. Long octyl and dodecyl linear chains have a detrimental effect on μ, likely because of a less compact molecular packing resulting in a decreased interaction between adjacent hopping sites.

Similarly, short methyl substituents induce low mobility values, but because of a highly disordered arrangement of polymer chains in the solid phase, also leading to an

increased charge trapping. A decreasing mobility with the amount of methyl chains in the molecular structure is clearly observed.

Finally, the used experimental conditions, allowing for a straight comparison of the investigated films, definitely confirmed the better properties of random polymers, compared to the counterpart based on well-defined side-chain.

3.3. Effect of changing position of anthracene group on transport property of holes and electron in anthracene containing MEH-PPE1-PAnV$_2$ and MEH-PAnE1-PPV$_2$ copolymers

The family of anthracene containing copolymers discussed in sections 3.1 and 3.2 are quite different from MEH-PPE$_1$-PAnV$_2$ and MEH-PAnE$_1$-PPV$_2$ copolymers. The significant structural difference among MEH-PAnE$_1$-PPV$_2$ and MEH-PPE$_1$-PAnV$_2$ and the other low bandgap anthracene containing copolymers, AnE-PV were shown in Figure 2.1. In the case of AnE-PVs the anthracene unit is located between two triple bonds in the center; and in MEH-PAnE$_1$-PPV$_2$ its position is at the center of backbone between a double bond and a triple bond; but in MEH-PPE$_1$-PAnV$_2$ the anthracene moiety is located between two double bonds from either side in the backbone [27, 42, 80, 186].

Effect of shifting the position of anthracene unit on the photovoltaic performance of MEH-PAnE$_1$-PPV$_2$:PCBM and MEH-PPE$_1$-PAnV$_2$:PCBM bulk heterojunction solar cells was studied [40]. Comparable photovoltaic performances were reported between MEH-PAnE$_1$-PPV$_2$ and MEH-PPE$_1$-PAnV$_2$. In order to correlate the photovoltaic performances with hole mobility, hole mobility of these polymers were tried measure using CELIV technique [40].

According to previous report hole mobility of MEH-PAnE$_1$-PPV$_2$ was 7.1 x 10^{-5} cm^2/Vs from drop-casted films; but no charge carriers mobility value of MEH-PPE$_1$-PAnV$_2$ was detected by CELIV method. Electron mobility both in MEH-PAnE$_1$-PPV$_2$ and MEH-PPE$_1$-PAnV$_2$ polymers was not reported before this work [27, 40]. As anthracene containing polymers are good candidate for OPVs, OLEDs and OFETs, not only hole mobility but also study of electron transport properties in MEH-PAnE$_1$-PPV$_2$ and MEH-PPE$_1$-PAnV$_2$ has paramount impact on the performance of these optoelectronic devices [187 - 189].

Here, in this study, we investigated the hole and electron drift mobility and their nature of dependence on applied electric field across the two anthracene- containing polymers MEH-PPE$_1$-PAnV$_2$ and MEH-PAnE$_1$-PPV$_2$, in which position of anthracene unit was varied in the backbones of the polymer. The role of position of anthracene unit in the backbone of the polymers of MEH-PPE$_1$-PAnV$_2$ and MEH-PAnE$_1$-PPV$_2$ on the transport of holes and electros were studied using differential time of flight method.

3.3.1. Optical study

The films of MEH-PPE$_1$-PAnV$_2$ and MEH-PAnE$_1$-PPV$_2$ were drop-casted on quartz substrate; absorption spectra were measured by Perkin Elmer lambda 950 spectrophotometer. The resulting normalized spectra are depicted in Figure 3.3.1. As indicated by the figure, the maximum absorption spectrum of MEH-PAnE$_1$-PPV$_2$ (at λ_{max} = 491nm) has shown significant red shift than MEH-PPE$_1$-PAnV$_2$ (at λ_{max} = 451nm).

The position of anthracene unit in the polymeric backbone have an influence on the tuning of the backbone planarity, and consequently on the bandgap of the system.

When the anthracene unit is in the center of the polymer backbone (in MEH-PAnE$_1$-PPV$_2$ case) [27], the backbone palanarity is improved, that means the polymer chain can attain suitable conformation for charge transport.

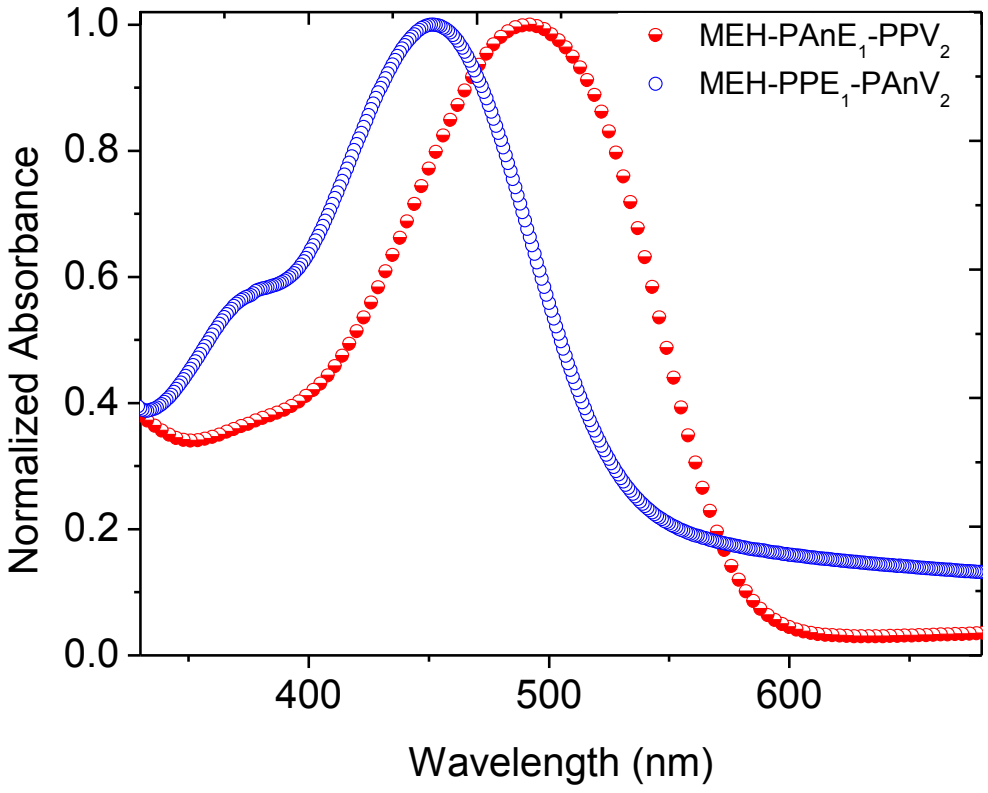

Figure 3. 3. 1. The normalized absorption spectra of MEH-PPE$_1$-PAnV$_2$ and MEH-PAnE$_1$-PPV$_2$ films deposited from chlorobenzene.

In π-conjugated polymers, orbital delocalization over the planar region is quite effective in order to obtaining high charge carriers mobility, because the delocalized orbitals provide the ideal pathways for coherent charge transport [78].

Generally, in the conjugated system, the absorption edges of the polymers can be controlled by their degree of planarity. The degree of planarity of these polymers is improved when the electron rich anthracene unit is in between double and triple bonds. This planarity change in the polymers following the change in position of

electron-rich anthracene unit and, this phenomena has been manifested by red shift in absorption spectral shown in Figure 3.3.1.

For case of the polymer with anthracene unit in the center, the effective conjugation can be enhanced; as the result π-electron delocalization (intra-chain transport) will be facilitated [190]. For shifting anthracene unit from between two double bonds (MEH-PPE_1-$PAnV_2$) to the bridge between double bond and triple bond (MEH-$PAnE_1$-PPV_2) bathochromic shift of 40 nm was observed, which is attributed to the extension of conjugation in the same order. Thus, intra-chain charge transport expected to be improved. As transport properties of charge carriers in the bulk of the device is the sumover effect of inter-chain and intra-chain charge transport, the structural effect that boosts either of these transports results in enhancement of the entire bulk transport [191].

3.3.2. Investigation of hole and electron mobility in MEH-PPE_1-$PAnV_2$ and MEH-$PAnE_1$-PPV_2 polymers

In this study, effect of position of anthracene unit in the transport property of MEH-PPE_1-$PAnV_2$ and MEH-$PAnE_1$-PPV_2 were investigated using Time Of flight (TOF) technique. Thick films (6 - 8 μm) of MEH-PPE_1-$PAnV_2$ and MEH-$PAnE_1$-PPV_2 were sandwitched between two aluminum electrodes. The differential TOF measurements were performed on the sandwich-type samples having the device structure of Al (18 nm)/polymer/Al(85 nm). Nitrogen laser pulse with higher energy (λ = 337nm) than the polymer bandgap was irradiated on the semitransparent Al (18 nm) electrode for a short time, and then the transit time (τ) of photogenerated charge carriers were measured.

Both electron and hole mobility of both samples were measured by alternatively reversing the polarity of applied bias to the illuminated electrode. The resulting photocurrent transient was collected by a digital oscilloscope (Tektronix TDS620A). The illuminated electrode was positively biased for hole mobility measurement and negatively biased for electron mobility measurement. The collected data of hole mobility measurement of MEH-PPE_1-$PAnV_2$ and MEH-$PAnE_1$-PPV_2 are presented in Table 3. 3. 1 and Table 3. 3. 2, respectively; and electron mobility data of MEH-PPE_1-$PAnV_2$ and MEH-$PAnE_1$-PPV_2 are presented in Table 3. 3. 3 and Table 3. 3. 4, respectively.

Table 3. 3. 1. Data of field dependent hole mobility of MEH-PPE_1-$PAnV_2$ with device structure of Al (85 nm)/ MEH-PPE_1-$PAnV_2$ /Al (18 + 90 nm).

Bias (V)	E (V/cm)	$E^{1/2}$ $(V/cm)^{1/2}$	Transit time, (t_{tr}) (s)	Mobility, μ (cm^2/Vs)
100	1.25×10^5	3.54×10^2	4.67×10^{-5}	1.37×10^{-4}
120	1.50×10^5	3.87×10^2	3.27×10^{-5}	1.63×10^{-4}
140	1.75×10^5	4.18×10^2	2.11×10^{-5}	2.16×10^{-4}
160	2.00×10^5	4.47×10^2	1.46×10^{-5}	2.74×10^{-4}
180	2.25×10^5	4.74×10^2	1.16×10^{-5}	3.07×10^{-4}

E is electric field; $E^{1/2}$ is square root of electric field.

The hole photocurrent signals of MEH-PPE_1-$PAnV_2$ and MEH-$PAnE_1$-PPV_2 are shown in Figure 3.3.2a and 3.3.2b, respectively. The photocurrent signals of MEH-PPE_1-$PAnV_2$ and MEH-$PAnE_1$-PPV_2 have no much clear and distinct plateau indicative of dispersive charge transport [192]. MEH-$PAnE_1$-PPV_2 photocurrent signals have a bit clearer inflection point (cusps) than that of signals of MEH-PPE_1-

$PAnV_2$, indicating that MEH-$PAnE_1$-PPV_2 has a less dispersive hole transport than that of MEH-$PAnE_1$-PPV_2 [193].

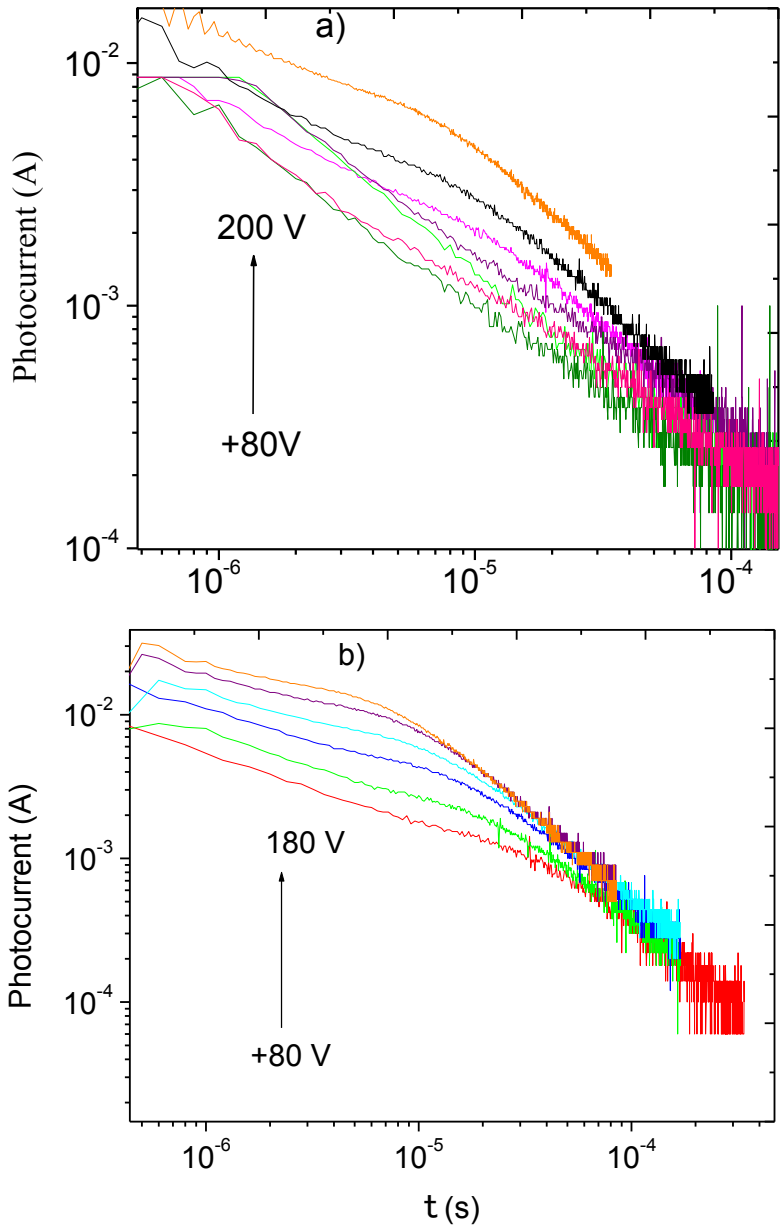

Figure 3. 3. 2. TOF photocurrent signals of holes for a) MEH-PPE_1-$PAnV_2$ and b) MEH-$PAnE_1$-PPV_2 in log-log scales at different DC field.

This phenomenon is further confirmed by redshift in absorption spectra of MEH-$PAnE_1$-PPV_2, indicating that MEH-$PAnE_1$-PPV_2 films have more ordered chain organization than MEH-PPE_1-$PAnV_2$. With increasing applied bias, the cusps

(inflection points, i.e the point where transit time is determined) of photocurrent signals become more and more clear and shift to lower transit time. This indicates that hole mobilities in MEH-PAnE$_1$-PPV$_2$ and MEH-PPE$_1$-PAnV$_2$ devices are positively dependent on applied field.

Table 3. 3. 2. TOF hole transport behaviors of MEH-PAnE$_1$-PPV$_2$ such as applied bias, transit time, and mobility at different field are collected in this table.

Bias (V)	E (V/cm)	$E^{1/2}$ $(V/cm)^{1/2}$	Transit time, t_{tr} (s)	Mobility, μ (cm^2/Vs)
100	1.67×10^5	4.08×10^2	2.40×10^{-5}	1.50×10^{-4}
120	2.00×10^5	4.47×10^2	1.55×10^{-5}	1.93×10^{-4}
140	2.33×10^5	4.83×10^2	1.02×10^{-5}	2.53×10^{-4}
160	2.67×10^5	5.16×10^2	7.37×10^{-6}	3.05×10^{-4}

The decrease in transit time with increasing strength of applied field, signifies that hole transport resistivity of the polymer in the devices decreases with increasing electric field. Apart from transit time, the slopes of pre-and post-transit photocurrents (Figure 3.3.3**)** have often been used to characterize the TOF transients. Those currents can be approximated by power laws according to Scherr and Montroll model [171];

$$I_{ph}(t) \alpha\, t^{-(1-\alpha_1)},\ t < t_T$$

$$I_{ph}(t) \alpha\, t^{-(1+\alpha_2)},\ t > t_T \qquad (3.3)$$

and the best fitting values of α_1 and α_2 are taken as experimental data. The fact that the current slopes are negative in both regions is due to carrier trapping into localised states that are located deep enough to prevent re-emission of the charge within the elapsed time.

The transport is called (anomalously) dispersive in that case; at higher temperatures non-dispersive transport with a constant initial current, i.e. $\alpha_1 = 1$. Then the charge mobility (μ) is determined using the following relation:

$$\mu = \frac{d}{E.\tau} = \frac{d^2}{V.\tau} \qquad (3.4)$$

Where d, E, τ and V are the thickness of film, an electric field, transit time and an applied voltage, respectively [48, 194, 195].

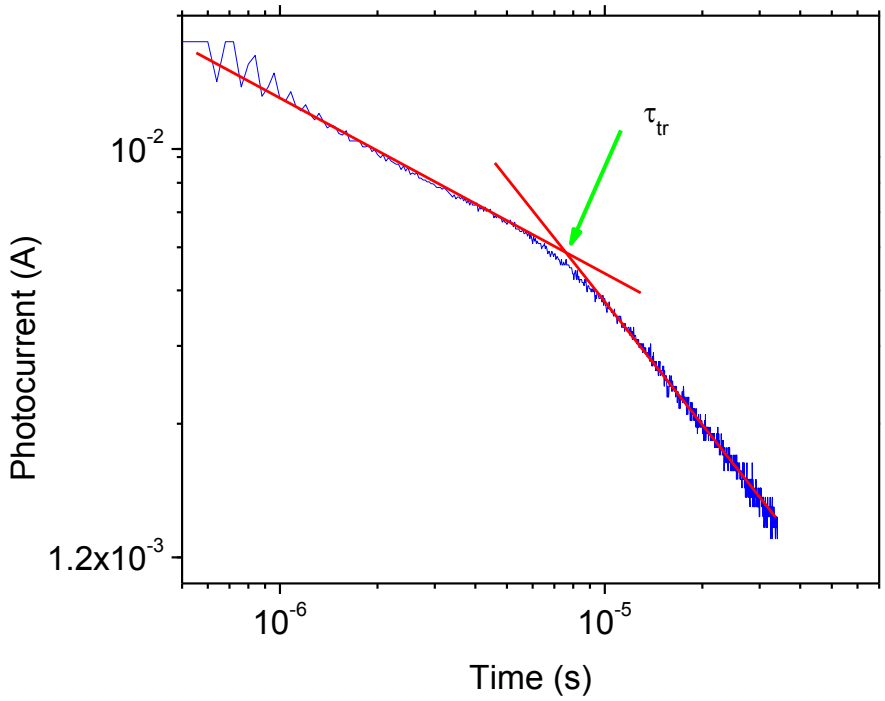

Figure 3. 3. 3. TOF photocurrent transient showing how to determine transit time of carriers from intersection point of the two slopes. The arrow indicates the transit time, t_{tr}.

The transit time of charge carriers was determined from the log *i*– log *t* plot from the crossing of the asymptotes to the plateau and the declining slope (Figure 3.3.3), measured at room temperature for an applied electric field of ~ 5 x 10^5 V/cm.

The log-log plot of TOF photocurrent signals of electrons in MEH-PPE_1-$PAnV_2$ and MEH-$PAnE_1$-PPV_2 are indicated in Figure 3.3.4a and 3.3.4b, respectively. The inflection points (points from which transit time is extracted) in the photocurrent signals of electrons in both MEH-PPE_1-$PAnV_2$ and MEH-$PAnE_1$-PPV_2 are not clear as that of the holes. This indicates that electron mobilities in MEH-PPE_1-$PAnV_2$ and MEH-$PAnE_1$-PPV_2 are more dispersive than the corresponding holes mobilities [170].

Table 3. 3. 3. TOF electron transport behaviors of MEH-PPE_1-$PAnV_2$: applied bias, transit time, and mobility at different fields.

Bias (V)	E (V/cm)	$E^{1/2}$ $(V/cm)^{1/2}$	Transit time, t_{tr} (s)	Mobility, μ (cm^2/Vs)
10	1.66×10^4	1.30×10^2	2.39×10^{-5}	1.50×10^{-3}
20	3.33×10^4	1.83×10^2	1.23×10^{-5}	1.46×10^{-3}
30	5.00×10^4	2.24×10^2	8.66×10^{-6}	1.39×10^{-3}
40	6.67×10^4	2.58×10^2	6.38×10^{-6}	1.41×10^{-3}
50	8.33×10^4	2.89×10^2	5.15×10^{-6}	1.40×10^{-3}
60	1.00×10^4	3.16×10^2	4.15×10^{-6}	1.44×10^{-3}
65	1.08×10^4	3.29×10^2	4.07×10^{-6}	1.36×10^{-3}

In the case of polymer structure when anthracene unit is located in the center of backbone of the polymer, the electron mobility is much higher than in the case MEH-PPE_1-$PAnV_2$. That means when electron reach anthracene unit and electron deficient triple bond are in adjacent to each other, as in MEH-$PAnE_1$-PPV_2, intra-chain electron delocalization could be enhanced; and then intra-chain charge transport is more favourable here than in the case of MEH-PPE_1-$PAnV_2$.

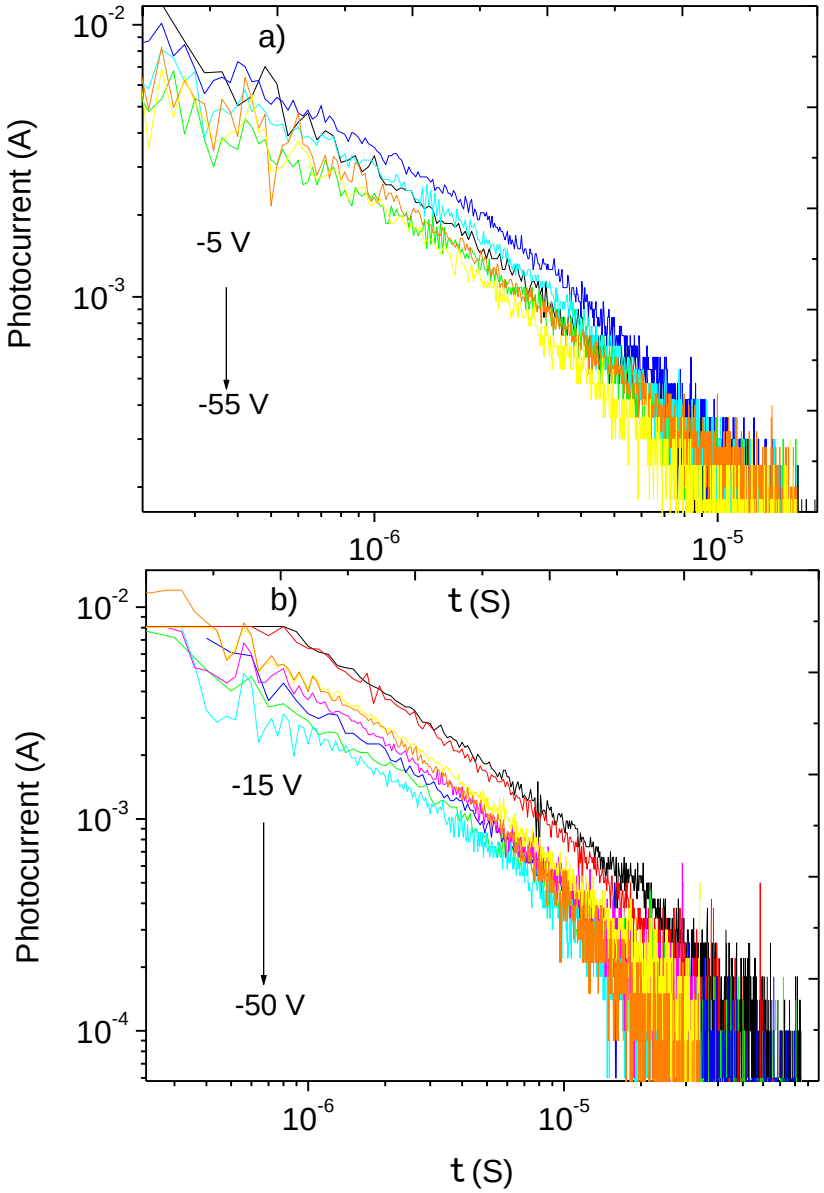

Figure 3. 3. 4. TOF photocurrent signals of electrons in log-log scales at differenent applied electric field for polymer of MEH-PPE$_1$-PAnV$_2$ (a) and MEH-PAnE$_1$-PPV$_2$ (b).

The electron rich and electron deficient moieties in the conjugated system to produce the so-called push-pull effect, which modulate bandgaps [155], resulting in enhanced polymer backbone planarity (confirmed by the redshift in absorbance for MEH-PAnE$_1$-PPV$_2$ in Figure 3.3.1), and as a result it has demonstrated higher electron mobility than MEH-PPE$_1$-PAnV$_2$.

The hole mobility of MEH-PAnE$_1$-PPV$_2$ is greater than that of MEH-PPE$_1$-PAnV$_2$ for all ranges of applied electric field (shown by Figure 3.3.5, Table 3.3.1 and 3.3.2). This may be correlated with the differences in polymer chain organization and order between the two polymers. More ordered sample show higher mobility than the less ordered one [186].

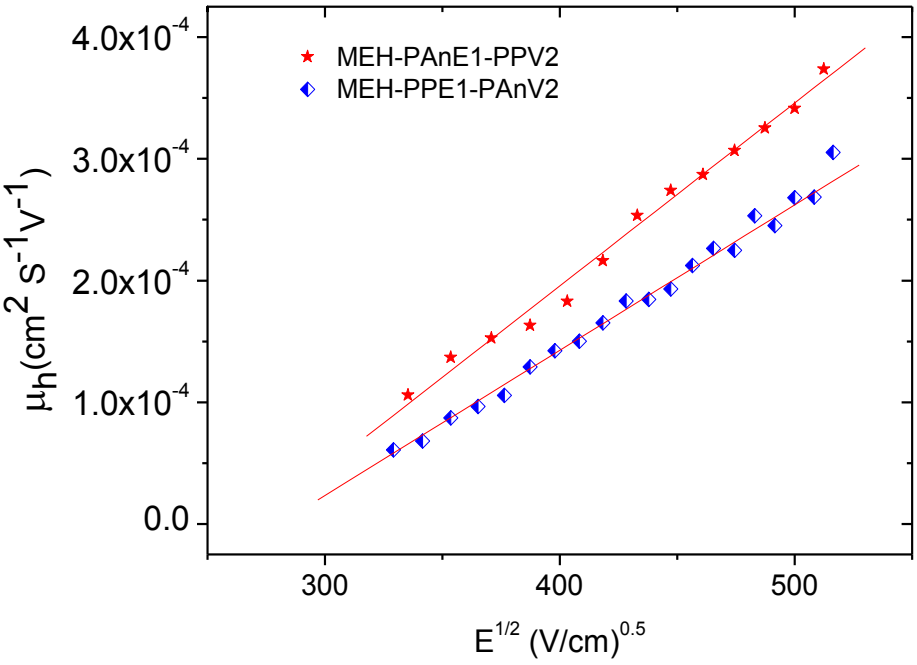

Figure 3. 3. 5. Hole mobility behaviors with DC electric field investigated with TOF mobility technique for MEH-PPE$_1$-PAnV$_2$ and MEH-PAnE$_1$-PPV$_2$.

In the case of polymer MEH-PPE$_1$-PAnV$_2$, the electron mobility is observed to be very smaller than in MEH-PAnE$_1$-PPV$_2$ and the mobility is almost independent of electric field. This might not be only because of the polymer MEH-PPE$_1$-PAnV$_2$ is less amorphous than that of MEH-PAnE$_1$-PPV$_2$. It also may be due to the change in relative position of the electron-deficient triple bond and the electron-rich anthracene group, which results in reduced rate of electron hopping from one energetic site to the

other higher energetic sites [184] in MEH-PPE_1-$PAnV_2$ than in the case of MEH-$PAnE_1$-PPV_2.

Table 3. 3. 4. Data of field dependent electron mobility of MEH-$PAnE_1$-PPV_2 with device structure of Al (85 nm)/ MEH-$PAnE_1$-PPV_2/Al (18 + 90 nm).

Bias (v)	E (V/cm)	$E^{½}$ (V/cm)$^{1/2}$	Transit time, t_{tr} (s)	Mobility, μ (cm^2/S.V))
10	1.25×10^4	1.12×10^2	3.49×10^{-6}	1.83×10^{-2}
20	2.50×10^4	1.58×10^2	2.72×10^{-6}	1.18×10^{-2}
25	3.13×10^4	1.77×10^2	2.48×10^{-6}	1.03×10^{-2}
30	3.75×10^4	1.94×10^2	2.35×10^{-6}	9.07×10^{-3}
40	4.38×10^4	2.09×10^2	2.12×10^{-6}	8.63×10^{-3}
50	5.63×10^4	2.37×10^2	1.77×10^{-6}	8.04×10^{-3}

As presented by Figure 3.3.5, for all the indicated range of applied electric field, the hole mobilities in MEH-$PAnE_1$-PPV_2 is a bit greater than that of MEH-PPE_1-$PAnV_2$. This indicates that, the hole mobility is affected by changing the position of anthracene unit from between triple bond and double bond at center to the positions between two double bonds of the backbone at the edge. As indicated by Figure 3.3.5, the increase in hole mobility was observed with increasing electric field for both MEH-PPE_1-$PAnV_2$ and MEH-$PAnE_1$-PPV_2. However, a significant difference was demonstrated in electron mobility behavior between MEH-PPE_1-$PAnV_2$ and MEH-$PAnE_1$-PPV_2. This indicates that effect of shifting of position of anthracene unit in the backbone of the polymers is more significant in the electron mobilities changes between these polymers than holes (Figure 3.3.6). That might be because of 1) the

interaction between the triple bond and anthracene unit in the center, and 2) acting of the anthracene unit as a bridge in the center, favors the electron mobility.

The strength of dependency of hole and electron mobility on the electric field clearly shown in Figures 3.3.5 and 3.3.6, respectively from plot of logarithm of mobility *versus* square root of electric field (using Poole-Frenkle relationship). Parameters such as β_e and β_h which are collected in Table 3.3.5 describe strength of charge carriers‟ mobility dependence on electric field. The value of β_h for MEH-PAnE$_1$-PPV$_2$ is comparable with tha of MEH-PPE$_1$-PAnV$_2$, indicating field dependencies of hole mobility in MEH-PAnE$_1$-PPV$_2$ is not significantly different from that of MEH-PPE$_1$-PAnV$_2$.

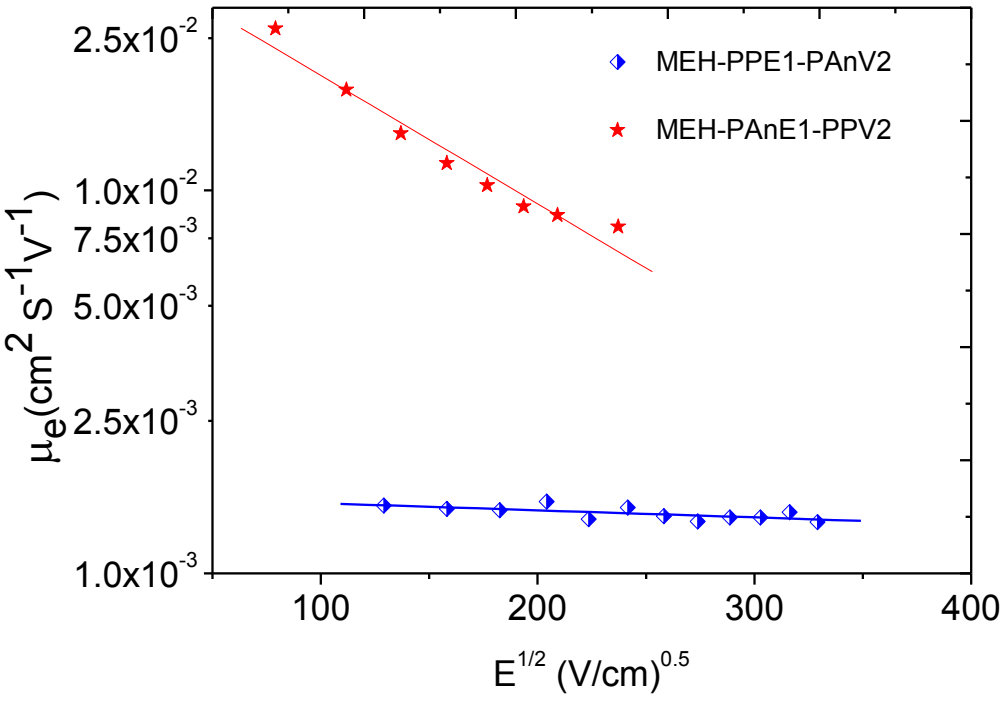

Figure 3. 3. 6. TOF electron mobility of MEH-PPE$_1$-PAnV$_2$ (half-filled square symbol) and MEH-PAnE$_1$-PPV$_2$ (star symbol) with variation of square root of electric field for films of 6 - 8 **µ**m thick.

There are big difference between β_e of MEH-PPE_1-$PAnV_2$ and MEH-$PAnE_1$-PPV_2. β_e MEH-$PAnE_1$-PPV_2 is bigger than β_e of MEH-PPE_1-$PAnV_2$, showing strong field dependent electron mobility for MEH-$PAnE_1$-PPV_2 and weak dependence for MEH-PPE_1-$PAnV_2$. Eventhough Poole Frenkle (PF) behavior is followed in both polymers for hole mobility, in MEH-$PAnE_1$-PPV_2 the mobility dependence on electric field is stronger than in MEH-PPE_1-$PAnV_2$, and this might be probably because of the difference in degree of order between the films of MEH-$PAnE_1$-PPV_2 and MEH-PPE_1-$PAnV_2$.

Table 3. 3. 5. The hole (β_h) and electron mobility (β_e) dependency factor for polymers MEH-PPE_1-$PAnV_2$ and MEH-$PAnE_1$-PPV_2, and hole and electron mobility at zero electric field (μ_{ho} and μ_{eo}) calculated from the slope of log of hole and electron mobility linear fit agaist square root of electric field.

Polymer	β_e	β_h	μ_{eo}	μ_{ho}
MEH-PPE_1-$PAnV_2$	-4.27×10^{-4}	1.32×10^{-2}	-6.44312	-11.35236
MEH-$PAnE_1$-PPV_2	-8.09×10^{-3}	6.87×10^{-3}	-2.70740	-14.12468

3.3.3. Conclusions

Effect of changing the position of anthracene unit from bridging between double bonds and triple bonds at the center (MEH-$PAnE_1$-PPV_2) to the position between two double bonds (MEH-PPE_1-$PAnV_2$) in the polymers backbones resulted in changes in charge carriers‟ mobility. Significant redshift in absorption spectra observed for MEH-$PAnE_1$-PPV_2, possibily signifying that MEH-$PAnE_1$-PPV_2 polymer attained better planarity than MEH-PPE_1-$PAnV_2$.

Eventhough electrons‟ and holes‟ mobility were affected by anthracene position, electron mobilities were more significantly affected than hole mobility. Location of the electron rich anthracene unit adjacent to the triple bond (in case of MEH-PAnE$_1$-PPV$_2$) may create favorable condition for better electron transport than in MEH-PPE$_1$-PAnV$_2$ through establishing push-pull effect.

The significant difference in charge carriers transport properties were manifested by different Poole-Frenkel behaviors of hole mobilities and electron mobilities between MEH-PPE$_1$-PAnV$_2$ and MEH-PAnE$_1$-PPV$_2$, may be indicating the difference in degree of order between these polymers.

3.4. Determination of photogenerated hole mobility in alkoxy-substituted phenylene-ethylene/phenylene-vinylene (PE/PV) hybrid conjugated polymer using Integral Time Of flight (I-TOF)

The differential type of Time-of-flight (TOF) technique is a widely used method to measure the charge carrier mobility as a function of electric field and temperature [196]. However, this technique has its own shortcomings. The limitation of differential TOF when studying disordered organic materials comes from the dispersive nature of the carrier transport in these materials. In addition, in disordered materials, the carrier transit time is usually observed only in the log-log plot of the current transients and the carrier mobility is dependent on the sample thickness. Another problem associated with differential (current mode) TOF is that the time taken by circuit to react or RC time constant (τ_{RC}) $\ll$ charge carrier transit time (τ), therefore in order to apply TOF the sample bulk conductivity has to be low and, otherwise the redistributed electric field and short carrier relaxation time distort the carrier package transit through the film [197, 198].

To avoid these limitations associated with differential TOF measurement, one has to use the integral mode time of flight (I-TOF); and the transit time can be determined in the absence of kinks shown in differential TOF and used in transit time extraction [199].

The advantage of using integral mode TOF in π-conjugated polymers is (i) its high sensitivity, (ii) possibility to measure transit time even in thin films (a few hundred nanometers) consistent with device format and (iii) the possibility to probe the initial fast transport characteristics [199, 200]. Through the I-TOF method, hole mobility was studied on regio-random poly(3-hexylthiophene) (RRa-P3HT) for films as thin as below 500 nm [201].

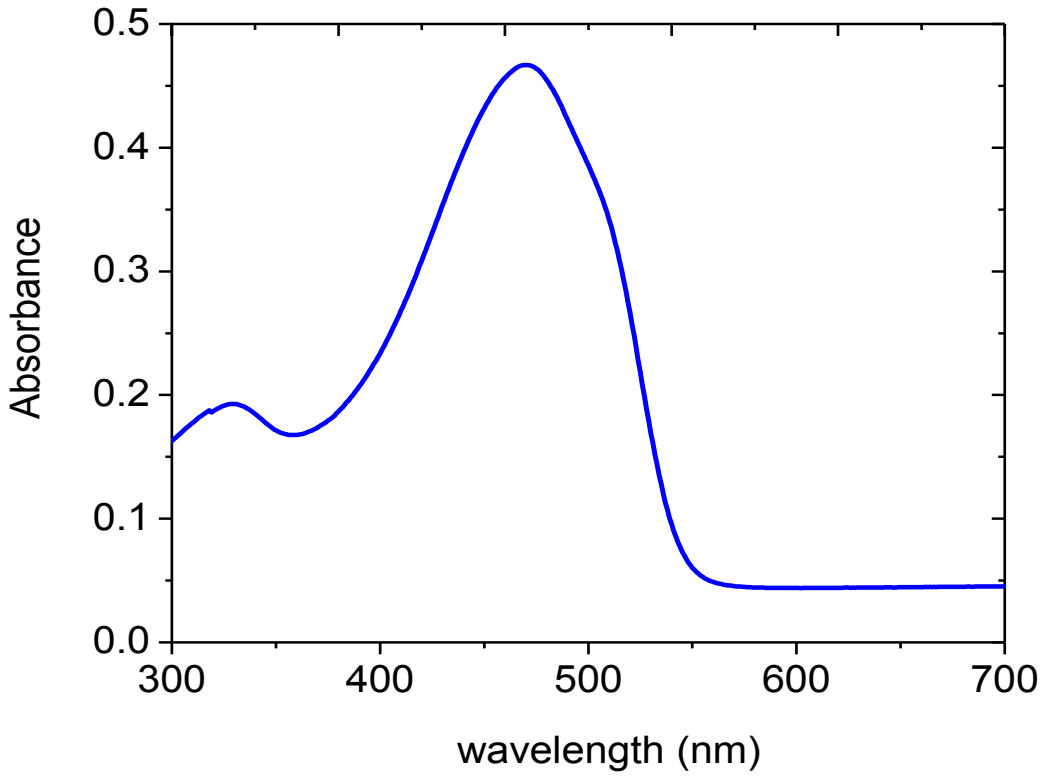

Figure 3. 4. 1. Absorbance spectra of P(PE-PV) hybrid polymer film spin-coated with chlorobenzene (CB) solution with spin-coating speed of 1000 rpm.

Photophysical properties of P(PE-PV) polymer have already been investigated by D. A. M. Egbe *et al* [155]. The molecular structure and absorption spectrum of the copolymer is already shown in Figure 2.2c and Figure 3.4.1 respectively. The polymer has a triple bond in the center of backbone with symmetrically substituted long/linear octyloxy and octadecyloxy side chains. The absorption spectra measured using Perkin Elmer lambda 950 nm spectrophotometer showing that the polymer has λ_{max} ~ 468 nm. Optically determined band gap of P(PE-PV) copolymer reported in [155], and is E^{opt} = 2.25 eV.

3.4.1. Measuring hole mobility of P(PE-PV) copolymer using I-TOF technique

Figure 3.4.2 is comparing transit time extracting approaches between differential and integral TOF methods. In integral TOF case, transit time extraction does not need kinks; it can easily be determined from the time when charge begins to saturate (Figure 3.4.2b).

In the integral mode TOF technique, a capacitor is added (as shown in Figure 2.4 in experimental part) into the circuit, so that the fast transit times of charge carriers ($\tau_{RC} \gg t_{tr}$) can easily be measured [201, 202].

The recorded charge signal of Al/P(PE-PV)/Al devices is indicated in Figure 3.4.3. The signal is showing the variation of the total charge $Q(t)$ accumulated at the exit electrode for an electric field of 5.9 x 10^5 V/cm. Q_f is charge build-up due to the fastest charge carriers, and τ_f is transit time for the fastest charge carriers and t_{tr} is the time when majority of charge carriers exit the device.

$$Q(t) = \int i(t)dt = \int_0^{t_{tr}} Q_0 \, \mu \frac{E}{d} \, e^{\frac{t}{\tau}} \, dt \qquad (3.5)$$

Where τ is lifetime of charge carriers, E is e applied electric field, d is thickness of film, Q_o is the initial charge stored in the sample [203]. Q(t) is photogenerated charge at any time t and it increases with time *t*, reaching a maximum value Q_m at $t = \infty$.

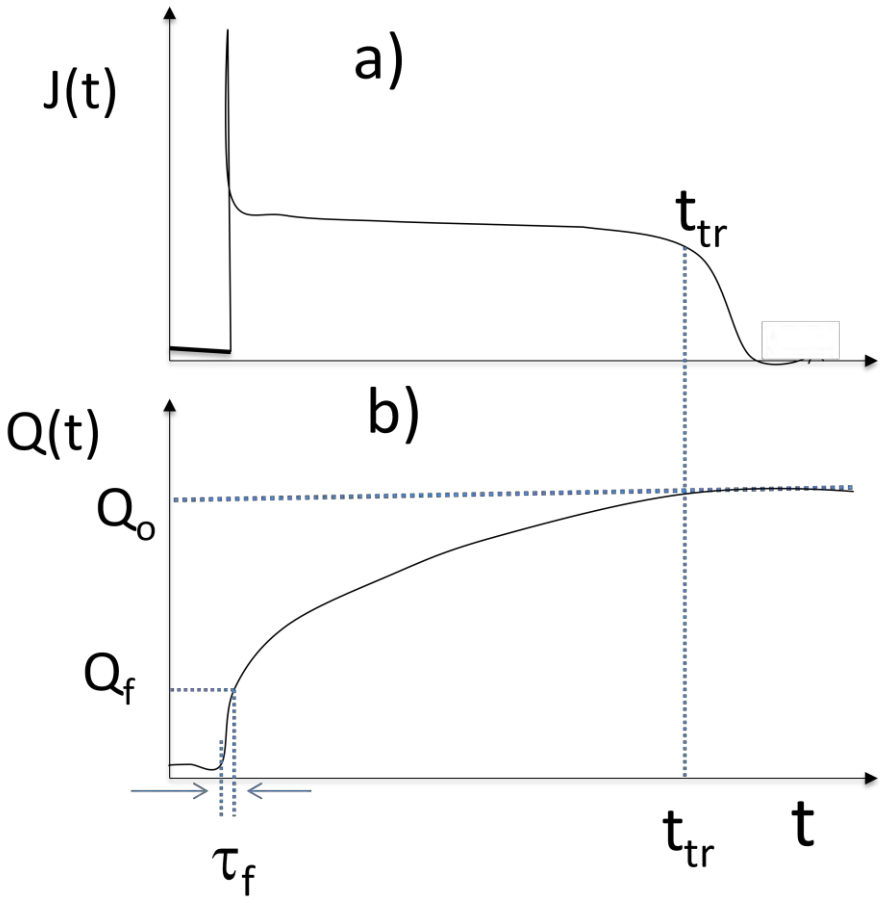

Figure 3. 4. 2. The difference between differential and integral TOF and transit time extractions, photocurrent transients in a) differential mode and b) integral mode [200].

Different approaches can be used to determine a transit time (t_Q) in I-TOF mode. If transport is dispersive, t_Q can be determined from when Q(t) reaches half its maximum value, i.e., $Q_{m/2}$ (as shown in Figure 3.4.3 for ITO/P(PE-PV)/Al devices), if transport is non-dispersive, transit time (t_{tr}) is extracted from the photocurrent signal, at the time generated charge starts saturating (as of Figure 3.4.2b). In the

former case, t_Q should be approximately equivalent to $t_{1/2}$ in the differential mode measurement. The advantage of the integration mode over the differential mode is that, because Q(t) increases with time towards a maximum limiting value it is possible to extract a transit time even when no clear change in slope can be identified in $i(t)$ (differential). Hence, it allows an effective mobility to be measured in dispersive samples, in thin films, and at relatively low fields for which differential mode TOF does not work [204, 205]. The samples used here have C = 100 nF giving the time constant of the measurement setup $RC \cong 100\ \mu$s and is higher than carriers transit time (Table 3.4.1) even with the lower resistor of 1 kΩ used.

The equivalence of the transit times extracted from the two methods (differential and integral TOF mode) was successfully demonstrated by other groups using polyflourene (PFO) polymer [135]. The hole mobility values of P3HT measured using I-TOF and CELIV technique have shown a good agreement [29].

Magnitude of signals in Figure 3.4.3 corresponds to amount of collected charges from the device. The time at which the vertical line intersects with charge signal shows the transit time of the fastest carriers and the time at which the horizontal dotted line intersects with point of charge saturation indicate transit time of slowest charge carriers [78]. Average mobility of charge carriers can be determined from the average transit time (t_Q) (average of fastest and slowest transit times of charge carriers at $Q_{m1/2}$ in Figure 3.4.3)

According to Campbell *et al* [135], for dispersed samples such as P(PE-PV), I-TOF mode is applied for determination of transit time. By determining the average transit time (t_Q) from the half of charge maximum ($Q_{m1/2}$), as shown in Figure 3.4.3, charge carrier mobility, μ, can easily be calculated by,

$$\mu = \frac{d}{t_Q E} \tag{3.6}$$

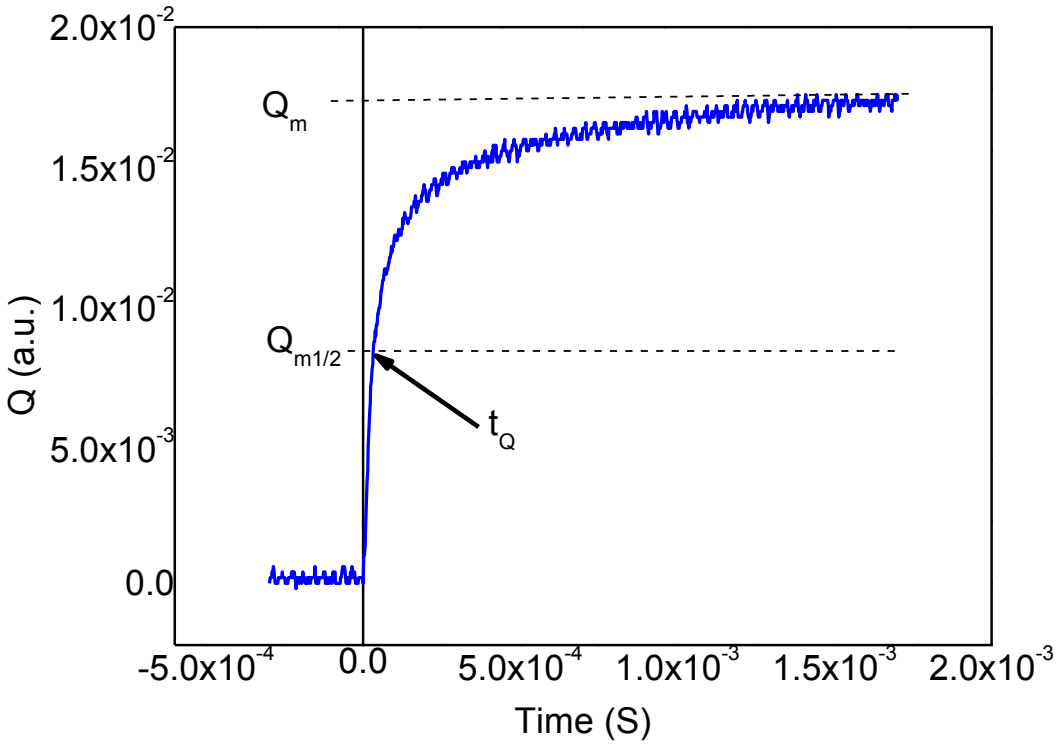

Figure 3. 4. 3. Typical integration mode time-of-flight transients for holes mobility of P(PE-PV) hybrid polymer at electric field of 5.9 x 10^5 V/cm on the film with thickness of 4.2 μm. Also shown is the method used to calculate the transit time, t_Q.

As indicated in Figure 3.4.4, an increased applied voltage from 190 V to 250 V caused an increase in charge stored at the surface of the sample, thus increasing the height of the voltage plateau. It is also possible to notice that the slope of the curves change, slope gets more and more steeper with increasing applied bias. This phenomenon indicates the shifting of transit time to the shorter time. It indicates that the mobility of holes being increased with increasing applied bias. This behavior is shown in Table 3.4.1 and Figure 3.4.4. The separation between plateaus of the charge

signals in successive voltages become closer and closer, as applied potential is getting raised, and become constat at voltage of 240 V (Figure 3.4.4).

Table 3. 4. 1. Integral TOF mobility parameters such as applied potential (E), charge (Q), transit time (t_Q) and hole mobility (μ).

Bias (V)	Capacitance (nF)	E(V/cm)	$E^{1/2}$ $(V/cm)^{1/2}$	Q_m	t_Q (s)	Mobility, μ (cm^2/Vs)
190	100	4.52×10^5	6.73×10^2	8.88×10^{-3}	6.40×10^{-5}	1.45×10^{-5}
200	100	4.76×10^5	6.90×10^2	1.17×10^{-2}	5.60×10^{-5}	1.57×10^{-5}
210	100	5.00×10^5	7.07×10^2	1.23×10^{-2}	5.20×10^{-5}	1.59×10^{-5}
220	100	5.23×10^5	7.24×10^2	1.44×10^{-2}	4.80×10^{-5}	1.67×10^{-5}
230	100	5.48×10^5	7.40×10^2	1.59×10^{-2}	3.70×10^{-5}	2.07×10^{-5}
240	100	5.71×10^5	7.56×10^2	1.74×10^{-2}	3.61×10^{-5}	2.04×10^{-5}
250	100	5.95×10^5	7.72×10^2	1.72×10^{-2}	3.21×10^{-5}	2.20×10^{-5}

As observed from I-TOF signals in Figure 3.4.4, the initial build up of charge and leakage current (i.e measured signal) were small, but as the charge continues to accumulate the leakage current (separation between plateaus) increases until it reaches saturation. That means at this level, the entire sheet of charges exit the sample (and further charge accumulation is halted). This indicates saturation of the charge at higher biases. That means all the photogenerated charges were evacuated from the device at 250 V. However, for applied voltage beyond 240 V, the increase in photogenerated charge is not shown, that means increase in applied voltage does not bring further increase in photogenerated charges, indicating that all holes were able to traverse the depletion layer without being trapped [206].

Expected trend of linear increase of the logarithm of hole mobility with square root of applied electric field for P(PE-PV) polymer was shown in Figure 3.4.5, following Poole-Frenkel type behavior.

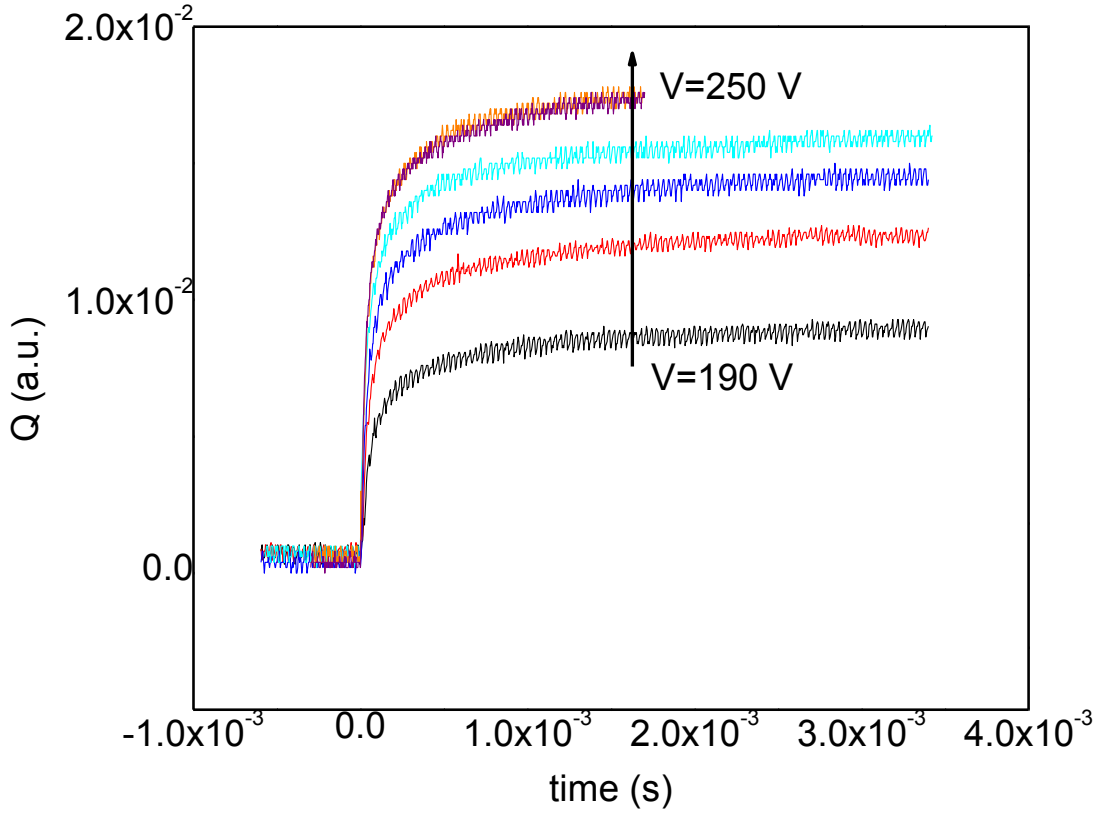

Figure 3. 4. 4. Oscillograms of integral mode TOF transients in a P(PE-PV) polymer film excited with N_2 laser at 337 nm, for several different applied bias from 190 V to 250 V with step of 10 V.

According to Gaussian disorder model (GDM), the increase of mobility in log μ *Vs* $E^{1/2}$ plot, in disordered molecular solids (polymers), is due to the tilting of density of states (DOS) by the applied potential that lead to the decrease of energetic barrier as shown by the charge carriers in their transit [48, 49, 207]. At higher electric field the energetic barriers between transport sites is negligibly small and this results in the saturation of drift velocity of the carrier [208].

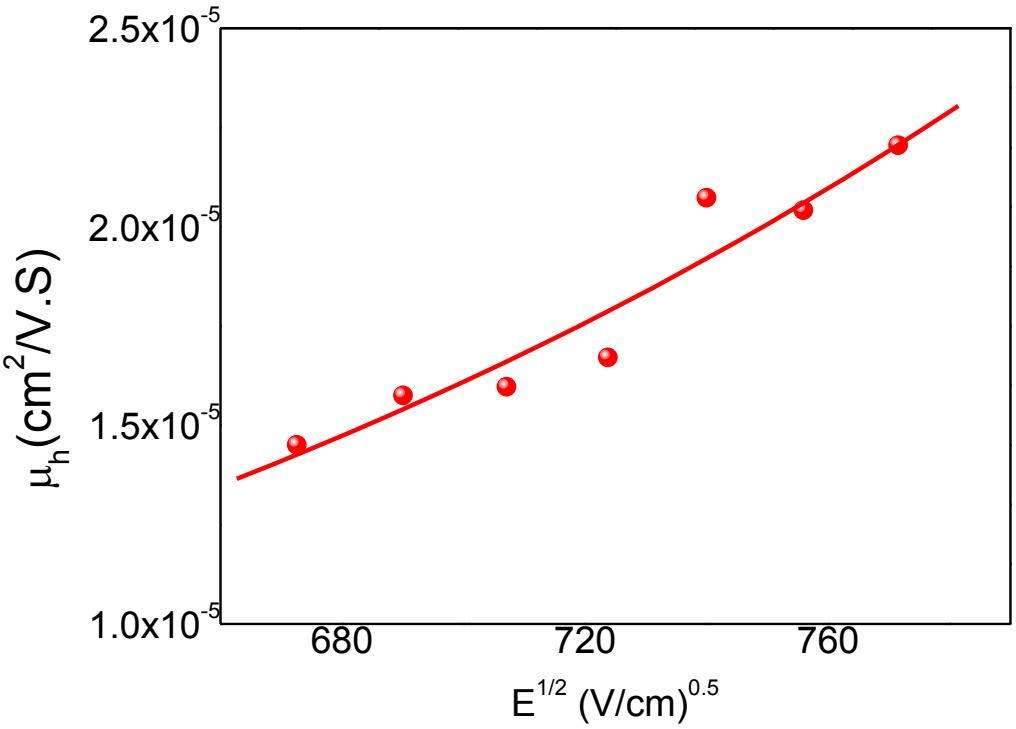

Figure 3. 4. 5. Hole mobility of P(PE-PV) polymer as function of square root of applied electric field.

3.4.2. Conclusions

Using the integral-type of time of flight method, transit times of holes in P(PE-PV) polymer even that are less than RC time constant of the device were able to be collected. The mobility extraction techniques in this experiment were easy and direct.

The initial slope of Q(t) is getting more and more steeper, confirming that transit time is shifted to the shorter time domain with increasing applied electric filed. Therefore, hole mobility was observed increasing with field. This might be because of that the activation energy for carriers hoping is decreasing with field [209].

I-TOF mode is advantageous over differential current mode; because Q(t) was observed to increases with time towards a maximum limiting value, therefore it was

possible to extract transit time even when no clear change in slope can be identified (as of section 3.3 of differential TOF cases).

3.5. Investigation of effect of electric field and temperature on carriers' mobility using admittance spectroscopy in anthracene containing polymers

In disordered organic semiconductors such as polymers mobility is many order of magnitude smaller than crystalline organic semiconductors (1 cm^2/Vs) and inorganic semiconductors (10 - 1000 cm^2/Vs), and charge carriers mobility in disordered organic semiconductors are also observed to be field and temperature dependent**.** Based on Monte Carlo (MC) simulations of charge transport in a Gaussian disorder model (GDM) the temperature and electric field dependent mobility was proposed by Equation 1.1 [48].

The field and temperature-dependence of the hole mobility has been given by Equation 1.1 appears to be generic for a large class of disordered materials such as polymers. The variations in the parameters such as σ, C, and T_0 (shown in the Equation) describing the field dependency. This suggests that the conduction mechanisms in conjugated polymers are similar to molecularly doped systems, where highly localized charge carriers are transported by a thermally assisted intermolecular hopping process [210, 211].

According to B*ä*ssler disorder theory [48, 184], it is suggested that the energy of the charge carriers at each hopping site as randomized by Gaussian distribution, characterized by an energy width σ of about 0 - 1 eV, determined by the local environment of the hopping sites. The hopping rate is assumed to be activated if it must hop up in energy or constant if it hops down in energy [184].

To understand the charge transport behaviors inside such devices, many experimental techniques are used to measure the carrier mobility of the organic films [45, 212]. From many of the techniques, time of flight (TOF), charge extraction with linearly increasing voltage (CELIV) and admittance spectroscopy are the common ones. In TOF technique, the problems of charge injection can be neglected; it is because this method is independent of the electrical contact at the metal/organic interface. Eventhough the TOF technique can be viewed as a standard means to measure carrier mobilities, it suffers from some limitations. This technique requires only thick films and do not work for more conductive materials [213, 214].

There is an alternative mobility measurement technique, the admittance spectroscopy (AS), which is simple to use and can work in samples of thin films. In addition, the film preparation for AS characterization is easily done using spin-coating method. While preparing samples for AS mobility measurement, polymer (material) consumption is more economical than TOF method. It is admittance spectroscopy (AS) we used in this experiment to study effect of electric field and temperature on charge transport properties in AnE-PVstat4 copolymer.

Recently, admittance spectroscopy (AS) based on small signal space-charge-limited current (SCLC) theory has been proposed to characterize the carrier dynamics in organic materials [215].

The AnE-PV polymers have good ambipolar electrical properties, and their resulting optical and electrical devices such as OLED, OFETs and OPVs exihibited temperature and electric field dependent behaviours [216 – 218]. Therefore, studying charge carriers mobility (that determines performances of the above-mentioned devices) in this polymer against temperature and electric field is so interesting.

AS is a powerful technique to investigate charge transport and relaxation processes in organic devices. With this method, the current response, i_{ac}, to a small oscillating voltage, v_{ac}, is monitored. The complex admittance, Y_{ac}, is the reciprocal of the impedance Z_{ac} and is related to i_{ac} and v_{ac} as follows:

$$Y_{ac} = \frac{1}{Z_{ac}} = \frac{i_{ac}}{V_{ac}} = G(\omega) + iB(\omega) = G(\omega) + i\omega C(\omega) \quad (3.7)$$

3.5.1. Electric field dependence of the charge carrier mobility at room temperature

The admittance characteristics of the diodes of devices with device structure of ITO/PEDOT:PSS/ AnE-PV /Ag were studied as a function of temperature from 5^{o}C to 85^{o}C in order to investigate the transport behaviours of charge carriers at different temperature. The carrier mobility, μ_h and μ_{ho}, varies with temperature according to,

$$\mu_h, \mu_{ho} = \mu * e^{-\Delta/kT} \quad (3.8)$$

Where μ_h is hole mobility, and μ_{ho} is hole mobility at zero-field, $\mu*$ is mobility prefactor, Δ the activation energy, and k is Boltzman constant.

Admittance spectroscopy (AS) is a viable technique to study carrier transport properties in organic thin films. The hole mobilities of anthracene containing polymer (AnE-PVstat4) (whose structure was shown in Figure 2.1) were investigated. In order to obtain ohmic/quasi-ohmic contact, poly(3,4-ethylenedioxythiopene) doped with poly(styrensulfonate) (PEDOT:PSS) is inserted between the anode and the organic layer in order to reduce the hole injection barrier between ITO and the polymer (as shown in Figure 3.5.1) [219].

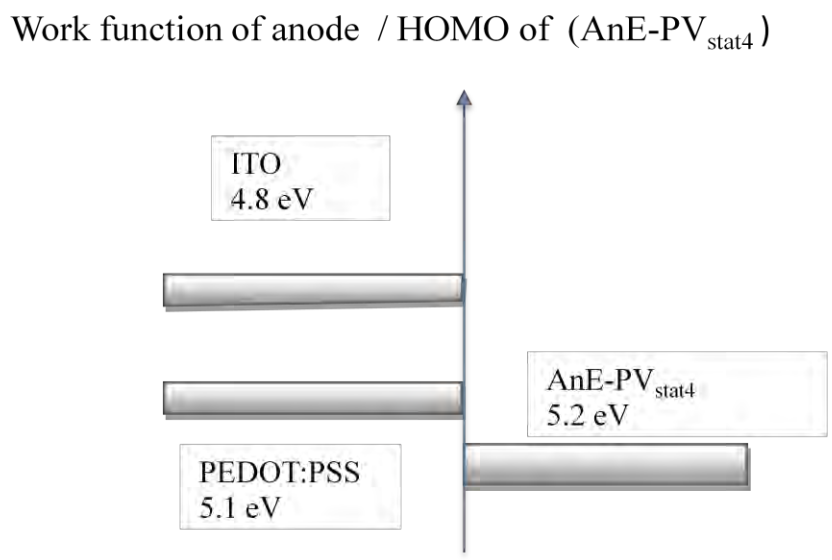

Figure 3. 5. 1. Relationship of work function of anode and HOMO of Anthracene containing copolymer (AnE-PV*stat4*).

When a positive bias greater than built-in-potential was applied on the ITO anode, holes are injected into AnE-PV*stat4* copolymer film and transit of carriers across the thickness of the film occurs. According to many reports, efficiency of injection and mobility of injected charges in to polymeric active material is affected by factors such as temperature and electric field [220, 221].

Inorder to investigate effect of electric field and temperature on hole mobility in anthracene containing statistical polymers, the devices with structure of ITO/-PEDOT:PSS/AnE-PV*stat4*/Ag were prepared in the open air. AS characterizations were done inside glove box. Figure 3.5.2 shows the frequency dependent conductance (Figure.3.5.2a), capacitances (Figure.3.5.2b) and negative change in susceptance (Figure 5.3.2c) of the AnE-PV*stat4* copolymer measured at room temperature at 0 V and 5 V of applied potentials. All the signals in Figure 3.5.2 exhibit the characteristic signatures of AS spectra.

As indicated by Figure 3.5.2b, the capacitance (represented by dotted symbols) at V = 0 V, is frequency independent and is equal to geometric capacitance, $C_{geo} = \varepsilon_o \varepsilon A/d$. where ε_o is dielectric constant of the vacuum, ε is dielectric constant of material (for polymer it is 2 - 3) and A is area of electrodes intercepted by active material or polymer film and ITO. In addition, at zero bias, no charge transport is possible due the built-in potential, V_{bi}, and hence the conductance indicated by dotted line in Figure 3.5.2a is entirely due to the dielectric response of AnE-PV*stat4* [222]. In the capacitance and change in susceptance plots for the polymers, the C_{geo} and inverse of the characteristic transit time ($\tau_{tr}{}^{-1}$) at applied potential of 5 V are shown by arrows in Figure 3.5.2b and Figure 3.5.2c respectively.

The characteristic frequency dependence of the conductance at non-zero bias can be reasonably explained using applied DC voltage of 5V as an example. As could be observed from Figure 3.5.2a, conductance (G) keeps fairly constant up to around 500 kHz. Then, it increases slightly and merges with G(ω) of zero bias. At frequency above 1 x 10^6 Hz, both conductances (conductance at V = 5 V and at V = 0 V) are the same. The reason for this is that at high frequencies, contribution from the injected carriers is not important and G(ω) is dominated by the relaxation processes that are likely related to the relaxation of permanent dipoles [223]. However, the device capacitance exhibits a significant frequency dependence when DC voltage is positive (i.e. V = 5V).

At frequencies, $f < \tau_{tr}{}^{-1}$ the capacitance is decreasing from the geometrical capacitance due to space-charge effect, while at $f \gg \tau_{tr}{}^{-1}$, the geometrical capacitance is restored. Where τ_{tr} is the characteristic transit time (the average of time taken by holes between injection and relaxation into equilibrium state).

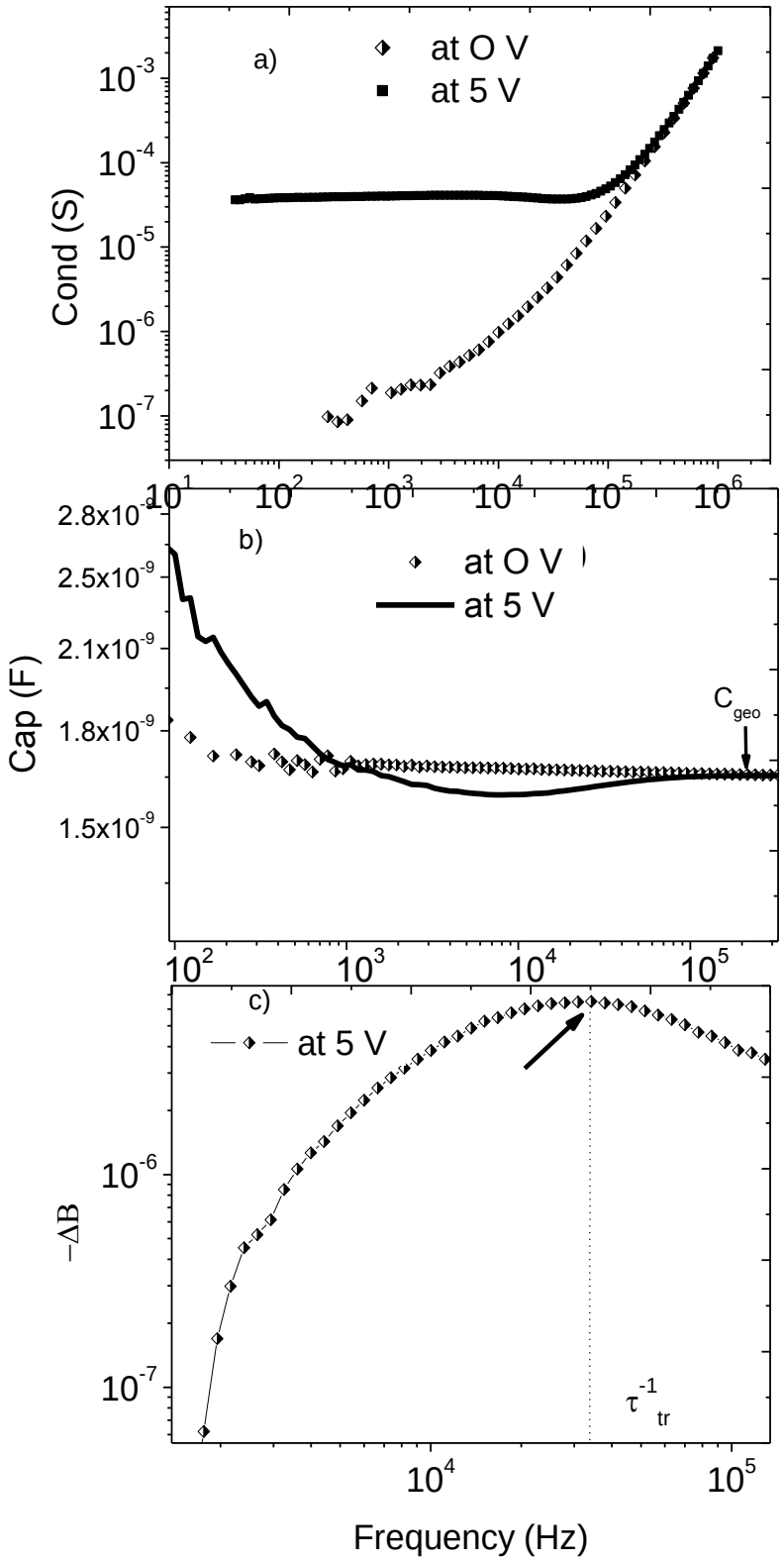

Figure 3. 5. 2. Frequency dependent signals of (a) conductance (G), (b) capacitance (C), (c) negative change in susceptance (-ΔB) of AnE-PV*stat4* at room temperature.

However it is more convenient to analyze the data by plotting the negative change in susceptance (Figure 3.5.2c), as a function of frequency, as it was suggested by Martens et al. and other groups [137, 223] using Equation,

$$\Delta B = -\omega(C - C_{\text{geo}}) \tag{3.9}$$

Clearly, -ΔB peaks at maximum a frequency, f_{max}, which scales with the corresponding transit time, τ_{tr}, according to an approximate relation;

$$\tau_{tr} \approx 0.54 {f_{max}}^{-1} \text{ [224]}, \tag{3.10}$$

and mobility can easily be obtained in terms f_{max} by,

$$\mu = \frac{\eta\, f_{\max}\, \mathrm{d}^2}{(V - V_{bi})} \tag{3.11}$$

where η is the proportionality coefficient. From the calculations presented here η is obtained to be $\approx$1.85; however the actual value of η may be somewhat different. Since the field-dependence of mobility and diffusion were neglected in the calculations; d is thickness of polymer film sandwiched between cathode and anode, V is applied potential, and V_{bi} is built in potential (work function difference between cathode and anode in the device).

Equation 3.11 provides a straightforward method to determine charge carrier mobility from complex admittance measurements by plotting the negative change in susceptance (–ΔB) as a function of frequency for different bias voltages V and determining f_{max} for different values of V. The relationship between transit time and frequency maxima that is extracted from the plot of -ΔB is related by Equation 3.9 [137].

The impact of an external electric field is to lower the barrier for upward energy hopping of carriers; this allows the charges to leave the states in the tail of the density of states (DOS) that would otherwise act as traps. In the presence of energetic disorder only, the Monte Carlo results generally yield a Poole-Frenkel behavior (linear behavior of charge transport with electric field, i.e $\mu \alpha E^{1/2}$ [225].

Figure 3.5.3 shows the measured capacitance (C) and conductance (G), and negative change in susceptance (-ΔB) of AnE-PV*stat4* as function of the AC modulation frequency *f* between 10^2 and 10^6 Hz and with variable applied dc voltages from 3 V up to 10 V. In Figure 3.5.3a, the G curves show a constant value in the low frequency regime, followed by a general increase of the signal at high frequency. The height of the conductance plateau increases with applied bias V, from a value of about 1.35 x 10^{-5} s at 3 V to the value of 2.80 x 10^{-4} s at 10 V. The region in which *G* increases with *f* begins at a threshold frequency depending on the applied bias and which is approximately equal to 6.73 x 10^{-5} Hz at 5 V. This behavior at high frequency is related to the series resistance of the device.

A small dip occurs in conductance spectra around the intermediate frequency region, just before the beginning of the increasing portion. These dips in conductance spectra are visible for applied voltages greater than 2 V. This is because injection of holes in to the AnE-PV film is insignificant for applied bias below 3 V. Position of the dip shifts into the higher frequency region when the bias voltage increases; indicating enhancement of charge injection with increasing DC bias and field dependent charge transport. In Figure 3.5.3b, the frequency-dependent capacitance (C) of an AnE-PV film is shown as a function of forward bias voltage.

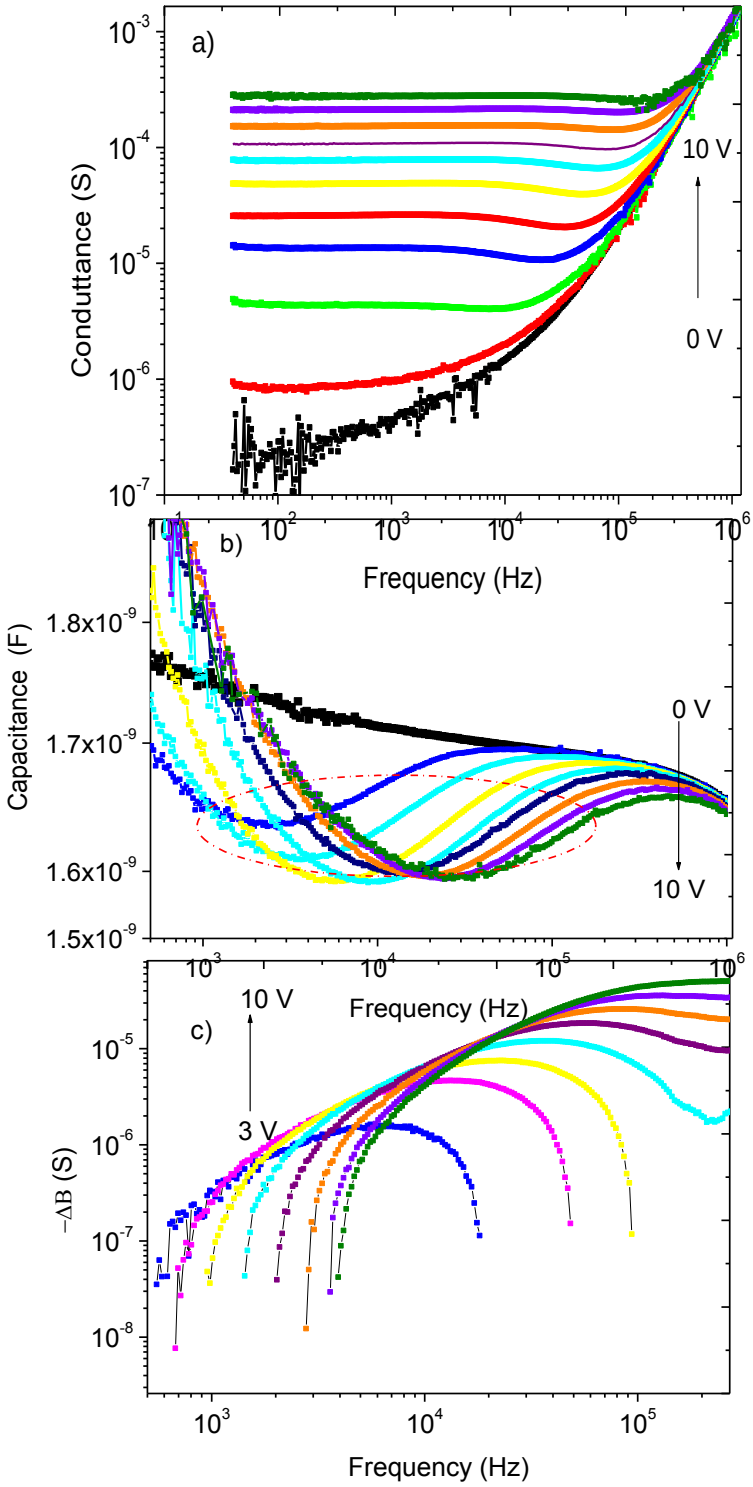

Figure 3. 5. 3. Important transport parameters on AnE-PV*stat* films such as a) conductance (G), b) capacitance (C), and c) negative change in susceptance (-ΔB) *versus* frequency measured at room temperature (298 K). The vertical arrows show direction of peak growth with increasing applied potential from 0 V to 10 V.

At zero bias *C* (represented by thicker line*)* is essentially frequency independent and equals the geometrical capacitance (C_{geo}). A capacitance-frequency curve shows plateau for all applied voltages at higher frequency, is interpreted as the dielectric capacitance of the device, and has constant value for all applied voltages. The lower frequency part of capacitance decreasing with frequency up the minimum point, this is due to trapping effect to the charge carriers. Capacitance *versus* frequency peak in Figure 3.5.3b shows capacitance minimum (at medium frequency range) at each applied potential. This minimum point (in capacitance) is corresponding to the frequency at which injected holes are relaxed to the equilibrium state at that applied potential. This capacitance minimum is shifted to higher frequency with increasing potential from 3 V to 10 V.

These phenomena indicate the field dependency of capacitance, and then field dependency of transport properties of holes. These field dependences of C are more clearly visualized by plotting the differential susceptance (-ΔB) against frequency. Figure 3.5.3c, displays -ΔB *as* a function of frequency.

In the -ΔB peak, frequency maximum (f_{max}), from which transit time, τ_{tr}, can be determined, is shifting to higher frequency region or to the lower transit time showing that mobility of holes increases with increasing applied bias. This means hole carrier mobility is directly proportional to electric field following Poole-Frenkel relationship (indicated in Figure 3.5.4), as that of other polymers reported elsewhere [224].

The reason behind increasing carrier mobility with electric field is that, when potential is applied to the amorphous materials, AnE-PV*stat4*, energetic disorder in the polymer films becomes narrow, and then carriers‟ hopping from one energy site to

the other energy site becomes easier [184]. The width of energetic disorder becomes more and more narrow with increasing applied electric field, and then charge carrier hopping is getting enhanced [184]. The carriers‟ mobility increase with the field is also because of the fact that the field can decrease the activation energy for forward jump of carriers, and then enabling motion of carriers [226]. Upon increasing positive applied bias to the sample, the density of holes injected to the polymer film increases [226].

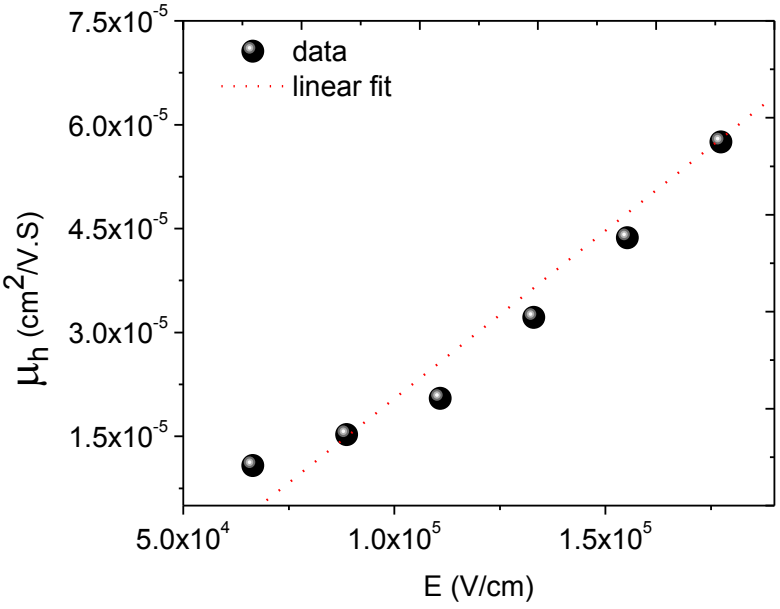

Figure 3. 5. 4. Field dependent hole mobility *versus* electric field measured at room temperature (298 K) by applying DC bias from 3 V - 10 V with step of 1 V. The solid line is the linear fit to the experimental data.

Figure 3.5.4 shows the mobility of holes in the film of AnE-PV*stat4* as a function of electric field applied perpendicular to the plane of ITO substrate at temperature of 298 K. The hole mobility in the polymer is not constant for different applied potential bias.

With increasing the amount of applied potential, the concentration of holes injected in to the film of the polymer sandwiched between the two parallel plate electrodes (ITO/PEDOT:PSS and Ag) increases.

The reason behind increasing carrier mobility with electric field is mainly because of filling traps sites [227, 228] and influence of the field on energetic disorder [48]. These additional charges fill more traps and the overall mobility increases. As we can observe from Figure 3.5.4 field dependent mobility is linear and follows Poole-Frenkel behavior.

3.5.2. Study of temperature dependent hole mobility in AnE-PV*stat4* using AS

Apart from room temperature measurements, we also performed temperature dependence of carrier mobilities measurement of the AnE-PV*stat4* polymer films at different temperatures using AS technique. The data were then analyzed in the framework of the Gaussian disorder model (GDM), first proposed by Bässler [48]. In GDM, charges hop in an amorphous solid whose transport site energies and positions are in Gaussian distributions [229]. The GDM can be embodied in the semi-empirical equation for the carrier mobility (Equation 1.1)

The effect of temperature on mobility of hopping transport is similar to that of electric field. Increasing the temperature raises the population of charge carriers to higher energies, where the DOS (density of states) is broader, and hence the mobility improves. Therefore, the mobility is a function of both temperature and electric field [230]. To get a closer insight into the processes determining the transport, temperature dependent admittance of AnE-PV*stat4* polymers were measured at five different temperatures from 5^{o}C to 85^{o}C with variation 20^{o}C. The resulting AS signals

(conductance, capacitance, and change in susceptance) were collected from HP 4294A Agilent Technology impedance analyzer.

Figure 3.5.5 demonstrates the conductance spectra as function of modulation frequency, measured on ITO/PEDOT:PSS/AnE-PVstat4/Ag device structure. For the temperature from 5°C to 45°C, the conductance increased almost by an order of magnitude at constant DC bias of 5 V (Figure 3.5.5). This is due to the increased injection of charges from electrode to the polymer [231] and improved translational motion of charge carriers within the polymer film with increasing temperature.

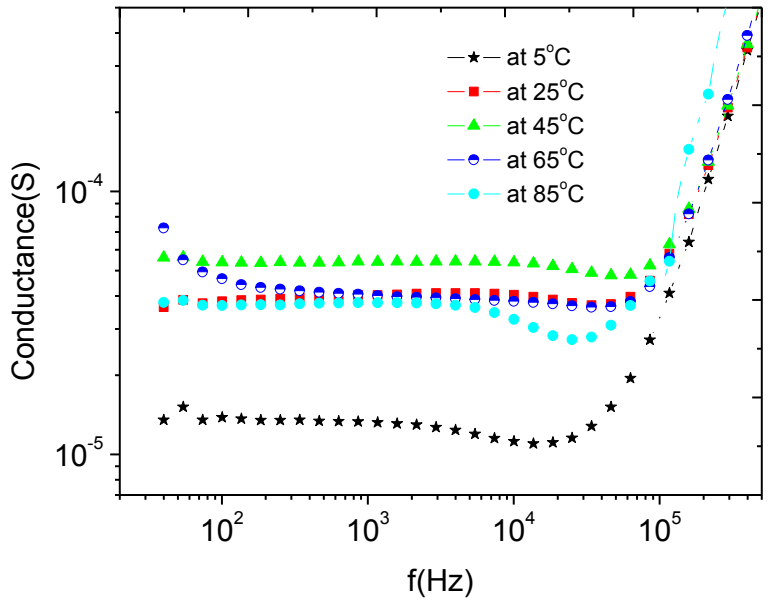

Figure 3. 5. 5. Frequency dependent conductance for the device of ITO/PEDOT:PSS/ AnE-PV*stat4*/Ag at different temperatures at a constant applied potential of 5 V.

As expected, conductance was greatly enhanced by increasing temperature (from 5°C to 45°C), indicating strongly thermally activated charge carrier mobility. In the frequency range between 5 x 10^3 and 10^5 Hz of the conductance spectra, the smaller dip is shown at intermediate frequency region and it shifts to the higher frequency for temperature from 5°C and 45°C and shifts to lower frequency for the temperature

change from 65°C to 85°C and it is bigger for 85°C. These dips are indication for injection of charges [232], and these dips are also shown in capacitance spectra in the corresponding frequency range (Figure 3.5.6).

The dips (capacitance minimum) points shift to higher frequency (for variation of temperature from 5°C to 45°C) and shift back to lower frequency (for temperature changes from 65°C to 85°C). This phenomena shows the temperature dependent capacitance behavior, which in turn means temperature dependence hole mobility.

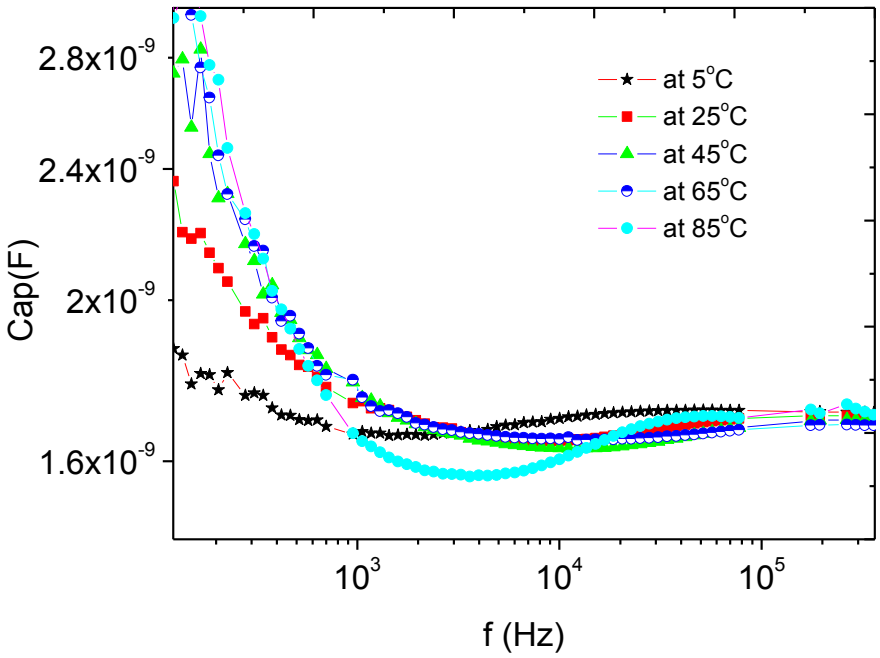

Figure 3. 5. 6. Frequency Dependent capacitance for the device of ITO/PEDOT :PSS/AnE-PV*stat*/Ag at different temperatures with constant applied potential of 5 V.

The condctance dips and capacitance minimum show positive shift with frequency (for 5°C to 45°C) and negative shift (for 65 °C to 85°C). This indicates positive and then negative temperature dependence of hole transport at a given range of temperatures.

Figure 3.5.7 presents the negative change in susceptance (-ΔB) peak as a function of frequency for temperatures from 5°C to 85°C. The -ΔB peak shifts to higher frequency from 5°C to 45°C and turns to lower frequency with temperature increases from 65°C to 85°C, indicating the decrease in transit time with temperature up to 45°C then increasing for temperatures above 45°C.

Using the Equation 3.11, hole mobility was calculated for all the temperatures and the values at the corresponding temperature were presented in Table 3.5.1.

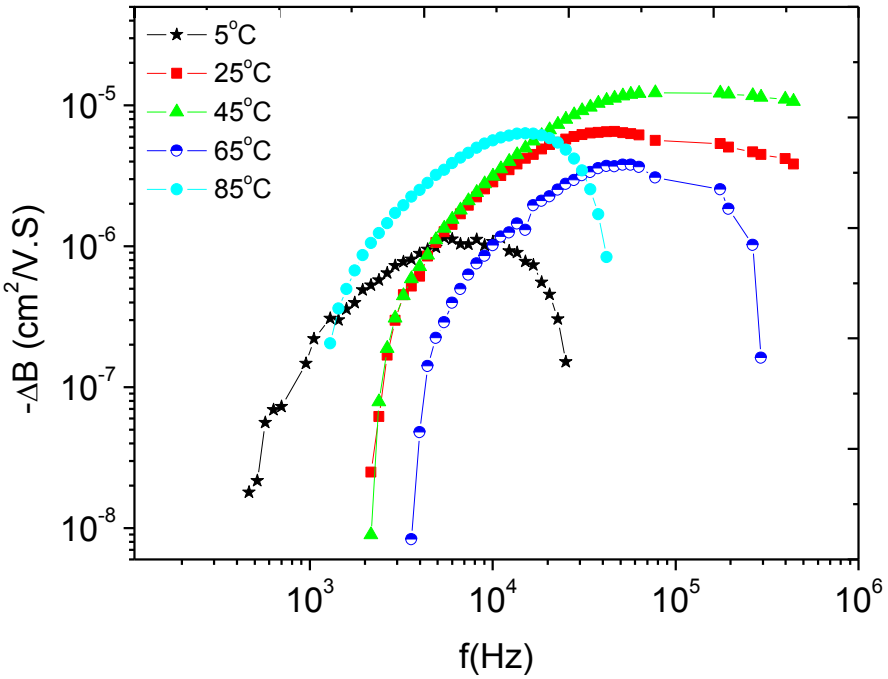

Figure 3. 5. 7. Temperature dependent negative change in susceptance (ΔB) as function of frequency at constant applied potential of 5 V.

The decrease in mobility dependence on the electric filed through increasing temperature is attributed to enhancement in crystallinity of polymer or organic material and decreasing disorder in polymer/organic film [233]. In many reports for charge transport property, mobility of charge carriers (either electrons or holes)

increases with temperature in amorphous materials such as polymers and small molecules [234, 235].

Table 3. 5. 1. Data of field dependent hole mobility (μ_h) of AnE-PVstat4 polymer measured at temperatures of 5^oC, 25^oC, 45^oC, 65^oC and 85^oC are recorded here.

Bias (V)	μ_h (@5^oC) ($cm^2/V\,S$)	μ_h (@25^oC) ($cm^2/V\,S$)	μ_h (@45^oC) ($cm^2/V\,S$)	μ_h (@65^oC) ($cm^2/V\,S$)	μ_h (@85^oC) ($cm^2/V\,S$)
3	…	4.82×10^{-6}	1.34×10^{-5}	…	…
4	…	8.07×10^{-6}	2.03×10^{-5}	…	5.27×10^{-6}
5	2.41×10^{-6}	1.12×10^{-5}	2.53×10^{-5}	1.52×10^{-5}	5.52×10^{-6}
6	4.08×10^{-6}	2.03×10^{-5}	3.05×10^{-5}	2.48×10^{-5}	7.18×10^{-6}
7	5.03×10^{-6}	2.07×10^{-5}	3.83×10^{-5}	2.82×10^{-5}	8.16×10^{-6}
8	6.47×10^{-6}	...	5.47×10^{-5}	3.28×10^{-5}	8.62×10^{-6}
9	8.16×10^{-6}	...	…	3.54×10^{-5}	9.35×10^{-6}
10	…	…	…	…	1.13×10^{-5}

Figure 3.5.8 and Table 3.5.2 shows the hole mobility *versus* electric field at five different temperatures. The symbols represent the experimental data and the solid lines represent the fit to the experimental data in the figure.

The temperature dependent mobility we investigated here for diode of AnE-PV*stat4* polymer is shown in Table 3.5.2 and Figure 3.5.8. The charge carriers‟ mobility at different temperatures show different dependency nature on electric field. First charge carriers‟ mobility increases with increment in temperature upto 45^oC. The increase of charge carriers‟ mobility with increasing temperature up to 45^oC, can be explained by thermally activated transport mechanism. By increasing temperature from 5^oC

through 25°C to 45°C carriers getting more and more sufficient thermal energy to escape from traps and then drift easily by applied electric field.

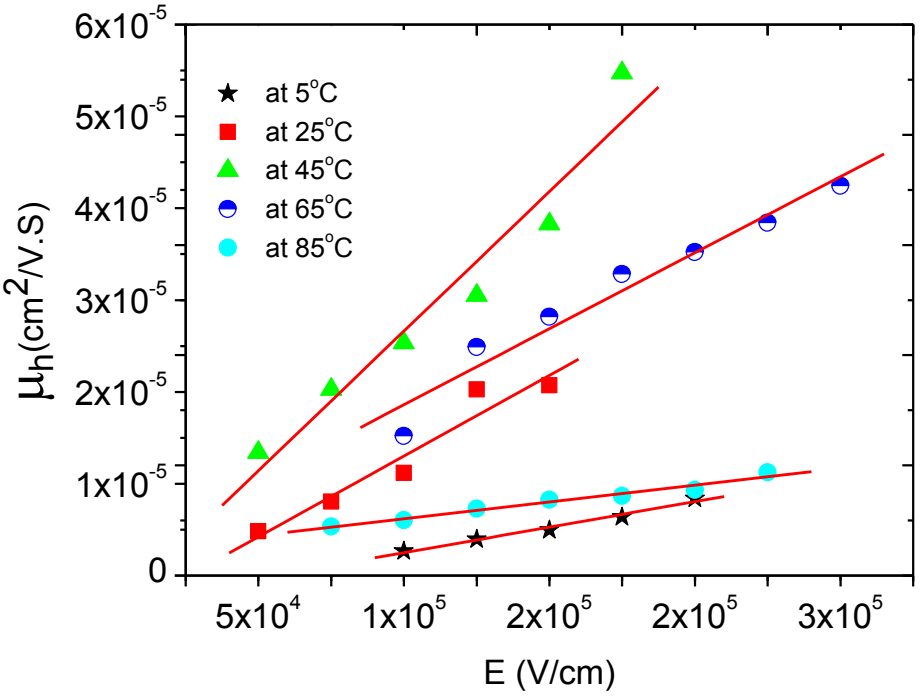

Figure 3. 5. 8. Electric field dependent of hole mobility of AnE-PV*stat4* polymer at five different temperatures from 5°C to 85°C in the devices structure of ITO/PEDOT:PSS/AnE-PV*stat4*/Ag. The lines are linear fits the experimental data.

Table 3. 5. 2. Nature of hole mobility with temperature for AnE-PV*stat4* polymer at electric field of 1.5 x 10^5 V/cm.

Electric field, E (V/cm)	Temperature (°C)	Mobility, μ_h (cm^2/VS)
1.50 x 10^5	5	4.95 x 10^{-6}
1.5 x 10^5	25	2.07 x 10^{-5}
1.5 x 10^5	45	3.83 x 10^{-5}
1.5 x 10^5	65	2.82 x 10^{-5}
1.5 x 10^5	85	8.25 x 10^{-6}

On the other hand, the decreasing of carriers‟ mobility with increasing temperature above 45°C can be explained by the intrinsic transport behavior dominated by phenomena of lattice scattering [236]. Lattice scattering decreases charge carriers‟ mobility in more crystalline samples. This is possibly because of the fact that, for temperature increase above 45°C, films of AnE-PV*stat4* become more ordered and crystalline.

Field dependent mobility at different temperatures shows linear behavior and follows the Poole-Frenkel trend (Figure 3.5.9). At lower temperature (5°C), field dependent mobility is not stronger. According to [237], carrier mobility showed lower field dependent at lower temperatures. At lower temperature tunneling, become the dominant charge transport mechanism because of the lack of thermal energy for charge carriers to overcome the barrier.

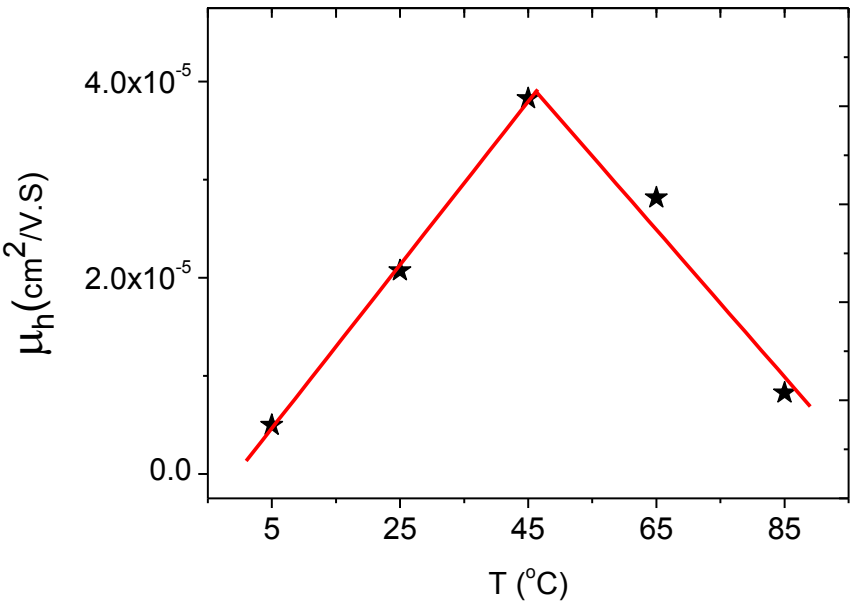

Figure 3. 5. 9. Temperature dependent hole mobility in AnE-PV*stat4* polymer at electric field of 1.5 x 10^5 V/cm, with film thickness of 400 nm, on mobility devices structure of ITO/PEDOT:PSS/ AnE-PV*stat4* /(400 nm)/Ag (70 nm).

As the measuring temperatures increases from 5^{o}C to 45^{o}C, strength of field dependent mobility increases. However, at temperatures above 45^{o}C, field dependency of the carriers‟ mobility declines with increasing temperature up to 85^{o}C. This decline in field dependency of mobility in disordered materials such as polymers is explained by multiple trap and release (MTR) model [238]. This type of decrease of dependency of hole mobility on the electric field was also shown in regio-regular P3HT [238].

At lower temperature and electric field, the carriers‟ mobility is smaller (Figure 3.5.9 Tables 3.5.1, and 5.3.2) because of presence of traps with depth (trapping energy) larger than K_BT [240, 241].

3.5.3. Conclusions

In the field dependent hole mobility study, the observed shift in capacitance minimum and negative change in susceptance maximum to the higher frequency regime, with increasing DC potential is indicating positive field dependence of hole mobility. Hole mobility was increased with increasing applied potential or field. The reason behind increasing hole mobility with electric field is that, when the applied potential to the AnE-PV*stat4* films was increased, the energetic disorder in the polymeric films become more and more narrow. Then the rate of charge carriers‟ hopping from one energetic site to the next higher energy site would be higher.

In the temperature dependent carrier mobility study, all admittance peaks such as conductance and capacitance dips and change in susceptance maximum showed shift to higher frequency range for temperature increase from 5^{o}C through 25 ^{o}C to 45^{o}C, and shifting back to lower frequency regime with increasing tempratures from 65 ^{o}C

to 85^{o}C. This indicates that the hole mobility showed positive temperature dependence from 5^{o}C to 45^{o}C, and negative dependence from 65^{o}C to 85^{o}C.

The decrease in mobility for increasing temperature beyond 45 ^{o}C may be due to enhancement of crystallinity as well as scattering of charge carriers due to phonons. The decrease of field dependency of the mobility above 25^{o}C showing usual type of enhancement in film crystalinity and decrease of energetic disorder expected from polymer materials.

3.6. Effect of Electrode barrier height on hole mobility in AnE-PVstat copolymer

The injection from metal into semiconductor is still poorly understood, and a deeper knowledge of the dynamics at the metal-semiconductor interface is one of the keys to improving device performance. Since organic semiconductors have no intrinsically free charge carriers, injection or extraction of charge will control the device performance [242]. Here, effect of electrode (metal)/semiconductor interface and injection barrier between cathode metal and polymer (AnE-PV*stat*) on the holes mobility was investigated.

Towards this end the devices with different electrode/semiconductor barrier height structures such as ITO/PEDOT:PSS/AnE-PV*stat*/Al, ITO/PEDOT:PSS/AnE-PV*stat*/-Ag, ITO/PEDOT:PSS/AnE-PV*stat*/ PEDOT:PSS/Ag, and ITO/PEDOT:PSS/AnE-PV*stat*/Au were constructed, and whose charge carriers mobility was investigated using admittance spectroscopy at room temperature.

The HOMO and LUMO energy levels of AnE-PV*stat* polymer and the work functions of ITO, PEDOT:PSS, Al, Ag and Au are presented in the Figure 3.6.1. The resulting devices with different top electrodes are presented by ITO/PEDOT:PSS/AnE-PV*stat*

/Al (Figure 3.6.1a), ITO/PEDOT:PSS/AnE-PV*stat*/Ag (Figure 3.6.1b), ITO/PEDOT:PSS/AnE-PV*stat*/Au (Figure 3.6.1c) and ITO/PEDOT:PSS/AnE-PV*stat* PEDOT-:PSS/Ag (Figure 3.6.1d).

The barrier heights for electron injection from cathode to the polymer are displayed in Table 3.6.1. Depending on the barrier height beween LUMO of AnE-PV*stat* and cathode work function, injection efficiency of the contact and thus density of injected electron in the device will be changed [243]. Accordingly, the mobilility of charge carriers are affected by concentration of injected charges to the polymer layer [225].

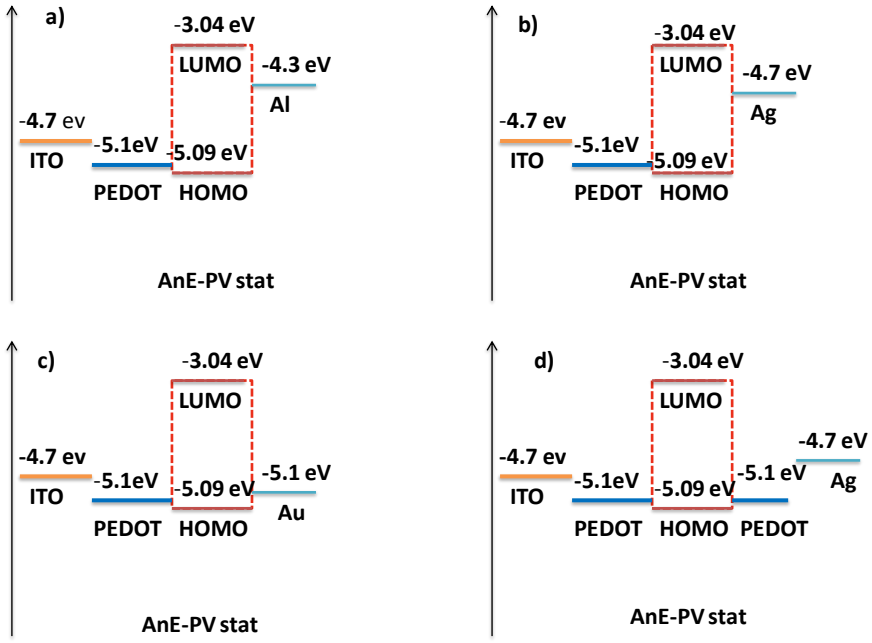

Figure 3. 6. 1. HOMO-LUMO energy levels of the polymer AnE-PV*stat* and work functions of electrodes in the four-different devices using a) Al, b) Ag, c) Au and d) PEDOT/Ag as top electrode.

It is only recently that the influence of charge carrier density on mobility has been carefully examined. Blom and co-workers [227] have shown experimentally that the hole carrier mobility in polyparaphenylene vinylene is increased with increasing

density of charge carriers in the diode type device [224, 227]. The diode type devices having different barrier heights for electron injection are presented in Table 3. 6. 1.

Table 3. 6. 1. Device profile and the barrier height inferred from the Fowler-Nordheim analysis for range of devices.

Device profile	Barrier height for electron injection (eV)
ITO/PEDOT:PSS/AnE-PV*stat*/Al	1.26
ITO/PEDOT:PSS/AnE-PV*stat*/Ag	1.66
ITO/PEDOT:PSS/AnE-PV*stat*/PEDOT:PSS/Ag	1.86
ITO/PEDOT:PSS/AnE-PV*stat*/Au	2.06

3.6.1. ITO/PEDOT:PSS/AnE-PVstat/Al

In this device profile (ITO/PEDOT:PSS/AnE-PV*stat*/Al (60 nm), ITO/PEDOT:PSS is the anode, while aluminum is served as cathode. PEDOT:PSS has a work function of about 5.1 eV [244] and used as quasi-ohmic contact for holes injection into the HOMO of the polymer layer at 5.2 eV and aluminum acts as cathode.

Capacitance and negative change in susceptance peaks for device ITO/PEDOT:PSS/AnE-PV*stat*/Al are shown in Figure 3.6.2. For higher applied voltages especially above 7V, the negative capacitance signals increase with the applied dc voltage at low frequency region (Figure 3.6.2). This negative capacitance in low frequency region signifies the injection of negative charge carriers [244]. That means not only holes are injected from anode but also electrons are being injected from Al electrode to the LUMO of the AnE-PV*stat* polymer. Electron injections were confirmed by light emission from the device while measuring mobility, which is attributed to electron-hole annihilation through recombination.

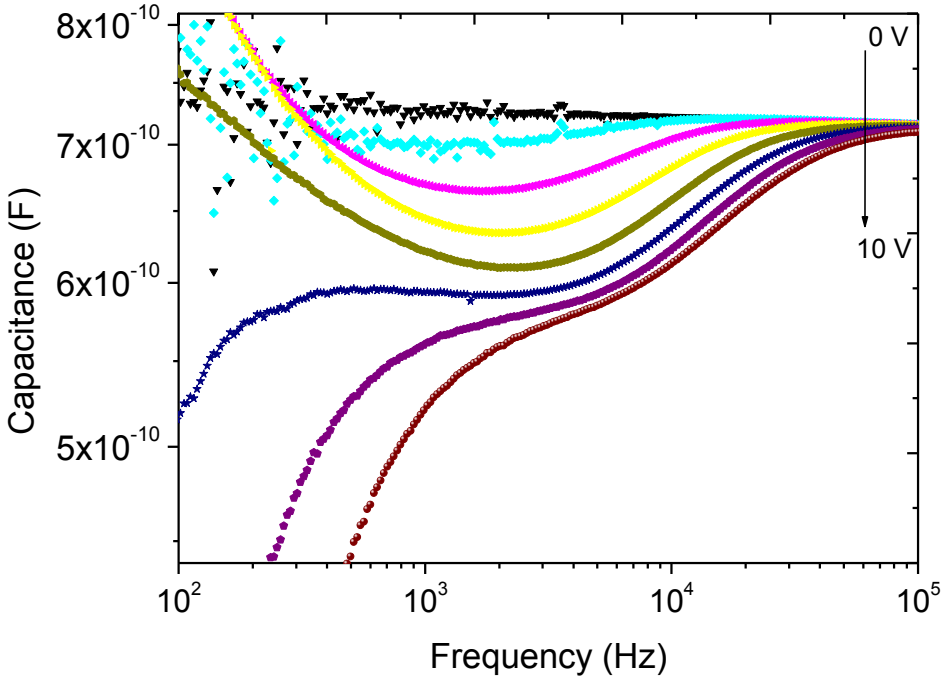

Figure 3. 6. 2. Frequency dependent capacitance signals for device ITO/PEDOT:PSS /AnE-PV*stat*/Al(60 nm) measured at biases from 0 - 10 V, with active layer thickness of 400 nm. The solid arrows are eye guides to the direction of peak growth with applied bias.

Two sets of change in susceptance peaks are shown in Figure 3.6.3. The one in medium frequency range belongs to hole transport and the other set at higher frequency domain stands for electron mobility [42]; confirmed from the study of hole and electron mobility in the AnE-PV*stat* polymer through TOF technique [42]. The signals for electrons are not clearly resolved (a set of peaks at higher frequency region in Figure 3.6.3), may be because of traps. From the change in the susceptance peak, hole signals are clearly seen and show visible shift in ΔB peak maximum to higher frequency region (lower transit time) with applied potential. The shift in the capacitance minimum towards higher frequency with electric field (applied potential) is also shown in the change in susceptace peaks depicted in Figure 3.6.2. These shifts

towards higher frequency region indicates the positive field dependency of hole mobility in the device.

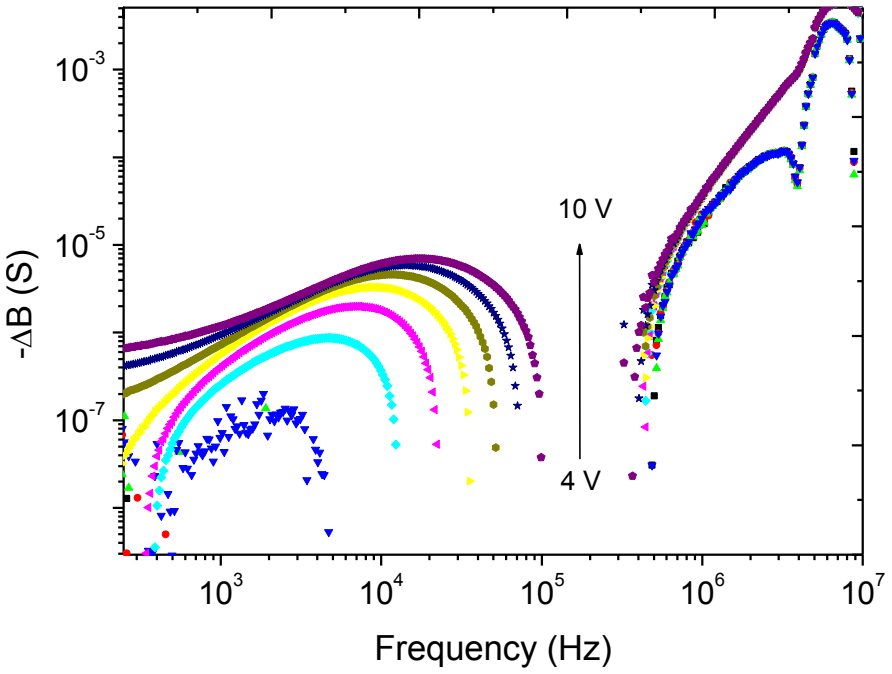

Figure 3. 6. 3. Frequency dependent negative change in susceptance (ΔB) spectra for device ITO/PEDOT:PSS/AnE-PV*stat*/Al(60 nm) measured at biases from 4 -10 V , with active layer thickness of 400 nm. The solid arrow is eye guides to the direction of peak growth with applied bias.

3.6.2. ITO/PEDOT:PSS/AnE-PV*stat* /Ag

This structure of device with Ag as top metal electrode (ITO/PEDOT:PSS/AnE-PV*stat*/Ag (60 nm), has ITO/PEDOT:PSS as an anode, Ag served as cathode with work function of 4.7 eV, which is deeper than work function of Al electrode. As can be observed from Figure 3.6.1, the energy barrier between Ag and LUMO of the polymers is higher than that between Al and LUMO of the polymer [244, 245]. Therefore, electron injection efficiency from Ag to LUMO of AnE-PV*stat* is expected

to be lower than that of Al. However, the negative capacitance in Figure 3.6.4 still show electrons injection from Ag to LUMO of AnE-PV*stat* films.

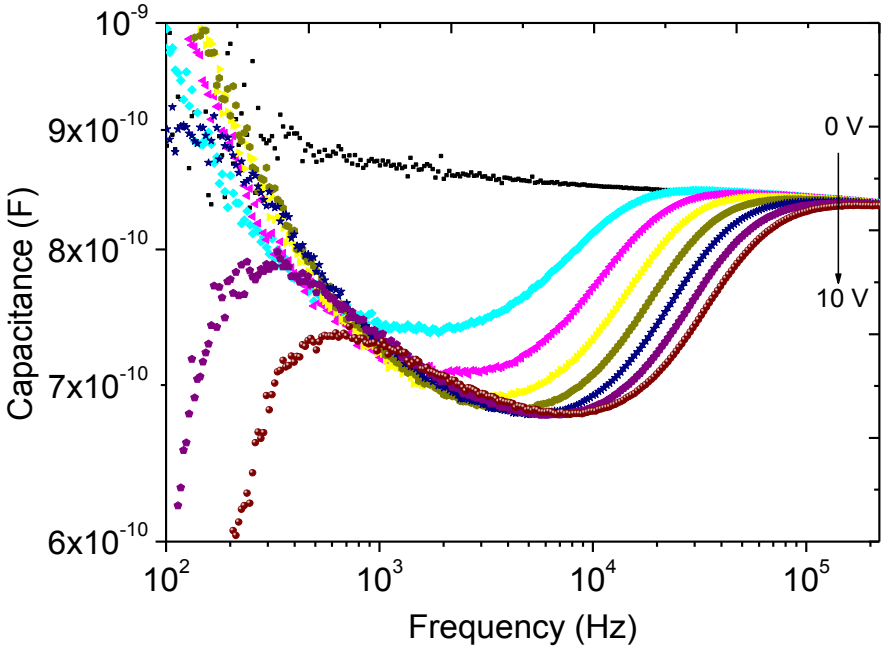

Figure 3. 6. 4. Capacitance spectra of the device with structure ITO/PEDOT:PSS/ AnE-PV*stat*(450 nm)/Ag (70nm). The solid arrow is an eye guide to the direction of peak shift with applied bias.

In Figure 3.6.5 at higher frequency region, small and unresolved change in susceptance peak (which stands for electron transport) indicates the decrease in electron injection efficiency from Ag to LUMO of the polymer than from Al. As it is shown in Figure 3.6.3 and Figure 3.6.5, the change in susceptance peak of holes in the medium frequency domain, become more and more clear and field dependent behaviour become more and more visibile in ITO/PEDOT:PSS/AnE-PV*stat*/Ag device than in ITO/PEDOT:PSS/AnE-PV*stat*/Al. However, the change in susceptance peaks for electrons becomes more and more unresolved in ITO/PEDOT:PSS/AnE-PV*stat*/Ag device than in ITO/PEDOT:PSS/AnE-PV*stat*/Al.

These phenomena indicate the decrease in electron injection efficiency upon changing the cathode material from Al to Ag. In ITO/PEDOT:PSS/AnE-PV*stat*/Ag device, light emission was observed during measurement only at DC voltages of 9 V and above (shown in Figure 3.6.5), indicating the decrease in electron injection and recombination with this device structure.

The work function of aluminum is 4.3 eV [246], which is not largely mismatched with LUMO of the AnE-PV*stat* (-3.04 eV) and could not effectively prevent injection of electrons in to the polymer film. This phenomenon, the enhancement in negative capacitance signals at lower frequency signifies injection of electron from the cathode to the polymer in this devices structure than the case of Ag.

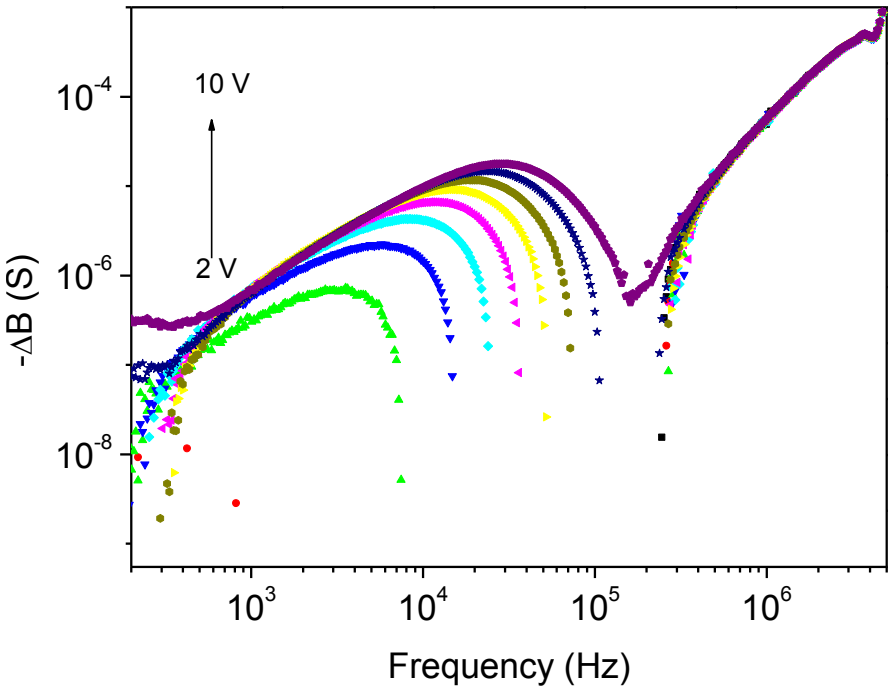

Figure 3. 6. 5. The negative change in susceptance (ΔB) spectra of the device with structure of ITO/PEDOT:PSS/AnE-PV*stat* (450 nm)/Ag (70 nm). The solid arrow is an eye guide to the direction of peak growth with applied bias.

3.6.3. ITO/PEDOT:PSS/AnE-PV*stat*/PEDOT:PSS/Ag

The device structure with ITO/PEDOT:PSS/AnE-PV*stat*/PEDOT:PSS/Ag was prepared by depositing PEDOT:PSS as top electrode interlayer, hopping to form electron blocking contact between LUMO of the polymer and cathode work function. To this purpose, first ethanol was spin-coated onto the polymer layer then PEDOT:PSS (Clevios P VP AI 4083 diluted with 20% of isopropanol) was spray-coated on top of the active layer. After drying, the samples were transferred to the glove box for Ag deposition and electrical characterization.

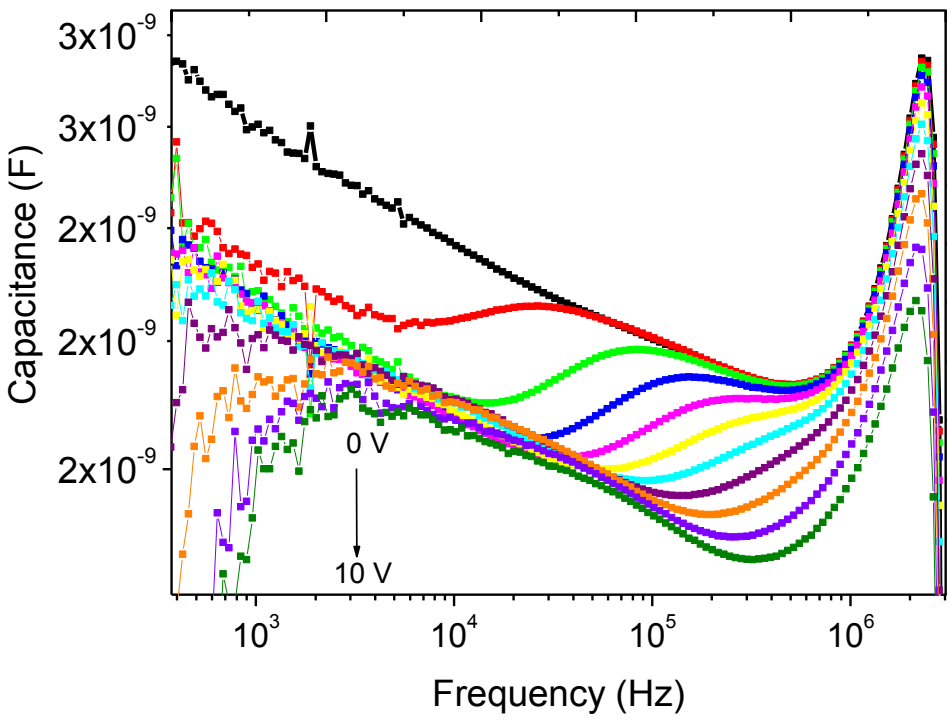

Figure 3. 6. 6. Capacitance spectra of the device with structure ITO/PEDOT:PSS/ AnE-PV*stat*/PEDOT:PSS/Ag. Arrow indicates the direction of peak growth in capacitance with applied bias.

Unexpectedly the device structure could not be an electron blocking any more, rather both hole and electron injecting that was confirmed by the corresponding AS signals.

Double injection was observed in the capacitance spectra (Figure 3.6.6), confirmed by light emission (electroluminescence) observed during the AS measurements at DC bias of more than 4 V.

Two sets of peaks in Figure 3.6.7 were obtained in the negative differential susceptance (-ΔB) spectra. Those set of peaks at lower frequency were reasonably attributed to positive carriers [165]; leading to mobilities of the order of 10^{-5} cm^2 V^{-1} s^{-1}, while higher frequency set of peaks are due to negative carriers, leading to electrons mobilities of 10^{-4} cm^2 V^{-1} s^{-1} [247].

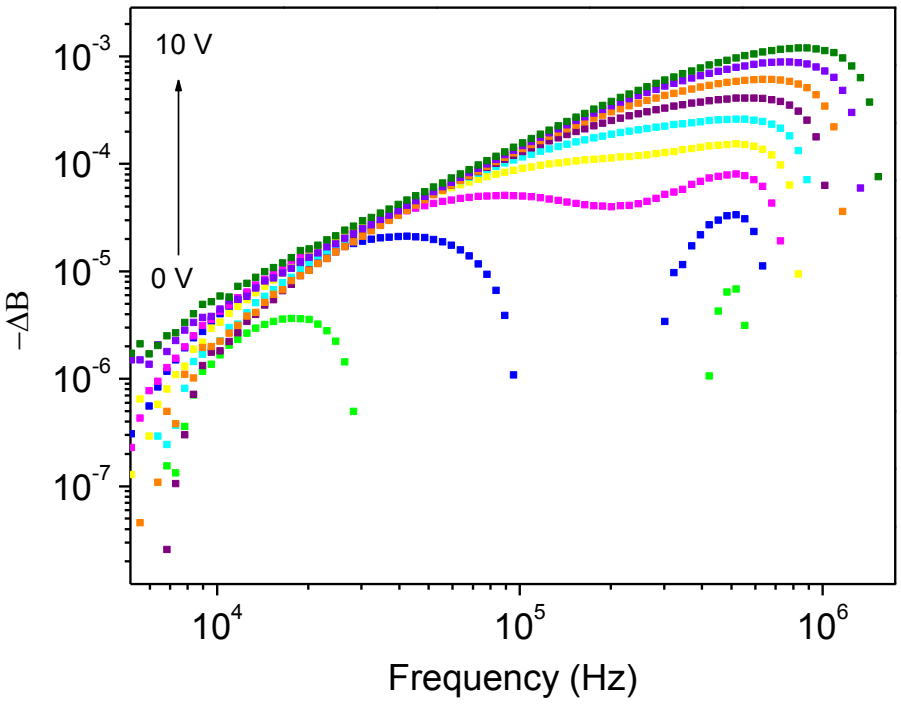

Figure 3. 6. 7. Negative change susceptance spectra of the device with structure ITO/PEDOT:PSS/AnE-PVstat/PEDOT:PSS/Ag. The solid arrow is an eye guide to the direction of peak growth with applied bias.

Because of the hydrophobic character of the underlying conjugated polymer, the quality of the top sprayed PEDOT:PSS layer is often very poor (a typical picture

captured from optical microscope, 560 μm x 460 μm, is shown in Figure 3.6.8) and in these cases double injection can be observed. In this device (ITO/PEDOT:PSS/AnE-PV*stat*/PEDOT:PSS/Ag), the poor quality of top PEDOT:PSS on some parts of polymer film exposed the active layer to the Ag electrode on top, and the resulting device structure may be approximately the same to that of ITO/PEDOT:PSS/AnE-PV*stat*/Ag, with significant amount of negative carriers injection (though the work function of Ag is not so low) occurring on parts of the film where PEDOT:PSS was not present.

Comparing this structure with ITO/PEDOT:PSS/AnE-PV*stat*/Ag, completely different electron injection capability was observed (Figure 3. 6.1 and Figure 3.6.5). In the cases where Al and Ag were used as top electrodes, there were double injections (Figures 3.6.3 and 3.6.5) in these devices. The change in susceptance peak corresponding to electrons transport is more visible in ITO/PEDOT:PSS/AnE-PV*stat*/PEDOT:PSS/Ag than the other devices with Al and Ag as top electrodes. As indicated by Figure 3.6.7, the electron injection efficieny is much higher in ITO/PEDOT:PSS/AnE-PV*stat*/PEDOT:PSS/Ag device than other devices with Al and Ag. One of possible suggestions for the excess double injuction in case of ITO/PEDOT:PSS/AnE-PV*stat*/PEDOT:PSS/Ag device, may be because of ethanol deposited on the top of the polymer film and PEDOT:PSS (containing 20% of isopropanol). The role of isopropanol in PEDOT:PSS solutions is to increase the conductivity of PEDOT:PSS; and improve electron affinity of the polymer film and then fostering the excessive electron injection [248, 249].

The other possible suggestion for the enhancement of electron injection in ITO/PEDOT:PSS/AnE-PVstat/PEDOT:PSS/Ag device is that, the spin-coated ethanol

on the top of photoactive layer causes local dipole rearrangements. The local dipole rearrangmet modifies contact between the polymer and electron injecting (collecting) electrode. In addition, the deposited ethanol on the surface of the active layer plays a role of passivating the surface traps for electrons [250].

A lot of studies have shown that polar solvents such as methanol and ethanol spin-coated onto surface of organic layer improve electron injection through effective modification of the interfaces between organic layer and cathode metal [251, 252] in light emiting diodes (OLED).

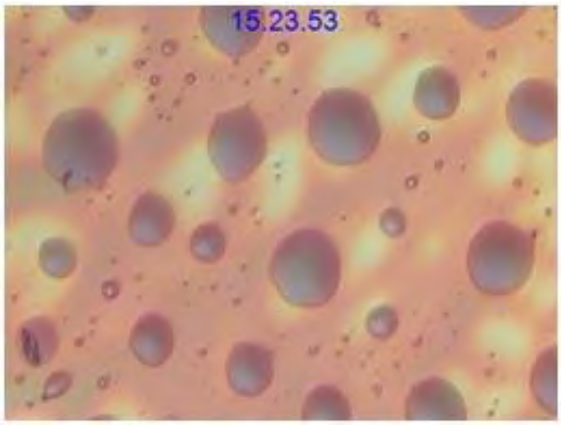

Figure 3. 6. 8. Typical image of the film taken from optical microscope showing non-uniform and poor PEDOT:PSS deposition on the top of AnE-PV*stat* polymer.

It might be because of these justifications, electron injecting efficiency of Ag in ITO/PEDOT:PSS/AnE-PV*stat*/PEDOT:PSS/Ag device is higher than the case of ITO/PEDOT:PSS/AnE-PV*stat*/Ag device.

The devices that we have studied here consist of a single AnE-PV*stat* copolymer layer sandwiched between two electrodes (ITO/PEDOT:PSS and the top electrode). The polymer is spin-coated on top of a patterned indium–tin–oxide (ITO) bottom electrode. HOMO of PEDOT:PSS lies between work function of ITO and HOMO of

the polymer to form ohmic contact and facilitate hole injection from ITO to the polymer; and the contact profile is shown in Figure 3.6.1 [247]. As a result, the hole injection into AnE-PV*stat* from the ITO/PEDOT:PSS contact gives rise to a space charge limited current (SCLC), which enables the determination of the hole mobility [215].

When sufficient voltage is applied to this diode, transport of hole through the polymer films is limited by space charge that accumulates [253] and SCLC is described by,

$$j = \frac{9}{8}\varepsilon_r \varepsilon_o \mu_h \frac{V^2}{L^3} \tag{3.12}$$

where ε_o is the permittivity of free space, ε_r is the dielectric constant of the polymer, μ_h is the hole mobility, V is the voltage drop across the device, and L is the thickness of polymer film sandwitched between the two electrodes. Equation 3.12 holds if the mobility is field independent. But for most conjugated polymers, which are intrinsically disordered, it has been found that the carrier mobility goes as $\mu_h = \mu_{ho} e^{\gamma\sqrt{E}}$, where E is the electric field, μ_{ho} the zero-field mobility, and γ the field dependence prefactor [253, 254].

3.6.4. ITO/PEDOT:PSS/AnE-PV*stat*/Au

The charge injection process may be hindered by the presence of an interface barrier between AnE-PV*stat* and Au. Such interface barriers result in an unbalanced charge carrier injection, which gives rise to an excess of one carrier type over the other and, this phenomena usually decreases the conversion efficiency in OLED device [255].

The capacitance spectra shown in Figure 3.6.9, is indicating single injection. As energy barriers between Au and AnE-PV*stat* is higher (Figure 3.6.1), the injection of

electron from cathode effectively supressed. Absences of illumination from the device while mobility measurement was an evidence for electrons have been blocked in this device setup.

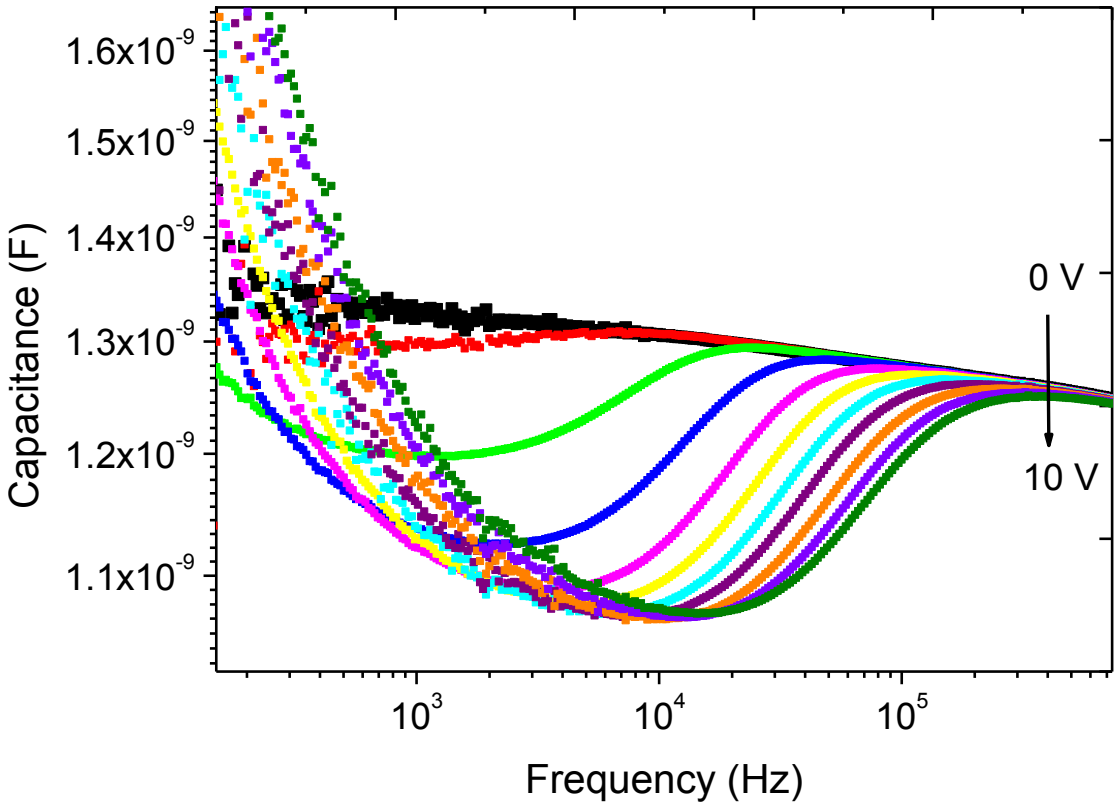

Figure 3. 6. 9. Capacitance spectra as a function of the frequency for device profile of ITO/PEDOT:PSS/AnE-PV*stat*(400 nm)/Au (61 nm), measured at applied voltage ranging from 0 to 10V, with step of 1V.

The well-resolved susceptance peaks (Figure 3.6.10) comfirms blockage of double injection. ΔB peaks for 1 V to 10 V applied DC bias were showing positive field dependent and belong to holes only.

So, the further step in the investigation of polymer AnE-PV*stat* was the realization of hole-only devices, with a top Au electrode. As expected, no double injection was observed, it assures that the low frequency set of peaks in ΔB spectra observed in

devices with Al, Ag and PEDOT:PSS/Ag were corresponding to hole mobility and thos at higher frequency set of peaks belong to electrons mobility.

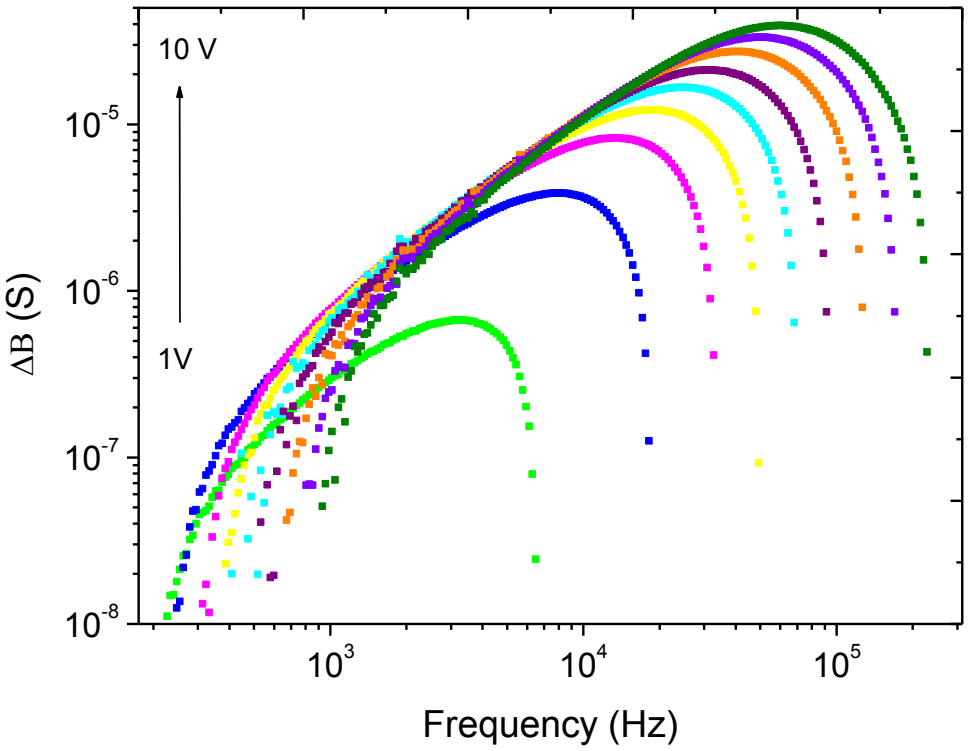

Figure 3. 6. 10. Negative change in susceptance (–ΔB) spectra as a function of the frequency for devices structure of ITO/PEDOT:PSS/AnE-PVstat(400 nm)/Au (61 nm), measured at applied voltage ranging from 1 to 10 V, with step of 1 V.

The hole mobility (μ_h) as a function of the square root of electric field ($E^{1/2}$) are shown by Figure 3.6.11. Mobility follows the well known Poole-Frenkel (PF) law, $\mu = \mu_0 \exp\left(\beta\sqrt{E}\right)$, where μ_0 is the zero-field mobility and β the parameter indicating how strong is the dependence of mobility on E. Figure 3.6.12, presents hole mobility as a function of electric field for devices of ITO/PEDOT:PSS/AnE-PV*stat*/Al (61 nm), ITO/PEDOT:PSS/AnE-PV*stat*/Ag (61 nm), and ITO/PEDOT:PSS/AnE-PV*stat*/Au (61 nm). Hole mobility in all the cases follows PF type behavior, with different strength of field dependence. The hole mobility from

ITO/PEDOT:PSS/AnE-PV*stat*/Au (61 nm) device is higher than that of the others. This may be because of single injection; holes are the only type of charge carries to drift in the device.

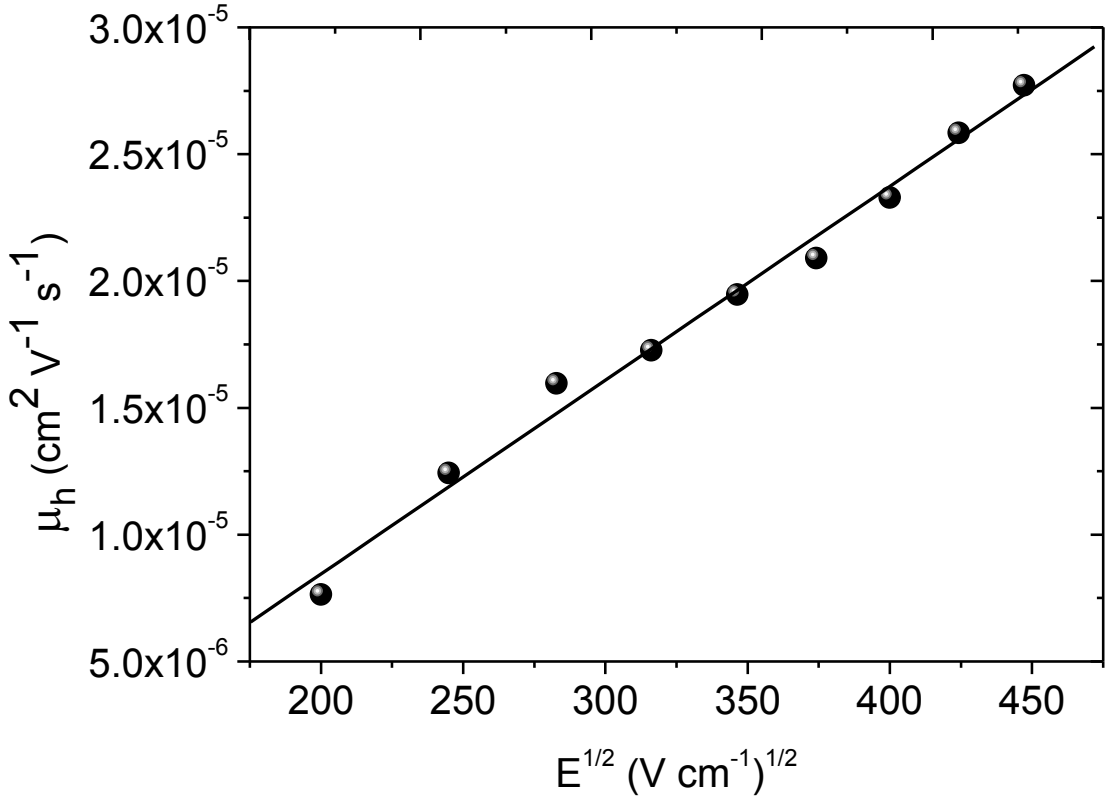

Figure 3. 6. 11. Hole mobility (μ_h) as a function of the square root of field (E) for devices of ITO/PEDOT:PSS/AnE-PV*stat* (400 nm)/Au (61 nm).

Electrons which recombine with the holes were already blocked here. As there was no recombination loss due to injected electrons, most of the injected holes could drift across the sample thickness easily. As the result hole mobility in the device ITO/PEDOT:PSS/AnE-PV*stat*/Au (61 nm) overweighed the holes mobility in the rest of devices. The device with the smallest barrier height for electrons injection, ITO/PEDOT:PSS/AnE-PV*stat*/Al (61 nm) can give a bit higher negative carrier injection than the device of ITO/PEDOT:PSS/AnE-PV*stat*/Ag (61 nm).

The least mobility value in device of ITO/PEDOT:PSS/AnE-PV*stat*/Al (61 nm) is due to much injection of electron, leads to much of annihilation of holes and electrons before they drifted across the sample, which leads to lower hole mobility. Mobility of charge carriers depends also on the concentration of the carriers.

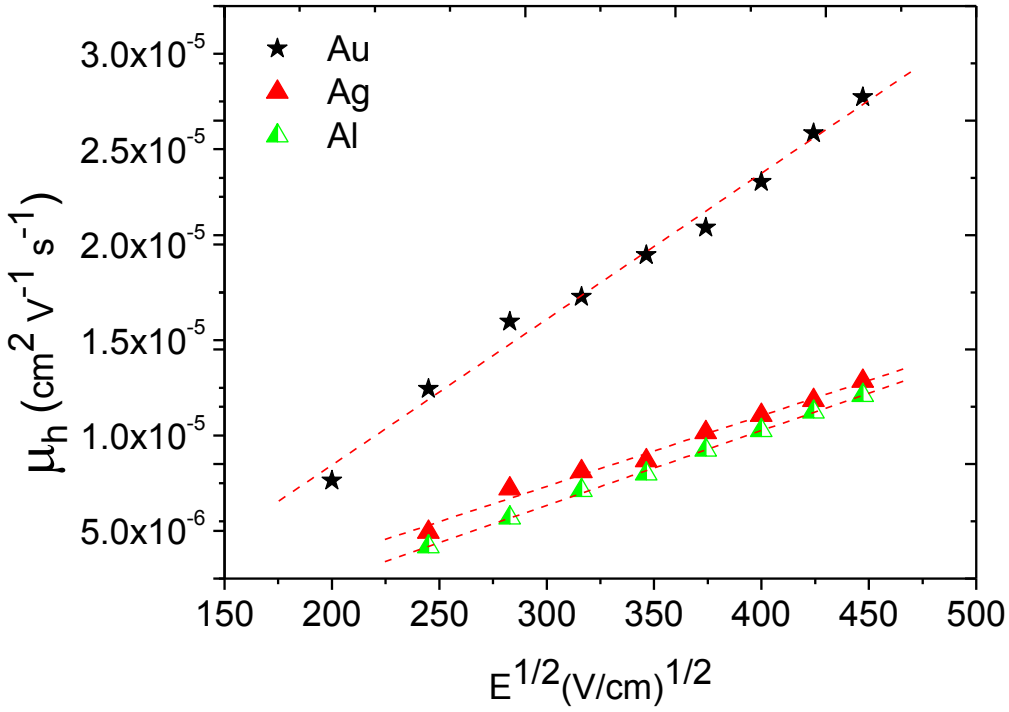

Figure 3. 6. 12. Logarism of field dependent hole mobility as function of square root of electric field for devices of ITO/PEDOT:PSS/AnE-PVstat/cathode. Here cathodes are Al, Ag, and Au.

3.6.5. Conclusions

Lower set of frequency peaks (hole peaks) in conductance, capacitance and negative change in susceptance peaks are clearly observed even at lower applied DC potential, higher frequency AS peaks (for electrons) are not clearly seen and unresolved except in the device that used PEDOT:PSS/Ag as top electrode.

The electron injection efficiency to LUMO of AnE-PV*stat* copolymer decreases upon changing cathode of the device from Al, through Ag and PEDOT:PSS/Ag to Au. When Au (metal with bigger barrier height for electron injection) is used as cathode, injection of electrons were completely prevented, the resulted device got the hole-only behavior.

3.7. Effect of solvent additives and double donor on the photovoltaic performance of PDTSTTz:PCBM Bulk Heterojunction (BHJ) solar cells

In this work, we investigated the effect of solvent additives, such as iodomethane (IMe), iodoethane (IEt), iodobuthane (IBu) and diiodomethane (DIMe) on the performance of BHJ solar cells prepared from the low bandgap conjugated polymer (PDTSTTz) and PCBM blend. The structure of the low bandgap donor polymer PDTSTTz is depicted in Figure 2.2.

One of the criteria for processing solvent additives is selective solubility of either fullerene or donor component, to control the morphology of bulk heterojunction (BHJ) materials used in the solar cells [255 - 257]. However, most iodine containing solvent additives dissolve fullerene (PCBM) more preferably than donor polymer [258]. A possible explanation for this phenomenon is that in the iodine containing solvent additives, the iodine atom bears a partial negative charge and PCBM is electro-deficient [258]. The strong interaction that exists between the iodine containing solvent additives and PCBM enhances solubility of PCBM [255 - 259]. Furthermore, the effect of addition of P3HT (as a secondary or additional donor) into PDTSTTz:PCBM blend system on the photovoltaic performance of the resulting solar cells was also investigated in this work.

3.7.1. Effect of solvent additives on the photovoltaic performance of PDTSTTz:PCBM BHJ solar cells

The absorption spectra of PDTSTTz:PCBM (1:1) films in the presence of the short chain iodoalkane and di-iodoalkane solvent additives were measured. In order to compare photovoltaic performances of solar cells processed from different solvent additives, all solar cell fabrication conditions (concentrations and spin-coating speeds) were kept the same.

The concept of incorporation of the solvent additives in to the host solvent is well capable of controlling the morphology of films of BHJ solar cells [260]. In the case of low boiling point solvent additives in this study such as IMe, IEt, IBu and DIMe, morphology of the blend is affected through selective solubility of one of the components in the blend (either donor or acceptor) [256, 257, 260].

In order to get insight of selective solubility between donor and acceptor with solvent additives, films of donor (PDTSTTz) and PDTSTTz:PCBM blends were prepared in DCB and deposited using spin-coating with spin-coating speed of 800 rpm for one minute. After drying, film of PDTSTTz:PCBM blend was soaked in IEt solvent additive for 3 seconds, and UV-Vis absorption of the films were measured before and after the soaking. To minimize solvent consumption, this test was done in IEt that have intermediate physical properties (solubilizing effect and dielectric constant) between IMe and IBu.

Figure 3.7.1 shows the UV- Visible absorption spectrum of PDTSTTz:PCBM films before soaking in to the solvent additives (shaded circle), after soaking in IEt (square), and absorption spectrum of a pristine PDTSTTz film (triangle).

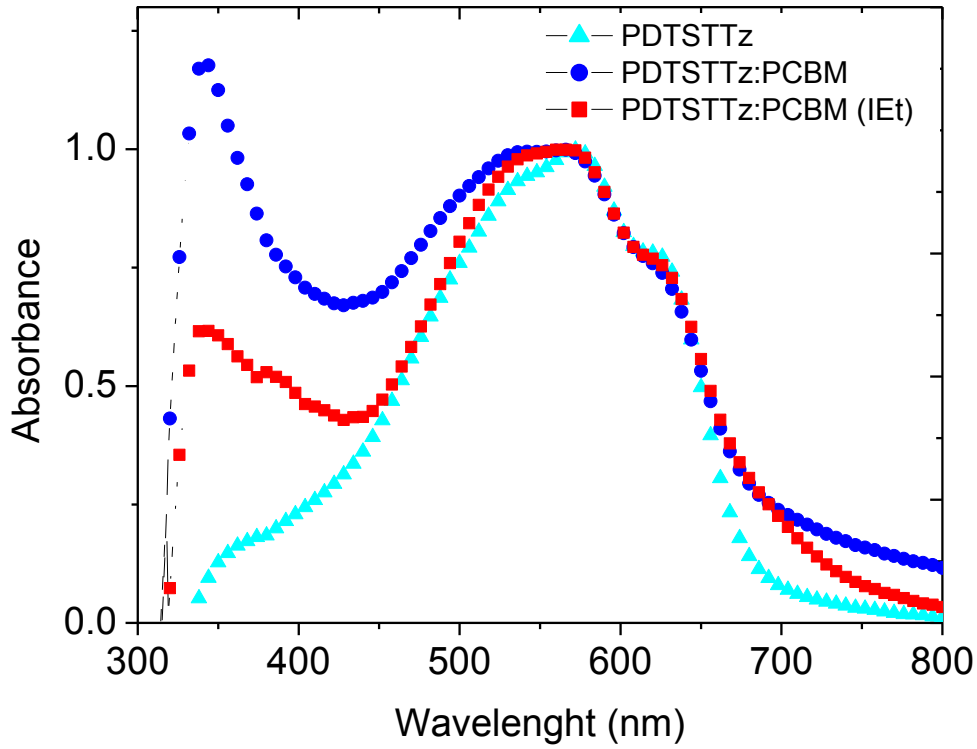

Figure 3. 7. 1. UV visible absorption spectra of PDTSTTz:PCBM films before soaking in solvent additives (shaded circle); after soaking in IEt (square), and the absorption spectrum of pristine PDTSTTz film (triangle).

Figure 3.7.1 demonstrated that there is difference in selective solubility of these iodoalkane solvent additives between PCBM and PDTSTTz in DCB. The fullerene is selectively dissolved in IEt solvent additive compared to the PDTSTTz. Consequently, three separate phases are expected to form during the process of liquid-liquid phase separation: a fullerene-iodoalkane phase, a polymer aggregate phase, and a polymer-fullerene phase [260]. In this case, the reason for the formation of phase separation between donor (PDTSTTz) and acceptor (PCBM) following incorporation of these iodoalkane solvent additives is selective solubility between PDTSTTz and PCBM. The effect has been proven by dipping the film in the IEt solvent; and observed removal of fullerene from the film of the blend of PDTSTTz:PCBM

(comparing absorption of PCBM before and after soaking at lower wavelength region, and absorption of PDTSTTz at ~ 560 nm).

Depicted in Figure 3.7.2, is the UV-Visible absorption spectra of PDTSTTz:PCBM films processed in dichlorobenzene (DCB) without and with 2.5% (v/v) of each of the solvent additives (IMe, IEt, IBu and DIMe). The absorption maximum generally shifted to the longer wavelength in the presence of additives. This might be attributed to the dissolution of PCBM aggregates that will segregate and redistribute throughout the polymer chain thereby improving their crystalline order.

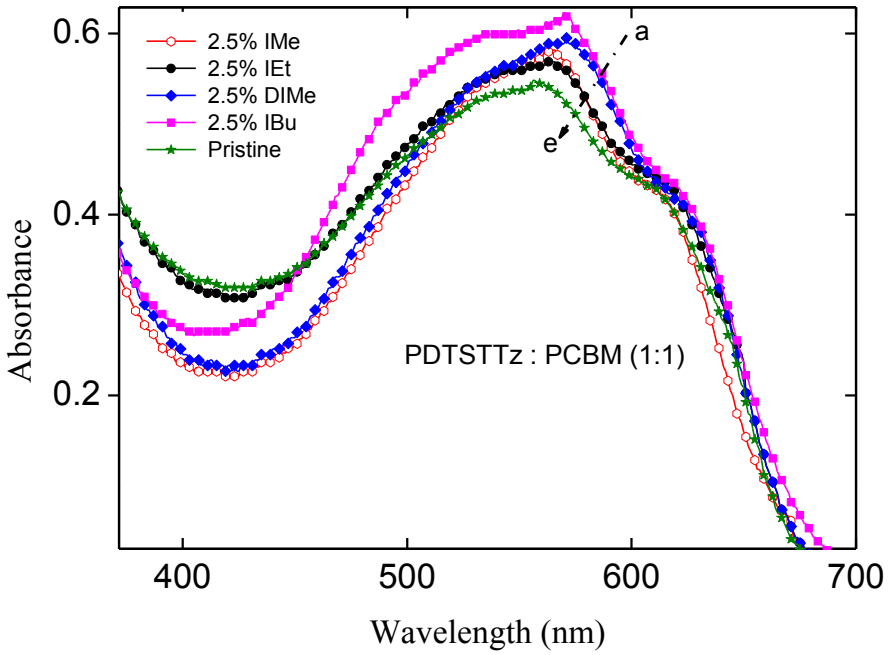

Figure 3. 7. 2. Absorption spectra of PDTSTTz:PCBM thin films spin coated on transparent glass slides at 800 rpm processed from 10 mg/mL of pure DCB, and DCB containing 2.5% (v/v) of each of the solvent additives; a) IBu, b) DIMe, c) IMe, d) IEt, and e) Pristine.

Also, the segregation of the relatively well dissolved PCBM molecules may cause twisted polymer chains to be aligned (stretched). This increases the effective

conjugation length with an ultimate lowering of bandgap and hence red-shift in absorption.

Solubility effect of additive to PCBM increases with increasing alkyl chain length of solvent additive. One rule of thumb is that long chain solvent additives are better than short chain ones in solubilising effect [261]. The observed significant red-shift in absorption spectra for the film processed from IBu than in films prepared from the other additives and pristine may indicate increase in crystallinity and order of the films of PDTSTTz:PCBM with increasing carbon chains of the additives (from IMe to IBu).

The J–V characteristics of all the solar cell devices were measured under 100 mW/cm^2 white light illumination in air. The J–V plots of all devices concerning solvent additives are depicted in Figure 3.7.3. The calculated values of the solar cell parameters are summarized in Table 3.7.1. As shown from the J-V curves, a significant increase in J_{sc} is clearly observed from 2.35 mA/cm^2 (with IMe) to 6.13 mA/cm^2 (with IBu), and the corresponding power conversion efficiency (PCE) of the cells were also increases from 0.51% to 2.02%.

The fill factor (FF) also increased from 0.32 (IMe) to 0.47 (IBu). In the case of solvent additive, the improvement in PCE is contributed not only from short circuit current, but also from the fill factor which could be raised from improved morphology and PDTSTTz crystallinity in the blend [262, 263]. Due to better and optimum nanoscale phase separation between PDTSTTz and PCBM, the device performance in the case of IBu is better than the case of the rest of additives.

The PCE of the reference (0.39%) is lower than reported value (3.5%) on PDTSTTz:PCBM based solar cells [264]. This difference might be because of the fact

that PDTSTTz:PCBM weight ratio was 1:1.5 and the film thickness was more than 400 nm in reported work [264]. Increasing proportion of PCBM in donor-acceptor blend mainly enhances FF, and slightly J_{sc}, and hence the PCE of the resulting solar cells [43, 265].

The observed increase in fill factor from 0.32 (in solar cells with IMe) to 0.47 (in solar cells with IBu) indicates the improvement in charge carriers‟ mobility in solar cells containing IBu. Strong relationship of fill factor of solar cell with charge carriers‟ mobility was reported in one of our papers [186] and in some others [266].

The observed red-shifted in absorption spectra, depicted in Figure 3.7.2, is probably due to better organization and crystallinity of the PDTSTTz film with the additives (from IMe to IBu). This means the polymer is enabled to collect low energy photons; and also improved morphology with IBu facilitated carrier mobility which in turn, might have led to enhanced J_{sc}.

This effect is further confirmed by the red-shift in IPCE spectra for devices with IBu than the other devices with the rest of solvent additives (IMe, IEt, and DiMe) as indicated by Figure 3.7.4.

Besides, more interestingly, in DIMe processed device, having J_{sc} of 4.90 mA/cm^2 and a FF of 0.48, led to a second highest overall PCE of 1.6%. This highly improved PCE of cell with DIMe compared to the device with IMe, might be due to the presence of extra polarizable iodine atom in DIMe that creates strong interaction to solublize PCBM aggregates and its high boiling point (slow drying effect) than IMe, that ultimately led to enhanced crystallinity of PDTSTTz chains.

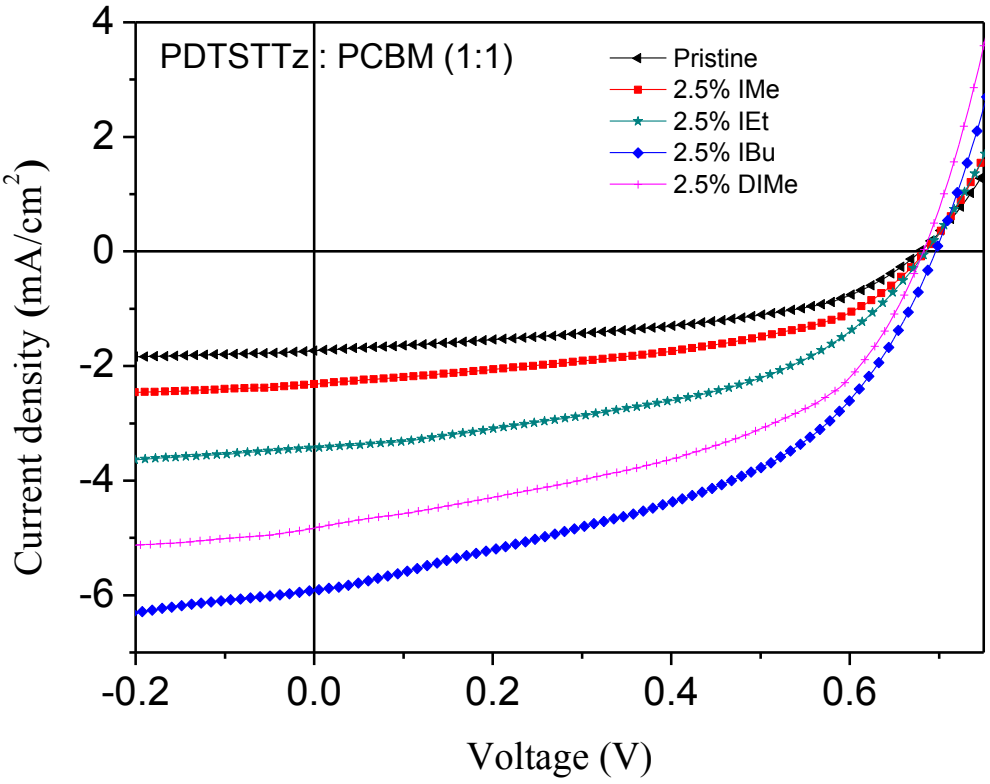

Figure 3. 7. 3. J-V curve of ITO/PEDOT:PSS/PDTSTTz:PCBM/Al (~97 nm) solar cells processed in pure DCB, and DCB containing 2.5% (v/v) of solvent additives under 100 mW/cm^2 white light illumination. The concentration of solution was 10 mg/mL, spin coated at 800 rpm.

Here, we obtained a PCE of 2.02% for PDTSTTz/PCBM solar cells, which is lower than the reported value of 5.59% of solar cell from PDTSTTz/$PC_{70}BM$ system, and of course with optimum thermal annealing treatment [267].

The higher hole mobility (3.56 x 10^{-3} $cm^2V^{-1}s^{-1}$) of PDTSTTz measured in space charge limited current (SCLC) method was contributed for larger J_{sc} (11.9 mA/cm^2) and FF (61%) of PDTSTTz: $PC_{70}BM$ solar cell [267].

Here in this work we used PCBM as an acceptor not $PC_{70}BM$ (that have a better photon absorbing property than PCBM). This lower efficiency associated with our

reference cells might be because of the preparations and characterization steps were done in an open air that leads to lower efficiency.

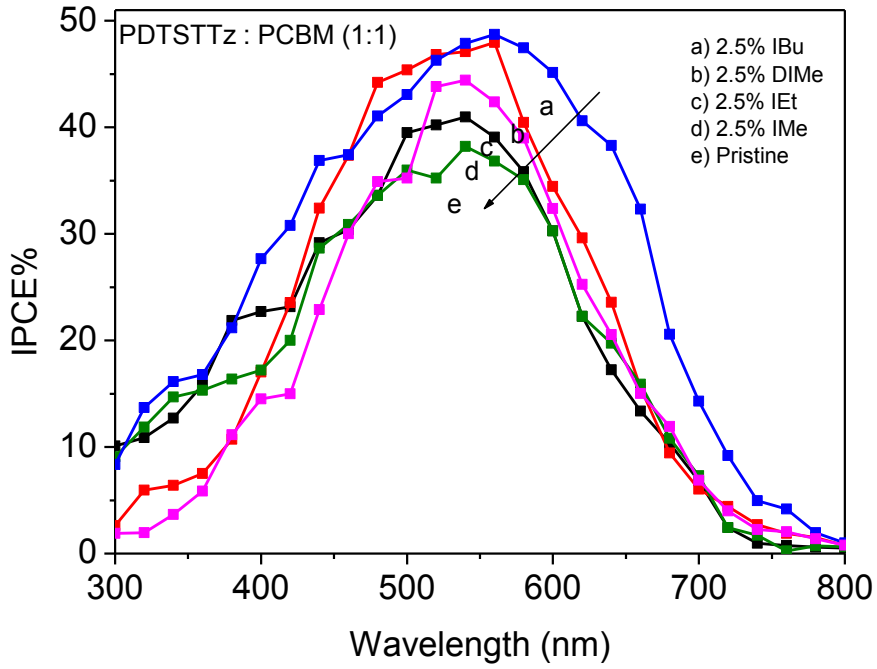

Figure 3. 7. 4. Incident photon-to-current conversion efficiency (IPCE) of ITO/ PEDOT:PSS/PDTSTTz:PCBM/Al (~97 nm) solar cells processed in pure DCB, and DCB containing 2.5% (v/v) of solvent additives. The concentration of solution was 10 mg/mL, and spin coated with 800 rpm.

Nevertheless, our results could adequately explain the effect of solvent additives on the PV parameters. The strong dependence of the absorption, the morphology and the performance of the resulting solar cells on solvent additives with different length of alkyl chains implies that chain length of these processing additives could influence the physical interactions between the polymer chains and/or between the polymer and fullerene acceptor [262].

However, the V_{oc} did not essentially changed with these additives, which might be due to the balanced effect of enhanced order that causes a slight decrease in V_{oc}, and

of the improved phase separated morphology that has a positive effect on V_{oc}. Then, it can be said that iodoalkane solvent additives provide an improvement in J_{sc}, FF, and hence the overall solar cell performance (with no essential change in V_{oc}), through efficient light harvesting following improved crystallinity of PDTSTTz, enhanced charge transport, and improved morphology. A five-fold PCE increase was observed for IBu (see Table 3.7.1) compared to the pristine device. Photocurrent generation improvements following processing solvent additives on to PDTSTTz:PCBM blends of PV cell was further confirmed by the EQE which is given in Figure 3.7.4.

Table 3. 7. 1. Summary of solvent additive effects on the photovoltaic parameters such as J_{sc}, V_{oc}, FF and PCE% of PDTSTTz:PCBM BHJ solar cells with and without additives (pristine).

Sample	J_{sc} (mA/cm^2)	V_{oc} (V)	FF	PCE%
Pristine	1.76	0.67	0.33	0.39
2.5% IMe	2.35	0.68	0.32	0.51
2.5% IEt	3.63	0.68	0.38	0.94
2.5% IBu	6.13	0.70	0.47	2.02
2.5% DIMe	4.90	0.68	0.48	1.60

Devices showed enhanced incident photon-to-current conversion efficiency (IPCE) in the longer wavelength region in the presence of solvent additives than the pristine devices (with no additives) with a significant effect in DIMe and IBu. Some devices exhibited a relatively low IPCE value eventhough they have good absorption at longer wavelengths, which may be due to the limited charge transport [268, 269].

3.7.2. Effect of Double donor on the photovoltaic performance of PDTSTTz:PCBM

The effect of secondary donor addition on the photovoltaic parameters of the resulting solar cell was investigated after the introduction of different proportions of P3HT into a PDTSTTz/PCBM system. The UV-Vis spectra (shown in Figure 3.7.5) of the respective binary of P3HT/PCBM and PDTSTTz/PCBM, and energy levels of these donor polymers (shown in Figure 3.7.6) gave a clue to extend our investigation using secondary donor addition. PDTSTTz has a broad absorption band predominantly between 500 and 700 nm, whereas P3HT absorbs at relatively shorter wavelengths than the former, between 400 and 600 nm.

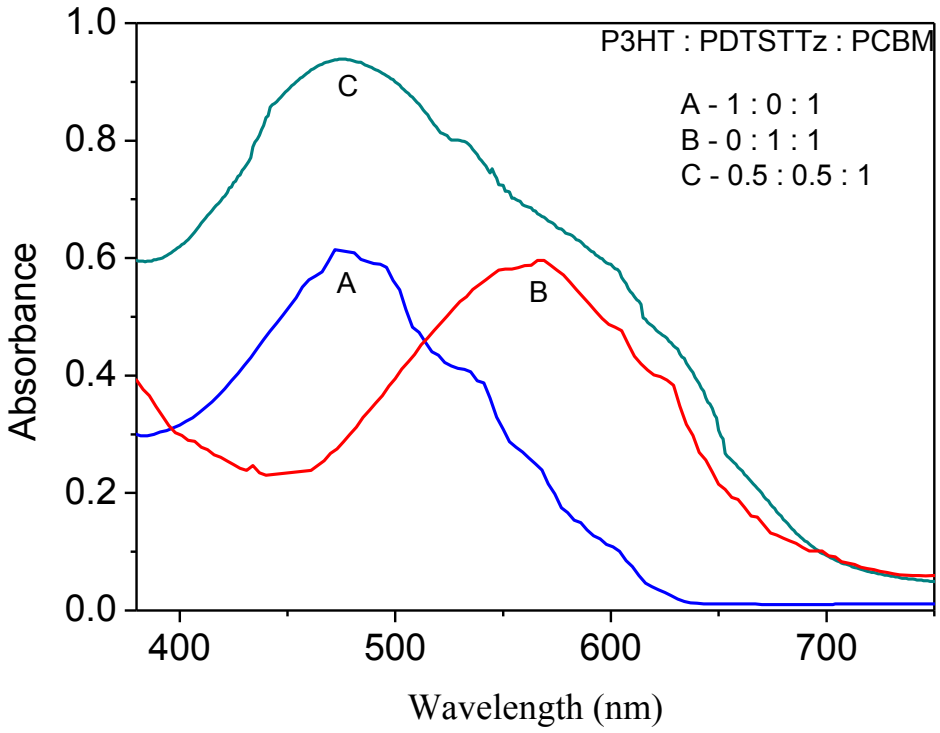

Figure 3. 7. 5. UV-Vis absorption spectra of P3HT/PCBM, PDTSTTz/PCBM and P3HT/PDTSTTz/PCBM films spin coated on a transparent glass slides from 10 mg/mL solution in pure DCB with 800 rpm.

The addition of P3HT into PDTSTTz/PCBM system was based on the expectation of two possible advantages: (i) to cover the absorption hollow, thus both thermalization and transmission loses can greatly be minimized, (ii) the compatibility with the HOMO/LUMO levels of PDTSTTz and of hole transporting layer, PEDOT:PSS, may improve hole extraction. The UV-Vis spectra indicated in Figure 3.7.5 has clearly shown that the addition of P3HT resulted in the broadening of absorption range of wavelength. This is due to the combining effect of the two polymers that contribute to increase the absorption coverage (area).

Then the best performing P3HT/PDTSTTz composition was optimized for the same PCBM level in the P3HT/PDTSTTz/PCBM blend as is explained below. Among the four iodoalkane solvent additives, IBu showed best performance than others, thus IBu was chosen as best additive to be used in ternary blend system.

For the ternary system, photovoltaic devices containing P3HT/PDTSTTz/PCBM blends with device configuration of ITO/PEDOT:PSS/P3HT:PDTSTTz:PCBM/Al (~97 nm) were fabricated in air. In order to compare the device parameters, the concentrations of all polymer/fullerene solutions were kept constant (10 mg/mL), and spin coated with 800 rpm.

Furthermore, in all cases the overall polymer:fullerene weight ratio was maintained at 1:1. In principle, the addition of the third component and its proportion to a binary system could affect the film morphology. Therefore, it is important to control the ratios of components in the active layer [270]. Accordingly, compositions of 25%, 50% and 75% (w/w) of P3HT with respect to PDTSTTz were introduced to form a blend of P3HT/PDTSTTz/PCBM solution in dichlorobenzene in the presence of 2.5% IBu as a phase separating agent.

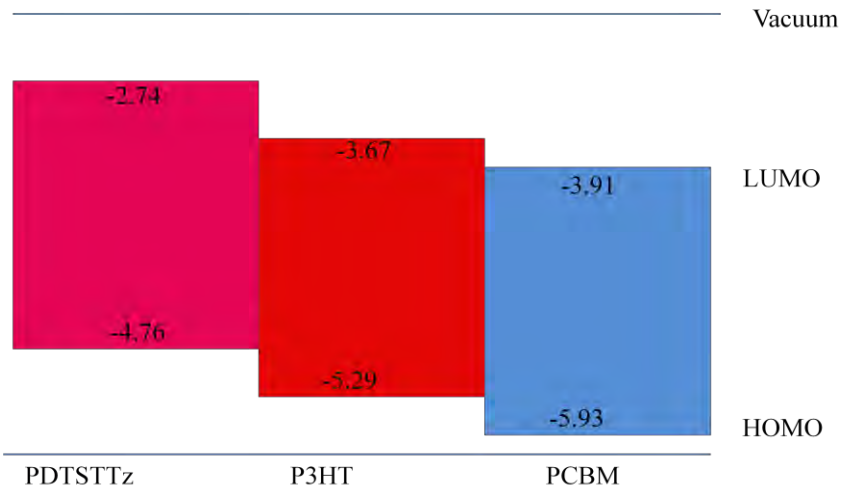

Figure 3. 7. 6. Relative HOMO/LUMO energy levels of P3HT, PDTSTTz and PCBM in eV.

From the data in Table 3.7.2 and Figure 3.7.6, it should be noted that although the HOMO energy level of PDTSTTz is lower by 0.55 eV than that of P3HT, the V_{oc} of the solar cells based on PDTSTTz:PCBM is only 0.20 V higher than that of the P3HT:PCBM based device. The V_{oc} value of the cells based on PDTSTTz:PCBM is lower than the of expected value from the lower HOMO energy level of PDTSTTz and LUMO level of PCBM, which could be limited by a relatively higher carrier recombination rate at the polymer–fullerene interface [268].

The J-V curves are depicted in Figure 3.7.7. The resulting photovoltaic parameters of P3HT:PDTSTTz:PCBM blend cells such as J_{sc}, V_{oc}, and FF, are listed in Table 3.7.2. Combining P3HT, PDTSTTz, and PCBM (forming a ternary blend) could lead to higher J_{sc} in all ternary blends than for either limiting PDTSTTz:PCBM binary blend (J_{sc} = 6.13 mA/cm^2, V_{oc} = 0.7 V, FF = 0.47 and PCE = 2.02%); and the P3HT:PCBM binary blend (J_{sc} = 7.01 mA/cm^2, V_{oc} = 0.5 V, FF = 0.45 and PCE = 1.6%). In ternary system V_{oc} was observed increasing with the increasing proportion

of PDTSTTz in cell, as V_{oc} of PDTSTTz: PCBM system was higher than that of P3HT:PCBM system. The smaller increment in V_{oc} shown in Table 3.7.2 for the ternary system in presence of IBu (from 0.55V to 0.56V) might be due to lower recombination loss following the film morphology improvement with the additive [268].

The increased J_{sc} was attributed to the wide range of photon absorption by the two donors (as has been demonstrated in Figure 3.7.5). The effect of IBu additive on the spectrum of ternary blend is indicated by Figure 3.7.8. The significant red shifts at absorption maximum in the ternary blend film (indicated by solid line) with IBu compared to the one without IBu (indicated by line and symbol) is due to improved crystallinity of the film with the additive [260, 271]. As indicated in Figure 3.7.9, J-V of the cell from optimized composition of the ternary blend gave higher J_{sc} with 2.5% IBu than the one without IBu. This is possibly because IBu helped better organization of polymer chains in the film. The corresponding J-V plot for the relative comparison of binary and ternary systems is given in Figure 3.7.10. A significant increase in J_{sc} (11.08 mA/cm^2) could couple with an intermediate V_{oc} of 0.56 V and FF of 0.39 to give an efficiency of 2.42%. As indicated in Table 3.7.2, the FFs of the ternary blend solar cells were lower than that of binary ones.

This loss in FF is due to increased series resistance in the ternary cells following formation of multiple junctions or interfaces among P3HT, PDTSTTz and PCBM which increase recombination and reduces carriers‟ collection efficiency in the cell [271].

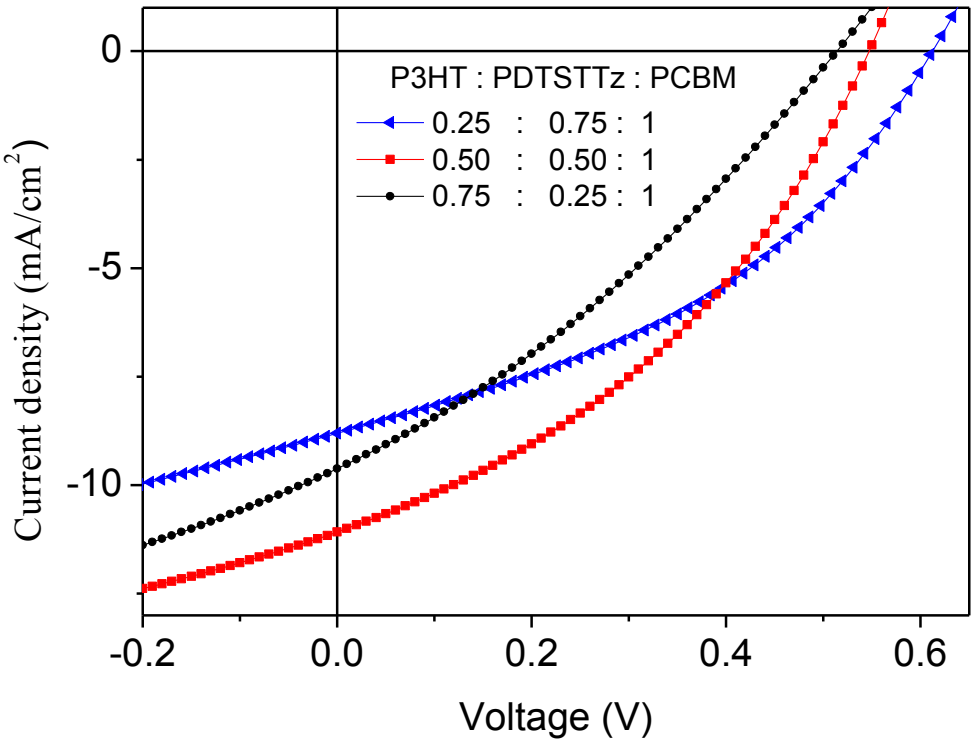

Figure 3. 7. 7. J-V plots for ITO/PEDOT:PSS/P3HT/PDTSTTz/PCBM/Al (97 nm) BHJ solar cell devices with different P3HT/PDTSTTz composition processed from 10 mg/mL solution of DCB containing 2.5% IBu, and with spin-coated speed of 800 rpm.

The enhancement of J_{sc} in the ternary system is obtained in expense of sacrification of FF. The ternary blend could thus give a higher efficiency than either limiting binary blend as a result of the higher attainable product of J_{sc} and V_{oc}.

Analogously, a similar observation has been achieved also for the pristine (without additive) and the results are listed in Table 3.7.2. The processing additives still have the potential to improve the morphology of ternary systems (as can be noted from Figure 3.7.9 and Table 3.7.2).

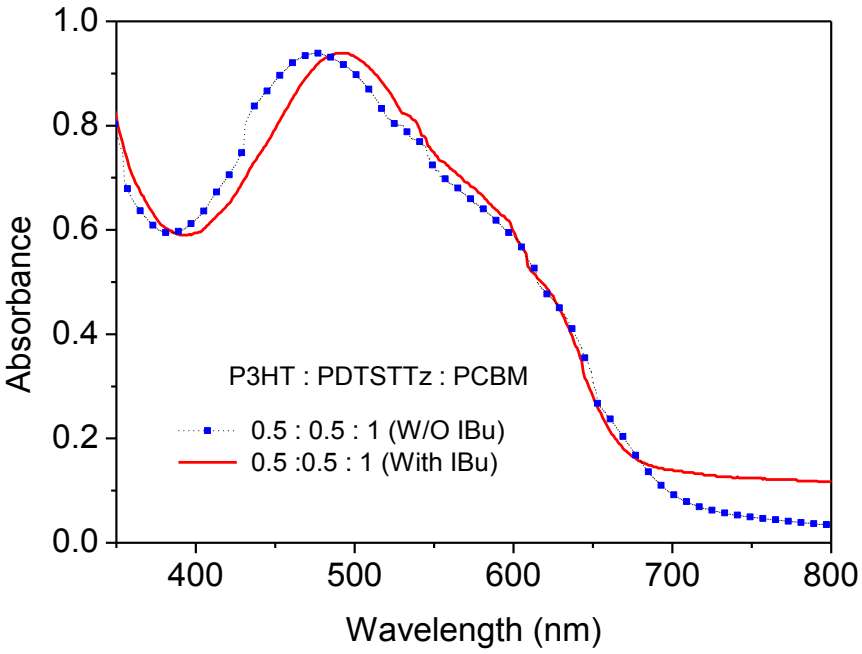

Figure 3. 7. 8. UV-Vis spectra of the P3HT/PDTSTTz/PCBM (0.5:0.5:1) thin films spin coated on glass slides from solution of 10 mg/mL in DCB with and without IBu, and spin coated with 800 rpm.

Thus, as described earlier, the best performing cell consisted of P3HT/PDTSTTz-/PCBM (0.5:0.5:1) could give better performance with maximum J_{sc} of 11.08 mA/cm^2 and compromised V_{oc} of 0.56 V, and then better efficiency of 2.42%, surpassing that of the corresponding binary cells based on P3HT/PCBM (PCE = 1.6%) or PDTSTTz/PCBM (PCE = 2.02%).

The increase in PCE in the ternary solar cells is by 19.8% with respect to PDTSTTz/PCBM and by 51.3% with respect to P3HT/PCBM binary devices. Figure 3.7.11 (a - c) depicts the J_{sc}, V_{oc} and PCE variations with proportions of P3HT in P3HT/PDTSTTz/PCBM system for the same amount of PCBM in the blend. Several significant observations can also be made from the data in Table 3.7.2.

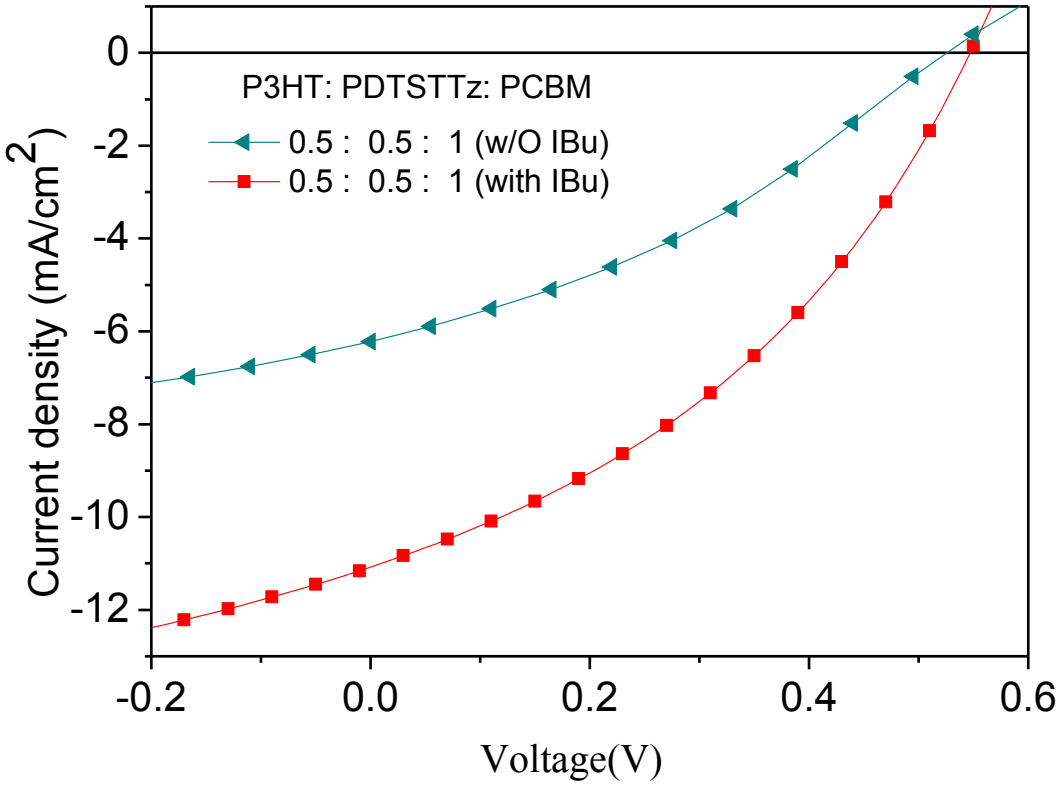

Figure 3. 7. 9. J-V plots for ITO/PEDOT:PSS/P3HT/PDTSTTz/PCBM/Al (~97 nm) (0.5:0.5:1) devices, prepared from 10 mg/mL of solution in DCB with and without IBu spin coated with 800 rpm.

Importantly, as is also illustrated in Figure 3.7.11 (b), V_{oc} values of the two-donor system showed a gradual decrease from 0.70 to 0.50 V following the increase in the proportion of P3HT in the ternary blend. The slight decrease in V_{oc} can be assigned to the effect of band bending due to disorder in the three-component system. Vacuum level alignment with flat bands away from the interface is found when the interface hole barrier is larger (≥ 0.6 eV) [272]. Thus, band bending away from the Fermi level occurs when the hole barrier is smaller than this value. Following the addition of P3HT, which is in ohmic contact with the Fermi level of the ITO with barrier (energy

level difference) of ~ 0.06 eV, interface charges will be injected and excess charge accumulate on the polymer.

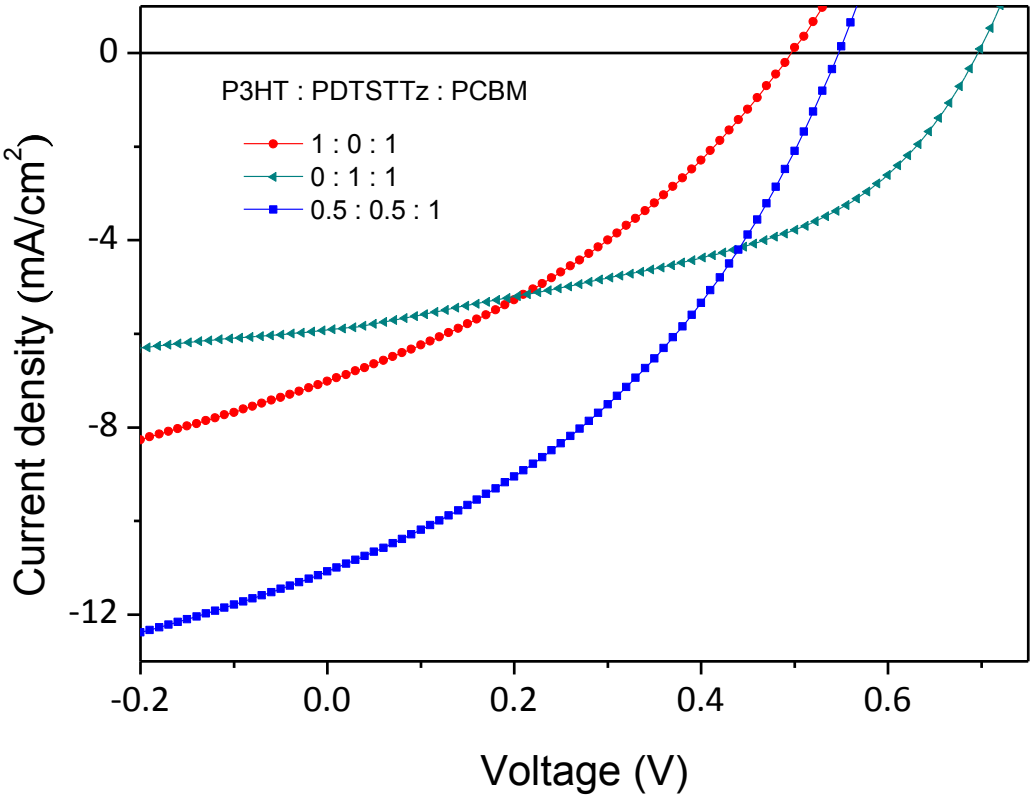

Figure 3. 7. 10. J-V plots of ITO/PEDOT:PSS/P3HT:PDTSTTz:PCBM/Al (~97 nm) (0.5:0.5:1) devices with the corresponding binary ones; all processed from 10 mg/mL of solution in DCB solution containing 2.5% IBu; spin coated with 800 rpm.

Besides, the FF almost remains constant for P3HT/PDTSTTz/PCBM based devices (with all proportions of P3HT added to the ternary system) which might be an evidence for the existence of balanced charge carrier transport. This concept supports our prediction that with this balanced free charge transport; band bending might be one factor for V_{oc} variation. The resulting field shifts the polymer levels to limit charge penetration in the bulk of the film thereby to reduce the V_{oc} [102, 154, 272, 273]. The V_{oc} attained minimum value (0.50 V) for pure P3HT/PCBM (greater band

bending) and maximum value (0.70) for pure PDTSTTz/PCBM with barrier ~ 0.6 eV (little band bending).

Table 3. 7. 2. Summary of the solar cell device performance and corresponding PV parameters for ITO/PEDOT:PSS/P3HT:PDTSTTz:PCBM/Al (~97 nm) films containing different composition of P3HT and PDTSTTz processed from 10 mg/mL in DCB with 2.5% IBu as a phase separating additive under 100 mW/cm^2 white light illumination.

P3HT :PDTSTTz: PCBM	J_{sc} (mA/cm^2)	V_{oc} (V)	FF	PCE%
1 : 0 : 1	7.01, 3.43*	0.50, 0.50*	0.45, 0.32*	1.60, 0.57*
0.75 : 0.25 : 1	9.21	0.51	0.37	1.74
0.50 : 0.50 : 1	11.08, 6.22*	0.56, 0.55*	0.39, 0.33*	2.42, 1.13*
0.25 : 0.75 : 1	8.94	0.62	0.39	2.16
0 : 1 : 1	6.13, 1.76*	0.70, 0.67*	0.47, 0.33*	2.02, 0.39*

* Pristine (without processing additive).

Another way of explaining the V_{oc} variation can be in terms of the relative positions of HOMO levels of P3HT and PDTSTTz. PDTSTTz has low lying HOMO level where as P3HT has shallow HOMO level.

Hence, maximum V_{oc} is determined by the HOMO of PDTSTTz and minimum V_{oc} by the HOMO of P3HT. Thus, with increasing the amount of P3HT in P3HT:PDTSTTz, the V_{oc} decreases up to the minimum value that corresponds to the pure P3HT.

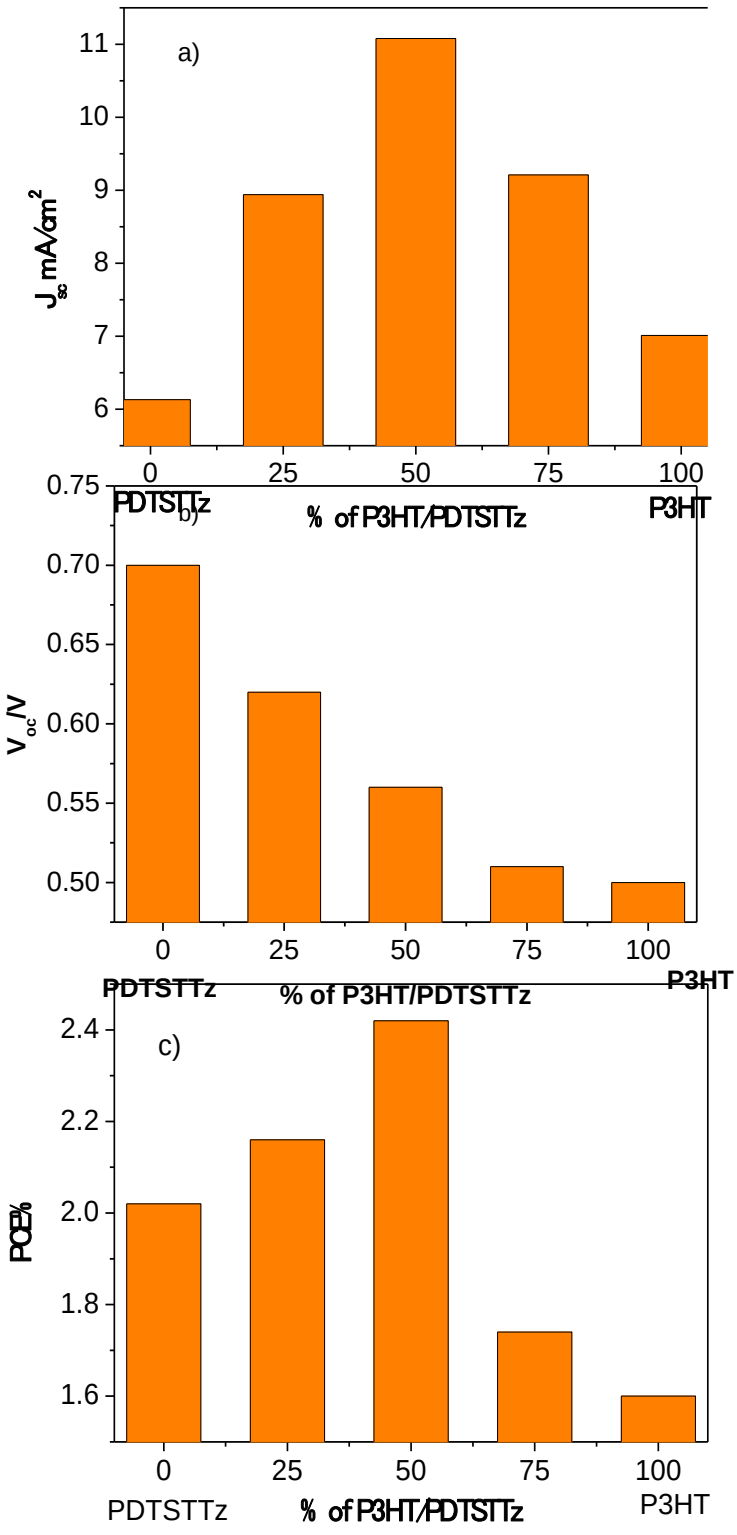

Figure 3. 7. 11. a) $J_{sc,}$ b) $V_{oc,}$ and c) PCE%; as a function of the relative composition of P3HT/PDTSTTz in the blend of PDTSTTz:PCBM BHJ solar cells.

Finally, it is important to note that the J_{sc} seems to govern the $J_{sc}V_{oc}$ product (see Table 3.7.2 and Figure 3.7.11(a-b) and hence the PCE regardless of the V_{oc} change. Thus, J_{sc} improvement is critical for essential improvement in PCE of solar cell devices.

3.7.3. Conclusions

To conclude, enhancing the J_{sc} of polymer solar cells through controlling the morphology by means of solvent additives has been realized. Applying short-chain iodoalkanes and diiodoalkane solvent additives to PDTSTTz/PCBM has been found to be effective in improving the morphology, which affects the J_{sc}, and FF. Performance improving effects of these short-chain solvent additives on solar cells, was observed increasing with increasing the length of carbon chains of the additives. Furthermore, by incorporating P3HT as secondary donor into PDTSTTz/PCBM blend system, the resulting ternary blend solar cells exhibited a higher PCE (2.42%) than the solar cells of binary (for PDTSTTz:PCBM, PCE = 2.0 % and for P3HT:PCB, PCE = 1.6%). The improved PCE in the case of ternary system was mainly contributed from enhancement in J_{sc} (up to 11.08 mA/cm^2) which is due the combined light harvesting effects of the two donors. Regarding further improvement in efficiency, there is still much capacity for increasing the J_{sc} and FF by using strong processing additive to control the morphology.

4. References

1. C. K. Chiang, C. R. Fincher, Y. W. Park, A. J. Heeger, H. Shirakawa, E. J. Louis, S. C. Gau, A. G. MacDiarmid, *Phys. Rev. Lett. 39* (**1977**) 1098.
2. M. S. Alsalhi, J. Alam, L. A. Dass, M. Raja, *Int. J. Mol. Sci. 12* (**2011**) 2036.
3. J. L. Bredas, R. R. Chance, R. Silbey, *Phys. Rev. B 26* (***1982***) 5843.
4. J. D. Stenger - Smith, *Prog. Polym. Sci. 23* (**1998**) 57.
5. H. Shirakawa, E. J. Louis, A. G. MacDiarmid, C. K. Chiang, A. J. Heeger, *J. Chem. Soc. Chem. Commun. 474* (**1977**) 578.
6. A. J. Heeger, S. Kivelson, J. R. Schrieffer, W. P. Su, *Rev. Mod. Phys. 60* (**1988**) 781.
7. A. O. Patil, A. J. Heeger, F. Wudl, *Chem. Rev. 88* (**1988)** 183.
8. J. H. Burroughes, D. D. C. Bradley, A. R. Brown, R. N. Marks, K. Mackay, R. H. Friend, P. L. Burns, A. B. Holmes, *Nature 347* (**1990)** 539.
9. D. Bradley, *Curr. Opin. Solid State. Mater. Sci. 1* (**1996)** 789.
10. K. C. Fox, *New Sci. 141* (**1994)** 33.
11. D. R. Baigent, N. C. Greenham, J. Grüner, R. N. Marks, R. H. Friend, S. C. Moratti, A. B. Holmes, *Synth. Met. 67* (**1994)** 93.
12. P. Yam, *Polymer electronics. Sci. Am. 273* (**1995)** 74.
13. M. H. Harun, E. Saion, A. Kassim, N. Yahya , E. Mahmud, *JASA 2* (**2007**) 63.
14. N. Kar, *Synth. Metals 133* (**2003**) 649.
15. W. R. Salaneck, R. H. Friend, J. L. Brédas, Phys. *Rep. 319* (**1999**) 231.
16. H. Klauk, *Chem. Soc. Rev. 39* (**2010**) 2643.
17. Q. Tang, L. Jiang, Y. Tong, H. Li, Y. Liu, Z. Wang, W. Hu, Y. Liu, D. Zhu, *Adv. Mater. 20* (**2008**) 2947.
18. A. Facchetti, *Mater. Today 16* (**2013**) 123.

19. H. F. Liu, L. Y. Fong, Y. Yang, *App. Phys. Let. 80* (**2002**)1891.

20. Q. Boughias, M. - S. Belkaid, F. Nemmar, D. Hatem, *IJRRAS 12* (**2012**) 244.

21. J. F. Mike, J. L. Lutkenhaus, *J. Polym. Sci. Part B: Polym. Phys. 51* (**2013**) 468.

22. T. M. Swager, *Acc. Chem. Res. 31* (**1998**) 201.

23. R. Gracia, D. Mecerreyes, *Polym. Chem. 4* (**2013**) 2206.

24. K. Tremel, S. Ludwigs, *Adv. Polym. Sci. 265* (**2014**) 39.

25. A. T. Taskin, A. Balan, Y. A. Udum, L. Toppare, *Smart. Mater. Struct. 19* (**2010**) 065005.

26. S. - S. Sun, N. S. Sariciftci. *Organic Photovoltaics Mechanisms, Materials, and Devices* (1st edn), CRC Press/Taylor & Francis, New York, USA, **2005,** p. 400.

27. A. Wild, D. A. M. Egbe, E. Birckner, V. Cimrova, R. Baumann, U. - W. Grummt, U. S. Schubert, *J. Polym. Sci.: Part A: Polym. Chem. 47* (**2009**) 2243.

28. H. Hrichi, K. Hriz, N. Jaballah, R. Ben Chaâbane, O. Simonetti, M. Majdoub, *J. Polym. Res. 20* (**2013**) 241.

29. D. A. M. Egbe, B. Carbonnier, L. Ding, D. Muhlbacher, E. Birckner, T. Pakula, F. E. Karasz, U. - W. Grummt, *Macromolecules 37* (**2004**) 7451.

30. D. A. M. Egbe, C. Ulbricht, T. Orgis, B. Carbonnier, T. Kietzke, M. Peip, M. Metzner, M. Gericke, E. Birckner, T. Pakula, D. Neher, U. - W. Grummt, *Chem. Mater. 17* (**2005**) 6022.

31. E. Tekin, H. Wiljaars, E. Holder, D. A. M. Egbe, U. S. Schubert, *J. Mater. Chem. 16* (**2006**) 4294.

32. H. Hoppe, D. A. M. Egbe, D. Muhlbacher, N. S. Sariciftci, *J. Mater. Chem. 14* (**2004**) 3462.

33. M. Al-Ibrahim, A. Konkin, H. K. Roth, D. A. M. Egbe, E. Klemm, U. Zhokhavets, G. Gobsch, S. Sensfuss, *Thin Solid Films 474* (**2005**) 201.

34. D. A. M. Egbe, L. H. Nguyen, B. Carbonnier, D. Muhlbacher, N. S. Sariciftci, *Polymer 46* (**2005)** 9585.

35. D. A. M. Egbe, T. Kietzke, B. Carbonnier, D. Muhlbacher, H. - H. Horhold, D. Neher, T. Pakula, *Macromolecules 37* (**2004**) 8863.

36. T. Kietzke, D. A. M. Egbe, H. - H. H*ö*rhold, D. Neher, *Macromolecules 39* (**2006**) 4018.

37. N. Tore, E. A. Parlak, O. Usluer, D. A. M. Egbe, S. E. San, P. Aydogan, *Sol. Energ. Mat. Sol. C.* (**2012**) 39.

38. H. Hrichi, K. Hriz, N. Jaballah, R. Ben Chaâbane, O. Simonetti, M. Majdoub, *J. Polym. Res. 20* (**2013**) 241.

39. D. A. M. Egbe, H. Neugebauer, N. S. Sariciftci, *J. Mater. Chem. 21* (**2011**) 1338.

40. S. G*ü*nes, A. Wild, E. Cevik, A. Pivrikas, U. S. Schubert, D. A. M. Egbe, *Sol. Energ. Mat. Sol. C. 94* (**2010**) 484.

41. Ö. Usluer, C. Kästner, M. Abbas, C. Ulbricht, V. Cimrova, A. Wild, E. Birckner, N. Tekin, N. S. Sariciftci, H. Hoppe, S. Rathgeber, D. A. M. Egbe, *J. Polym. Sci. Polym. Chem. 50* (**2012)** 3425.

42. F. Tinti, F. K. Sabir, M. Gazzano, S. Righi, Ö. Usluer, C. Ulbricht, T. Yohannes, D. A. M. Egbe, N. Camaioni, *Macromol. Chem. Phys. 215* (**2014)** 452.

43. Y. A. M. Ismail, T. Soga, T. Jimbo, ISRN *Renewable Energy* 2012 (**2012**) 1.

44. D. A. M. Egbe, S. T*ü*rk, S. Rathgeber, F. K*ü*hnlenz, R. Jadhav, A. Wild, E. Birckner, G. Adam, A. Pivrikas, V. Cimrova, G. Kn*ö*r, N. S. Sariciftci, H. Hoppe, *Macromolecules 43* (**2010**) 1261.

45. Y. Shirota, H. Kageyama, *Chem. Rev. 107* (**2007)** 953.

46. C. Gupta, M. A. Shannon, P. J. A. Kenis, *J. Phys. Chem. C 113* (**2009**) 4687.

47. a) P. M. Borsenberger, J. J. Fitzgerald, *J. Phys. Chem. 97* (**1993**) 4815; b) D. Braun, *J. Polym. Sci. B 41* (**2003**) 2622.

48. H. B*ä*ssler, *Phys. Stat. Sol. 175* (**1993**) 15.

49. P. M. Borsenberger, L. Pautmeier, H. B*ä*ssler, *J. Chem. Phys. 94* (**1991**) 5447.

50. Y. Kikuchi, T. Wakamatsu, H. Takahashi, I. Endo, *Elect. Engin. Japan 143* (**2003**) 59.

51. L. B. Schein, A. Peled, D. Glatz, *J. Appl. Phys. 66* (**1989**) 686.

52. S. Rackovsky, H. Scher, *J. Chem. Phys. 111* (**1999**) 3668.

53. a) M. Guo, X. Z. Yan, T. Goodson, *Adv. Mater. 20* (**2008)** 4167; b) M. Bouhassoune, S. L. M. Van Mensfoort, P. A. Bobbert, R. Coehoorn, *Organic Electronics 10* (**2009)** 437.

54. V. Kazukauskas, M. Pranaitis, V. Cyras, L. Sicot, F. Kajzar, *Thin Solid Films 516* **(2008)** 8988.

55. Y. Nagata, C. Lennartz, *J. Chem. Phys. 129* (**2008**) 034709.

56. J. G. Simmons, *Phys. Rev. 155* (**1967**) 657.

57. M. Ieda, G. Sawa, S. Kato, *J. Appl. Phys. 42* (**1971)** 3737.

58. K. C. Kao W. Hwang, *Electrical Transport in Solids*. Pergamon Press, Oxford, London, UK, **1981,** p. 314.

59. M. Jaiswal, R. Menon, *Polym. Int. 55* (**2006**)1371.

60. R. Pokrop, J. - M. Verilhac, A. Gasior, I. Wielgus, M. Zagorska, J. - P. Travers, A. Pron, *J. Mater. Chem. 16* (**2006**) 3099.

61. J. - M. Verilhac, G. Le Blevennec, D. Djurado, F. Rieutord, M. Chouiki, J. - P. Travers, A. Pron, *Synth. Metals 156* (**2006**) 815.

62. A. Zen, M. Saphiannikova, D. Neher, J. Grenzer, S. Grigorian, U. Pietsch, U. Asawapirom, S. Janietz, U. Scherf, I. Lieberwirth, G. Wegner, *Macromolecules 39* **(2006)** 2162.

63. A. Zen, J. Pflaum, S. Hirschman, W. Zhuang, F. Jaiser, W. Asawapirom, J. Rabe, U. Scherf, D. Neher, *Adv. Funct. Mater. 14* (**2004**) 757.

64. M. Tong, S. Cho, J. T. Rogers, K. Schmidt, B. B. Y. Hsu, D. Moses, R. C. Coffin, E. J. Kramer, G. C. Bazan, A. J. Heeger, *Adv. Funct. Mater. 20* (**2010)** 3959.

65. G. Horowitz, R. Hajlaoui, P. Delannoy, *J. Phys. 5* (**1995**) 355.

66. T. - Y. Chu, J. Lu, S. Beaupré, Y. Zhang, J. - R. Pouliot, J. Zhou, A. Najari, M. Leclerc, Y. Tao, *Adv. Funct. Mater. 22* (**2012**) 2345.

67. N. P. Holmes, S. Uluma, P. Sista, K. B. Burke, M. G. Wilson, M. C. Stefan, X. Zhou, P. C. Dastoor, W. J. Belcher, *Sol. Energy Mater. Sol. C. 128* (**2014**) 369.

68. R. J. Kline, M. D. McGene, E. N. Kadnikova, J. Liu, J. J. Ferechet, *Adv. Mater.15* (**2003**) 1519.

69. W. J. Cooper, P. D. Krasicky, F. Rodriguez, *Polymer 26* (**1985**) 1069.

70. J. Manjkow, J. S Papanu, D.W. Hess, D. S. Soong, A. T. Bell, *J. Electrochem. Soc. 134* (**1987**) 2003.

71. B. A. Miller - Chou, J. L. Koenig, *Prog. Polym. Sci. 28* (**2003**) 1223.

72. H. C. F. Martens, P. W. M. Blom, H. F. M. Schoo, *Phys. Rev. B 61* (**2000)** 7489.

73. F. C. Krebs, M. Jorgensen, *Macromolecules 36* (**2003)** 4374.

74. Freek J. M. Hoeben, P. Jonkheijm, E. W. Meijer, P. Albertus, H. J. Schenning, *Chem. Rev. 105* (**2005)** 1491.

75. Y. D. Park, D. H. Kim, Y. Jang, J. H. Cho, M. Hwang, H. S. Lee, J. A. Lim, K. Cho, *Organic Electronics 7* (**2006**) 514.

76. S. M. Tuladhar, M. Sims, J. Kirkpatrick, R. C. Maher, A. J. Chatten, D. D. C. Bradley, J. Nelson, *Phys. Rev. B 79* (**2009**) 035201.

77. H. S. Lee, J. H. Cho, K. Cho, Y. D. Park, *J. Phys. Chem. C 117* (**2013**) 11764.

78. D. A. M. Egbe, G. Adam, A. Pivrikas, A. M. Ramil, E. Birckner, V. Cimrova, H. Hopped, N. S. Sariciftci, *J. Mater. Chem. 20* (**2010**) 9726.

79. Y. - K. Lan, C. - H. Yang, H. - C. Yang, *Polym. Int. 59* (**2010**) 16.

80. S. Rathgeber, D. B. Toledo, E. Birckner, H. Hoppe, D. A. M. Egbe, *Macromolecules 43* **(2010**) 306.

81. Z. - G. Zhang, Y. Li, *Sci. China Chem.* 58 (**2015**)192.

82. a) B. J. Schwartz, *Annu. Rev. Phys. Chem. 54* (**2003)** 141; b) U. H. F. Bunz, *Chem. Rev. 100* (**2000)** 1605.

83. Y. Zhang, J. Zou, H. - L. Yip, K. - S. Chen, J. A. Davies, Y. Sun, A. K. - Y. Jen, *Macromolecules 44* (**2011**) 4752.

84. Y. - K. Lan, C. Huang, *J. Phys. Chem. B 113* (**2009**) 14555.

85. R. D. McCullough, R. D. Lowe, M. Jayaraman, P. C. Ewbank, D. L. Anderson, S. Tristramnagle, *Synth. Metals 55* (**1993)** 1198.

86. D. Wohrle, D. Meissner, *Adv. Mater. 3* (**1991**) 3.

87. A. M. Bagher, *Inter. J. Renew. Sust. Ener. 3* (**2014**) 53.

88. Y. Sun, M. Wang, X. Gong, J. H. Seo, B. B. Y. Hsu, F. Wudlab, A. J. Heeger, *J. Mater. Chem. 21* (**2011**) 1365.

89. T. C. B. McLeish, *Rheology Reviews* (**2003**) 197.

90. D. Venkateshvaran, M. Nikolka, A. Sadhanala, V. Lemaur, M. Zelazny, M. Kepa, M. Hurhangee, A. J. Kronemeijer, V. Pecunia, I. Nasrallah, I. Romanov, K. Broch, I. McCulloch, D. Emin, Y. Olivier, J. Cornil, D. Beljonne H. Sirringhaus, *Nature 515* (**2014**) 384.

91. X. Xu, Z. Li, O. Backe, K. Bini, D. I. James, E. Olsson, M. R. Andersson, E. Wang, *J. Mater. Chem. A 2* (**2014**) 18988.

92. Y. Yao, J. Hou, Z. Xu, G. Li, Y. Yang, *Adv. Funct. Mater. 18* (**2008**) 1783.

93. a) Y. - C. Huang, H. - C. Chia, C. - M. Chuang, C. - S. Tsao, C. - Y. Chen, W. - F. Su, *Sol. Energ. Mat. Sol. C. 114* (**2013**) 24; b)Y. Yao, J. Hou, Z. Xu, G. Li, Y. Yang, *Adv. Funct. Mater. 18* (**2008**) 1783.

94. W. Ma, J. Y. Kim, K. Lee, A. J. Heeger, *Macromol. Rapid Commun. 28* (**2007**) 1776.

95. M. Sommer, S. Hüttner, U. Steiner, M. Thelakkat, *Appl. Phys. Lett.* 95 **(2009)** 183308.

96. J. - H. Huang, A.TzuyuHuang, C. -Y. Hsu, J. - T. Lin, C. - W. Chu, *Sol. Energ. Mat. Sol. C. 98* (**2011**) 300.

97. D. J. D. Moet, M. Lenes, J. D. Kotlarski, S.C. Veenstra, J. Sweelssen, M. M. Koetse, B. de Boer, P. W. M. Blom, *Organic Electronics 10* (**2009**) 1275.

98. Y. Zhu, M. O. Wolf, *J. Am. Chem. Soc. 122* (**2000**) 10121.

99. C. H. Chen, C. H. Hsieh, M. Dubosc, Y. J. Cheng, C. S. Hsu, *Macromolecules 43* (**2010**) 697.

100. a) H. - C. Liao, C. - C. Ho, C. - Y. Chang, M. - H. Jao, S. B. Darling, W. - F. Su, *Materials Today 16* (**2013**) 326; b) H.- C. Liao, P. - H. Chen, R. P. H. Chang, W. - F. Su, *Polymers 6* (**2014**) 2784.

101. S. J. Lou, J. M. Szarko, T. Xu, L. Yu, T. J. Marks, L. X. Chen, *J. Am. Chem. Soc. 133* (**2011**) 20661.

102. S. Gün̈es, H. Neugebauer, N. S. Sariciftci, *Chem. Rev. 107* (**2007**) 1324.

103. M.C. Scharber, N.S. Sariciftci, *Prog. Polym. Sci. 38* (**2013**) 1929.

104. R. A. Street, P. P. Khlyabich, A. E. Rudenko, Barry C. Thompson, *J. Phys. Chem. C 118* (**2014**) 26569.

105. Z. Ma, W. Sun, S. Himmelberger, K. Vandewal, Z. Tang, J. Bergqvist, A. Salleo, J. W. Andreasen, O. Inganäs, M. R. Andersson, C. Müller, F. Zhang , E. Wang, *Energy Environ. Sci. 7* (**2014**) 361.

106. D. A. Gedefaw, Y. Zhou, Z. Ma, Z. Genene, S. Hellström, F. Zhang, W. Mammo, O. Inganäs M. R. Anderssona, *Polym. Int. 63* (**2014**) 22.

107. P. M. Beaujuge, C. M. Amb, J. R. Reynolds, *Acc. Chem. Res. 43* (**2010**)1396.

108. L. Yang, L. Yan, Wei You, *J. Phys. Chem. Lett. 4* (**2013**) 1802.

109. H. - C. Liao, P. - H. Chen, R. P. H. Chang, W. - F. Su, *Polymers 6* (**2014**) 2784.

110. T. Ameri, P. Khoram, J. Min, C. J. Brabec, *Adv. Mater. 25* (**2013**) 4245.

111. Y. Ohori, T. Hoashi, Y. Yanagi, T. Okukawa, S. Fujii, H. Kataura, Y. Nishioka, *J. Photopolym. Sci. Technol. 27* (**2014**) 569.

112. P. P. Khlyabich, B. Burkhart, B. C. Thompson, *J. Am. Chem. Soc. 133* (***2011***) 14534.

113. T. Ameri, J. Min, N. Li, F. Machui, D. Baran, M. Forster, K. J. Schottler, D. Dolfen, U. Scherf, C. J. Brabec, *Adv. Energy Mater. 2* **(2012)** 1198.

114. D. Jarzab, K. Szendrei, M. Yarema, S. Pichler, W. Heiss, M. A. Loi, *Adv. Funct. Mater. 21* (**2011**) 1988.

115. Q. D. Shan, L. G. Fang, Q. Wei, C. Lei, L. J. Suo, Z. J. Dong, Y. D. Hang, Sci. *China. Phys. Astron. 56* (**2013**) 530.

116. R. G. Kepler. *Phys. Rev.* 119 (**1960**) 1226.

117. O. H. Le Blanc. *J. Chem. Phys. 30* (**1959**) 1443.

118. W. E Spear, *J. Non-Cryst. Solids 1* (**1969**) 197.

119. A. Pivrikas, N. S. Sariciftci, G. Jüska, Rösterbacka, *Prog. Photovolt: Res. Appl. 15* (**2007**) 677.

120. A. J. Mozer, N. S. Sariciftci, A. Pivrikas, R. Österbacka, G. Juška, L. Brassat, H. Bässler, *Phys. Rev. B 71* (**2005**) 035214 .

121. M. Pope and C. E. Swenberg, *Electronic Progress in Organic crystal and polymers*, oxford University press, UK, **1999**, p. 712.

122. R. Österbacka, G. Juška, K. Arlauskas, A. J. Pal, K. - M. Kȁllman, H. Stubb, *J. Appl. Phys. 84* **(1998)** 3359.

123. K. Kashima, H. Sato, K. Musha, K. - I. Kanno. T. Takahashi, *Anal. Sci. 23* (**2007**) 1249.

124. M. Kawamoto, H. Mochizuki, T. Ikeda, H. Iino, J. - I. Hanna, *J. Phys. Chem. B 109* **(2005)** 9226.

125. S. Raj Mohan, M. P. Joshi*, Solid State Communications 139 (**2006**) 181.*

126. S. Gambino, I. D.W. Samuel, H. Barcena, P. L. Burn, *Organic Electronics 9* (**2008**) 220.

127. S. Tiwari, N. C. Greenham, *Opt. Quant. Electron. 41* (**2009**) 69.

128. K. K. Tsung, S. K. So, *J. Appl. Phys. 106* (**2009**) 083710.

129. N. R. Mirchin, A. Peled, *J. Sci. Eng. 1* (**2004**) 782.

130. M. Brinza, G. J. Adriaenssens, *J. Optoelectron. Adv. Mater. 8* (**2006**) 2028.

131. P. M. Borsenberger, D. S. Weiss, *"Organic Photoreceptors for Imaging Systems"*, Marcel Dekker, New York, **1993,** p. 239

132. D. F. Nelson, *Phys. Rev. B 25* (**1982**) 5267.

133. W. E. Spear, *Proc. Phys. Soc. B 70* (**1957**) 669.

134. G. Juška, G. Jukonis, J. Kočka, *J. Non-Cryst. Sol. 114* (**1989**) 354.

135. A. J. Campbell, D. D. C. Bradley, H. Antoniadis, *Appl. Phys. Lett. 79* (**2001**) 2133.

136. J. Shao, G. T. Wright, *Solid State Electron. 3* (**1961**) 291.

137. H. C. F. Martens, *Appl. Phys. lett.77* (**2000)** 1852.

138. D. Poplavskyy, F. So. *J. Appl. Phys. 99* **(2006)** 033707.

139. O. J. Weiß, R. K. Krause, A. Hunze, *J. Appl. Phys. 103* **(2008)** 043709.

140. S. W. Tsang, S. K. So, J. B. Xu, *J. Appl. Phys. 99* (**2006)** 013706.

141. M. Hoping, C. Schildknecht, H. Gargouri, T. Riedl, M. Tilgner, H. - H. Johannes, W. Kowalsky, *SPIE, 7051* (**2008**) 70511D.

142. A. Melianas, Z. Tang, G. Juska, K. Arlauskas, F. L. Zhang, L. D. A. Siebbeles, O. Inganas, T. J. Savenije, *Adv. Funct. Mater. 23* (**2013**) 4262.

143. T. Dzhafarov, *Silicon solar cells with nanoporous silicon layer*. INTECH Open Access, Azebaijan Academy of science, Azerbaijan, **2013,** p. 27.

144. M. D Archer, R. Hill, *Clean electricity from photovoltaics*, Imperial College Press, London, UK, **2001,** p. 337.

145. a) M. C. Scharber, N. S. Sariciftci, *Progress in Polymer Science 38* (**2013**) 1929; b) Y. Tamai, K. Tsuda, H. Ohkita, H. Bentena, S. Ito, *Phys. Chem. Chem. Phys. 16* (**2014**) 20338.

146. J. Simon, and J. J. Andre, *Molecular semiconductors*, Springer- Verlag, Berlin-Heidelberg, **1985,** p.142

147. B. A. Gregg, *Excitonic Solar Cells: The Physics and Chemistry of Organic-Based Photovoltaics,* ACS, Washington DC, USA, **2003,** p. 243.

148. H. Hoppe, N. S. Sariciftci, *J. Mater. Res. 19* (**2004**) 1924.

149. A. Mishra, P. Bäuerle, *Angew. Chem. 124* (**2012**) 2060.

150. H. Kiess, W. Rehwald, *Sol. Energ. Mat. Sol. C. 38* (**1995)** 45.

151. a) B. A. Gregg, *J. Phys. Chem. B 107* (**2003)** 4688; b) V. Dyakonov, *Physica E. 14* (**2002)** 53.

152. W. A. Hammed, R. Yahya, A. L. Bola, H. E. Mahmud, *Energies 6* (**2013**) 5847.

153. S. E. Shaheen, C. J. Brabec, N. S. Sariciftci, F. Padinger, T. Fromherz, *Appl. Phys. Lett. 78* (**2001**) 841.

154. S. H. Park, A. Roy, S. Beaupre, S. Cho, N. Coates, J. S. Moon, D. Moses, M. Leclerc, K. Lee1, A. J. Heeger, *Nature Photonics 3* (**2009**) 297.

155. D. A. M. Egbe, C. Bader, E. Klemm, L. Ding, F. E. Karasz, U. -W. Grummt, E. Birckner, *Macromolecules 36* (**2003**) 9303.

156. J. Min, Z. - G. Zhang, S. Zhang, M. Zhang, J. Zhang, Y. Li, *Macromolecules 44* (**2011**) 7632.

157. a) C. - K. Lu, S. - T. Pi, H. - F. Meng, Phys. Rev. B 75 (**2007**) 195206; b) Z. Chen, M. Bird, V. Lemaur, G. Radtke, J. Cornil, M. Heeney, I. McCulloch, H. Sirringhaus, *Phys. Rev. B 84* (**2011**) 115211.

158. R. Österbacka, G. Juška, K. Arlauskas, H. Stubb, *SPIE, 3145* (**1997**) 389.

159. J. S. Kim, M. Granstrom, R. H. Friend, N. Johansson, W. R. Salaneck, R. Daik, W. J. Feast, F. Cacialli, *J. Appl. Phys. 84* (**1998**) 6859.

160. M. Zhang, X. Guo, Y. Li, *Adv. Energy Mater. 1* (**2011**) 557.

161. a) D. - M. Smilgies, *J. Appl. Cryst. 42* (**2009**) 1030; b) T. J. Prosa, M. J. Winokur, *Macromolecules 25* (**1992**) 4364.

162. M. Brinkmann, P. Rannou, *Adv. Funct. Mater. 17* (**2007)** 101.

163. S. Joshi, S. Grigorian, U. Pietsch, *Phys. Stat. Sol. A 205* (**2008)** 488.

164. a) P. A. Troshin, O. A. Mukhacheva, Ö. Usluer, A. E. Goryachev, A. V. Akkuratov, D. K. Susarova, N. N. Dremova, S. Rathgeber, N. S. Sariciftci, V. F.

Razumov, D. A. M. Egbe, *Adv. Energy Mater. 3* **(2013)** 161; b) C. Kästner, C. Ulbricht, D. A. M. Egbe, H. Hoppe, *Polym. Sci. Polym. Phys. 50* (**2012**)1562.

165. N. Camaioni, F. Tinti, A. D. Esposti, S. Righi, Ö. Usluer, S. Boudiba, D. A. M. Egbe *Appl. Phys. Lett. 101* (**2012)** 053302.
166. S. Tirapattur, M. Belletête, N. Drolet, M. Leclerc, G. Durocher, *Chem. Phys. Lett. 370* (**2003)** 799.
167. J. Bouchard, M. Belletête, G. Durocher, M. Leclerc, *Macromolecules 36* (**2003**) 4624.
168. D. A. M. Egbe, B. Carbonnier, E. Birckner, U. - W. Grummt, *Prog. Polym. Sci. 34* (**2009)** 1023.
169. R. C. Hiorns, R. de Bettignies, J. Leroy, S. Bailly, M. Firon, C. Sentein, A. Khoukh, H. Preud"homme, C. Dagron - Lartigau, *Adv. Funct. Mater. 16* (**2006)** 2263.
170. P. M. Borsenberger, D. S. Weiss, *Organic Photoreceptors for Xerography*, Marcel Dekker, New York, 1998**,** p. 274.
171. H. Scher, E.W. Montroll, *Phys. Rev. B 12* (**1975)** 2455.
172. S. A. Choulis, Y. Kim, J. Nelson, D. D. C. Bradley, M. Gilles, M. Shkunov, I. McCulloch, *Appl. Phys. Lett. 85* (**2004)** 3890.
173. V. Kažukauskas, M. Pranaitis, V. Čyras, L. Sicot, F. Kajzar, *Eur. Phys. J. Appl. Phys. 37* (**2007**) 247.
174. L. Pautmeier, R. Richert, H. Bässler, *Synth. Metals 37* (**1990)** 371.
175. M. Helgesen, R. Søndergaard, F. C. Krebs, *J. Mater. Chem.* 20 (**2010**) 36.
176. C. J. Brabec, A. Cravino, D. Meissner, N. S. Sariciftci, T. Fromherz, M. T. Rispens, L. Sanchez, J. C. Hummelen, *Adv. Funct. Mater. 11* (**2001)** 374.

177. P. A. Troshin, O. A. Mukhacheva, O. Usluer, A. E. Goryachev, A. V. Akkuratov, D. K. Susarova, N. N. Dremova, S. Rathgeber, N. S. Sariciftci, V. F. Razumov, D. A. M. Egbe, *Adv. Energy Mater. 3* (**2013)** 161.

178. H. S. Lee, J. H. Cho, K. Cho, Y. D. Park, *J. Phys. Chem. C 117* (**2013)** 11764.

179. C. Di, K. Lu, L. Zhang, Y. Liu, Y. Guo, X. Sun, Y. Wen, G. Yu, D. Zhu, *Adv. Mater. 22* (**2010)** 1273.

180. A. J. Campbell, D. D. C. Bradley, D. G. Lidzey, *J. Appl. Phys. 82 (***1997)** 6326.

181. H. T. Nicolai, M. Kuik, G. A. H. Wetzelaer, B. de Boer, C. Campbell, C. Risko, J. L. Brédas, P. W. M. Blom, *Nat. Mater. 11* (**2012)** 882.

182. H. H. Poole, *Philos. Mag. 32* (**1916)** 112.

183. J. Frenkel, *Phys. Rev. 54* (**1938)** 647.

184. H. Bassler, A. Kohler, *Top. Curr. Chem. 1* (**2012)** 312.

185. T. Tiedje, A. Rose, *Solid State Commun. 37* (**1981)** 49.

186. F. Tinti, F. K. Sabir, M. Gazzano, S. Righi, C. Ulbricht, Ö. Usluer, V. Pokorna, V. Cimrova, T. Yohannes, D. A. M. Egbe, N. Camaioni, *RSC Advances 3* (**2013**) 6972.

187. H. P. Klug and L. E. Alexander, *X-ray diffraction procedures for polycrystalline and amorphous materials*, John Wiley, New York, 2nd edn, **1974**, 966.

188. W. Li, Y. An, M. M. Wienk, R. A. J. Janssen, *J. Mater. Chem. A 3* (**2015**) 6756.

189. X. Dai, Z. Zhang, Y. Jin, Y. Niu, H. Cao, X. Liang, L. Chen, J. Wang, X. Peng, *Nature 515* (**2014**) 96.

190. D. A. M. Egbe, E. Birckner, E. J. Klemm, *Polym. Sci. A: Polym. Chem. 40* (**2002**) 2670.

191. H. - W. Lin, W. - Y. Lee, W. - C. Chen, *J. Mater. Chem. 22* (**2012**) 2120.

192. R. Noriega, A. Salleo, A. J. Spakowitz, *PNAS, 110* (**2013**) 16315.

193. a) S. A. Choulis, Y. Kim, J. Nelson, D. D. C. Bradley, *Appl. Phys. Lett. 85* (**2004**); b) S. Lattante, *Electronics 3* (**2014**) 132.

194. J. Y. Kim, H. Cho, S. Noh, Y. Lee, Y. M. Nam, C. Lee, W. H. Jo, *J. Appl. Phys. 111* (**2012**) 043710.

195. S. A. Choulis, Y. Kim, J. Nelson, D. D. C. Bradley, *Appl. Phys. Lett. 85* (**2004)** 3890.

196. Y. Kim, S. Cook, S. A. Choulis, J. Nelson, J. R. Durrant, D. D. C. Bradley, *Chem. Matt. 16* **(2004**) 4812.

197. A. J. Mozer, N. S. Sariciftci, *Appl. Phys. Lett. 86* (**2005**) 112104.

198. G. J*ü*ska, K. Genevič*i*us, K. Arlauskas, R. *Ö*sterbacka, H. Stubb, *Phys. Rev. B 65* (**2002**) 233208.

199. G. Juška, G. Jukonis, J. Kočka, *J. Non-Cryst. Solids 114* (**1989**) 354.

200. G. Juška, K. Genevičius, R. Österbacka, K. Arlauskas, T. Kreouzis, D. D. C. Bradley, H. Stubb, *Phys. Rev. B 67* (**2003**) 081201.

201. G. Juska, K. Arlauskas, R. *Ö*sterbacka, H. Stubb, *Synth. Metals 109* (**2000**) 173.

202. K. H. Hecht, *Z. Phys. 77* (**1932**) 235.

203. A. J. Campbell, D. D. C. Bradley, H. Antoniadis, *Appl. Phys. Lett. 79* (**2001**) 2133.

204. R. Österbacka, K. Genevičius, A. Pivrikas, G. Juška, K. Arlauskas, T. Kreouzis, D. D. C. Bradley, H. Stubb, *Synth. Metals 139* (**2003**) 811.

205. G. Juska, K. Arlauskas, R. *Ö*sterbacka, H. Stubb, *Synth. Metals 109* (**2000**) 173.

206. S. A. Dinca, E. A. Schiff, W. N. Shafarman, B. Egaas, R. Noufi, D. L. Young, *Appl. Phys. Lett. 100* (**2012**) 103901.

207. L. Pautmeier, R. Richert, H. B*ä*ssler, *Synth. Metals 37* (**1990**) 271.

208. D. Venkateshvaran, M. Nikolka, A. Sadhanala, V. Lemaur, M. Zelazny, M. Kepa, M. Hurhangee, A. J. Kronemeijer, V. Pecunia, I. Nasrallah, I. Romanov, K. Broch, I. McCulloch, D. Emin, Y. Olivier, J. Cornil, D. Beljonne, H. Sirringhaus, *Nature 515* (**2014**) 384.

209. S. H. Evan, K. - E. Kim, *Sci. Rep. 5* (**2015**) 8396.

210. P. W. M. Blom, M. C. J. M. Vissenberg, *Mater. Sci. Eng. R, 27* **(2000**) 53.

211. P. J. Jadhav, B. N. Limketkai, M. A. Baldo, *Adv. Polym. Sci. 223* (**2010**) 29.

212. S. K. So, S. C. Tse, K. L. Tong, *J. Displ. Technol. 3* (**2007**) 225.

213. A. Pivrikas, N. S. Sariciftci, G. Juška, R. Österbacka, *Prog. Photovoltaics 15* (**2007**) 677.

214. R. Pacios, J. Nelson, D. D. C. Bradley, C. J. Brabec, *Appl. Phys. Lett. 83* (**2003**) 4764.

215. H. C. F. Martens, H. B. Brom, P. W. M. Blom, *Phys. Rev. B 60* (**1999**) R8489.

216. J. Bolink, E. Coronado, D. Repetto, M. Sessolo, E. M. Barea, J. Bisquert, G. Garcia-Belmonte, J. Prochazka, L. Kavan, *Adv. Funct. Mater. 18* (**2008)** 145.

217. a) D. R. Gamota, P. Brazis, K. Kalyanasundaram, J. Zhang, *Printed Organic and Molecular Electronics,* Kluwer Academic, Norwell, MA, USA, **2004,** p 347 ; b) A. J. Heeger, *Chem. Soc. Rev. 39* (**2010)** 2354.

218. G. Li, R. Zhu, Y. Yang, *Nature Photonics 6* (**2012)** 153.

219. K. H. Chan, S. K. So, *SPIE 1* (**2011**) 011112.

220. M. Jakobsson, S. Stafström, *J. Chem. Phys. 135* (**2011**) 134902.

221. T. Nga, W. R. Silveira, J. A. Marohn, *Phys. Rev. Lett. 98* (**2007**) 066101.

222. H. H. P. Gommans, M. Kemerink, *Phys. Rev. B 69* (**2004**) 155216.

223. T. K. Djidjou, T. Basel, A. Rogachev, *J. Appl. Phys. 112* (**2012**) 024511.

224. P. W. M. Blom, H. C. F. Martens, J. N. Huiberts, *Synth. Metals 121* (**2001**) 1621.

225. V. Coropceanu, J. Cornil, D. A. da Silva Filho, Y. Olivier, R. Silbey, J. - L. Brédas, *Chem. Rev. 107* (**2007**) 926.

226. M. Jakobsson, S. Stafström, *J. Chem. Phys. 135* **(2011)** 134902.

227. W. F. Pasveer, J. Cottaar, C. Tanase, R. Coehoorn, P. A. Bobbert, P. W. M. Blom, D. M. de Leeuw, M. A. J. Michels, *Phys. Rev. Lett. 94* (**2005**) 206601.

228. S. Olthof, S. Mehraeen, S. K. Mohapatra, S. Barlow, V. Coropceanu, J. - L. Bredas, S. R. Marder, A. Kahn, *PRL* 109 (**2012**) 176601.

229. K. L. Tong, S. W. Tsang, K. K. Tsung, S. C. Tse, S. K. So, *J. Appl. Phys. 102* (**2007**) 093705.

230. a) S. Marianer, B. Shklovskii, *Phys. Rev. B 46* (**1992**) 13100; b) V. Arkhipov, E. Emelianova, G. J. Adriaenssens, *J. Appl. Phys. 93* (**2003**) 6150.

231. S. E. Debebe, W. Mammo, T. Yohannes, F. Tinti, A. Zanelli, N. Camaioni, *Appl. Phys. Lett. 96* **(2010)** 082109.

232. F. Tinti, S. E. Debebe, W. Mammo, T. Yohannes, N. Camaioni, *Synth. Metals 161* (**2011**) 794.

233. S. J. Martin, A. Kambili, A. B. Walker, *Phys. Rev. B 67* (**2003)** 165214.

234. J. Y. Kim, H. Cho, S. Noh, Y. Lee, Y. M. Nam, C. Lee, W. H. Jo, *J. Appl. Phys. 111* (**2012**) 043710.

235. I. I. Fishchuk, A. K. Kadashchuk, J. Genoe, M. Ullah, H. Sitter, T. B. Singh, N. S. Sariciftci, H. Bässler, *Phys. Rev. B 81* (**2010**) 045202.

236. S.Terao, T. Hirai, N. Morita, H. Maeda, K. Kojima, M. Tachibana, *J. Appl. Phys. 108* (**2010**) 124511.

237. J. - F. Chang, H. Sirringhaus, M. Giles, M. Heeney, I. McCulloch, *Phys. Rev. B 76* (**2007**) 205204.

238. I. I. Fishchuk, A. K. Kadashchuk, J. Genoe, V. N. Poroshin, H. Bässler, *Mol. Cryst. Liq. Cryst. 535* (**2011**) 1.

239. A. J. Mozer, N. S. Sariciftci, *Chem. Phys. Letter. 389* (**2004**) 438.

240. R. Zeis, C. Besnard, T. Siegrist, C. Schlockermann, X. L. Chi, C. Kloc, *Chem. Mater. 18* (**2006**) 244.

241. V. Podzorov, E. Menard, A. Borissov, V. Kiryukhin, J. A. Rogers, M. E. Gershenson, *Phys. Rev. Lett. 93* (**2004**) 086602.

242. E. V. Emelianova, G. J. Adriaenssens, *Adv. Mater. 6* (**2004**) 1105.

243. L. G. Wang, H. W. Zhang, X. L. Tang, Y. Q. Song, Z. Y. Zhong , Y. X. Li, *Phys. Scr. 84* (**2011**) 045701.

244. T. M. Brown, J. S. Kim, R. H. Friend, F. Cacialli, R. Daik, W. J. Feast, *Appl. Phys. Lett. 75* (**1999**)1679.

245. N. D. Nguyen, M. Schmeits, *Phys. Rev. B 75* (**2007**) 075307.

246. E. W. J. Mitchell, J. W. Mitchell, *JSTOR 210* (**1951**) 70.

247. H. Campbell, T. W. Hagler, D. L. Smith, J. P. Ferraris, *Phys. Rev. Lett. 76* (**1996**) 1900.

248. Y. Xia, J. Ouyang, *J. Mater. Chem. 21* (**2011**) 4927.

249. D. Alemu, H. - Y. Wei, K. - C. Hod, C. - W. Chu, *Energy Environ. Sci. 5* (**2012**) 9662.

250. O. Synooka, F. Kretschmer, M. D. Hager, M. Himmerlich, S. Krischok, D. Gehrig, F. Laquai, U. S. Schubert, G. Gobsch, H. Hoppe, *ACS Appl. Mater. Interfaces 14* (**2014**) 11068.

251. Q. Wang, Y. Zhou, H. Zheng, J. Shi, C. Li, C. Q. Su, L. Wang, C. Luo, D. Hu, J. Pei, J. Wang, J. Peng, Y. Cao, *Org. Electron. 12* (**2011**)1858.

252. a) H. Zhou, Y. Zhang, J. Seifter, S. D. Collins, C. Luo, G. C. Bazan, T. - Q. Nguyen, A. J. Heeger, *Adv. Mater. 25* (**2013**) 1646; b) X. Liu, W. Wen, G. C. Bazan, *Adv. Mater. 24* (**2012**) 4505.

253. P. N. Murgatroyd, *J. Phys. D 3* **(1970)**151.

254. H. T. Nicolai, G. A. H. Wetzelaer, M. Kuik, A. J. Kronemeijer, B. de Boer, P. W. M. Blom, *Appl. Phys. Lett. 96* (**2010**) 172107.

255. H. Ma, H. - L. Yip, F. Huang, A. K. - Y. Jen, *Adv. Funct. Mater. 20* (**2010**) 1371.

256. J. Peet, J. Y. Kim, N. E. Coates, W. L. Ma, D. Moses, A. J. Heeger, G. C. Bazan, *Nat. Mater. 6* (**2007**) 497.

257. C. V. Hoven, X. - D. Dang, R. C. Coffin, J. Peet, T. - Q. Nguyen, G. C. Bazan, *Adv. Mater. 22* (**2010**) 63.

258. a) S. J. Lou, J. M. Szarko, T. Xu, L. Yu, T. J. Marks, L. X. Chen, *J. Am. Chem. Soc. 133* (**2011**) 20661; b) J. - L. M. Abboud, R. Notario, *Pure Appl. Chem. 71* (**1999**) 645.

259. P. M. Beaujuge, J. M. J. Fréchet, *J. Am. Chem. Soc. 133* **(2011**) 20009.

260. J. K. Lee, W. L. Ma, C. J. Brabec, J. Yuen, J. S. Moon, J. Y. Kim, K. Lee, G. C. Bazan, A. J. Heeger, *J. Am. Chem. Soc. 130* (**2008**) 3619.

261. J. H. Seo, A. Gutacker, Y. Sun, H. Wu, F. Huang, Y. Cao, U. Scherf, A. J. Heeger, G. C. Bazan, *J. Am. Chem. Soc. 133* (**2011**) 8416.

262. J. Liu, Y. Shi, Y. Yang; *Adv. Funct. Mater. 11* (**2001**) 420.

263. X. Liu, S. Huettner, Z. Rong, M. Sommer, R. H. Friend; *Adv. Mater. 24* (**2012**) 669.

264. J. E. Carlé, M. Helgesen, M. V. Madsen, E. Bundgaard, F. C. Krebs, *J. Mater. Chem. C 2* (**2014)**1290.

265. Y. - X. Liu, L. - F. L*ü*, N. Yu, Y. - Z. Lu, Q. - P. Lu, C. - M. Zhang, F. Yi, T. Ai - Wei, Y. - F. Hu, Z. - D. Lou, T. Feng, Y. - B. Hou, *Chin. Phys. B 23* (**2014**) 118802.

266. a) L. M. Andersson, C. M*ü*ller, B. H. Badada, F. Zhang, U. W*ü*rfel, O. Ingan*ä*s, *J. Appl. Phys. 110* (**2011**) 024509; b) Y. - C. Huang, S. - Y. Chuang, M. - C. Wu, H. - L. Chen, C. - W. Chen, W. - F. Su, *J. Appl. Phys. 106* (**2009**) 034506.

267. M. Zhang, X. Guo, Y. Li, *Adv. Energ. Mater. 1* (**2011**) 557.

268. M. D. Perez, C. Borek, S. R. Forrest, M. E. Thompson, *J. Am. Chem. Soc. 131* (**2009**) 9281.

269. R. Kroon, M. Lenes, J. C. Hummelen, P. W. M. Blom, B. De Boer, *Polym. Rev. 48* (**2008**) 531.

270. Y. - C. Chen, C. - Y. Hsu, R. Y. - Y. Lin, K. - C. Ho, J. T. Lin, *Chem. Sus. Chem. 6* (**2013**) 20.

271. C. K. stner, S. Rathgeber, D. A. M. Egbe, H. Hoppe. *J. Mater. Chem. A 1* (**2013**) 3961.

272. R. Qin, W. Li, C. Li , C. Du, C. Veit, H. - F. Schleiermacher, M. Andersson, Z. Bo, Z. Liu, O. Inganäs, U. Wuerfel, F. Zhang, *J. Am. Chem. Sol. 131* (**2009**) 14612.

273. Y. Kim, S. Cook, S. M. Tuladhar, S. A. Choulis, J. Nelson, J. R. Durrant, D. D. C. Bradley, M. Giles, I. Mcculloch, C.- S. Ha, M. Ree, *Nature Materials 5* (**2006**) 197.